Comprehensive insights into the impedimetric characterization of dielectric thin films

Zur Erlangung des akademischen Grades eines
DOKTORS DER INGENIEURWISSENSCHAFTEN (Dr.-Ing.)

von der KIT-Fakultät für Chemieingenieurwesen und Verfahrenstechnik
des Karlsruher Instituts für Technologie (KIT)
genehmigte

DISSERTATION

von
M. Sc. Benedikt Sapotta
aus Heilbronn

Tag der mündlichen Prüfung: 24.01.2023

Erstgutachter: Prof. Dr.-Ing. Matthias Franzreb
Zweitgutachter: Prof. Dr.-Ing. Dr. h.c. Wilhelm Schabel

Acknowledgement

Abstract

This work aims to provide practical insights into the opportunities offered by impedance spectroscopy for the characterization and analysis of thin film coatings. The primary focus is laid on coating materials with no or negligible electronic conduction and exhibiting film thicknesses in the low nano- to micrometer range. Although based on the electrical stimulation of the coated system by an alternating voltage signal, the impedimetric method of analysis is not intended to alter the sample under investigation and, accordingly, allows for a non-destructive testing of the coated system. In general, recording of an impedance response is remarkably straightforward and can be conducted with relatively inexpensive equipment. The key challenge of impedance analysis is found in the mathematical processing of the inherently non-specific impedance data in order to gain access to the underlying physical parameters describing the sample system under test. In this regard, purposeful modelling of impedance data requires a profound awareness of the dominant charge transport mechanisms anticipated for the experimental sample system. In order to establish a basic understanding of the measurement technique in this work, several physicochemical processes of relevance and their individual contributions to the recorded impedance data are introduced. In particular, the influence and determination of fundamental material properties such as ionic conductivity and relative static permittivity are addressed. Furthermore, the characteristic differences of an impedance spectrum obtained with coated and uncoated electrode systems in contact to a fluidic reference medium are highlighted. For this purpose, generalized models are presented and discussed in detail which serve as potential starting points for the comprehensive interpretation of impedance data collected with uncoated and coated electrode systems. The models illustrate the pivotal role of the fluidic reference medium as well as the electrode geometry on the individual opportunities available for coating analysis. In this context, the beneficial properties of the interdigitated microelectrode structure for the characterization of thin films are mapped out.

The centerpiece of this work represents the experimental demonstration of the impedimetric thin film analysis technique conducted with commercially available interdigitated electrode chips. The impedance spectra were collected with a fully automated microfluidic system which was specifically designed and optimized within the scope of this work. Owing to the complete disclosure of the individual impedance spectra together with the associated Python scripts used to process the data sets in the online repository *KITOpenData*, the reader is offered the opportunity to independently reflect upon (and potentially improve) the evaluation strategies proposed throughout this work.

The electrode chips were covered with model thin film coatings prepared from materials known as *HKUST-1* and *ZIF-8* which belong to the material class of metal-organic frameworks. As crystalline coordination polymers, both HKUST-1 and ZIF-8 have gained considerable attention due to their inherent nanoporosity and their well-defined chemical structure. The bottom-up synthesis of surface-mounted HKUST-1 coatings, in particular, has already been extensively characterized with well-established thin film analysis techniques such as quartz-crystal microbalance and surface-plasmon resonance which allows for a direct comparison with the proposed impedimetric method of analysis.

The impedance data collected during the cycle-by-cycle coating process with the surface mounted HKUST-1 thin film reveal a near linear growth rate of (1.5±0.3) nm/cycle following the initial nucleation step. The general validity of the impedimetric thickness estimation is substantiated by the visualization of the coated electrode structures by scanning electron microscopy. In addition, the solvent medium the HKUST-1 thin film is exposed to is shown to significantly alter the dielectric properties of the coating material which clearly indicates the accessibility of the solvent molecules to the intracrystalline pore network of HKUST-1. It is particularly noteworthy that the variations of the dielectric properties are coincident with variations of the ionic conductivity of the coating material. The general relationship between dielectric and conductive properties of HKUST-1 corresponds well to the dielectric exclusion effect which hypothesizes a partitioning of the ionic concentration at the phase boundary between a liquid medium and a nanoporous material. The more decisive influence on the ionic conductivity of the coating, however, appears to originate from a strong chemical interaction of the HKUST-1 material with the solvent molecules. Polar protic molecules coordinated to the open metal sites of the crystalline framework are known to be rendered more acidic thereby amplifying the degree of solvent autoprotolysis and, accordingly, the amount of charge carriers available for ionic migration.

In contrast to the well established HKUST-1 thin film synthesis, the deposition of the ZIF-8 thin films on the electrode structures was performed with a modified coating process. The aqueous synthesis procedure is shown to produce high quality ZIF-8 thin film with a preferential crystalline orientation depending on the host substrate. While the impedance data collected with a ZIF-8 coated IDE structure clearly indicate the presence of the thin film, no quantitative information on the dielectric or conductive properties of the coating material could be derived from the data. Scanning electron micrographs of the ZIF-8 coated electrode structures following the impedimetric characterization indicate a chemical incompatibility of the coating material with the fluidic testing media.

Zusammenfassung

Das Ziel der vorliegenden Arbeit ist die Vermittlung praktischer Einblicke in die Charakterisierung und Analyse dünner Schichten mithilfe der Impedanzspektroskopie. Der Fokus liegt hierbei auf Schichtdicken im unteren Nano- bis Mikrometerbereich sowie Schichtmaterialien mit vernachlässigbarer Elektronenleitung. Obwohl die impedimetrische Analyse auf der Anregung des beschichteten Systems durch Anlegen einer Wechselspannung beruht, führt die Messung an sich zu keiner Veränderung der untersuchten Probe, wodurch die Impedanzspektroskopie zu den zerstörungsfreien Prüfmethoden zählt. Das Aufzeichnen von Impedanzspektren ist bemerkenswert unkompliziert und lässt sich mit relativ kostengünstiger Hardware durchführen. Die eigentliche Herausforderung der Impedanzanalyse liegt vielmehr in der Modellierung der im Grunde unspezifischen Impedanzwerte zur Bestimmung konkreter, physikalischer Parameter des untersuchten Systems. Die mathematische Aufbereitung von Impedanzdaten erfordert hierbei ein tiefgreifendes Verständnis der zu erwartenden Ladungstransport-Mechanismen.

Um einen prinzipiellen Überblick über die Messmethodik zu vermitteln, werden zu Beginn der Arbeit eine Reihe relevanter physikalisch-chemischer Prozesse sowie deren charakteristischen Beiträge zu einer gemessenen Impedanzantwort vorgestellt. Hierbei wird insbesondere auf den Einfluss und die Ermittlung grundlegender Materialeigenschaften wie der Ionenleitfähigkeit und der relativen statischen Permittivität eingegangen. Im Anschluss werden die wesentlichen Unterschiede eines Impedanzspektrums, das mit einem beschichteten bzw. unbeschichteten Elektrodensystem in Kontakt mit einem fluidischen Referenzmedium aufgezeichnet wurde, herausgearbeitet. Zu diesem Zweck werden verallgemeinerte Ansätze zur Modellierung der frequenzabhängigen Impedanzantwort in Abhängigkeit des Beschichtungszustandes des Elektrodensystems detailliert vorgestellt. Anhand der dargelegten Modelle lässt sich die entscheidende Bedeutung des fluidischen Referenzmediums sowie der verwendeten Elektrodengeometrie auf die zur Verfügung stehenden Möglichkeiten zur Dünnschichtcharakterisierung ableiten. Insbesondere ein gezielter Einsatz der interdigitalen Mikroelektrodenstruktur bietet in diesem Zusammenhang ideale Voraussetzungen zur impedimetrischen Dünnschichtanalyse.

Das Herzstück dieser Arbeit ist die experimentelle Demonstration der impedanzbasierten Dünnschicht-Analysetechnik mithilfe von handelsüblichen, interdigitalen Elektrodenchips. Die hierfür verwendeten Impedanzspektren wurden in einem vollautomatisierten, mikrofluidischen Messsystem aufgenommen, welches im Rahmen dieser Arbeit speziell entwickelt und optimiert wurde. Durch die vollständige Offenlegung der aufgezeichneten Impedanzspektren zusammen mit den für die Auswertung verwendeten Python-Skripten im Repository *KITOpenData* wird

dem Leser die Gelegenheit geboten, die in dieser Arbeit vorgeschlagenen Auswertestrategien selbständig nachzuverfolgen (und möglicherweise sogar zu verbessern).

Als Modelldünnschichten wurden die Materialien *HKUST-1* und *ZIF-8*, welche zur Material-klasse der metallorganischen Gerüstverbindungen gezählt werden, auf die interdigitalen Elek-trodenchips aufgetragen. Als kristalline Koordinationspolymere haben sowohl HKUST-1 als auch ZIF-8 aufgrund ihrer Nanoporösität und ihrer wohl-definierten chemischen Struktur in den letzten Jahren erhebliches Forschungsinteresse erregt. Insbesondere die Bottom-up-Synthese von oberflächenverankerten HKUST-1-Beschichtungen wurde bereits intensiv mit etablierten Dünnschicht-Analyseverfahren wie der Quarzkristall-Mikrowaage und Oberflächenplasmonen-resonanz analysiert, was eine direkte Gegenüberstellung mit der in dieser Arbeit vorgestellten impedimetrischen Charakterisierungsmethode ermöglicht.

Die Impedanzdaten, die während des zyklusweisen Beschichtungsprozesses mit der oberflächen-verankerten HKUST-1-Dünnschicht gesammelt wurden, belegen eine nahezu lineare Wachs-tumsrate von (1.5±0.3) nm/Zyklus im Anschluss an den anfänglichen Keimbildungsschritt. Die Zuverlässigkeit des impedanzbasierten Schichtdickenschätzwertes ließ sich durch die Visua-lisierung der beschichteten Elektrodenstrukturen mittels Rasterelektronenmikroskopie validieren. Darüber hinaus konnte gezeigt werden, dass die dielektrischen Eigenschaften von HKUST-1 er-heblich von der Lösemittelzusammensetzung des verwendeten Referenzmediums abhängen. Auf Basis der strukturellen Eigenschaften von HKUST-1 lässt sich hierbei eine freie Zugänglichkeit des intrakristallinen Porennetzwerks für die verwendeten Lösungsmittelmoleküle ableiten. Zeit-gleich mit der Variation der dielektrischen Eigenschaften lässt sich zudem eine signifikante Verän-derung der Ionenleitungseigenschaften von HKUST-1 detektieren. Die allgemeine Beziehung zwischen den dielektrischen Eigenschaften und der Ionenleitfähigkeit von HKUST-1 entspricht dabei qualitativ den für nanoporöse Materialien postulierten dielektrischen Ausschlusseffekt, welcher eine Partitionierung der Ionenkonzentration an der Phasengrenze zwischen dem flüssigen Referenzmedium und der Dünnschicht vorhersagt. Der entscheidendere Einfluss auf die Ionen-leitfähigkeit der Beschichtung scheint jedoch von einer starken chemischen Wechselwirkung des HKUST-1 Materials mit den Lösungsmittelmolekülen auszugehen. Die HKUST-1 Struktur ver-fügt über lewissaure Koordinationsstellen, welche mit polar protischen Lösungsmittelmolekülen interagieren und somit den Autoprotolysegrad des in den Nanoporen befindlichen Lösungsmit-tels modifizieren. Als Folge scheint sich die innerhalb des HKUST-1 Materials für die ionische Migration zur Verfügung stehende Ionenkonzentration auf Basis der Lösungsmittelzusammenset-zung des Referenzmediums beeinflussen zu lassen.

Im Vergleich zu der bereits etablierten HKUST-1 Dünnschichtsynthese wurden die ZIF-8 Schichten auf den Elektrodenstrukturen über einen modifizierten Beschichtungsprozess herge-stellt. Mit der in der Arbeit vorgestellten wässrigen Syntheseroutine lassen sich qualitativ hochwertige ZIF-8 Dünnschichten herstellen, welche eine bevorzugte Wachstumsorientierung aufweisen. Zwar lassen sich aus den mit ZIF-8 beschichteten interdigitalen Elektrodenstruk-turen aufgezeichneten Impedanzspektren eindeutig die Präsenz der Dünnschicht ableiten, eine quantitative Eingrenzung der Dünnschichteigenschaften erschien jedoch nicht möglich.

Contents

List of Symbols

Symbols representing Constants

symbol	value	unit	name
e	$1.60218 \cdot 10^{-19}$	C	elementary charge
ε_0	$8.85419 \cdot 10^{-12}$	F/m	vacuum permittivity
F	96485.3	C/mol	Faraday constant
R	8.31446	J/mol/K	universal gas constant
π	3.14159	-	Pi
N_A	$6.02214 \cdot 10^{23}$	1/mol	Avogadro number

physical constants retrieved from [1]

Latin Symbols

symbol	unit	representing	symbol	unit	representing
A	m²	electrode area	c_M	mol/m³	molar concentration in the reference medium
A_C	m²	coated electrode area			
A_{IDE}	m²	interdigitated area	d_P	m	IDE electric field penetration length
a	m	cubic lattice constant			
a_{cov}	-	surface coverage	d_f	m	IDE finger thickness
C_C	F	coating capacitance	d_C	m	coating thickness
$C_{C,LS}$	F	coating capacitance during the linker step	$d_{C,MHDA}$	m	thickness of the MHDA SAM
$C_{C,MS}$	F	coating capacitance during the metal step	$\boldsymbol{E}$	V/m	electric (vector) field
			f	Hz	AC frequency
C_{DL}	F	double layer capacitance	f_{CR}	Hz	characteristic relaxation frequency
$C_{DL,uc}$	F	double layer capacitance of the uncoated electrode			
			f_δ	Hz	characteristic frequency of diffusion
$\bar{c}_{DL}$	F/m²	area normalized double layer capacitance			
			f_{res}	Hz	resonance frequency
C_{Geo}	F	geometric capacitance	I	A	current
C_P	F	parasitic capacitance	I_A	A	current amplitude
$C_{P,1}$	F	parasitic capacitance of the electrical connection	I_D	A	displacement current
			I_{DL}	A	electrical double layer charging current
$C_{P,2}$	F	parasitic capacitance of the IDE chip			
			I_{D+P}	A	displacement + polarization current

Latin Symbols

symbol	unit	representing
$I_{D+P,A}$	A	displacement + polarization current amplitude
I_F	A	Faradaic current
$I_{F,A}$	A	Faradaic current amplitude
I_M	A	migration current
$I_{M,A}$	A	migration current amplitude
I_P	A	polarization current
j	-	imaginary unit
K_{Cell}	1/m	cell constant
$K_{Cell,theo}$	1/m	theoretical cell constant
L	m	electrode separation distance
L_f	m	IDE finger length
$L_{f,eff}$	m	effective IDE finger length
L_P	H	parasitic inductance
$L_{P,1}$	H	parasitic inductance of the electrical connection
$L_{P,2}$	H	parasitic inductance of the IDE chip
N_f	-	number of IDE fingers
N_{freq}	-	number of frequency points
n_d	-	order of diffraction
p_{IR}	-	peak intensity ratio
P_{MC}	-	molar partitioning coefficient between sample medium and coating
Q_{DL}	S·s$^{\alpha_{DL}}$	double layer CPE capacitance parameter
R_E	Ω	electrolyte resistance
$R_{E,LS}$	Ω	electrolyte resistance during the linker step
$R_{E,MS}$	Ω	electrolyte resistance during the metal step
R_C	Ω	coating resistance
R_{ct}	Ω	charge transfer resistance
$R_{ct,0}$	Ω	charge transfer resistance of the bare surface
R_P	Ω	parasitic resistance
$R_{P,1}$	Ω	parasitic resistance of the electrical connection

symbol	unit	representing
$R_{P,2}$	Ω	parasitic resistance of the IDE chip
R_W	Ω	Warburg resistance
r	m	radius
r_s	m	solvated ion radius
s	m	electrode spacing
T	K	temperature
t	s	time
t_L	m	truncated length
Δt	s	time interval
U	V	voltage
U_A	V	voltage amplitude
v	m/s	ionic drift velocity
W	Ω/s$^{0.5}$	Warburg coefficient
$\Delta W_{S,i}$	J/mol	change in solvation energy
$\Delta W_{S,B,i}$	J/mol	change in Born solvation energy
w	m	electrode width
w_i	-	weighting factor during data fit
Z	Ω	impedance
$|Z|$	Ω	impedance, modulus
Z_{diff}	Ω	diffusion impedance
Z_{eq}	Ω	equivalent impedance
Z_F	Ω	Faradaic impedance
Z_{FLW}	Ω	finite length Warburg impedance
Z_{FSW}	Ω	finite space Warburg impedance
Z_{imag}	Ω	impedance, imaginary part
Z_{IDE}	Ω	impedance response of the IDE chip
Z_k	Ω	individual impedance contribution
Z_M	Ω	measured impedance response
Z_{real}	Ω	impedance, real part
Z_S	Ω	sample system impedance response
Z_W	Ω	Warburg impedance
z_i	-	valency

Greek Symbols

symbol	unit	representing
α_{DL}	-	double layer CPE exponent
β	°	angle of circular segment
γ_{Born}	-	Born ratio
$\delta_{i,C}$	m²/s	diffusion coefficient of i in the coating
$\delta_{i,M}$	m²/s	diffusion coefficient of i in the sample medium
ε	F/m	permittivity
ε_r	-	relative permittivity
$\varepsilon_{r,C}$	-	relative permittivity of the coating
$\varepsilon_{r,C,MHDA}$	-	relative permittivity of the MHDA SAM
$\varepsilon_{r,w}$	-	relative permittivity of water
$\varepsilon_{r,eff}$	-	efffective relative permittivity
$\varepsilon_{r,eff,LS}$	-	efffective relative permittivity during the linker step
$\varepsilon_{r,eff,MS}$	-	efffective relative permittivity during the metal step
$\varepsilon_{r,real}$	-	relative permittivity, real part
$\varepsilon_{r,imag}$	-	relative permittivity, imaginary part
$\varepsilon_{r,S}$	-	relative static permittivity
ζ	-	linear interpolation parameter
ζ_{LS}	-	linear interpolation parameter during the linker step
ζ_{MS}	-	linear interpolation parameter during the metal step
η	-	metallization ratio of IDE geometry
η_M	kg/m/s	dynamic viscosity of sample medium
θ_d	°	diffraction angle
κ_M	S/m	electrolytic conductivity of the reference medium
κ_C	S/m	electrolytic conductivity of the coating
Λ_m	S·m²/mol	molar conductivity
λ	m	spatial wavelength of IDE geometry
λ_X	m	X-ray wavelength
μ	m²/V/s	ionic mobiliy
Φ	°	phase shift
$\tilde{\Phi}$	rad	phase shift
Φ_{D+P}	°	phase shift of displacement + polarization current
Φ_{DL}	°	phase shift of double layer (dis-)charge current
Φ_F	°	phase shift of Faradaic current
Φ_M	°	phase shift of migration current
ϕ	V	electric potential
χ^2	-	squared sum of weighted residuals
Ψ_A	V·m	electric flux
ω	rad/s	angular frequency

List of Abbreviations

AC	alternating current
BDS	broadband dielectric spectroscopy
BET	Brunauer–Emmett–Teller
BSE	backscattered electron contrast
BTC	benzene-1,3,5-tricarboxylic acid
CIF	crystallographic information file
CPE	constant phase element
CRM	conductivity reference medium
CuAc	copper(II) acetate
DC	direct current
DRM	dielectric reference medium
ECM	equivalent circuit model
ECM 1	equivalent circuit model 1, see Fig 4.4 A)
ECM 2	equivalent circuit model 2, see Fig 4.4 B)
FM	Frank-van der Merwe
HKUST-1	Hongkong University of Science and Technology - 1
H_2SO_4 CV	cyclic voltammetry using diluted sulfuric acid
IDE	interdigitated electrode

ID-IS	interdigitated impedance spectroscopy
IS	impedance spectroscopy
IUPAC	International Union of Pure and Applied Chemistry
KCl	potassium chloride
MC	Monte Carlo
MHDA	16-Mercaptohexadecanoic acid
MOF	metal-organic framework
OMS	open metal site
QCM	quartz crystal microbalance
RMS	root mean square
SAM	self-assembled monolayer
SE	secondary electron contrast
SEM	scanning electron microscopy
SK	Stranski-Krastanov
SPR	surface plasmon resonance
SURMOF	surface mounted metal-organic framework
UV	ultraviolet irradiation
VM	Volmer-Weber
XRD	X-ray diffraction
ZIF-8	zeolitic imidazolate framework - 8
ZnAc	zink acetate

List of Tables

List of Figures

1. Motivation and Scope

The impedimetric analysis of dielectric thin films has been, is still, and will continue to be pursued across a variety of different research fields. Historically, oxidic thin films which develop on metal surfaces appear to have been the first instances of *coated electrode systems* which have been systematically investigated by impedance measurements. The early studies were driven with the intent to characterize and optimize anodic oxide films which form on valve metals [2, 3] or assess the long-term passivation of metallic components which are exposed to a corrosive environment [4]. The impedimetric characterization of *coated electrode systems* in corrosion science has since expanded to encompass not only native corrosion layers [5] but also polymeric anti-corrosion layers applied to metal surfaces [6, 7]. Likewise, early impedimetric research projects on oxidic thin films have demonstrated the opportunity to quantify the diffusive mass transport of electroactive species in the coating material [8]; a concept which has since found entry into basic battery research [9]. In a similar manner, impedance spectroscopy has proven to be a useful tool to assess the performance of moisture barrier layers protecting sensitive organic semiconductor components [10, 11]. A completely different set of applications has evolved from the study of microelectrode systems coated with a functional material. Examples include chemocapacitive [12, 13] or chemiresistive [14, 15] gas sensing which detect the selective adsorption of target molecules through the associated change in the dielectric or ionic conduction properties of the thin film. Furthermore, the impedance based growth monitoring and susceptibility testing of biofilm matrices is being actively explored [16]. Additionally, coated microelectrode structures are also frequently employed for impedimetric bioaffinity probing as well as label-free immunosensing for biomedical applications [17].

The broad recognition of impedimetric techniques as a powerful tool for the characterization of thin films covering electrode surfaces, however, coincides with an unavoidable lack of coordination between individual scientific contributions. Owing to an increasing degree of specialization into the respective research fields, the focus is often laid on a single aspect of the impedance analysis while the full spectrum of potential characterization opportunities remains overlooked. Newcomers to impedance analysis will also notice a considerable ambiguity of terminology and

a plethora of modelling approaches which further complicate the mutual comprehension and scientific transfer between separate research fields.

This work aims to provide an extensive yet compact overview on what impedance spectroscopy has to offer for the characterization of thin films. To conceptualize the individual opportunities within one consistent theoretical framework, a slightly modified equivalent circuit model is used which was originally devised in the field of corrosion science. After a brief introduction into the relevant fundamentals in chapter 2, the model is comprehensively outlined in chapter 3. For this purpose, the circuit model is broken down into its individual components detailing their physical origin and potential appropriation for thin film analysis. The second part of this work is dedicated to showcase the practical application of the theoretical concepts mapped out in chapter 2 and 3 using two model thin film coatings covering interdigitated microelectrode chips. The coating materials belong to the family of metal-organic frameworks and are commonly referred to by their respective acronyms *HKUST-1* and *ZIF-8*. The impedance data sets were generated with a purposefully designed experimental setup comprised of a variety of testing solutions which could be sequentially supplied to a custom-built microfluidic flow cell housing the (coated) electrode chip under investigation. Chapter 4 provides practical insights into experimental details as well as the mathematical processing of the impedance raw data. To verify the functionality of the experimental setup as well as the fundamental validity of the evaluation procedure, the system was tested against a set of dielectric and conductive reference media featuring well-defined material properties which will be addressed in chapter 5. By making use of the programming interface of all relevant hardware components, the native HKUST-1 coating process could be emulated inside the experimental setup together with scheduled impedance spectrum recordings at predetermined time intervals. The data collected during the coating process is comprehensively discussed and analyzed in chapter 6 by taking advantage of the theoretical framework outlined in chapter 3. Additionally, the impedimetric method of analysis provided unique insights into the ionic transport properties of the coating material which will be addressed as well. The final chapter details the progress made during the ZIF-8 thin film preparation and initial impedance testing.

The impedance raw data as well as the proposed data processing approach was comprehensively disclosed in the supplementary research data to facilitate scientific transfer with interested readers. Particular emphasis was laid on the validation of the evaluation procedure with the help of reference data sets, careful compensation of parasitic impedance contributions and scanning electron microscopy. It is suggested that interdigitated impedance spectroscopy represents a promising alternative to complementary thin film analysis strategies based on the well established surface plasmon resonance or quartz-crystal microbalance techniques.

2. Fundamentals

Herein, a selection of theoretical concepts will be briefly outlined which will facilitate the understanding of the following chapters. To obtain more detailed information on impedance spectroscopy as a measurement technique, the following textbooks are highly recommended [18, 19, 20, 21, 22, 23].

2.1. Impedance Spectroscopy

Impedance refers to the total opposition to alternating current (AC) flow exerted by a system under test [24]. The impedance value Z at the AC frequency $f = \omega/2\pi$ is derived from a comparison of periodic input to output signal. When working under potentiostatic control and assuming sinusoidal shape of the signal, the transient input voltage $U(t)$ with the amplitude U_A can be mathematically described as

$$U(t) = U_A \sin(\omega t). \tag{2.1}$$

The associated current response $I(t)$ with the amplitude $I_A(\omega)$ will be of the same frequency as $U(t)$ however accompanied by a characteristic phase shift $\Phi(\omega)$.

$$I(t) = I_A \sin(\omega t - \tilde{\Phi}) \tag{2.2}$$

In this work, $\tilde{\Phi}$ and Φ are used to differentiate the phase shift in units of radian and degree, respectively. A graphical representation of the input and output signals as defined in equations 2.1 and 2.2 is provided in Fig 2.1. For every frequency ω, the impedance $Z(\omega)$ is comprised of a total of two independent parameters. For this purpose, $Z(\omega)$ is usually expressed as a complex number by virtue of a real $Z_{Real}(\omega)$ and imaginary $Z_{Imag}(\omega)$ part.

$$Z = Z_{Real} + j \cdot Z_{Imag} \tag{2.3}$$
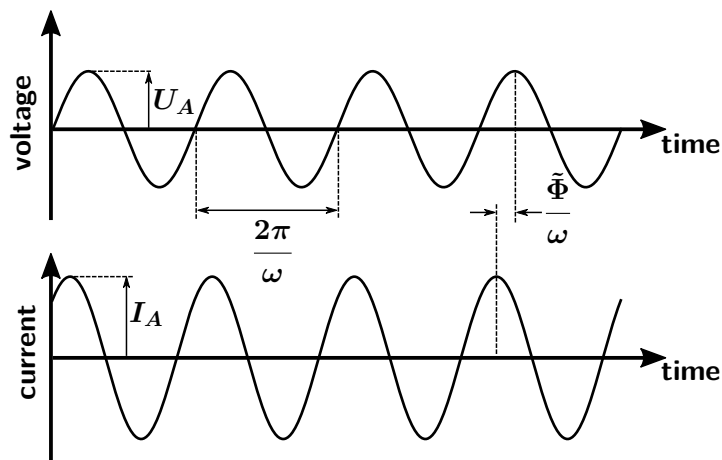
Figure 2.1. Graphical illustration of the transient voltage and current signals defined in equations 2.1 and 2.2.

When working with sinusoidal signals, real and imaginary contribution to Z can be computed from the transient $U(t)$ and $I(t)$ functions via the amplitude ratio

$$\frac{U_A}{I_A} = |Z| = \sqrt{Z_{Real}^2 + Z_{Imag}^2} \tag{2.4}$$

and the phase shift Φ

$$tan(\Phi) = \frac{Z_{Imag}}{Z_{Real}}. \tag{2.5}$$

The uptake an impedance spectrum requires the measurement of Z at several different ω within the intended frequency range.

Impedance spectroscopy (IS) is closely related to a technique known as (broadband) dielectric spectroscopy (BDS). Both spectroscopy variants rely on the frequency dependent current/voltage relationship which, however, is interpreted in different ways [18, 19]. Traditionally, IS appears to primarily focus on interfacial/electrochemical processes [18] whereas the same technique is referred to as BDS when studying bulk relaxation processes of electronic dipoles [19]. In this work, no clear distinction between IS and BDS is made to provide a holistic framework for the analysis of dielectric thin films on the basis of current/voltage relationship at AC frequencies up to the MHz range.

2.1.1. Categorization of Current Responses

In general, the total current response $I(t)$ of a sample medium stimulated by a periodic voltage signal $U(t)$ at the frequency ω stems from the overlap and interaction of a variety of different physicochemical phenomena. The naming of the individual current contributions varies from author to author. To avoid ambiguity of terminology, the naming of ionic current contributions used in this work complies with the 2019 IUPAC recommendations for electrochemistry [25]. The application of a voltage difference between two electrodes as schematically drawn in Fig 2.2 induces an electric (vector) field $\boldsymbol{E}$ leading, by definition, from the surface of the positively
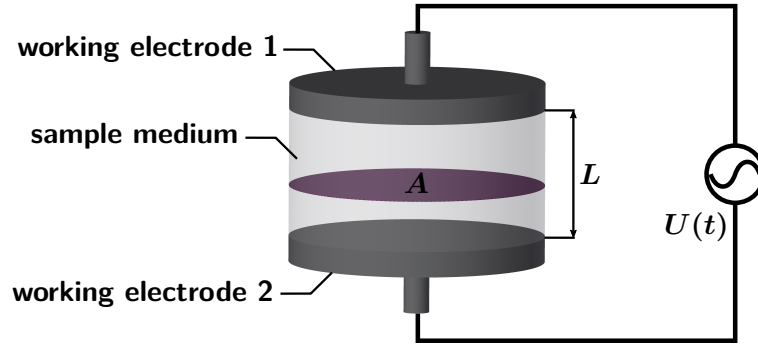
Figure 2.2. Schematic representation of a symmetrical electrode setup enclosing a homogeneous sample medium and stimulated by an alternating input signal $U(t)$. The parallel plate electrodes each have a surface area of A and are separated by a constant distance d. When neglecting fringing effects at the outer edges, the total electric flux Ψ_A at the area A between the electrodes can be reasonably approximated with equation 2.6.

charged electrode to the surface of the negatively charged electrode. To facilitate the theoretical description of the resulting current flow in this chapter, it is inferred that a homogeneous electric flux Ψ of $\boldsymbol{E}$ orthogonal to the electrode area $\boldsymbol{A}$ can be assigned to the electrode geometry by means of the effective electrode separation distance L in the form of

$$\Psi_A = \iint_A \boldsymbol{E} \cdot d\boldsymbol{A} \cong \frac{U}{L} A = \frac{U}{K_{Cell}}. \tag{2.6}$$

The effective ratio of L/A is often reduced to a more generalized geometry factor or 'cell constant' K_{Cell} of the respective electrode setup.

The displacement current contribution I_D is independent of the sample medium in between the electrodes. I_D originates from the alternation of the electric field and can be formulated with the help of equation 2.6 and the vacuum permittivity ε_0 as [26]

$$I_D = \varepsilon_0 \frac{\partial \Psi_A}{\partial t} = \frac{\varepsilon_0}{K_{Cell}} \frac{\partial U}{\partial t}. \tag{2.7}$$

In addition to I_D, the derivative $\frac{\partial U}{\partial t}$ also induces polarization of the sample medium giving rise to the polarization current I_P. The magnitude of I_P depends on the bulk dielectric properties of the specific sample medium e.g. the presence of molecules with permanent dipole moments which may rotate freely under the influence of an electric field [27]. When assuming linear, isotropic and sufficiently frequency invariant dielectric behavior, I_P can be written in the form of a *dielectric* displacement current [28]

$$I_P = \frac{\varepsilon_0(1 - \varepsilon_r)}{K_{Cell}} \frac{\partial U}{\partial t}. \tag{2.8}$$

The prerequisites under which a constant relative permittivity ε_r parameter can be used as a proportionality factor in equation 2.8 will be revisited in section 2.3. Formulation of I_P in accordance to equation 2.8 is advantageous for it allows merging of I_D and I_P into a unified

I_{D+P} contribution given their mathematical similarity.

$$I_{D+P} = I_D + I_P = \frac{\varepsilon_0 \varepsilon_r}{K_{Cell}} \frac{\partial U}{\partial t} \tag{2.9}$$

When applying the voltage input signal $U(t)$ defined in equation 2.1 to equation 2.9 one arrives at

$$I_{D+P} = U_A \omega \frac{\varepsilon_0 \varepsilon_r}{K_{Cell}} \cos(\omega t) \tag{2.10}$$

with current amplitude $I_{D+P,A}$ and phase shift Φ_{D+P} of

$$I_{D+P,A} = U_A \omega \frac{\varepsilon_0 \varepsilon_r}{K_{Cell}} \quad , \quad \Phi_{D+P} = -90°. \tag{2.11}$$

In addition to I_{D+P}, the spatial potential distribution also induces the movement of charge carriers in the bulk of the sample medium. When assuming the sample medium to be an electrolyte containing solvated ions, i.e., positively charged cations and negatively charged anions as charge carriers, the associated ionic migration current I_M can be written as

$$I_M = \kappa_M \Psi_A = \frac{\kappa_M}{K_{Cell}} U. \tag{2.12}$$

The electrolytic conductivity κ_M appearing in equation 2.12 will be discussed in detail in chapter 2.2. Application of the voltage input signal $U(t)$ from equation 2.1 to equation 2.12 leads to

$$I_M = \frac{\kappa_M}{K_{Cell}} U_A \sin(\omega t) \tag{2.13}$$

with current amplitude $I_{M,A}$ and phase shift Φ_M of

$$I_{M,A} = \frac{\kappa_M}{K_{Cell}} U_A \quad , \quad \Phi_M = 0° \tag{2.14}$$

Both I_M and I_{D+P} derive from the bulk between the two electrodes. While $I_{M,A}$ in equation 2.14 is frequency-invariant, $I_{D+P,A}$ increases linearly with f. Equality of $I_{D+P,A}$ and $I_{M,A}$ is observed at the characteristic relaxation frequency f_{CR}, which can be expressed as

$$2\pi U_A f_{CR} \frac{\varepsilon_0 \varepsilon_r}{K_{Cell}} = \frac{\kappa_M}{K_{Cell}} U_A \quad \Leftrightarrow \quad f_{CR} = \frac{1}{2\pi} \frac{\kappa_M}{\varepsilon_0 \varepsilon_r}. \tag{2.15}$$

Importantly, f_{CR} is a function of ε_r and κ_M stemming from the sample medium alone and does not depend on the electrode geometry that is being used.

The application of the voltage input signal $U(t)$ to equation 2.12 is valid only for a small period of time following the introduction of the voltage perturbation, i.e., at sufficiently large frequencies. As ions start to accumulate in the electric double layers at the surface of the charged electrodes, the "bulk" of the sample medium between the electrodes is gradually deprived of the actual potential gradient which is schematically illustrated in Fig 2.3. With the potential dropping significantly across the relatively thin electric double layers, the measured current signal no longer primarily derives from the "bulk" of the sample medium but is rather dominated by physicochemical processes occurring in close proximity to electrode surface; a phenomenon
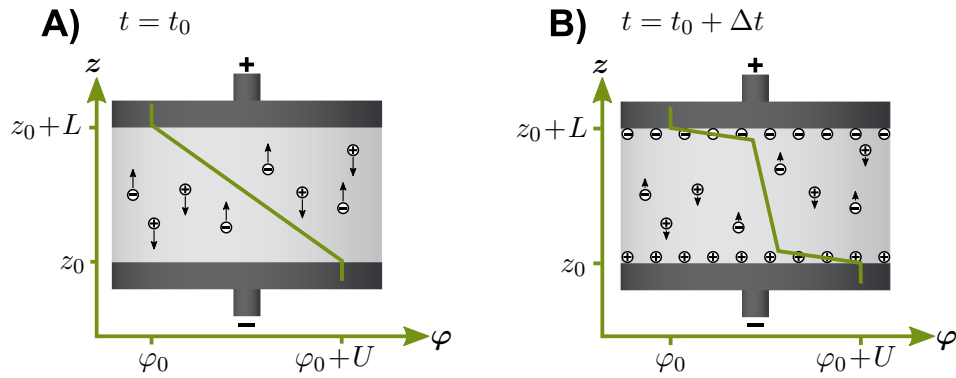
Figure 2.3. Schematic potential map of a parallel plate sample cell A) immediately after a potential U is applied and B) after an additional time Δt has passed. The ionic migration towards the respective countercharged electrode surface leads to the accumulation of charge carriers in ionic double layers at the electrode surface. As a result, the applied potential drops significantly across the few nanometer thick layers while the potential gradient through the "bulk" of the electrode geometry is steadily reduced.

commonly referred to as "electrode polarization" [29]. Interfacial current contributions may be dominated by the charge and discharge current of the electric double layer I_{DL} with commonly expected phase shifts Φ_{DL} larger than the ideal -90°. In case electroactive species are present in the sample medium and the applied potential difference exceeds a specific threshold value (e.g. by employing a constant DC bias in addition to the sinusoidal voltage perturbation), heterogeneous charge transfer (redox) reactions may take place at the interface between electrode and sample inducing Faradaic current contributions I_F which, in the simple case, can be modelled by the Butler-Volmer equation [20]. From a geometrical perspective, interfacial current contributions depend on the electrode area A rather than the generalized cell constant K_{Cell}.

The dominant contributing effects to $I(t)$ in equation 2.2 for a homogeneous sample medium as a function of the frequency f are schematically summarized in Fig 2.4. In contrast to f_{CR} marking the boundary between which I_{D+P} or I_M represent the major contributor to $I(t)$, an equivalent, universally valid boundary between I_M and, e.g., I_{DL} at the lower frequency end cannot be easily drawn. The reason is that interfacial effects depend on a variety of factors [18] such as surface roughness, presence of adsorbed dielectric species, chemical groups at the surface, etc.

2.1.2. Interpretation of Impedance Spectra

Impedance data sets are evaluated on the basis of physical models with the goal to establish an appropriate transfer function coupling the current and voltage signal [30]. In this chapter it is inferred, that the impedance response of the system under test satisfies the conditions of linearity, causality and stability [21]. Importantly this includes that the system under test stimulated by the voltage perturbation does not significantly change during the timeframe the impedance spectrum is recorded.

Several approaches have been developed to model the frequency dependent current-voltage
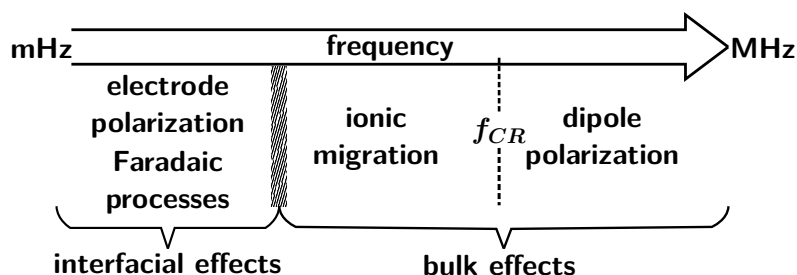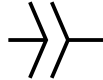
Figure 2.4. Simplified categorization of dominant current response mechanisms relevant for impedance spectroscopy of a homogeneous sample medium as a function of frequency. The practical frequency bandwidth available for impedimetric analysis usually ranges from a few milli- to a few megahertz.

relationship. On the fundamental level, the current response can be computed directly from the underlying physical principles, a simplified perspective thereon was provided in the previous chapter. A useful starting point for direct physical modelling is in general a Poisson-Nernst-Planck system of equations equipped with appropriate boundary conditions [30]. There are a few specialized cases for which elaborate physical models have already been firmly established allowing a direct modelling of the impedance data; e.g. the point defect model considering the growth and failure of a passive film on a metal surface in a corrosive environment [4] or in the field of solid oxide fuel cells [31]. While being considered the most informative method of interpretation [30], the challenge associated to the direct modelling of the current response is not to be underestimated.

An alternative approach is the abstraction of the physical current-voltage relationship into a lumped element model as it is routinely done in electrical systems engineering. For this purpose, each physical effect imparting an impedance (current) contribution is mimicked by an idealized electric component such as a resistor or capacitor. The individual electric components (i.e. physical effects) are subsequently assembled into an electric network thereby generating an equivalent circuit analog which is intended to mimic the total impedance response of the respective system under test. To facilitate the understanding, the theoretical description of the bulk dielectric polarization, bulk ionic migration and non-ideal interfacial electrode polarization by means of equivalent circuit parameters is provided in table 2.1.

The impedance contribution of the geometric capacitance C_{Geo} representing dielectric polarization and the electrolyte resistance R_E representing ionic migration can be derived directly from their respective current contribution outlined in chapter 2.1.1 and equations 2.4 and 2.5. In most practical cases, the electrode polarization effect at the solid electrode/electrolyte interface does not behave ideally capacitive. A variety of different factors have been suggested to contribute to the deviation from ideally capacitive behavior [32]. Within the framework of equivalent circuit modelling, the impedance contribution stemming from the charge and discharge of the electrical double layer is often mimicked by a constant phase element CPE_{DL} whose impedance response is a function of the capacitance parameter Q_{DL} and the constant phase α_{DL} [29]. An effective value for the interfacial capacitance C_{DL} can be estimated on the basis of Q_{DL}, α_{DL} and R_E with the help of the the Brug equation [33].

Table 2.1. Modelling of the impedance contribution originating from I_{D+P}, I_M and I_{DL} as equivalent circuit components.

	geometric capacitance	electrolyte resistance	non-ideal double layer capacitance
circuit component	$C_{Geo} = \dfrac{\varepsilon_r \varepsilon_0}{K_{Cell}}$	$R_E = \dfrac{K_{Cell}}{\kappa_M}$	CPE_{DL}
representing	dipole polarization	ionic migration	electrode polarization
impedance	$Z = -\dfrac{j}{\omega C_{Geo}}$	$Z = R_E$	$Z = \dfrac{1}{Q_{DL}(j\omega)^{\alpha_{DL}}}$

A) circuit components in series
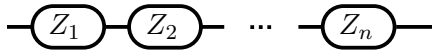
$$Z_{eq} = \sum_{k}^{n} Z_k$$

B) circuit components in parallel
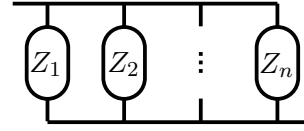
$$\frac{1}{Z_{eq}} = \sum_{k}^{n} \frac{1}{Z_k}$$

Figure 2.5. Schematic outlining how an equivalent impedance value Z_{eq} is calculated for A) serial and B) parallel connection of individual circuit components.

$$C_{DL} \approx Q_{DL}^{\frac{1}{\alpha_{DL}}} R_E^{\frac{(1-\alpha_{DL})}{\alpha_{DL}}} \tag{2.16}$$

Bare planar surfaces are expected to provide area normalized double layer capacitances $\bar{c}_{DL}$ in the range of 10 - 50 µF per cm^2 of surface area depending on the chemical environment (see for instance [20, 18]). The interfacial capacitance is often smaller than the expected C_{DL} for a bare surface due to the presence of dielectric contaminants e.g. metal oxides or adsorbed organic molecules.

The basic principles of how impedance contributions of individual circuit components combine under serial or parallel connection are summarized in Fig 2.5. A reasonable combination of the single circuit components outlined in table 2.1 into a full equivalent circuit model (ECM) is provided in Fig 2.6 which, from now on, will be referred to as *ECM 1*. The upper branch of ECM 1 takes into account the displacement and polarization current I_{D+P} passing through the electrode geometry which is independent of the ionic conduction pathway represented by the lower circuit branch. Serial connection of R_E with CPE_{DL} is reasonable since the the ionic migration current I_M passing through the bulk is eventually curtailed by the charging/discharging rate of the double layer as indicated in Fig 2.3.
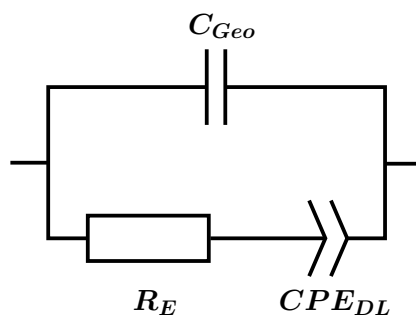
Figure 2.6. Equivalent circuit model 1 (ECM 1) which is a useful starting point for the analysis of impedance data recorded from a homogeneous sample medium under non-Faradaic conditions. ECM 1 accounts for dipole polarization, ionic migration and electrode polarization.
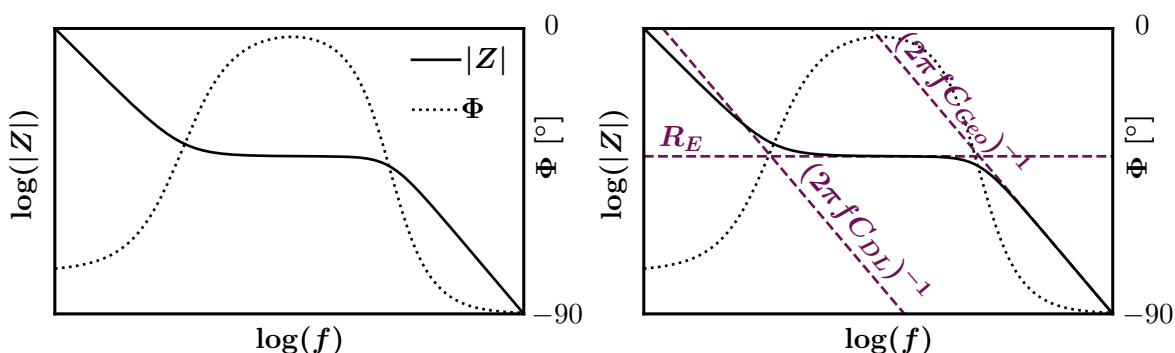
Figure 2.7. Impedance data characteristic for a homogeneous, non-Faradaic system modelled with ECM 1 and visualized by a Bode plot. The Bode plot displays the absolute impedance value $|Z|$ and phase shift Φ as a function of the AC frequency f. The frequency regimes for which the impedance spectrum is dominated by either the geometric capacitance C_{Geo}, solution resistance R_E or the (non-ideal) double layer capacitance C_{DL} are easily recognisable as indicated in the graph on the right.

2.1.3. Graphical Representation of Impedance Response

There are several different methods of impedance spectrum visualization each of which may have distinct advantages [20, 23]. Throughout this work, impedance data is visualized by a *Bode plot* which is considered beneficial in providing a comprehensive overview of an impedance spectrum in its entirety [34]. For the Bode representation of impedance data, both impedance modulus $|Z|$ and phase angle Φ are plotted as a function of the AC frequency f. $|Z|$ and f are displayed on a logarithmic scale as their values usually range across several orders of magnitude. An example Bode plot visualizing impedance data modelled with ECM 1 (Fig 2.6) is provided in Fig 2.7. To facilitate the understanding of data visualization, the isolated impedance responses of C_{Geo}, R_E and C_{DL} are shown in the graph on the right. A Bode plot allows for a clear distinction between capacitively (C_{Geo}, C_{DL}) or resistively (R_E) dominated frequency ranges of the impedance spectrum.

2.2. Electrolytic Conductivity

The capability of an electrolyte solution to conduct current originates from the presence of charge carriers in the form of solvated ionic species which migrate under the influence of

a electric potential gradient. All solvated ionic species (anions and cations) present in the electrolyte solution contribute to the electrolytic conductivity κ_M via [35]

$$\kappa_M = \sum_{i=1}^{N_i} c_i \Lambda_{m,i} \tag{2.17}$$

with c_i referring to the molar concentration and $\Lambda_{m,i}$ to the molar conductivity of the solvated ionic species i. $\Lambda_{m,i}$ depends on the valency z_i and mobility μ_i of the ionic species i which can be modelled with the help of the Faraday constant F [35].

$$\Lambda_{m,i} = F|z_i|\mu_i \tag{2.18}$$

μ_i is defined as the ratio of ionic drift velocity v_i divided by the magnitude of the electric field vector $\boldsymbol{E}$ acting upon the ionic species i. When establishing force balance between viscous drag force expressed by Stokes' law and the electric force imparted on the spherical ionic species i by $\boldsymbol{E}$, an approximate link between μ_i and the sample medium viscosity η_M together with the radius of the solvated ionic species $r_{s,i}$ and the elementary charge e can be obtained [35].

$$\mu_i = \frac{v_i}{\| \boldsymbol{E} \|} = \frac{|z_i|e}{6\pi\eta_M r_{s,i}} \tag{2.19}$$

In addition to equation 2.19, μ_i is also connected to the diffusion constant of the ionic species within the electrolytic medium $\delta_{i,M}$ via the Einstein relation as a function of the universal gas constant R, the absolute temperature T and F [35].

$$\delta_{i,M} = \frac{RT}{F}\frac{\mu_i}{|z_i|} \tag{2.20}$$

Combination of equations 2.17, 2.18 and 2.20 provides a direct link between ionic diffusivity in the electrolyte solution and its bulk electrolytic conductivity.

$$\kappa_M = \frac{F^2}{RT}\sum_{i=1}^{N_i} c_i \delta_{i,M} \tag{2.21}$$

Importantly, the concentration of the solvated ionic species c_i was used in the formulation of equations 2.17 - 2.21. Undissociated or associated ion pairs do not carry a net charge and, accordingly, do not contribute to κ_M. This circumstance is relevant for weak electrolytes which only partially dissociate when dissolved. Also, ion pairing needs to be considered when working with low permittivity solvents [36].

2.2.1. Measurement

κ_M is a non-specific parameter which can be used as an estimate of an electrolyte solution's ionic concentration [37]. Measurement of κ_M is routinely carried out as part of a regular quality assurance routine in various industrial and laboratory applications [38]. Accordingly, several standard test methods for the measurement of κ_M in aqueous solutions have been specified [39, 40, 41]. When applied as an electroanalytical tool to, e.g., track the progression of a

chemical reaction, the measurement of κ_M is also referred to as *conductometry* [25]. κ_M is obtained from impedance measurement by identifying the contribution of the electrolyte resistance R_E contribution. R_E can be transformed into κ_M when accounting for the electrode geometry by making use of the cell constant K_{Cell}.

$$\kappa_M = \frac{K_{Cell}}{R_E} \tag{2.22}$$

K_{Cell} is usually determined experimentally with the help of (certified) conductivity reference solutions. For unknown reasons, a slight dependence of an electrode geometry's K_{Cell} value on the actual conductivity level has been repeatedly reported [38]. Extraction of R_E from the impedance response requires compensation of unwanted contributions stemming from electrode polarization, the cabling, etc. [38] As κ_M is expected to increase by 1 - 3 % per °C [42], the measurement temperature should always be provided alongside κ_M. At field strengths exceeding several 10^6 V/m, κ_M may become a function of E which is referred to as the Wien effect [43]. A frequency dependence of κ_M was postulated as well but is generally treated as negligible [44, 45].

2.3. Relative Permittivity

The relative permittivity ε_r is a bulk material property describing its polarizability under the influence of an electric field. It is defined as the relative increase in permittivity ε as compared to the permittivity of vacuum ε_0 [26].

$$\varepsilon_r = \frac{\varepsilon}{\varepsilon_0} \tag{2.23}$$

The term "dielectric constant" is frequently used in reference to ε_r however considered obsolete following modern terminology [46, 47]. From a phenomenological perspective, ε_r constitutes the macroscopic representation of a material's dielectric properties [19]. These include for instance the rotation of mobile molecules with a permanent dipole moment in the fluid phase to partially align to an external electric field (orientation polarization) or the introduction of dipole moments in ionic crystals such as NaCl, KCl (ionic polarization) [48, 27]. From a fundamental perspective, ε_r needs to be treated as tensor, which however can be neglected when isotropic dielectric material properties are assumed [49].

2.3.1. Frequency Dependence

In general, ε_r is frequency dependent, thus ε_r becomes $\varepsilon_r(f)$. Moreover, when accounting for both dielectric dispersion and absorption, $\varepsilon_r(f)$ is treated as a complex number [49].

$$\varepsilon_r(f) = \varepsilon_{r,real}(f) - j \cdot \varepsilon_{r,imag}(f). \tag{2.24}$$

For comparative reason, the complex dielectric spectra of pure water and ethanol at 25 °C is provided in Fig 2.8 which were generated from literature data [50, 51]. Importantly, $\varepsilon_r(f)$
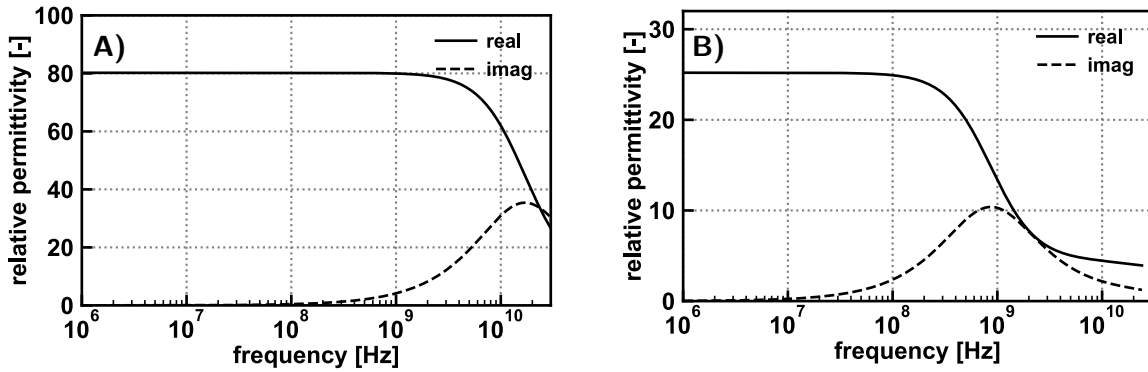
Figure 2.8. Complex dielectric function of A) water [51] and B) ethanol [50] at 25°C. The complex nature of $\varepsilon_r(f)$ is usually confined to frequencies exceeding several MHz.

usually converges to a static, real value $\varepsilon_{r,S}$ at "low" frequencies [49].

$$\lim_{f \to 0} \varepsilon_r(f) = \varepsilon_{r,S} - j \cdot 0 = \varepsilon_{r,S} \tag{2.25}$$

The static permittivity assumption at "low" frequencies has been suggested to be sufficiently justified for a variety of liquids at 1 MHz and below [52]. With this work focusing primarily on "low" frequency techniques, ε_r is treated as frequency independent, i.e., equivalent to $\varepsilon_{r,S}$ in the following chapters. For most materials, $\varepsilon_{r,S}$ is expected to range between 1 and 100 (see e.g. [53]).

2.3.2. Permittivity of Mixtures

There appears to be no universally applicable mixing law to estimate the effective permittivity of a mixture comprised of two or more molecular species. Conversely, the effective permittivity inherently depends on the respective molecular interactions and the resulting microstructure [54, 55]. As an example, the change in effective permittivity values observed for n-alcohols of varying chain length upon addition of water molecules are plotted in Fig 2.9. When comparing Fig 2.9 A) and B) it is important to highlight, that the effective relative permittivity of a binary mixture does not necessarily range in between the relative permittivity of its individual constituents. Rather, the effective permittivity of molecular mixtures provides the unique opportunity to deduce potential interaction mechanisms of its individual constituents [56].

2.3.3. Measurement

ε_r is a non-specific parameter which can be used to assess a material's dielectric properties. In comparison to κ_M, measurement of ε_r appears rare. Knowledge of a material's ε_r is relevant in the electronic industry for, among other, performance optimization of miniaturized integrated circuits [59, 60]. Accordingly, a standard test method for solid electrical insulators has been defined [61]. When applied as an electroanalytical tool e.g. to track the progression of a chemical reaction, the measurement of ε_r is also referred to as *dielectrometry* [25]. One notable application is the monitoring of curing reactions observed for thermoset polymers

A)

B)
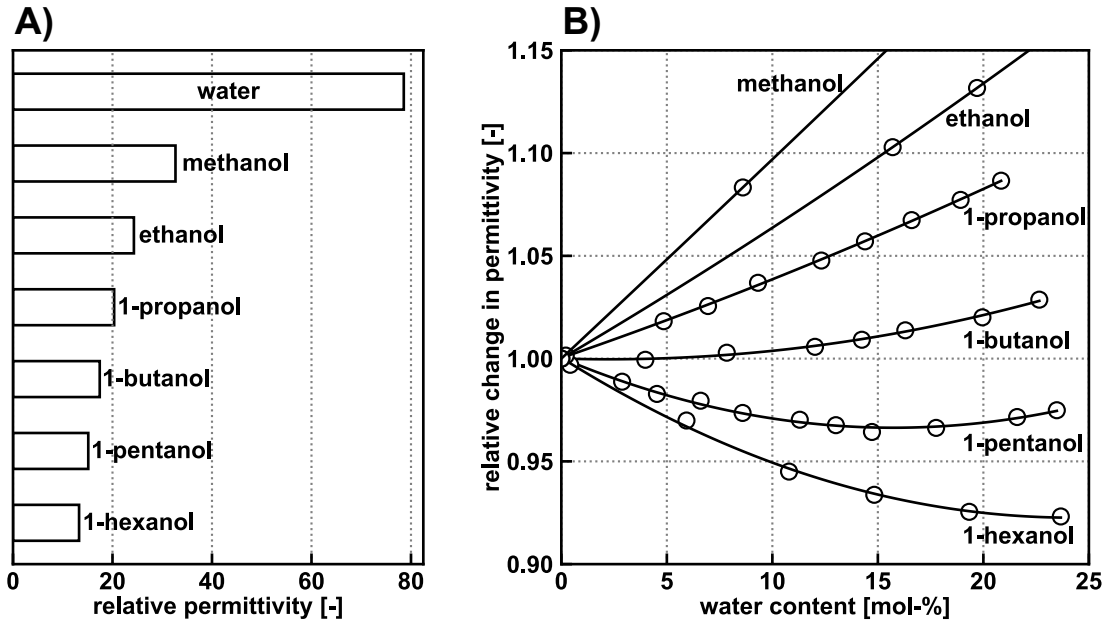
Figure 2.9. A) Relative permittivity of water [44] and various n-alcohols [56, 57, 58] at 25 ^{o}C. B) Relative change in permittivity observed for the same n-alcohols at 25 ^{o}C as a function of the molar water content of the binary mixture which was adapted from [56].

[62, 63].

ε_r is obtained from impedance measurements by identifying the geometric capacitance C_{Geo} contribution. C_{Geo} can be transformed into ε_r when accounting for the cell constant K_{Cell} and vacuum permittivity ε_0.

$$\varepsilon_r = \frac{K_{Cell}C_{Geo}}{\varepsilon_0} \tag{2.26}$$

Provided that parasitic capacitive contributions are sufficiently taken care of, K_{Cell} can be obtained by using reference materials whose ε_r have already been precisely determined. Importantly, C_{Geo} should be extracted at frequencies for which the impedance response is unaffected by electrode polarization, e.g., at frequencies above the characteristic relaxation frequency f_{CR} defined in equation 2.15 [18]. The reason is that the non-ideal double layer capacitance C_{DL} acts both in parallel to, and, is usually several orders of magnitude larger than C_{Geo}. A satisfactory compensation of the non-ideal C_{DL} to gain reliable access to C_{Geo} is often not possible [52]. For conductive media, electrode polarization may impart non-negligible contributions to the impedance response even at frequencies in the MHz range. In this case, the static $\varepsilon_{r,S}$ cannot be directly measured. However, $\varepsilon_{r,S}$ can still be estimated from an extrapolation of the complex permittivity function of the same medium [64]. As $\varepsilon_{r,S}$ is usually expected to decrease with an increase in temperature, the measurement temperature should always be provided alongside $\varepsilon_{r,S}$ [44]. An E-field dependence of a material's $\varepsilon_{r,S}$ value is possible, usually at field strengths in the order of 10^6 V/m [19] which may be related to the dielectric breakdown of the material.
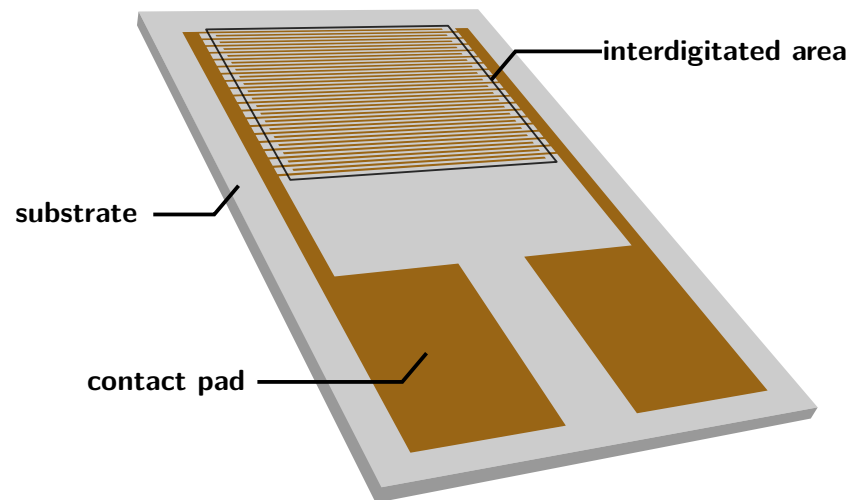
Figure 2.10. Model of an interdigitated thin film electrode chip. For impedimetric analysis, the sample medium under test is placed onto the interdigitated area.
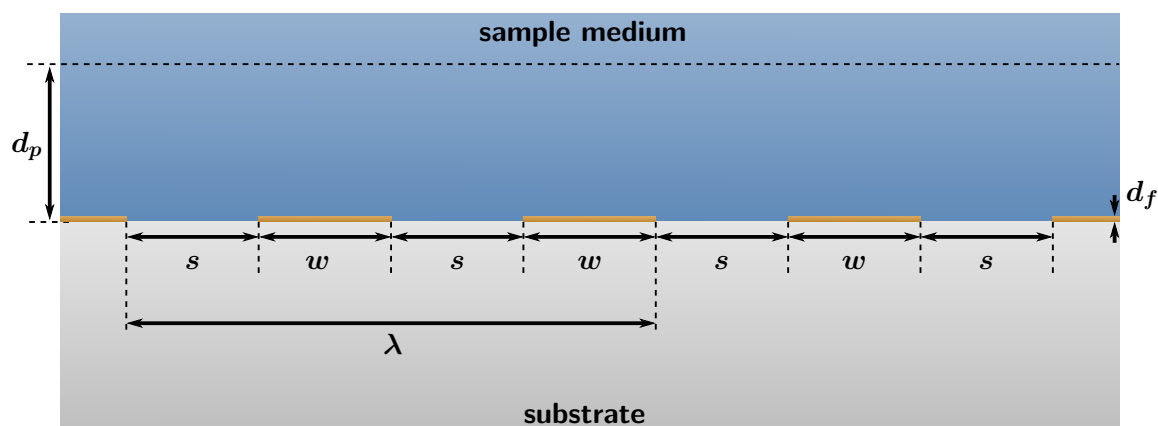
Figure 2.11. Schematic cross section of the interdigitated area outlining the geometrical parameters electrode width w, electrode spacing s, spatial wavelength λ, electric field penetration length d_p and electrode finger thickness d_f.

2.4. Interdigitated Electrode Geometry

The "interdigital" or "interdigitated" electrode (IDE) is a distinct type of planar microelectrodes comprised of two interlaced, non-contacting comb-structures deposited on a dielectric substrate. For practical reasons, the IDE geometry is usually realized in the form of low-cost, disposable electrode chips, a representative model of which is displayed in Fig 2.10. The miniaturized and standardized nature of the IDE geometry are particularly attractive for the reproducible impedimetric analysis of sample media at low volume requirements. In addition, owing to the unique spatial arrangement of the electrode fingers, IDEs are capable of providing conclusive current signals over a broad range of frequencies even for highly resistive sample media. Accordingly the IDE geometry has been proposed for a variety of impedance based sensing applications [65]. The geometry of an IDE structure is defined by the length L_f and number of electrode fingers N_f as well as the electrode width w, spacing s and finger thickness d_f illustrated in the schematic cross section of the interdigitated area in Fig 2.11. Due to the periodicity of the
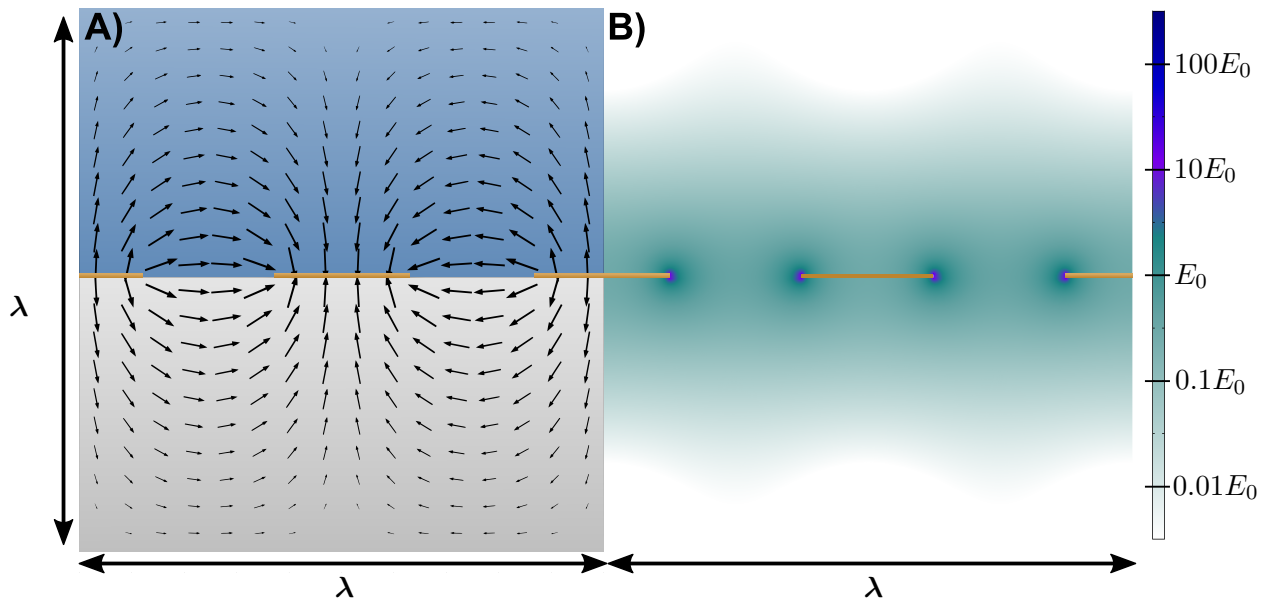
Figure 2.12. Schematic electric field E distribution at the cross section of an IDE geometry visualized by A) the vector field and B) its magnitude normalized to $E_0 = U/s$. The potential distribution was computed through finite element modelling of Poisson's equation for electrostatics with the help of the Comsol Multiphysics 5.5 software.

electrode structure, a spatial wavelength λ can be assigned to an IDE geometry defined as

$$\lambda = 2(s + w). \tag{2.27}$$

Furthermore, IDE structures are usually characterized by their total metallization ratio of the interdigitated area η defined as

$$\eta = \frac{w}{s + w}. \tag{2.28}$$

The electric vector field through the sample medium in contact with the interdigitated area as well as the substrate underneath is indicated in Fig 2.12. The curvature of the electric field make IDEs sensitive only to effects occurring in close proximity of the electrode fingers. The corresponding effective electric field penetration depth d_p is subject to the inhomogeneous potential distribution and often approximated to range between $\lambda/4$ and $\lambda/3$ [66].

2.4.1. Cell Constant

The cell constant K_{Cell} of a periodic IDE structure can be estimated based on its metallization ratio η, the number N_f and length L_f of the electrode fingers [67]. First, let $K(k)$ describe the complete elliptic integral of the first kind

$$K(k) = \int_0^{\frac{\pi}{2}} \frac{d\phi}{\sqrt{1 - k^2 sin^2(\phi)}} \tag{2.29}$$

with the modulus k defined as

$$k = sin\left(\frac{\pi}{2}\eta\right) \tag{2.30}$$
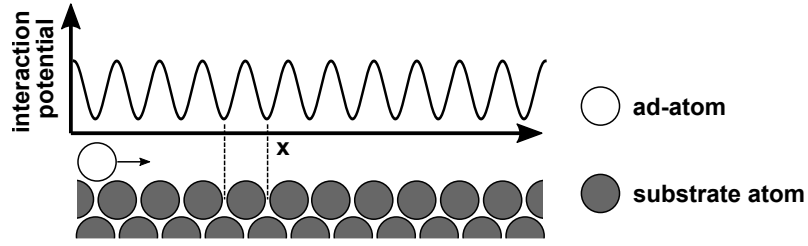
Figure 2.13. Schematic 1D representation of the periodic interfacial interaction potential experienced by a single ad-atom moving across a crystalline substrate [73]. Thin film growth is referred to as "epitaxial" if nucleation of ad-atoms to the actual crystalline layer is influenced by the atomic arrangement of the crystalline substrate imparting favorable potential minima.

and k' as

$$k' = \sqrt{1 - k^2} \tag{2.31}$$

then

$$K_{Cell} = \frac{2}{L_f(N_f - 1)} \frac{K(k')}{K(k)}. \tag{2.32}$$

A Python script solving equation 2.32 as a function of η, N_f and L_f is provided in chapter 1 of the supplementary research data. Importantly, equation 2.32 assumes an idealized IDE geometry with negligible finger thickness d_f and does not account for fringing effects at the edge of the interdigitated area.

2.5. Epitaxial Growth of Thin Films

The term *epitaxy* introduced by Royer in 1928 [68] describes a distinct type of heterogeneous nucleation process of a crystalline material on a preexisting substrate. Epitaxy requires the host substrate to expose a well-defined crystalline surface area to the supersaturated phase containing the target atoms/precursors to nucleate. The characteristic feature of epitaxy is that the atomic arrangement of the newly formed epitaxial layer is influenced by the crystalline structure of the substrate surface imparting a preferential *epitaxial orientation* [69, 70]. The energetic effect of the substrate surface on the nucleation of newly arriving ad-atoms is schematically portrayed in Fig 2.13 highlighting *interaction potential troughs* experienced by ad-atoms diffusing across the interface which are being exploited during epitaxial nucleation.

For a successfully grown epitaxial thin film, the crystallographic planes in contact at the substrate/thin film interface share symmetry and feature closely related lattice parameters [68]. This assimilation of crystalline arrangement during nucleation allows for an epitaxially formed thin film to potentially feature unique properties otherwise unattainable in bulk crystallization processes of the same material [71]. Epitaxy can be initiated from a supersaturated vapor, liquid or solid phase and in general requires thorough optimization of process parameters such as substrate preparation, degree of supersaturation, etc. [72]

The early phase of epitaxial thin film formation can be differentiated on the basis of surface energy considerations into three classical growth modes schematically outlined in Fig 2.14. In
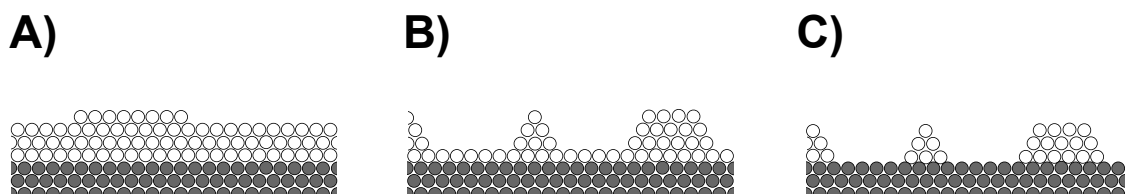
Figure 2.14. The three classical growth modes of epitaxy. A) Frank-Van der Merwe (layer by layer), B) Stranski-Krastanov (layer plus island), C) Volmer-Weber (island) growth mode [69].

the idealized case of the Frank-van der Merwe growth (FM) behavior shown in Fig 2.14 a), epitaxy is initiated by a two-dimensional nucleation of a crystalline monolayer covering the substrate material. FM is characteristic for negligible lattice mismatch between epitaxial layer and substrate featuring continuous crystalline monolayer additions to the growing thin film. For this reason, FM is also referred to as "layer-by-layer" or "step-flow growth" and provides access to crystalline thin films of highest quality [72]. The Stranski-Krastanov growth (SK) mode shown in Fig 2.14 B) is similar to FM insomuch as it starts by two-dimensional nucleation on the crystalline substrate. In contrast to FM however, the SK growth mode continues with the formation of three dimensional islands on top of the initial monolayer. The Volmer-Weber (VM) growth model in Fig 2.14 C) refers to the initiation of the epitaxial growth through three-dimensional nucleation of individual islands. With the continuation of the epitaxial process, the islands grow in size leading to eventual intergrowth and complete surface coverage of the substrate surface.

2.6. Metal-Organic Framework Thin Films

The materials prepared as model thin films in this work belong to the family of coordination polymers and are commonly referred to as metal-organic frameworks (MOFs) [74]. MOFs are comprised of two building blocks, namely metal or metal-oxo centers which are interconnected by organic linker molecules featuring two or more functional groups. In comparison to other polymeric materials, MOFs stand out for two reasons. First, the highly ordered, periodic arrangement of their building blocks impart crystallinity meaning the MOF structure itself can be comprehensively analyzed by X-ray diffraction. Second, owing to the spatial arrangement of the crystal lattice, MOFs are inherently porous with internal pore sizes ranging up to a few nanometers. The synthesis of a MOF structure is usually based on two precursor solutions containing a metal source and the organic linker molecules, respectively. Mixing of the two precursor solutions under optimized synthetic conditions (e.g. temperature, solvent environment, etc.) leads to the nucleation and growth of individual MOF particles.

Preparation of MOFs as a thin film coating covering a substrate surface can be achieved through a variety of different synthetic approaches [75, 76]. A straighforward method is for example the placement of the substrate to be coated into the precursor solution mixture which may induce heterogeneous nucleation on the substrate surface together with an eventual crystal intergrowth to a pinhole-free MOF coating. An alternative approach which produces
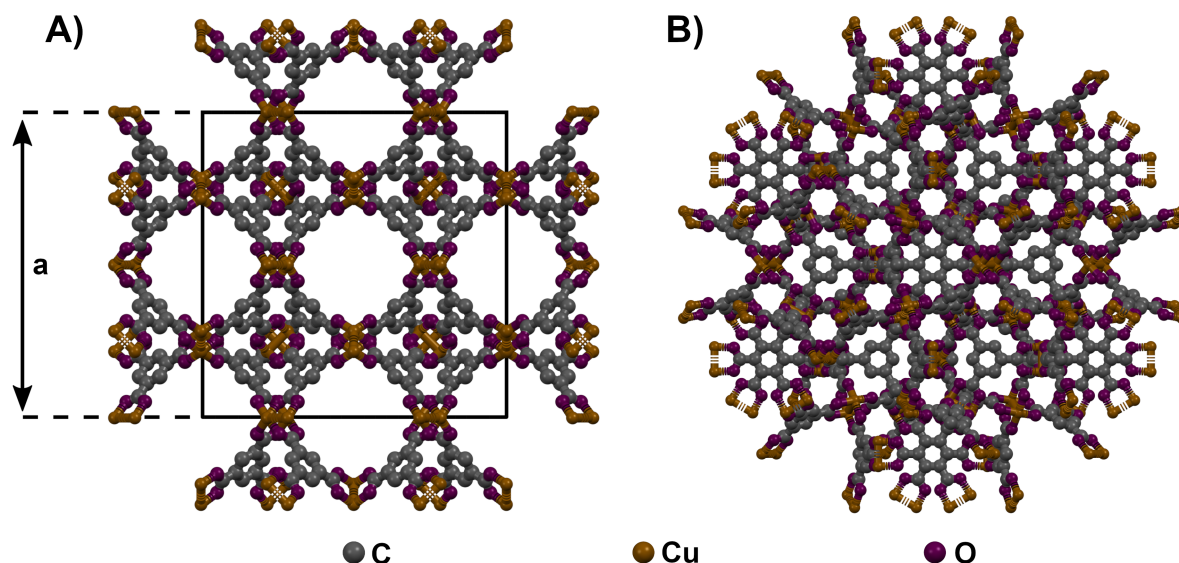
Figure 2.15. HKUST-1 metal-organic framework viewed along the A) [100] and B) [111] direction. At 293 K, the cubic lattice constant a is estimated at 2.63 nm [90]. The square shaped pores visible in A) are computed to be 0.95 x 0.95 nm in size and penetrate the crystalline material along the three main crystallographic axes thereby establishing a 3D network of interconnected pores [90]. The models shown in the figure were generated from the crystallographic information file (CIF) deposited by the authors of [90].

so called "surface mounted metal-organic framework" relies on the sequential exposure of a functionalized surface to the metal and linker precursor solution separated by an additional rinsing step. While time consuming, the resulting film thickness can be directly controlled by the amount of sequential exposure steps. The underlying synthetic approach is usually referred to as "layer-by-layer liquid phase epitaxy" (e.g. in [77],[78],[79],[80],[81],[82]). Importantly, the prefix "layer-by-layer" is used to emphasize the self termination of the thin film growth during each exposure step [83, 84] rather than to refer to the classical Frank-Van der Merwe mode of epitaxial growth. When described in accordance to the epitaxial thin film growth mechanisms shown in Fig 2.14, the SURMOF synthesis has been reported to be consistent with the classical Volmer-Weber growth mode [85, 86, 87, 88, 89].

2.6.1. *HKUST-1 SURMOF* Coating

The material known as *HKUST-1* was prepared as the primary model thin film in this work to be studied by impedimetric techniques. The name of this "archetypical" MOF structure [74] derives from the place where it was first described in 1999, the Hongkong University of Science and Technology [90]. From a crystallographic perspective, HKUST-1 is comprised of copper(II) dimers serving as metal centers interconnected by 1-3-5 benzenetricarboxylate ligands as linker molecules which self-assemble within the cubic space group no. 225 $Fm\bar{3}m$. A model of the HKUST-1 crystal structure is shown in Fig 2.15. Due to the spatial arrangement of the crystal lattice, the HKUST-1 structure is interpenetrated by a highly ordered 3D-pore system. The largest pore is about 0.9x0.9 nm in size and can be easily identified from the [100] perspective shown in Fig 2.15 A) as the pores penetrate the material along its three main crystallographic

axis. A characteristic feature of the HKUST-1 structure are the open metal sites in axial position to the copper(II) dimers which allow the chemisorption of polar guest molecules such as water to the crystalline framework [91]. Brunauer-Emmet-Teller (BET) specific surface areas of the HKUST-1 structure based on nitrogen adsorption isotherms are in the order of 1000 m^2/g [92]. Pristine HKUST-1 behaves as an electric insulator preventing intralattice electron transport. The electric properties of the nanoporous material may however be influenced by the guest molecules loaded into the internal pore structure [93]. In general, HKUST-1 is not water stable and the crystal structure will degrade when in contact with liquid water or water adsorbed from humid air [94]. When prepared as individual particles by homogeneous nucleation, HKUST-1 nuclei usually adopt octahedral morphology as indicated in Fig 2.16 A). HKUST-1 was the first SURMOF structure to be successfully coated on a functionalized surface by the aforementioned liquid phase epitaxy method in 2007 [95]. Depending on the chemical functionalization of the surface to be coated, the HKUST-1 structure can be prepared into a preferential orientation [96]. The film thickness of fully developed HKUST-1 SURMOFs usually ranges from a few hundreds of nanometers up to a few micrometers.
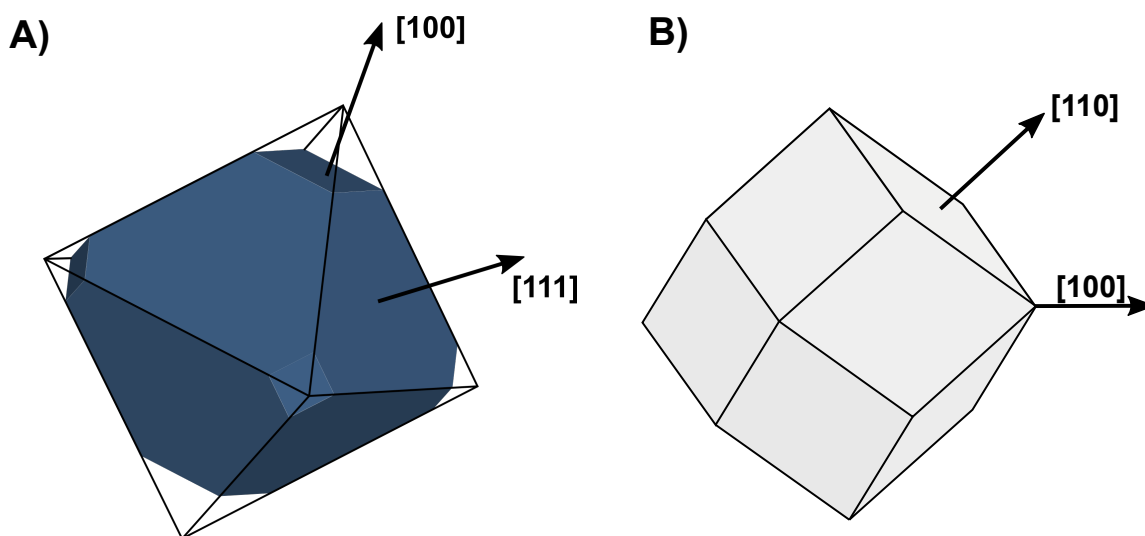
Figure 2.16. Schematic representation of the A) (truncated) octahedral shape usually observed for HKUST-1 nuclei [97] and B) rhombic dodecahedral morphology characteristic for ZIF-8 crystals [98]. As indicated, HKUST-1 adopts a bluish color owing to the copper species present in the crystal lattice.

2.6.2. *ZIF-8* Coating

The material now known as ZIF-8 was first described in 2006 [99]. The name of the MOF sub-group of zeolitic imidazolate frameworks (ZIFs) was chosen to highlight to structural similarity to zeolites which are a class of nanoporous, aluminosilicate minerals. The zeolitic imidazolate framework 8 (ZIF-8) is composed of a single Zn(II) metal center and 2-methylimidazolate organic ligands which self-assemble within the cubic space group no. 217 $I\bar{4}3m$. A model of the ZIF-8 crystal structure is shown in Fig 2.17.
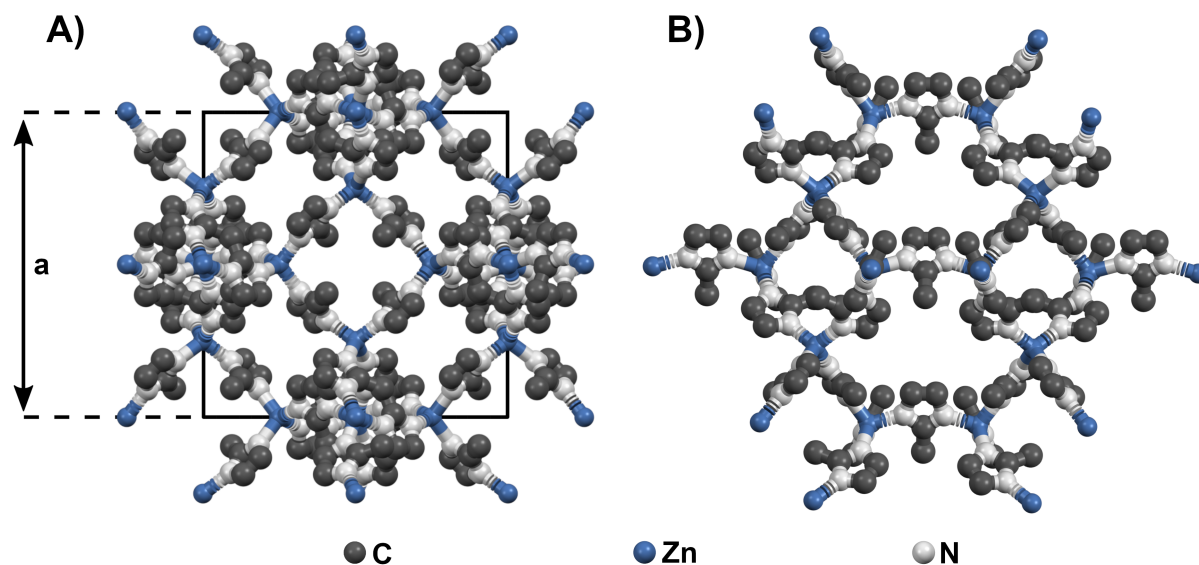
Figure 2.17. ZIF-8 metal-organic framework viewed along the A) [100] and B) [110] direction. At 298 K, the cubic lattice constant a is estimated at 1.70 nm [100]. The ZIF-8 pore structure is comprised of individual cages computed at 1.16 nm in diameter and interconnected by narrow apertures of only 0.34 nm [99]. The models shown in the figure were generated from the CIF deposited by the authors of [100].

The ZIF-8 pore network consists of 0.34 nm windows interconnecting individual cages of roughly 1.16 nm in diameter [99]. In contrast to zeolites [101] as well as HKUST-1 [102], ZIF-8 is categorized as a soft porous material exhibiting structural flexibility [103]. This is because guest molecules with a kinetic diameter significantly larger than the actual aperture size have been observed to enter the intracrystalline ZIF-8 pore structure which has been ascribed to the so-called the gate-opening effect [104]. Typical BET specific surface areas of ZIF-8 range between 1000 and 2000 m^2/g [105, 106]. Similar to HKUST-1, the pristine ZIF-8 structure is an electric insulator [107] and will readily degrade when in contact with pure water [108, 109]. When prepared as individual particles by homogeneous nucleation, ZIF-8 nuclei usually adopt rhombic dodecahedral morphology as indicated in Fig 2.16 B). ZIF-8 thin films used as membranes have received considerable attention for gas separation applications. A frequently employed thin film preparation method in this field is the (seeded) one-pot synthesis by placing the substrate to be coated into a fresh mixture of the precursor solutions [102, 103, 110].

3. Impedimetric Opportunities for the Characterization of Dielectric Thin Films

Over the past decades, a variety of different impedimetric strategies for the characterization of dielectric thin films have been described. The purpose of this chapter is to provide a broad yet non-exhaustive conceptual framework on how the frequency dependent current flow is affected by an electronically non-conducting thin film within an electrode setup and, more importantly, what specific properties can be derived from it. The generalized experimental setting considered throughout this chapter is outlined in Fig 3.1 which involves a reference medium, the electrode and the dielectric thin film covering the electrode surface to, in a sense, shield the electrode from the reference medium.

It is important to note that the impedance spectrum is affected by both the morphology and the material of the thin film. Morphological artifacts of the coating such as a disproportionate degree of surface roughness, incomplete surface coverage, structural heterogeneity, etc. may lead to a spatial distribution of current flow at the surface of the electrode thereby complicating the subsequent interpretation of the recorded spectra [20, 111]. In case meaningful material properties are to be extracted from the impedance response, the coating should preferably be free of morphological artifacts to avoid uncertainty during data interpretation. For method validation and to raise confidence in the evaluation procedure, it is useful to cross check tangible physical properties extracted from the impedance data through separate methods of analysis.
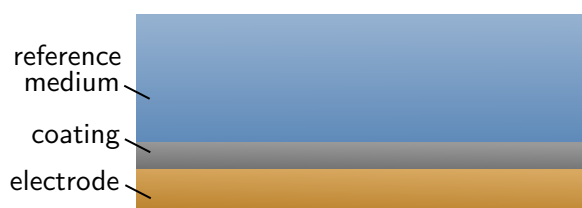
Figure 3.1. Experimental setting of the impedimetric analysis strategies addressed in this chapter involving an electrode covered by the dielectric thin film and exposed to a reference medium.
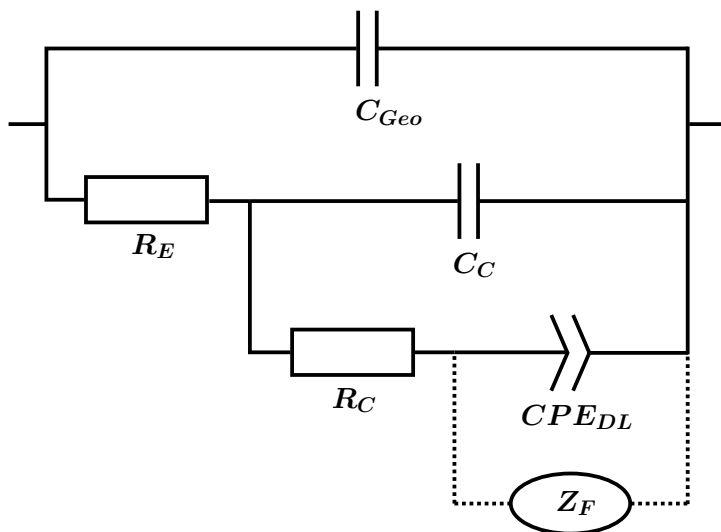
Figure 3.2. Practical equivalent circuit representation to model the impedance response of a coated electrode. The circuit model can be considered an extension to ECM 1 shown in Fig 2.6 by a coating capacitance C_C, coating resistance R_C as well as a potential Faradaic impedance Z_F stemming from an electrochemical process.

A useful starting point for the analysis of impedance data recorded with a dielectrically coated electrode is the equivalent circuit model (ECM) provided in Fig 3.2 which from now on will be referred to as *ECM 2*. In addition to the uncoated case modelled by ECM 1 displayed in Fig 2.6, ECM 2 takes into account a dielectric coating's obstruction to E-field induced ionic migration towards the countercharged electrode surface. In particular, it is assumed that ionic migration through the reference medium occurs more quickly than through the coating leading to an accumulation of ions, i.e., charge, at the interface between coating and reference medium modelled as the coating capacitance C_C. Furthermore, a coating resistance R_C is introduced in parallel to C_C accounting for the ionic migration through the coating towards the electrode surface allowing a buildup of the electric double layer. Additionally, a Faradaic impedance branch Z_F is indicated in ECM 2 in case a Faradaic redox reaction is to be considered. The design of ECM 2 was strongly inspired by the ECM comprehensively reviewed by Mansfeld [112] in the context of polymeric anti-corrosion coatings and credited to the work of Beaunier et al. [113]. The distinguishing feature of ECM 2 lies in the addition of the displacement plus polarization current branch in the form of C_{Geo} which is usually neglected in traditional impedance spectroscopy.

The sections following this introduction will provide further insights into ECM 2 detailing what essential thin film information is conveyed in each of its circuit components. ECM 2 contains a minimum of potential physical processes that are expected for an impedimetric analysis of electronically non-conducting thin films. Depending of the complexity of the impedance spectrum however, it may become reasonable to add more components to the circuit model.

3.1. Non-Faradaic Processes

This section addresses the non-Faradaic processes in the presence of a dielectric coating covering the electrode surface. All of the underlying processes should be present in an impedance response although not every circuit component may be reasonably identifiable within the recorded frequency range.

3.1.1. Coating Capacitance

The physical process modelled by the coating capacitance C_C originates from the migration of ionic species (charge) towards and accumulation at the interface between reference medium and coating. C_C itself accounts for the effective charge separation between the interfaces of coating/electrode and coating/reference medium and is proportional to the coated area A_C, the permittivity of the coating $\varepsilon_0 \varepsilon_{r,C}$ as well as reciprocally proportional to the coating thickness d_C.

$$C_C = \varepsilon_0 \varepsilon_{r,C} \frac{A_C}{d_C} \tag{3.1}$$

The evaluation of C_C using equation 3.1 is made difficult by the fact that, in general, neither $\varepsilon_{r,C}$ nor d_C are known beforehand. To estimate d_C, $\varepsilon_{r,C}$ is often approximated from the dielectric properties of the bulk material the thin film is suspected to be composed of. Irrespective of this difficulty, C_C may be evaluated in terms of solvent uptake into the coating over time which induces a change in $\varepsilon_{r,C}$. The Brasher-Kingsbury approach [114] has found widespread application for aqueous reference media providing an estimate for the volume fraction of water $v_w(t)$ as a function of time inside the coating without requiring $\varepsilon_{r,C}$ and d_C as input parameters.

$$v_w(t) = \frac{log(C_C(t)/C_C(t=0))}{log(\varepsilon_{r,w})} \tag{3.2}$$

Importantly, equation 3.2 is based on a simplistic dielectric mixing model assuming the amount of water absorbed to be small as well as homogeneously distributed within the layer. Additionally, the swelling of the thin film upon water uptake is neglected. Evaluation of $C_C(t)$ based on the Brasher-Kingsbury approach has been demonstrated to provide reasonable diffusion coefficients of water molecules diffusing into a dielectric coating [115, 116]. Similar to the double layer effect, the coating capacitance effect is rarely purely capacitive meaning the quality of data fit is often significantly improved when substituting the C_C circuit component by a constant phase element CPE_C [117] in ECM 2. Conversion of the two CPE_C model parameters into a tangible estimate of the coating capacitance value, however, requires an educated guess concerning the physical origin imparting CPE behavior to the experimental system [118, 119].

3.1.2. Coating Resistance

The coating resistance R_C models the ionic migration through the coating and depends on the presence/formation of ion conducting paths through the coating, effectively connecting the electrode surface to the reference medium[7]. Ion conducting paths can derive from an

inherent (nano-)porosity of the coating or, alternatively, from macroscale defects such as cracks, delamination, formation of water pockets, etc. thereby exposing the bare electrode surface to the electrolyte [7, 120, 112]. For this reason, a coating's R_C value is considered a useful indicator for a coating's corrosion protection performance [121]. When assuming the coating to fully cover the electrode surface and to be free of macroscale defects, it is reasonable to convert R_C into an ionic conductivity κ_C similar to how the electrolyte resistance R_E is converted into the electrolytic conductivity of the reference medium κ_M.

$$\kappa_C = \frac{1}{R_C}\frac{d_C}{A_C} \tag{3.3}$$

κ_C is proportional to the ionic migration through the coating and can be described in accordance to equation 2.21 with the diffusion coefficient of the ionic species inside the coating $\delta_{i,C}$ as [122]

$$\kappa_C = \frac{F^2}{RT}\sum_{i=1}^{N_i} c_{M,i} P_{MC,i}\delta_{i,C}. \tag{3.4}$$

In the equation above, $P_{MC,i}$ constitutes the ionic partitioning coefficient of the ionic species i between reference medium and the coating which may originate, e.g., from a combination of steric, Donnan and dielectric exclusion mechanisms [123, 124].

3.1.3. Double Layer Capacitance

It is possible to estimate an effective surface coverage a_{cov} of the dielectric coating on the basis of the double layer capacitance C_{DL} extracted from the impedance data [112, 20]. When assuming the ionic permeability of the coating material itself to be negligible, i.e. $\kappa_C \to 0$, it follows that a detectable C_{DL} would derive solely from defects exposing the bare electrode surface to the reference medium as indicated in Fig 3.3. Comparison of C_{DL} to a theoretical double layer capacitance of the uncoated electrode surface $C_{DL,uc}$ allows for an estimation of a_{cov}.

$$a_{cov} = 1 - \frac{C_{DL}}{C_{DL,uc}} = 1 - \frac{C_{DL}}{\bar{c}_{DL}A} \tag{3.5}$$

$C_{DL,uc}$ can be obtained from total electrode area A together with an estimate of the area normalized double layer capacitance $\bar{c}_{DL}$ [125]. This approach however should provide only a rough estimate of a_{cov} given that $\bar{c}_{DL}$ is usually not precisely known and may vary depending on the chemical environment [20]. Alternatively, an impedance spectrum evaluation of an identical electrode setup without the dielectric thin film exposed to the same reference medium could yield a useful $C_{DL,uc}$ input value for the computation of a_{cov} in equation 3.5. Given the non-ideality of the double layer effect as well as a potential overlap with other effects such as the coating capacitance and Faradaic processes however, application of equation 3.5 is further complicated by the modelling uncertainty at which C_{DL} may in fact be identified from an impedance response.

Figure 3.3. Defective coating exposing portions of the bare electrode surface to the reference medium highlighted in red color.
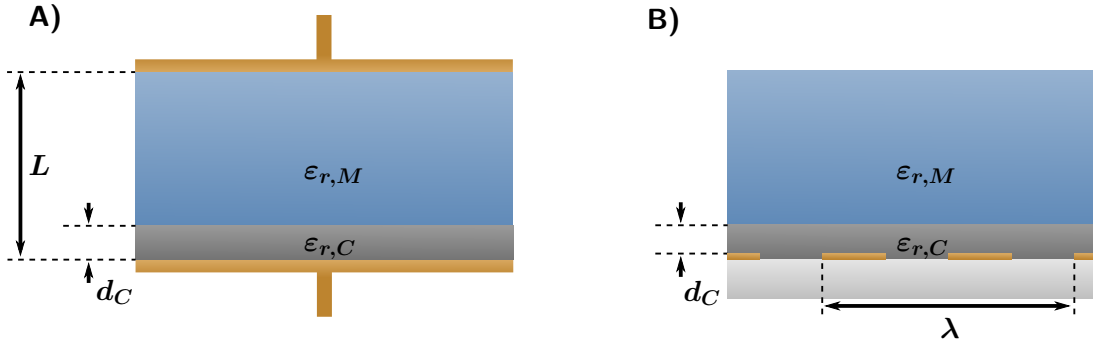
Figure 3.4. Dielectric coating inside a A) parallel plate and B) interdigitated electrode geometry together with the relevant geometric dimensions. If both the reference medium and the dielectric thin film occupy a sizable portion of the electrode sample volume, an effective relative permittivity $\varepsilon_{r,eff}$ ranging in between $\varepsilon_{r,M}$ and $\varepsilon_{r,C}$ can be measured.

3.1.4. Geometric Capacitance

In case a dielectric coating comprises a sizable portion of the sample volume within the electrode geometry used, the thin film may impart characteristic changes to the bulk effects related to the cell constant K_{Cell}. Consequently, application of equation 2.26 to the geometric bulk capacitance C_{Geo} of the electrode geometry will provide an effective relative permittivity value $\varepsilon_{r,eff}$ ranging in between the relative permittivity of the sample medium $\varepsilon_{r,M}$ and the relative permittivity of the coating $\varepsilon_{r,C}$.

$$\varepsilon_{r,eff} = \frac{K_{Cell}C_{Geo}}{\varepsilon_0} \tag{3.6}$$

Conversion of the geometry dependent $\varepsilon_{r,eff}$ into tangible thin film properties such as $\varepsilon_{r,C}$ or coating thickness d_C requires recording of C_{Geo} for at least two different reference media as well as an appropriate effective medium model adapted to the electrode geometry used [126, 127]. When working with a customary parallel plate geometry as illustrated in Fig 3.4 A) $\varepsilon_{r,eff}$ would calculate as [128]

$$\varepsilon_{r,eff} = \frac{\varepsilon_{r,M}\varepsilon_{r,C}}{\varepsilon_{r,M}\frac{d_C}{L} + \varepsilon_{r,C}(1 - \frac{d_C}{L})}. \tag{3.7}$$

Importantly, with regard to equation 3.7, the electrode separation distance of a parallel plate geometry L needs to be chosen at best one or two orders of magnitude larger than the anticipated d_C for the dielectric thin film to affect the bulk C_{Geo} in a significant manner. For this reason, carrying out conclusive and reproducible $\varepsilon_{r,eff}$ measurements with d_C values ranging in the nano- or micrometer range may become challenging with parallel plate geometries. As an

alternative, interdigitated (micro-)electrodes (IDEs) can be used whose electric field penetration length into the bulk of the sample medium is inherently tied to its spatial wavelength λ [126, 127]. When assuming an idealized IDE geometry with negligible finger thickness and neglecting fringing effects at the edges of the interdigitated area, $\varepsilon_{r,eff}$ of a coated IDE geometry as shown in Fig 3.4 B) can be modelled based on conformal mapping techniques. In the case of $\varepsilon_{r,C} > \varepsilon_{r,M}$, $\varepsilon_{r,eff}$ can be calculated as [129, 130]

$$\varepsilon_{r,eff} = (\varepsilon_{r,C} - \varepsilon_{r,M})\frac{C_{IP}}{C_{I,\infty}} + \varepsilon_{r,M}. \tag{3.8}$$

The capacitance $C_{I,\infty}$ is a function of the IDE metallization ratio η

$$C_{I,\infty} = \frac{K(k_I)}{K(k_I')} \, , \, k_I = \sin\left(\frac{\pi}{2}\eta\right), \, k_I' = \sqrt{1 - k_I{}^2}. \tag{3.9}$$

In contrast, the capacitance C_{IP} depends on how the coating thickness d_C compares to the IDE wavelength λ, i.e., the IDE sensing range

$$C_{IP} = \frac{K(k_{IP})}{K(k_{IP}')} \, , \, k_{IP} = t_2\sqrt{\frac{t_4{}^2 - 1}{t_4{}^2 - t_2{}^2}} \, , \, k_{IP}' = \sqrt{1 - k_{IP}{}^2}, \tag{3.10}$$

$$t_2 = sn(K(k)\eta, k) \, , \, t_4 = \frac{1}{k} \, , \, k = \left(\frac{\vartheta_2(0,q)}{\vartheta_3(0,q)}\right)^2 \, , \, q = exp\left(-4\pi\frac{d_C}{\lambda}\right). \tag{3.11}$$

In the equations above, sn refers to the 'sinus amplitudinis' whereas ϑ_2 and ϑ_3 denote the respective 'Jacobi theta functions'.

When considering the opposite case $\varepsilon_{r,C} < \varepsilon_{r,M}$, $\varepsilon_{r,eff}$ can be computed as [131, 130]

$$\frac{1}{\varepsilon_{r,eff}} = \left(\frac{1}{\varepsilon_{r,C}} - \frac{1}{\varepsilon_{r,M}}\right)\frac{C_{I,\infty}}{C_{IS}} + \frac{1}{\varepsilon_{r,M}} \tag{3.12}$$

$C_{I,\infty}$ calculates in accordance to the first case with equation 3.9. The capacitance C_{IS} again accounts for the ratio $\frac{d_C}{\lambda}$

$$C_{IS} = \frac{K(k_{IS})}{K(k_{IS}')} \, , \, k_{IS} = t_2 \, , \, k_{IS}' = \sqrt{1 - k_{IS}{}^2}, \tag{3.13}$$

$$t_2 = sn(K(k)\eta, k) \, , \, k = \left(\frac{\vartheta_2(0,q)}{\vartheta_3(0,q)}\right)^2 \, , \, q = exp\left(-4\pi\frac{d_C}{\lambda}\right). \tag{3.14}$$

A Python script solving equations 3.8-3.14 as a function of d_C, λ, η, $\varepsilon_{r,M}$ and $\varepsilon_{r,C}$ is provided in chapter 2 of the supplementary research data. From a mathematical standpoint, the computation of $\varepsilon_{r,eff}$ can be understood as an interpolation between $\varepsilon_{r,C}$ and $\varepsilon_{r,M}$ by means of an interpolation parameter ζ so that the following expression hold true

$$\varepsilon_{r,eff} = \varepsilon_{r,C}\zeta + \varepsilon_{r,M}(1 - \zeta) \, , \, \zeta = \frac{\varepsilon_{r,eff} - \varepsilon_{r,M}}{\varepsilon_{r,C} - \varepsilon_{r,M}}. \tag{3.15}$$
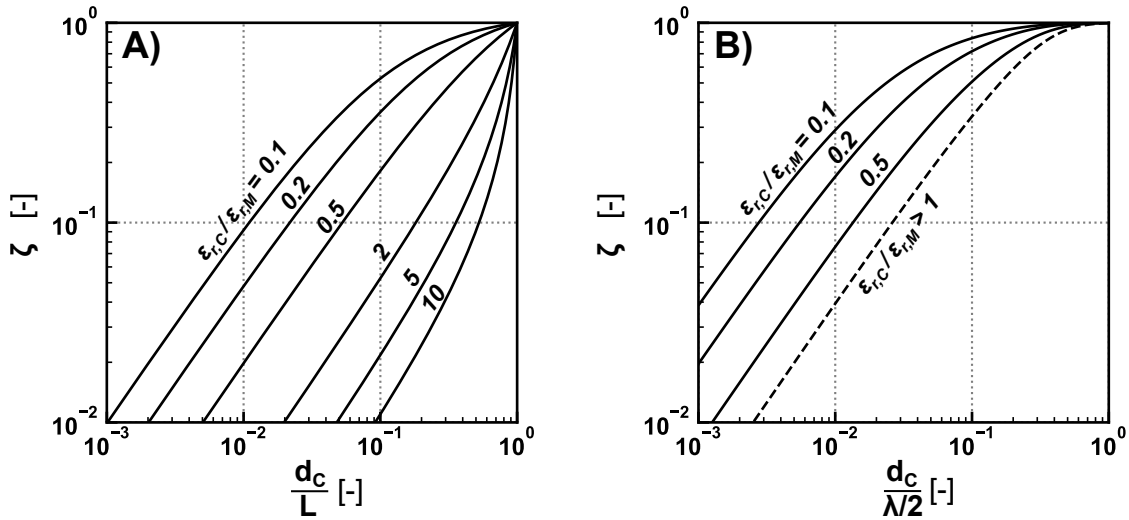
Figure 3.5. Linear interpolation parameter ζ as a function of the coating thickness A) normalized to the electrode separation distance L of a parallel plate electrode electrode geometry and B) normalized to half the spatial wavelength λ of an interdigitated electrode geometry assuming a metallization ratio of $\eta = 0.5$.

ζ as a function of a normalized film thickness is displayed in Fig 3.5 for both a parallel plate and an interdigitated electrode (IDE). It is important to note that in the general case, ζ itself is inherently a function of the ratio between $\varepsilon_{r,C}$ and $\varepsilon_{r,M}$. Interestingly, the case $\varepsilon_{r,C}/\varepsilon_{r,M} > 1$ for an IDE geometry appears to represent an exception to this general rule. The concept of limited electric field penetration length of an IDE structure is clearly visible in Fig 3.5 B) with ζ quickly converging towards unity as d_C approaches $\lambda/2$.

3.1.5. Electrolyte Resistance

Similarly to the geometric capacitance in the previous chapter, the bulk electrolyte resistance R_E will also be affected by a thin film comprising a sizable portion of an electrode's sample volume. An extensive theory on how R_E is affected by the presence of a dielectric thin film however appears to be missing up to now.

Treatment of the electrolytic conductivity on the basis of an effective medium approximation similar to $\varepsilon_{r,eff}$ in the previous chapter is complicated considering migration current passing through inhomogeneous media of varying electrolytic conductivities gives rise to interfacial polarization phenomena at the internal phase boundaries [22]. Interfacial polarization during the impedimetric analysis of dielectric thin films is best exemplified at the phase boundary between coating and reference medium leading to the build-up of the coating capacitance C_C due to the mismatch between the electrolytic conductivity of the reference medium κ_M and coating κ_C. The details on how R_E is affected by the volume fraction occupied by the dielectric thin film is likely to be influenced on how κ_M and κ_C compare to each other as well as the intricacies of the electrode geometry employed. One interesting opportunity for analysis would arise when working with coated interdigitated electrodes (IDEs) with the coating thickness d_C exceeding the practical sensing range of the sensor geometry. Provided the coating
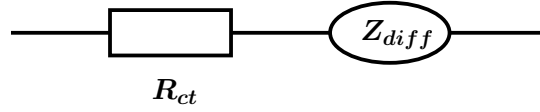
Figure 3.6. Equivalent circuit model accounting for the Faradaic impedance branch Z_F in Fig 3.2 comprised of the charge transfer resistance R_{ct} and a diffusion impedance Z_{diff}.

is homogeneous, both coating capacitance and resistance should vanish from the impedance response. With the coating comprising the entire "bulk" exposed by the electric field, the data might again follow the physical processes conceptualized in ECM 1 with the coating acting as a solid electrolyte. As a result, the ionic conductivity of the coating material κ_C defined in equation 3.3 could be directly obtained from the bulk ionic migration resistance R_E and the cell constant K_{Cell} via

$$\kappa_C = \frac{K_{Cell}}{R_E}. \tag{3.16}$$

3.2. Faradaic Processes

The influence of a dielectric coating on Faradaic processes involving a heterogeneous charge transfer reaction at the electrode surface conveys additional information on a dielectric thin film which can be analyzed by impedance spectroscopy. Faradaic impedance spectroscopy relies on the presence of electroactive species which are usually added to the reference medium or may even be native to the experimental system under investigation. The recording of reliable impedance data under Faradaic conditions generally requires the addition of a reference electrode as well as a clear distinction to be made between working and counter electrode. The details of a Faradaic impedance response Z_F depends on the underlying reaction mechanism. The Z_F model provided in Fig 3.6 accounts for a reversible, single-step charge transfer reaction together with the diffusion of reactants to the electrode surface [21].

3.2.1. Charge Transfer Resistance

The charge transfer resistance R_{ct} may be understood as the (electrical) resistance which needs to be overcome to pass an electron from an electroactive substance to the electrode or vice versa. The theoretical background on how R_{ct} has been proposed for thin film characterization is equivalent to the evaluation strategy of the double layer effect in 3.1.3. Only the portion of the electrode area directly in contact with the reference medium containing the electroactive species will contribute to measured Faradaic current imparting a reduced R_{ct}. Provided the charge transfer resistance of the identical, uncoated electrode setup $R_{ct,0}$ for the same reference medium is known, a_{cov} can be estimated as [132, 112]

$$a_{cov} = 1 - \frac{R_{ct}}{R_{ct,0}}. \tag{3.17}$$

It is important to note that equation 3.17 is based on the simplifying assumption of the coating being impermeable to the electroactive species. The change in R_{ct} is a frequently employed

transduction mechanism for impedimetric immunosensing [133], signalling the adsorption of, e.g., target molecules [134], virus particles [135] or even entire bacteria [136] to a functional coating grafted on an electrode surface.

3.2.2. Diffusion Impedance

Depending on the timescale of the impedance measurement, i.e., the AC frequency applied, a distinct mass transport limitation of the Faradaic impedance contribution may be detected. In case the assumption of complete surface coverage and the coating being permeable to the electroactive species holds, the mass transport of the electroactive species i through the coating may develop into the bottleneck constraining the electrochemical reaction rate. Diffusion limitation of Faradaic processses impart characteristic contributions to the total impedance response and provide additional information on the thin film coating.

The diffusion impedance Z_{diff} discussed in this section is derived from Fick's second law of diffusion as expressed in its one-dimensional form in equation 3.18. Let t describe the time, x refer to the coordinate perpendicular to the coated surface, c_i describe the concentration of the electroactive species i and $\delta_{i,C}$ refer to the diffusion coefficient of i in the coating, then

$$\frac{\partial c_i}{\partial t} = \delta_{i,C} \frac{\partial^2 c_i}{\partial x^2} \tag{3.18}$$

As a consequence, mass transport of the reduced and oxidized form of the electroactive species is thereby solely attributed to the concentration gradient originating from the electrochemical conversion at the electrode surface. In contrast, an additional ionic migration of charged electroactive species owing to the electric potential gradient is intentionally neglected which would require more elaborate modelling efforts on the basis of the Nernst-Planck equation [21, 137]. Accordingly, for this modelling approach of Z_{diff} to be valid, inert supporting electrolyte species (e.g. KCl) need to be present in the experimental system, usually at concentrations orders of magnitude larger than the concentration of the actual electroactive species. The fundamental role of the supporting electrolyte is to shoulder the majority share of mass transport through ionic migration along the potential gradient [21].

At the initial stage of diffusion limitation, a stationary concentration profile has not yet fully developed. Accordingly, the diffusion case is appropriately described by a semi-infinite boundary condition applied to equation 3.18. Computation of the associated impedance response leads to the so-called *Warburg* impedance Z_W [138] which is frequently employed to mimic the diffusion impedance contribution as a stand-alone equivalent circuit element.

$$Z_W(f) = \frac{W}{\sqrt{2\pi f}} - j \frac{W}{\sqrt{2\pi f}} \tag{3.19}$$

The Warburg coefficient W in equation 3.19 represents the sole fitting parameter which is adjusted during data analysis. If mass transport through the thin film develops into the rate limiting step of the Faradaic reaction, the coating thickness d_C will eventually constitute the fundamental length-scale of the diffusion process [21]. For this purpose, a characteristic
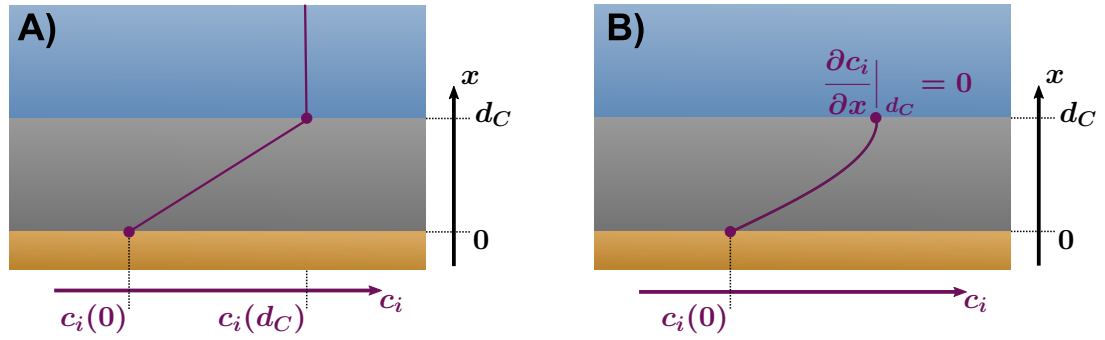
Figure 3.7. Schematic educt diffusion profile within the dielectric coating following the assumption of A) finite length and B) finite space Warburg modelling of the diffusion impedance Z_{diff}. Both modelling approaches derive from a solution of Fick's second law satisfying a different set of boundary conditions. Figure adapted from [20].

frequency of diffusion f_δ can be defined as

$$f_\delta = \frac{1}{2\pi} \frac{\delta_{i,C}}{d_C{}^2}. \tag{3.20}$$

When the applied AC frequency f approaches or falls below f_δ, the diffusion limitation of the electrochemical reaction imparted by the dielectric coating becomes visible in the impedance data. There are two classical cases which are being differentiated during this stage of the diffusion impedance. The associated concentration profiles are schematically portrayed in Fig 3.7. The diffusion case displayed in Fig 3.7 A) assumes the electroactive species to be present in the reference medium and providing, in a sense, an unlimited supply of educts for the electrochemical reaction. Application of the initial values $c_i(x = 0)$ and $c_i(x = d_C)$ as boundary conditions to equation 3.18 followed by the computation of the impedance response leads to the 'finite length Warburg element' with Z_{FLW} as

$$Z_{FLW}(f) = R_W \frac{\tanh\left(\sqrt{jf/f_\delta}\right)}{\sqrt{jf/f_\delta}} \tag{3.21}$$

The second diffusion case displayed in Fig 3.7 B) assumes the electroactive species to be present in the dielectric coating alone. The exchange of educts and products with the reference medium is neglected which may be a valid assumption in, e.g., some battery systems [20]. Consequently, a zero gradient boundary condition is applied to the interface between reference medium and coating leading to the impedance response of the 'finite space Warburg element' Z_{FSW} [8].

$$Z_{FSW}(f) = R_W \frac{\coth\left(\sqrt{jf/f_\delta}\right)}{\sqrt{jf/f_\delta}} \tag{3.22}$$

For both Z_{FLW} and Z_{FSW}, the equivalent Warburg resistance R_W and f_δ serve as regression parameters. The typical Bode plots obtained by the three idealized modelling approaches for Z_{diff} are provided in Fig 3.8. It is worth noting that at frequencies $f >> f_\delta$, Z_W, Z_{FLW} and Z_{FSW} provide identical impedance responses.

Various extensions to the classical diffusion impedance models outlined in this chapter have been proposed in case impedance data might potentially be affected by, among other, a CPE-blocked [139], unsupported [140, 141], multilayer [142] or anomalous [143] diffusion process.
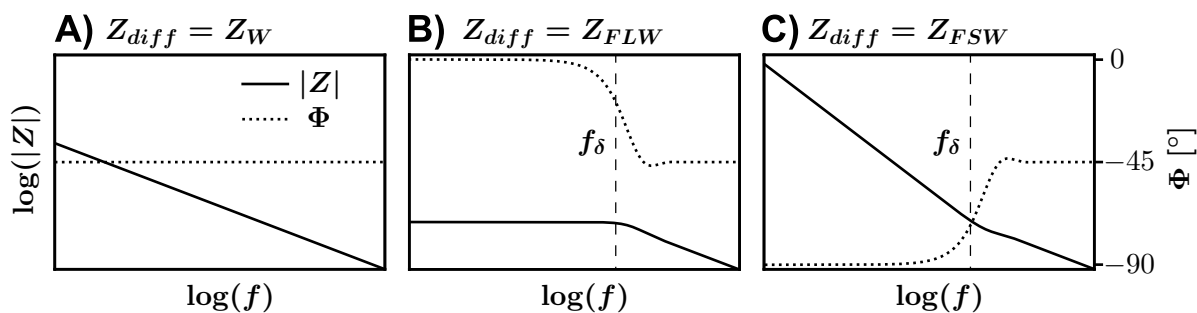
Figure 3.8. Characteristic Bode representation of the diffusion impedance Z_{diff} response modelled by A) the semi-infinite Warburg Z_W, B) the finite length Warburg Z_{FLW} and C) the finite space Warburg Z_{FSW} element. All three approaches to model Z_{diff} provide an identical impedance response at $f >> f_\delta$ with a characteristic phase angle $\Phi = -45$ °. At $f < f_\delta$, Z_{FLW} approaches a purely resistive profile due to the stationary supply of electroactive species from the reference medium. In contrast, Z_{FSW} develops a purely capacitive profile owing to the depletion of electroactive species in the thin film.

4. Experimental Section

This chapter provides practical insights into the experimental approach and evaluation procedure which were employed to demonstrate the impedimetric characterization strategies in the following chapters. The individual devices, substances and software relied upon are listed in tables 4.1, 4.2 and 4.3, respectively.

Table 4.1. Device List.

Name of Object/Device	Description	Supplier
Gamry Reference 600+	potentiostat	Gamry Instruments
Reference 600+ Cell Cable, 60 cm	shielded potentiostat cell cable	Gamry Instruments
Gamry calibration shield	Faraday cage	Gamry Instruments
OB1 MK3+	pneumatic pressure controller	Elveflow
Rheodyne MHP7970-500-4	flow distributor valve	Cetoni
MUX Distributor	flow distributor valve	Elveflow
Synergy Water Purification System	deionized water dispenser	Merck
Asiga Max X35	3D-printer	Asiga
WTW LF 330	conductivity probe	WTW
Checktemp 2	temperature probe	Hanna Instruments
ED-IDE3-Au	5 µm-IDE chip	Micrux Technologies
ED-IDE1-Au	10 µm-IDE chip	Micrux Technologies
UV Ozone Cleaner	UV/ozone treatment	Ossila
ESEM XL30 FEG	scanning electron microscope	Philips
MED 020	sputtercoating system	Baltec
Adventurer™ Analytical	scales	Ohaus
D8 ADVANCE	X-ray diffractometer	Bruker

Table 4.2. Chemical list. All chemicals were used as received.

Substance	Purpose	Supplier
ethanol (99.97 %)	solvent, DRM	VWR
1-butanol (anhydrous, 99.9 %)	DRM	Alfa Aesar
water (deionized)	solvent, DRM	see table 4.1
conductivity standard 25.0 µS/cm at 25°C	CRM	VWR
TLS 01 control standard for conductivity cells (10 mM KCl)	CRM	Xylem Analytics
Asiga PlasGRAY V2	photoresin	LithoLabs
Fluorolink MD® 700	monomer for photoresin	Solvay
Sudan Orange G (85 %)	photoblocker	Sigma Aldrich
phenyl-bis-(2,4,6-trimethylbenzoyl)-phosphinoxid (97 %)	photoinitiator	Sigma Aldrich
acetic acid (99 %)	SAM preparation, cleaning agent	VWR
16-mercaptohexadecanoic acid (90 %)	SAM preparation	VWR
copper(II) acetate, hydrated (99.9 %)	HKUST-1 metal source	VWR
1,3,5-benzenetricarboxylic acid	HKUST-1 linker	Sigma Aldrich
zinc acetate dihydrate (99.9 %)	ZIF-8 metal source	Fluka
2-methylimidazole (99 %)	ZIF-8 linker	VWR
potassium chloride (100 %)	electrolyte	VWR
nitrogen (pressurized)	DRM, pressure source	Air Liquide

Table 4.3. Software list.

Program	Purpose	Developer
Anaconda3 2021.5	Python distribution	Anaconda
Spyder 3.8	Python development environment	see [144]
Autodesk Inventor Professional 2019	computer aided design	Autodesk
COMSOL Multiphysics 5.5	finite element modelling	COMSOL
Gamry Echem Analyst 7.8.2	impedance modelling	Gamry Instruments
Mercury 2020.2.0	XRD modelling	CCDC
Diffrac.Eva 5.1.0.5	XRD data analysis	Bruker AXS

4.1. Impedance Measurement System

The impedance data collected throughout this work was recorded exclusively with commercially available interdigitated electrode (IDE) chips comprised of a gold electrode structure deposited on a glass substrate. The disposable IDE chips were composed of a circular interdigitated area with a diameter of 3.6 mm and two contact pads for electric connection. Two IDE geometry variants were available. Both featured an equidistant electrode width w and spacing s at either
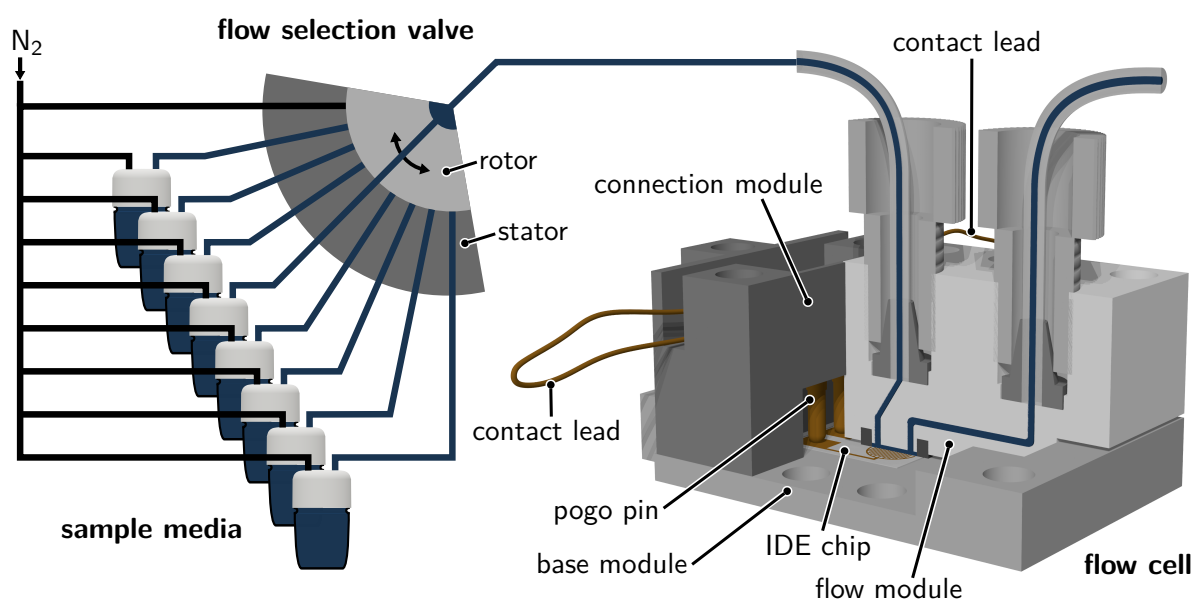
Figure 4.1. Schematic outline of the fluidic setup. The bottles containing the fluidic sample media were connected to a flow selection valve and pressurized with nitrogen gas. The valve's rotor position determined which sample medium would be supplied to the microfluidic flow cell housing the electrode chip. The flow cell was electrically connected to a potentiostat equipped with a frequency response analyzer for impedance data uptake with the help of the contact leads.

5 or 10 μm which within the scope of the work will be referred to as "5 μm-IDE chip" and "10 μm-IDE chip", respectively.

For impedance measurement uptake, the IDE chips were operated under continuous flow conditions meaning the sample medium under test in contact with the interdigitated area was repeatedly exchanged within the timeframe the total impedance spectrum was recorded. Alternative modes operation for which contact between sample medium and interdigitated area is realized through e.g. pipetting of individual droplets to the interdigitated area or vertical immersion of the IDE chip into the sample medium were considered difficult to automate in a robust manner and accordingly not implemented. In addition, the continuous flow method reduces the risk of contamination and minimizes environmental factors influencing the reference medium under test such as evaporative cooling or gradual absorption of atmospheric gases. A schematic portrayal of the flow setup designed in this work is shown in Fig 4.1. The sample media under test were stored in glass containers sealed from the outside environment and pressurized with inert nitrogen gas at up to 500 mbar above atmospheric pressure. The pressure level was set with a commercially available four-channel pneumatic pressure control system. Fluidic connection of the pressurized sample media to a flow selection valve provided the opportunity to chose which sample medium to be supplied to the microfluidic cell housing the IDE chip. Electrical connection between a potentiostat with frequency response analyzer and the flow unit was realized with the two contact leads located at the rear part of the microfluidic cell. In case current signals in the nA or pA range were expected, the flow cell was placed inside a Faraday cage connected to the floating ground terminal end of the potentiostat in order to improve the signal-to-noise ratio.

The measurement system operated fully automated with the pneumatic pressure system, flow
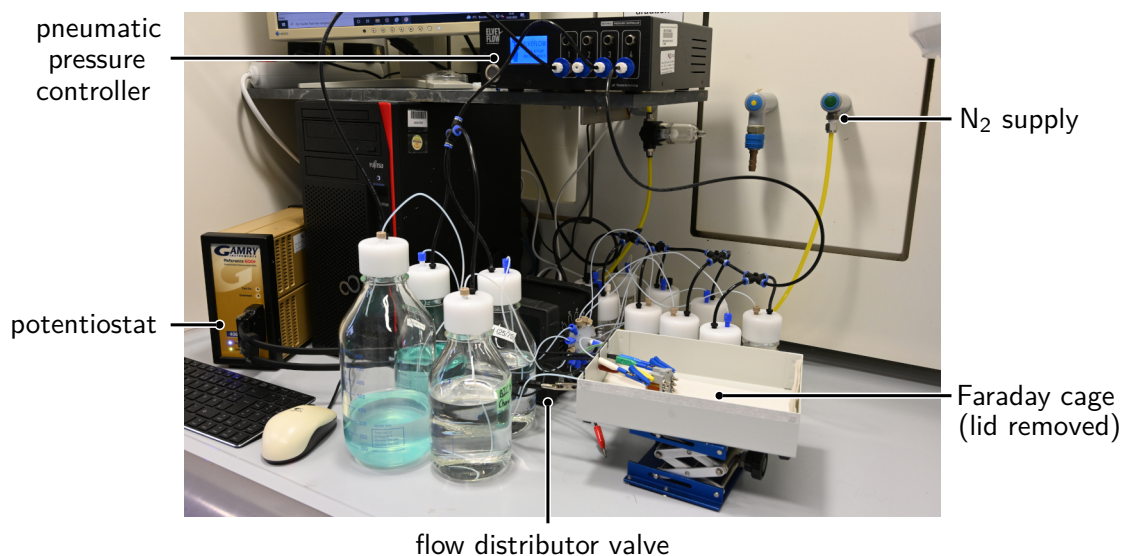
Figure 4.2. Photograph of the experimental setup taken during the ionic permeation measurements discussed in chapter 6.2. The HKUST-1 synthesis solution together with the pressurized waste bottle can be seen in the foreground. The 100 mL bottles containing the ethanol water mixtures at varying molar composition are visible in the background behind the Faraday cage and flow distributor valve.

selection valve as well as the potentiostat controlled by custom written Python scripts which were continuously adapted to meet current impedance measurement objectives. The automated system was designed in a robust manner and thus could operate and generate impedance data for several days on end with minimal experimental oversight. During system operation, the flow cell and potentiostat cabling were left undisturbed to prevent the impedance data being potentially affected by triboelectric phenomena or changes to the capacitive coupling with the environment. Prior to an experiment, the fluidic channels were extensively rinsed with an aqueous 20 vol-% acetic acid solution, deionized water and subsequently dried by supplying pressurized nitrogen to the flow cell.

A photograph of the measurement system in its final state is shown in Fig 4.2 which was taken during the measurements which will be discussed in chapter 6.2. The setup depicted included a total of twelve different sample media as well as a pressurized waste bottle. Waste bottle pressurization reduced the risk of air bubble intrusion into the flow cell which would compromise the quality of impedance spectra.

4.1.1. Custom-built Flow Cell

The flow cell shown in Fig 4.1 and 4.2 was purposefully designed and manufactured to meet a variety of specific technical requirements. Preparation of the modular flow cell was largely based on additive manufacturing using the digital light processing method. The liquid connections and fluidic channels passing through the flow cell were confined to a designated *flow module*. Inlet and outlet of the flow unit were furnished with manually carved 1/4"-28 UNF flat bottom internal threads for reversible liquid connection using customary chromatography fittings. The bottom side of the flow unit featured a cylindrical flow chamber of 4 mm in diameter guiding fluid flow across the interdigitated area of the electrode chip. The thickness of the gasket
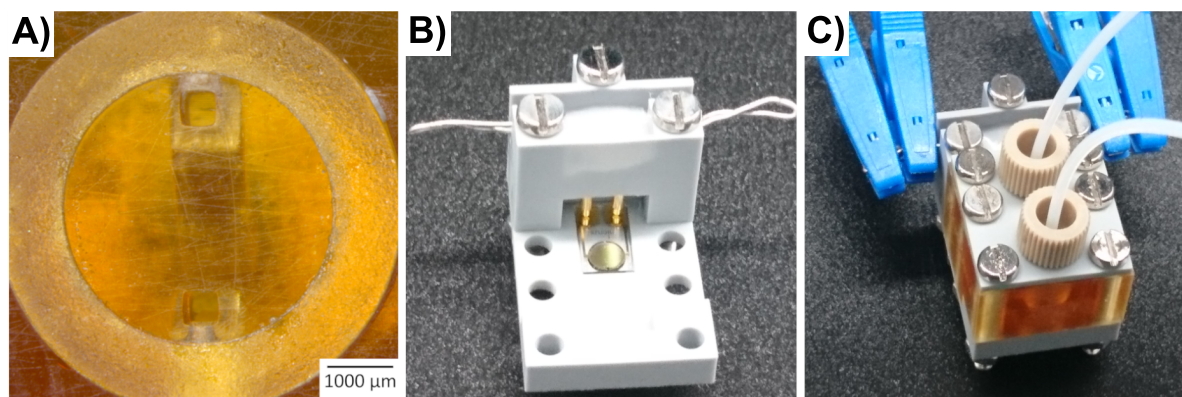
Figure 4.3. A) Micrograph of the cylindrical flow chamber facing the interdigitated area and photographs of the flow cell B) without flow unit installed and C) when fully assembled. Owing to the softness of the fluorpolymer, an additional pressure plate was installed between screw head and flow unit during the assembly of the three main modules.

inserted into the flow unit defined the height of the flow chamber at roughly 200 µm. A micrograph of the fluid chamber is provided in Fig 4.3 A). Flow module and fluidic gasket were 3D-printed using a highly fluorinated methacrylate to guarantee chemical stability when in contact with the sample media containing organic solvents [145]. The photoresin was prepared with the commercially available MD700 resin as monomer supplemented with 5 mg/mL phenyl-bis-(2,4,6-trimethylbenzoyl)- phosphinoxid as photoinitiator and 0.2 mg/mL Sudan Orange G as photoblocker (see table 4.2 for reference).

Electrical contacting of the IDE chip was realized with two Pogo pins housed in the *connection module*. Each Pogo pin was soldered to a wire loop end subsequently embedded into the connection module using a UV-polymerized MD700 photoresin without the photoblocker. The wire loops protruded from the connection module at opposite ends to minimize parasitic capacitance as well as the risk of an accidental short circuit.

To provide accurate liquid and electric contacting to the IDE chip, the position of the electrode chip relative to the flow and connection module was defined with the *base* module. The base module featured an inspection window located underneath the interdigitated area to check for potential air bubbles trapped inside the flow chamber. Both connection module and base module were printed with the commercially available PlasGray photoresin.

A photograph of an IDE chip installed into the base and connection module is shown in Fig 4.3 B). This configuration allowed the IDE chip to be operated with single liquid droplets placed onto the interdigitated area for preliminary experiments. A photograph of the fully assembled flow cell is depicted in Fig 4.3 C). For electric contacting, the two wire loops protruding at opposing ends from the connection module were connected to the working/working sense and counter/reference terminal ends of the potentiostat, i.e., the impedance spectra were recorded using the two-electrode configuration.

4.1.2. Description of the Impedance Measurement Hardware

A Gamry Reference 600+ potentiostat with frequency response analyzer connected to the flow cell with a 60 cm shielded cell cable was used for the uptake of impedance spectra. The hardware allowed impedance measurements at frequencies at up to 5 MHz and an RMS voltage amplitude of up to 2.8 V. The output current signal could be measured across eleven decadic current ranges covering current responses from 60 pA to 600 mA. The potontiostat was controlled by a Python script with the help of custom-written functions for e.g transient single frequency impedance measurements or for the recording of an entire impedance spectrum. The functions required a variety of input parameters such as the initial and final frequency, the amount of frequency point per decade, the RMS voltage amplitude etc. Provided the measurement was stable and the frequency applied sufficiently large, an impedance data point was generated every 0.3 - 0.4 s, meaning an uptake of an entire impedance spectrum covering the frequency range from 5 MHz to 50 Hz at 15 frequency points per decade took roughly between 22.5 and 30 s to record. Impedance spectra were taken from large to small frequencies.

4.2. Impedance Data Evaluation

The impedance data obtained with the automated measurement system was interpreted on the basis of equivalent circuit models (ECMs). An impedance spectrum taken with uncoated IDEs was anticipated to be comprised of three physical processes, namely dipole polarization and ionic migration in the bulk of the sample medium stimulated by the potential gradient as well as the double layer effect at the interface between sample medium and interface. The interplay of how these three processes enter the measured impedance response is modelled by ECM 1 and shown in Fig 4.4 A). On the other hand, to model impedance data taken with coated electrodes, ECM 1 was expanded to ECM 2 provided in Fig 4.4 B) taking into account the ionic accumulation at the interface between sample medium and coating in addition to the ionic migration through the coating towards the electrode surface. To facilitate the understanding of how ECM 2 may be applied to impedance data collected with IDEs, a projection of ECM 2 onto the schematic cross section of two electrode fingers is illustrated in Fig 4.4 C). The coating thickness d_C is assumed small in comparison to the curvature radius of the fringing field defining the effective penetration length d_S. For data evaluation, it is important to understand the model parameters CPE_{DL}, C_C and R_C as effective serial connection of the respective processes at the two oppositely charged sets of electrode fingers.

Depending on the experimental conditions, the respective ECMs were simplified in case individual physical processes were considered negligible within the recorded frequency range. For instance, an impedance spectrum recorded with nitrogen as reference medium was not expected to provide a measurable electrolyte resistance R_E, therefore simplifying both ECM 1 and ECM 2 to the geometric capacitance C_{Geo} circuit component.

In the opposite case of processes of unknown physical origin entering the measured impedance response, no attempts were made to expand ECM 1 or 2 with indiscriminate circuit elements to e.g. increase the quality of data fit. This evaluation approach was motivated by the frequently

A)

ECM 1
uncoated
electrode

C_{Geo}

R_E CPE_{DL}

B)

ECM 2
coated
electrode

C_{Geo}

R_E C_C

R_C CPE_{DL}

C)

reference medium

R_E

$R_{C,1}$ $C_{C,1}$ C_{Geo} $C_{C,2}$ $R_{C,2}$

d_P

d_C

$CPE_{DL,1}$ $CPE_{DL,2}$

electrode
finger 1

dielectric coating

electrode
finger 2

$C_{P,2}$

substrate

w s w
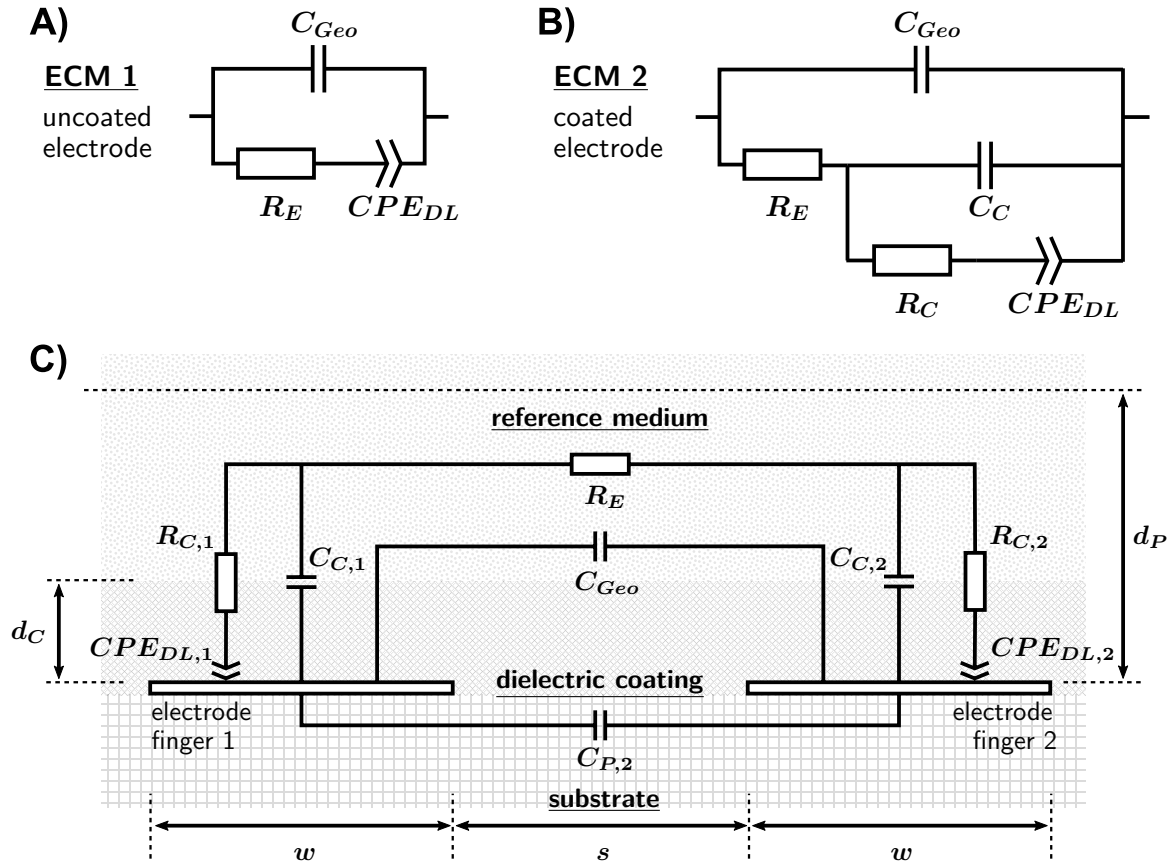
Figure 4.4. Equivalent circuit representations to model the sample system impedance contribution Z_S of the A) uncoated (ECM 1) and B) coated electrode structure (ECM 2). A schematic projection of ECM 2 to the cross section of two electrode fingers of an IDE structure is shown in C). Importantly, depending on the frequency range and sample system under investigation, impedance spectra recorded with IDE chips may significantly deviate from the desired Z_S owing to inevitable parasitic contributions such as a geometric capacitance related to the electrode substrate $C_{P,2}$ which will is addressed in chapter 4.2.3

voiced criticism regarding the modelling of impedance data through arbitrarily designed circuit models [21]. In some cases, impedance spectra inconsistent with either ECM 1 or ECM 2 originated from erroneous experimental conditions and, thus, a repetition of the experiment would resolve the modelling difficulties. On the other hand, in case inconsistent behavior at either ends of the recorded frequency range was reproducible whereas the data by and large would conform with the designated circuit model, the impedance data was occasionally truncated for data analysis.

4.2.1. Model Fitting

The *Gamry Echen Analyst* software was used for impedance modelling which allowed the drafting of an ECM as well as the subsequent regression analysis to the experimental data. The software employed the Nelder-Mead algorithm to iteratively narrow down best-fit estimates for the individual circuit components of the model. The quality of fit between the modelled and measured impedance response was expressed in χ^2. Let N_{freq} denote the amount of frequency data points of the spectrum, Z_{real} and Z_{imag} denote real and imaginary part of the measured

impedance response and $\hat{Z}_{real}$ together with $\hat{Z}_{imag}$ denote the real and imaginary part of the modelled impedance response at the frequency f_i, then χ^2 was computed as

$$\chi^2 = \sum_{i=1}^{N_{freq}} w_i \left[\left(Z_{real}^2(f_i) - \hat{Z}_{real}^2(f_i) \right) + \left(Z_{imag}^2(f_i) - \hat{Z}_{imag}^2(f_i) \right) \right]. \tag{4.1}$$

With the impedance response usually varying across several orders of magnitude within the recorded frequency range, the residuals in equation 4.1 were weighted to ensure a proper data fit of the entire spectrum. For this purpose, the measured impedance modulus at the frequency $|Z(f_i)|$ was employed as weighting factor w_i.

$$w_i = \frac{1}{|Z(f_i)|} \tag{4.2}$$

A maximum likelihood estimation of the variance-covariance matrix during the data fit provided standard uncertainties of the individual model parameters.

4.2.2. Interpretation of Coating Capacitance and Resistance for Interdigitated Electrodes

The interpretation of coating capacitance C_C and resistance R_C obtained from an impedance response collected with an IDE structure requires a conceptual understanding of how the migration of ionic species towards the countercharged electrodes is affected by the presence of a dielectric thin film covering the interdigitated area. Within the equivalent circuit modelling approach pursued in this work, the coating thickness is assumed small in comparison to the IDE sensing range ($d_C << d_P$) and the electrolytic conductivity of the coating is assumed negligible in comparison to the electrolytic conductivity of the reference medium ($\kappa_C << \kappa_M$). The resulting ionic migration under these conditions is schematically outlined in Fig 4.5 A).
 Owing to the curvature of the electric field lines, ions migrating towards the countercharged electrode fingers accumulate at only a fraction of the total interfacial area between reference medium and thin film. This fraction of the interfacial area experiencing ionic accumulation is located directly above the electrode fingers and may be approximately assumed equivalent to the horizontal electrode area of the interdigitated structure as shown in Fig 4.5 B). Thus, the coating capacitance can be interpreted with the coating thickness d_C as separation distance and the metallized fraction of the interdigitated area ηA_{IDE} as coated electrode area A_C in equation 3.1.

$$C_C = \varepsilon_0 \varepsilon_{r,C} \frac{\eta A_{IDE}}{4 d_C} \tag{4.3}$$

The factor 4 located in the denominator of equation 4.3 derives from the serial connection of C_C as indicated in Fig 4.4 C) with ηA_{IDE} representing the sum of both countercharged electrode areas.
Analogous to equation 4.3, R_C may be interpreted as

$$R_C = \frac{4}{\kappa_C} \frac{d_C}{\eta A_{IDE}}. \tag{4.4}$$
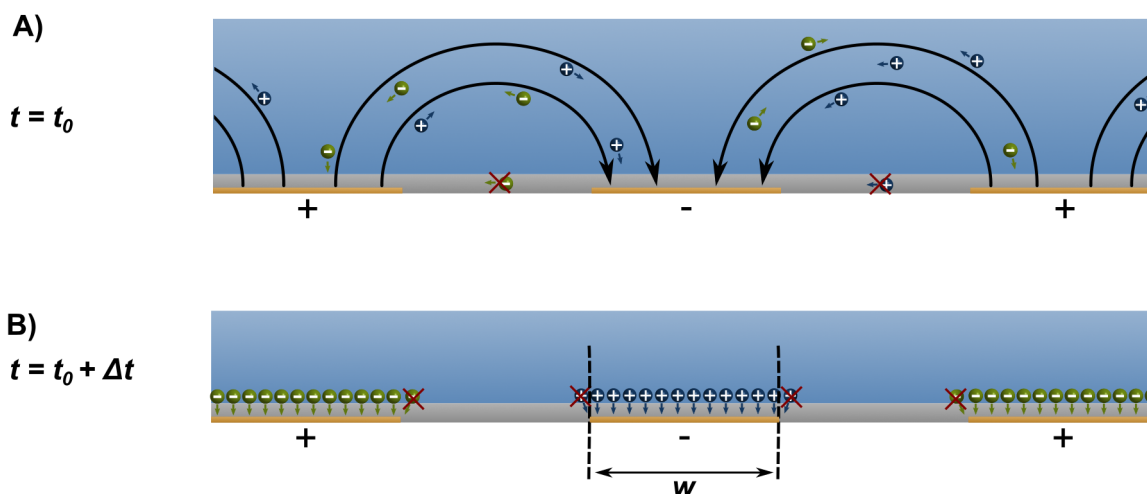
Figure 4.5. Schematic representation of how the concepts of coating capacitance C_C and coating resistance R_C may be applied to interdigitated electrode structures. The thin film covering the electrode fingers is assumed thin in comparison to the curvature of the electric field lines, i.e., $d_C \ll d_P$. Additionally, the bulk migration current is inferred to derive solely from the ionic movement within the reference medium above the thin film as indicated in A). In contrast, ionic migration along potential gradients running exclusively through the dielectric thin film is neglected, i.e., $\kappa_C \ll \kappa_S$. The accumulation of ionic species is primarily restricted to the portion of the reference medium/thin film interface directly above the planar electrode surface as shown in B) which justifies a simplified evaluation of C_C and R_C in accordance to equations 4.3 and 4.4.

The geometric parameters η and A_{IDE} required for the application of equations 4.3 and 4.4 to the impedimetric data are determined through microscopic analysis of the uncoated electrode structures which will be discussed in chapter 5.1.

4.2.3. Compensation of Parasitic Contributions to the Measured Impedance Data

In this work, the measured impedance response Z_M is differentiated from the impedance contribution imparted by the sample medium under test Z_S. In addition to the sample medium, the impedance data is also affected by the electrical integration of the impedance measurement setup which may restrict or, alternatively, provide unwanted opportunities for current flow thereby imparting parasitic contributions to the impedance data.

While impedimetric setups are usually designed to minimize parasitic contributions to Z_M, impedance spectra recorded with IDE chips deserve special attention. For instance, the finite metal film thickness of only a few hundred nanometers or below (e.g. [146, 147, 13]) is a factor worth considering which may limit the current flow through a highly conductive sample medium in contact with the interdigitated area. Also, as indicated in Fig 2.12, the potential gradient not only develops through the sample medium above the interdigitated area but also through the substrate located below. For this reason, a parasitic geometric capacitance related to the IDE chip substrate will always be present along the geometric capacitance of the sample system under test.

A generalized approach to compensate for parasitic contributions to Z_M through equivalent circuit modelling is shown in Fig 4.6 A). The circuit model is comprised of a parasitic resistance

A)

B)
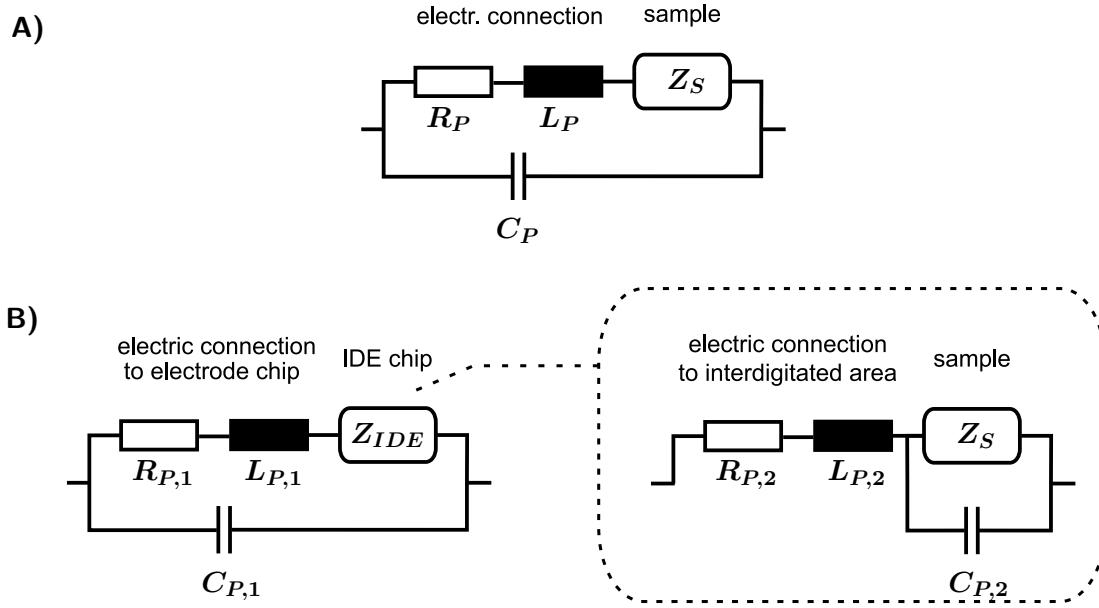
Figure 4.6. A) Generalized equivalent circuit model (ECM) to compensate parasitic influences to the measured impedance data. B) ECM to differentiate between the parasitic contributions imparted by the cabling in between the IDE chip and potentiostat and the parasitic contributions imparted by the IDE chip itself. During data processing, the measured impedance response Z_M is carefully differentiated from the actual impedance response exerted by the sample system under test Z_S.

R_P and inductance L_P in series to Z_S as well as parasitic capacitance C_P in parallel. An additional resistance in parallel to Z_S accounting for leakage current effectively bypassing the actual sample medium under test was not necessary in this work and therefore omitted in Fig 4.6 A). During the design and characterization phase of the experimental system outlined in chapter 4.1, the parasitics were further broken down into the parasitic contributions stemming from the electric connection to the IDE chip and the parasitic contributions of the IDE chips themselves as indicated in Fig 4.6 B). While the parasitic contributions of the IDE chip were considered unavoidable, the electrical connection between IDE chip and potentiostat could be purposefully designed to minimize unwanted effects on the current flow by e.g. making the connecting leads as direct and short as possible. R_P, L_P and C_P were assumed approximately equal to sum of both contributions i.e.,

$$R_P \approx R_{P,1} + R_{P,2} \tag{4.5}$$

$$L_P \approx L_{P,1} + L_{P,2} \tag{4.6}$$

$$C_P \approx C_{P,1} + C_{P,2} \tag{4.7}$$

The determination of the individual parasitic circuit parameters will be addressed in chapter 5.3.

4.2.4. Dielectric Reference Data for the Evaluation of Impedance Data

Having access to accurate estimates for both the cell constant K_{Cell} and parasitic capacitance C_P of the electrode chip was of pivotal importance for the quantitative evaluation of the

impedance data. To pinpoint K_{Cell} and C_P, calibration measurements were carried out using dielectric reference media whose relative static permittivity ε_r was reliably determined in previously published studies.

The temperature dependent static ε_r of water and a variety of pure organic liquids is available from the extensive data published by Gregory and Clarke [44] who used a temperature controlled, shielded two terminal cell with parallel plate geometry in their measurements [52]. Likewise, temperature dependent reference values for the dielectric properties of ethanol/water mixtures can be retrieved from the data published by Petong, Pottel and Kaatze [50] who used a cut off type reflection cell in their measurements [148]. The relative permittivity of gases such as nitrogen [149] was not expected to be distinguishable from that of vacuum within the instrument's precision and consequently the reference value was set to 1.0 with no uncertainty attached.

The calibration measurements for the uncoated electrode structures tested in this work were conducted with air/nitrogen, ethanol and 1-butanol as dielectric reference media (DRMs) at the high frequency end for which interfacial contributions to the impedance response of the DRMs were negligible. The high frequency data revealed a capacitance C which is assumed to derive from the effective sum of geometric sample capacitance C_{Geo} (equation 2.26) and the parasitic C_P.

$$C = C_{Geo} + C_P = \frac{\varepsilon_0 \varepsilon_r}{K_{Cell}} + C_P \qquad (4.8)$$

The determination of K_{Cell} and C_P of an electrode chip with the help of equation 4.8 requires measurement of C for at least two different DRMs together with their estimated ε_r values. For each DRM in use, the expected ε_r was computed at the measurement temperature of 21.0 °C with an expanded uncertainty accounting for i) the standard uncertainty as stated in the reference source, ii) the temperature uncertainty stated in the reference source and iii) the temperature uncertainty of this measurement estimated at $\pm$ 0.5 °C. A detailed list outlining the reference values and uncertainties is provided in the appendix B. The validity of equation 4.8 when working with interdigitated structures is comprehensively addressed in chapter 5.3.1

4.2.5. Propagation of Uncertainty

The evaluation methods discussed in this work rely on a variety of different input parameters which are available only at varying degrees of certainty. To quantify the certainty at which the individual output parameters may be determined from the evaluation of the impedance data, the Monte Carlo method (MC) was used to model the propagation of uncertainty across the various steps of the evaluation process (see e.g. [150]). While computationally inefficient, MC allows for the treatment of even complex relationships in a straightforward manner. MC was implemented using custom-written Python scripts which are disclosed together with the supplementary research data.

MC was initiated through random sampling of normally distributed input parameters which were assumed mutually uncorrelated. The associated sampling size was set to 10^6 at all times. Throughout this work, uncertainties are stated at a coverage factor of 2 roughly equivalent

to a 95 % confidence interval. An exhaustive demonstration on how the uncertainty of input parameters affected the extraction of ε from an impedance spectrum is showcased in Fig 4.7.

4.3. Interfacial Pretreatment of the Electrode Structure

To improve the reproducibility of the interfacial contribution to the impedance response, the electrodes were cleaned and/or functionalized with standardized protocols prior to the experimentation. The effects of the individual pretreatment methods on the impedance response is discussed in chapter 5.2.

4.3.1. Cyclic Voltammetry with Sulfuric Acid

A potential sweep with diluted sulfuric acid was suggested by the electrode supplier to clean the gold surface. For this purpose, a 20 µL droplet of 0.05 M aqueous sulfuric acid solution was placed on the interdigitated area. Subsequently, cyclic potential sweeps from -1.0 to 1.3 V were applied at a sweep rate of 100 mV/s (two-electrode setup, no reference electrode). After the completion of 20 potential sweeps, the droplet was rinsed off with deionized water. As a final step, the remaining water film was gently driven off the interdigitated area with a pressurized nitrogen stream.

4.3.2. UV/Ozone Dry Etching

For UV/ozone cleaning of the IDE chips, the electrodes were initially rinsed with deionized water. After the removal of liquid water from the chip with a pressurized nitrogen stream, the electrode chips were placed in the UV/ozone surface cleaning unit. Inside the machine, the electrode chips were exposed to UV irradiation at key wavelengths of 185 and 254 nm. The interaction of the UV light with atmospheric oxygen generates ozone which enhances the surface cleaning effect. After a UV/ozone treatment of 10 min, the electrode chips were removed from the chamber.

4.3.3. Synthesis of Self-Assembled Monolayer

In this work, the electrode fingers were covered with a self assembled monolayer (SAM) of 16-mercaptohexadecanoic acid (MHDA) molecules to support the oriented growth of the HKUST-1 SURMOF. For this purpose, a SAM synthesis solution was prepared of 50 µM MHDA dissolved in a 9:1 volumetric mixture of ethanol (absolute) and acetic acid (glacial). Following the pretreatment with either UV/ozone or the cyclic voltammetry in diluted sulfuric acid, the electrodes chips were immersed into the SAM synthesis solution for a total of 72 hours. Subsequently, the SAM-covered IDE chips were thoroughly rinsed with ethanol and dried in a pressurized nitrogen stream. A schematic drawing of the MHDA-SAM is provided in Fig 4.8.

A)

$$C = C_{Geo} + C_P = (120.3 \pm 0.9) \; pF$$

$$R_E = (100 \pm 10) \; k\Omega$$

B)

$$\frac{(C - C_P) \cdot K_{Cell}}{\varepsilon_0} = \varepsilon_r$$
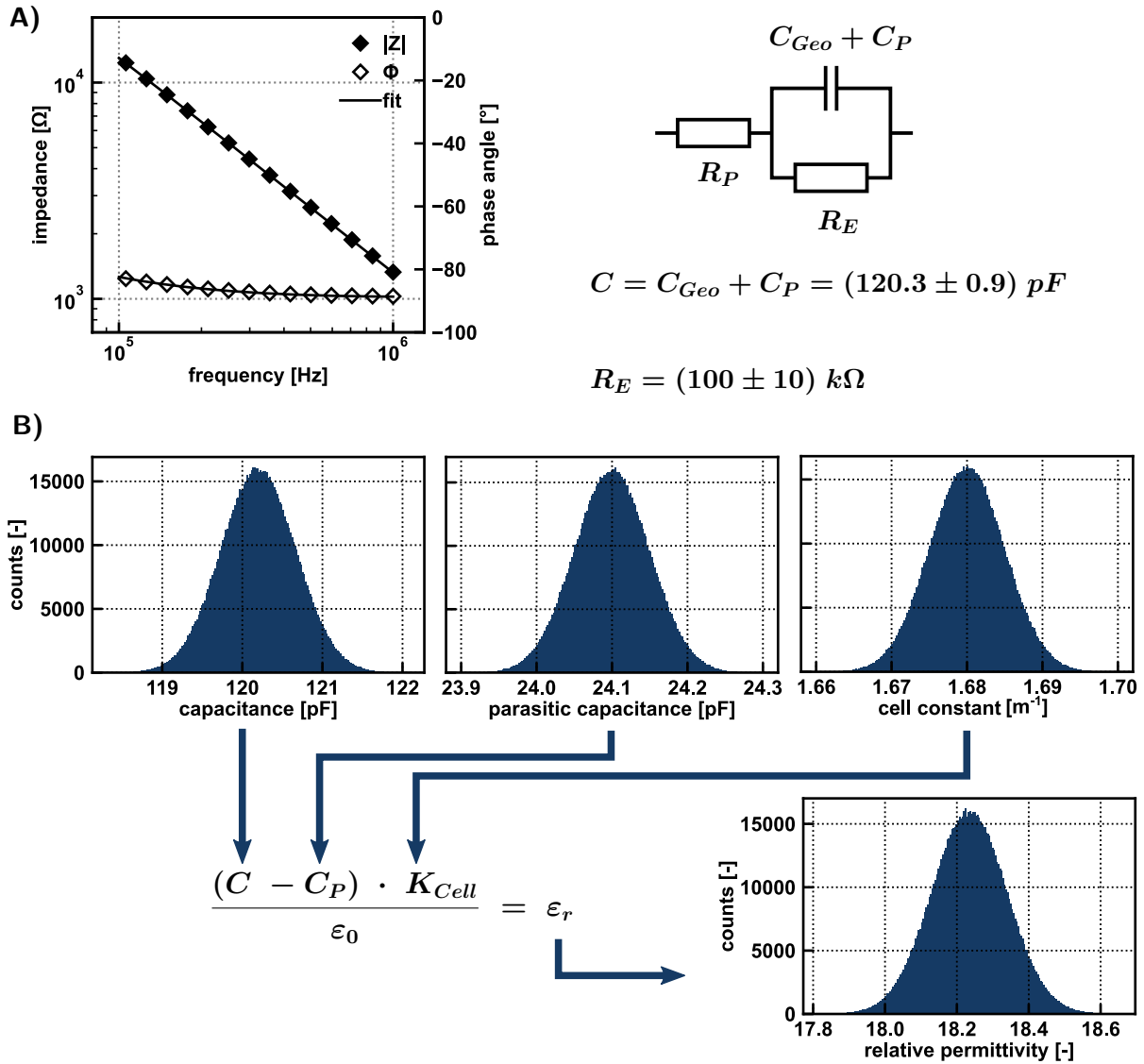
Figure 4.7. Illustrated example of how measurement uncertainty and its propagation was treated in this work. An impedance spectrum taken with a 5 µm-IDE chip using 1-butanol as sample medium is shown in A). The equivalent circuit to model the given impedance data derives from the application of ECM 1 into the generic ECM shown in Fig 4.6 A) to account for parasitics affecting the measurement. The influence of both CPE_{DL} and L_P are negligible within the recorded frequency range and therefore dropped from the circuit model. While the ECM may be fit to the data at a convincing $\chi^2 < 10^{-5}$, the data fit does not provide direct access to C_{Geo} as C_P acts in parallel to C_{Geo} and thus only the effective sum $C = C_{Geo} + C_P$ can be obtained. To compute ε_r from the data, C needs to be compensated by the parasitic C_P and can then be applied to equation 2.26 as indicated in B). Both C_P=(24.1±0.1) pF and K_{Cell}=(1.68±0.01) m^{-1} are known from previous calibration measurements. To visualize the application of the Monte Carlo method, the histograms obtained from random, uncorrelated sampling of 10^6 sets of the normally distributed input parameters C, C_P and K_{Cell} and their effect on the computed output parameter ε_r are plotted in B). The evaluation procedure suggests ε_r=18.2±0.2 for the sample medium investigated. A similar application of R_E and K_{Cell} to equation 2.22 would provide an estimated κ_M=(170±20) nS/cm. Given that ionic migration has only a minor impact on the impedance data within the recorded frequency range, the κ_M estimate is subject to significant uncertainty. It is important to note that C_P and K_{Cell} are in fact correlated which however was neglected to keep the example simple. To obtain correlated data sets of C_P and K_{Cell}, the Monte Carlo model may be expanded by the calibration data evaluation process.
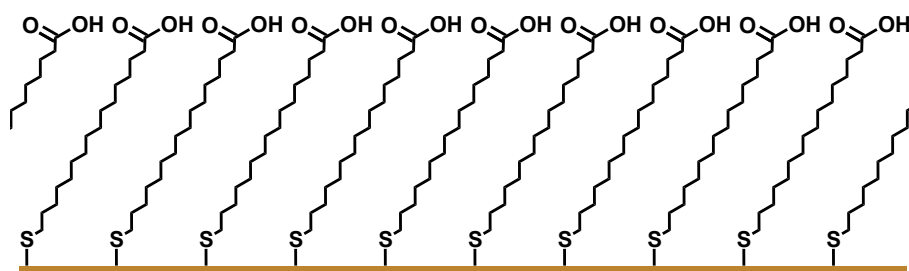
Figure 4.8. Schematic representation of a self-assembled monolayer (SAM) prepared with 16-mercaptohexadecanoic acid (MHDA) molecules covering a gold surface.

4.4. Synthesis of Model Thin Films

4.4.1. HKUST-1 SURMOF Coating

The HKUST-1 SURMOF coating process is based on two precursor and a rinse solution. An ethanolic solution of 1 mM copper(II) acetate (CuAc) served as metal precursor solution and 0.2 mM benzenetricarboxylic acid dissolved in an ethanolic solution containing 25 mol-% water was used as linker precursor solution. An identical mixture of 25 mol-% water and 75 mol-% ethanol also served as the rinsing solution. The addition of water to the linker and rinse solutions has been reported to play a major role enhancing the quality of the synthesized thin film [151, 152]. In a typical HKUST-1 coating process, the functionalized surface to be coated is repeatedly exposed to the metal and linker precursor solution separated by a rinsing step [95]. The exposure sequence *metal - rinse - linker - rinse* is referred to as *growth cycle*. Owing to the removal of excess ligands during the rinsing step, the HKUST-1 SURMOF grows in a highly self-limiting manner with the resulting layer thickness proportional to the amount of growth cycles completed [153].

In this work, MHDA-functionalized IDEs were coated with the HKUST-1 SURMOF using the experimental system outlined in chapter 4.1. For this purpose, the precursor and rinse solutions were among the *sample media* pressurized with nitrogen in Fig 4.1. Every growth cycle consisted of a 10 min exposure to the metal and 15 min exposure to the linker solution passing through the flow cell at a targeted flow rate of 1 µL/s. The rinse step was initially chosen at an increased flow rate of 10 µL/s for 15 seconds for the data which will be discussed in chapter 6.1 but later changed to the same flow rate as the precursor solutions for an extended period of 120 s. With the native HKUST-1 SURMOF synthesis procedure emulated inside the experimental system, impedance spectroscopy could be applied in a straightforward manner for the in-situ monitoring of the actual coating process. Impedance spectra were recorded during the final 30-40 s of the linker and metal precursor exposure step during the first and subsequently every fifth growth cycle. As the growth process was intended to be observed in its native state, the RMS amplitude of the AC voltage signal was deliberately chosen not to exceed 25 mV. Also, to avoid unreasonably long measurement times, impedance data was not collected at frequencies below 2 Hz.

Figure 4.9. Photograph of an IDE chip immersed into a freshly prepared mixture of the ZIF-8 precursor solutions. To avoid the sedimentary deposition of homogeneously nucleated ZIF-8 particles on the surface to be coated, the electrode chip was kept in a vertical position.

4.4.2. ZIF-8 Coating

The majority of published research studies on ZIF-8 thin films, including the cycle-by-cycle grown ZIF-8 SURMOF variant[154][155], employ *methanolic* synthesis conditions [103], [156], [157]. As a mean to simplify the synthetic effort, an alternative *aqueous* preparation strategy was pursued in this work which required neither heating nor pre-seeding of the surface to be coated [158, 159]. The thin film synthesis was conducted using an aqueous 25 mM *zinc acetate* solution as metal and an aqueous 750 mM *2-methylimidazole* solution as linker precursor solution. The surface to be coated was immersed vertically in a freshly prepared 1:1 volumetric mixture of the precursor solutions as displayed in Fig 4.9. Within a few minutes after preparation, the appearance of the precursor solution mixture changed from transparent into whitish, cloudy; indicating the homogeneous nucleation of ZIF-8 crystallites in the solution. Following a 24 h immersion in the ZIF-8 mother solution at room temperature, the sample was removed, briefly rinsed and subsequently dried in a nitrogen stream. The film thickness of the coating could be increased through repetition of the synthesis process by an additional growth cycle with a freshly prepared precursor solution mixture.

Interestingly, while ZIF-8 is not stable in water, it may still be synthesized in aqueous precursor solutions. The key component to stall hydrolytic degradation of ZIF-8 in water appears to be a surplus concentration of linker molecules present in the aqueous solution [109]. In fact, the ZIF-8 preparation strategy described above relies on a 15-fold stoichiometric excess of linker molecules during synthesis.

The ZIF-8 coatings were initially prepared on gold and silicon surfaces to allow for conclusive XRD and SEM assessments of the thin film quality which will the focus of chapter 7.1. For impedimetric characterization, ZIF-8 coated IDE chips were inserted into the impedance measurement system after completion of the synthesis. In contrast to the HKUST-1 coating process, an in-situ impedimetric monitoring of the ZIF-8 coating process on the IDE structure was not pursued within the scope of this work.

4.5. Additional Methods of Analysis

4.5.1. X-Ray Diffraction

Out-of-plane X-ray diffraction patterns using a Bragg-Brentano geometry were recorded for the metal-organic framework (MOF) model thin films to verify the presence of the desired crystalline phase within the coating. Based on Bragg's equation provided in 4.9, a characteristic set of peaks at the diffraction angles θ_d is expected to appear in the X-ray diffractogram which is coupled to the lattice separation distances d_l and the whole-numbered diffraction order n_d of the respective crystalline sample.

$$n_d \lambda_X = 2d_l \sin(\theta_d) \tag{4.9}$$

Copper was used as X-ray source emitting at a characteristic K_α wavelength of $\lambda_X = 0.15406$ nm. A background correction was performed for each diffractogram using the Diffrac.eva software. The out-of-plane mode provides only diffraction peaks of lattice planes parallel to the substrate surface the thin film was deposited on. In contrast, lattice planes tilted towards the substrate surface by an angle larger than $3°$ are not visible in the diffractogram [160]. For this reason, a potential preferential growth orientation can be deduced by comparing the relative peak intensities of the recorded out-of-plane diffraction pattern to that of a (simulated) powder pattern of the same crystalline material. The out-of-plane diffraction pattern of randomly oriented HKUST-1 and ZIF-8 was modelled using the Mercury software on the basis of the crystallographic data deposited by the authors of [90] and [100], respectively.

4.5.2. Scanning Electron Microscopy

Scanning electron microscopy (SEM) was used extensively throughout this work to visualize the morphology of the (coated) electrode fingers. For this reason, SEM greatly facilitated the understanding of the impedance response obtained from a coated IDE chip. Additionally, SEM provided the opportunity to validate the interpretation of the impedance data through comparison of the computed coating thickness d_C value with a coating's cross sectional micrograph. For electron microscopy, the coated electrode chip was mounted on a flat aluminum sample stub with the help of an adhesive carbon pad as displayed in Fig 4.10 A). To prevent accumulation of electrons on the sample surface during visualization, every sample was sputtercoated with a 5-10 nm thick layer of platinum prior to microscopic inspection. Cross sections of the coated IDE structure were prepared through fastening of the IDE mounted flat aluminum stub in a bench vise followed by the fragmentation of the electrode chip through gentle treatment with hammer and chisel. A fragment of the IDE chip was then transferred to a sample stub for cross sectional electron microscopy displayed in Fig 4.10 B) and C). The electron microscope allowed a dynamic adaptation of the focal plane to a constant tilt angle providing complete depth of field for the microscopic setting in Fig 4.10 B). In addition, electron micrographs could be generated by both secondary electron (SE) and backscattered electron (BSE) signal emitted from the sample surface exposed to the primary electron beam. The SE signal was

used for general imaging of the sample morphology. With the image contrast of the BSE signal strongly dependent on the atomic weight of the sample exposed to the primary electron beam, BSE micrographs allowed visual segmentation of the sample structure on the basis of atomic composition to, e.g., differentiate between the gold electrode fingers and the metal-organic coating.
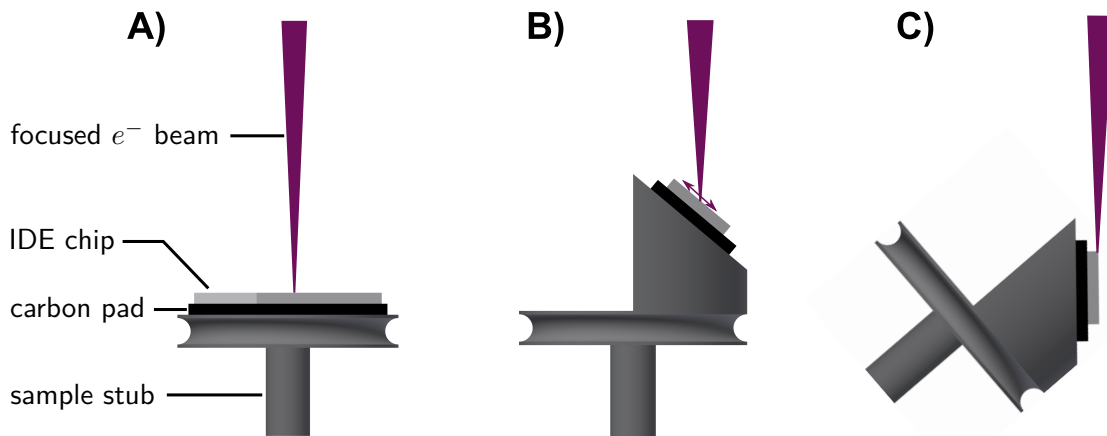
Figure 4.10. Schematic placement of the interdigitated electrode (IDE) chip in relation to the focused electron beam for obtaining A) topview B) tilted and C) cross sectional electron micrographs. The electron microscope allowed the adaptation of the focal plane of the electron beam to a constant sample tilt angle allowing full depth of field in B). To visualize the cross section, the IDE chip was cleaved in two through cautious treatment with hammer and chisel.

5. Characterization of Impedance Measurement Setup and Formal Validation of Functionality

5.1. Microscopic Investigation of the Interdigitated Electrode Structures

The geometry of the electrode sample used for spectrum uptake exerts a pronounced influence on the impedance response recorded with it. In order to facilitate the interpretation of the corresponding impedance spectra as well as to gain a comprehensive understanding of the electrode structure in detail, the pristine IDE chips employed in this work were investigated by a set of microscopic techniques.

A representative light micrograph of a 5 µm-IDE chip is provided in Fig 5.1 A) which allows for a clear distinction between the thin gold electrode structure from the glass substrate onto which the electrode structure is deposited. The 5 and 10 µm-IDE geometries differed solely on the amount N_f, width w and spacing s of the electrode fingers. Both electrode chips featured a circular interdigitated area A_{IDE} with two segments cut off at opposing ends. With the help of the micrograph of the interdigitated area itself shown in Fig 5.1 B), A_{IDE} may be calculated as

$$A_{IDE} = \pi r^2 - r^2(\beta - sin(\beta)) \tag{5.1}$$

with the central angle of the circular segment β accessible via

$$\beta = 2cos^{-1}\left(\frac{t_L}{2r}\right) \tag{5.2}$$

Closeups of the periodic electrode finger structure of the 5 and 10 µm-IDE chips are provided in Fig 5.2 A) and B), respectively, which were taken by scanning electron microscopy. For the 10 µm-IDE geometry, w and s correspond well to the specifications of the supplier whereas for the 5-µm geometry w appears 0.4 µm larger than the expected value at the expense of s. Fig
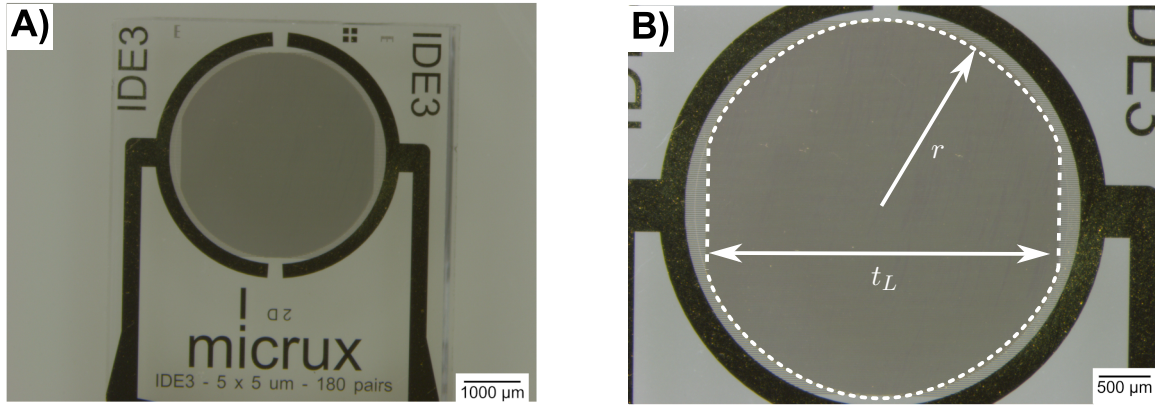
Figure 5.1. Light micrographs of a 5 µm-IDE chip, A) overview and B) closeup of the interlaced comb structures. The interdigitated area is circular in shape with two segments cut off at opposing ends and can be geometrically characterized by its radius $r = 1.80$ mm and truncated length $t_L = 3.40$ mm.
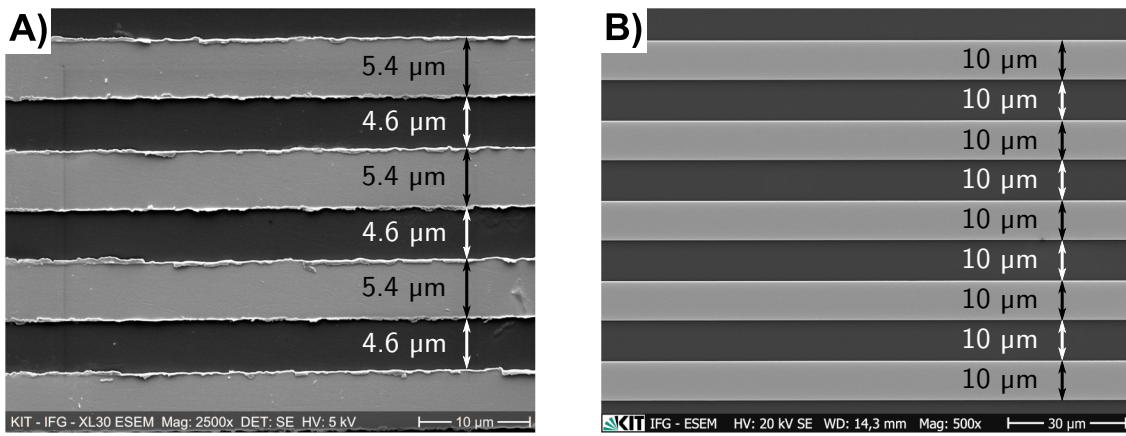
Figure 5.2. Sections of the interdigitated structure of the A) 5 µm and B) 10 µm electrode as observed by scanning electron microscopy. Electrode width w and spacing s are indicated for comparative purposes. For the 5 µm-IDE, a minor mismatch between w and s can be observed.

5.1 and 5.2 provide the necessary information for equation 2.32 to estimate the cell constants K_{Cell} of the IDE chips. As equation 2.32 assumes a rectangular A_{IDE}, an effective rectangular finger length $L_{f,eff}$ of the IDE chips can be computed as

$$L_{f,eff} = \frac{A_{IDE}}{N_f(w + s)}. \tag{5.3}$$

The geometrical parameters characterizing the interdigitated structures are listed in table 5.1. The estimation of K_{Cell} in equation 2.32 is based on the assumption of negligible finger thickness as well as an idealized IDE geometry. While the electrode thickness appears negligible in comparison to w amd s, the tilted cross-sectional micrographs of the 5-µm chip shown in Fig 5.3 reveal roughened electrode edges which may stem from the microfabrication process. The backscattered electron micrograph shown in Fig 5.3 B) confirms the rough edges to be of the same material as the electrode fingers (gold). For this reason, experimental estimates for K_{Cell} are likely to deviate from the values listed in table 5.1.

Table 5.1. Geometrical parameters of the interdigitated electrodes obtained from the micrograph analysis. During impedance data analysis, a conservative estimate of 3 % uncertainty for ηA_{IDE} is used in the following chapters.

Parameter	Unit	5 µm-IDE	10 µm-IDE
w	µm	5.4	10.0
s	µm	4.6	10.0
λ	µm	20	40
η	–	0.54	0.50
N_f	–	360	180
$L_{f,eff}$	mm	2.78	2.78
t_L	mm	3.40	3.40
r	mm	1.80	1.80
A_{IDE}	mm^2	10.0	10.0
$K_{Cell,theo}$	m^{-1}	1.89	4.00
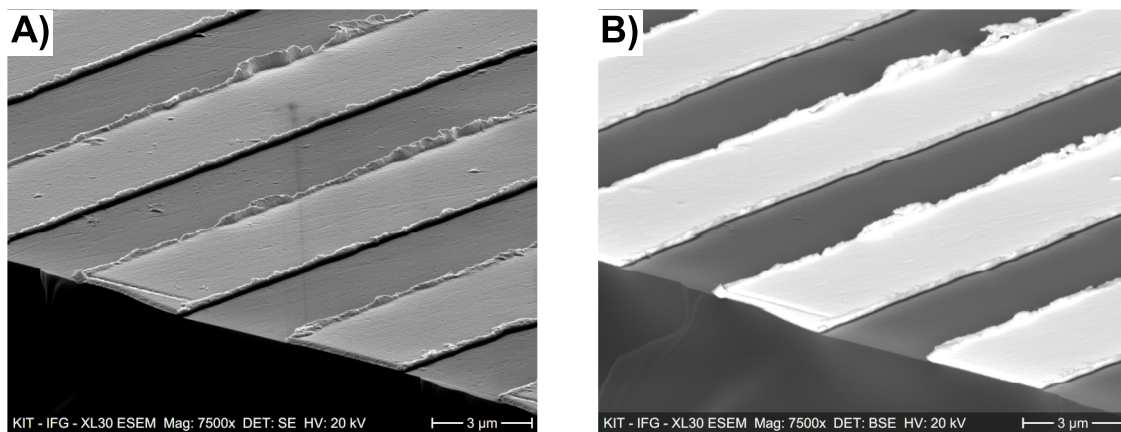
Figure 5.3. Electron micrographs of the tilted cross section of a 5 µm-IDE recorded with the A) secondary electron and B) backscattered electron signal. The roughened edges of the electrode fingers deviate from the idealized IDE geometry.

5.2. Assessment of Interfacial Contributions to the Impedance Response

While not the primary focus of this work, impedance contributions arising at the metal/electrolyte interface deserve special attention for the impedimetric thin film analysis. Identification and proper treatment of such interfacial processes is crucial in order to gain unequivocal access to other relevant parameters such as the coating capacitance C_C or the geometric bulk capacitance C_{Geo}.

Interfacial contributions to the impedance response are intricate as they depend on, among other, the chemical nature, surface area and roughness of the metal/electrolyte interface [29]. Even in the simplest case when Faradaic reactions are absent, the double layer effect at a solid/liquid interface is rarely ideally capacitive and requires modelling by e.g. the generalized

constant phase element CPE_{DL}.

To gain a fundamental understanding of how the interfacial impedance contribution of the gold IDE structures is influenced by the interfacial pretreatment methods outlined in chapter 4.3, impedance spectra were taken using an aqueous 0.5 mM KCl solution as reference medium. The experimental details are outlined in table 5.2. Prior to the experiment, the respective 5-µm electrode chips were preconditioned with potential sweeps in a diluted sulfuric acid solution (H_2SO_4 CV), dry etched in a UV/ozone chamber or furnished with a 16-mercaptohexadecanioc acid self-assembled monolayer (MHDA SAM).

Table 5.2. Outline of the experimental data discussed in chapter 5.2. The raw data are disclosed in the chapter 3.2 of the supplementary research data.

sample medium	interfacial pretreatment	frequency range	RMS voltage	IDE
0.5 mM KCl in water	H_2SO_4 CV	10 Hz - 1 MHz	25 mV	5-µm
0.5 mM KCl in water	UV/ozone	10 Hz - 1 MHz	25 mV	5-µm
0.5 mM KCl in water	MHDA SAM	10 Hz - 1 MHz	25 mV	5-µm

The corresponding impedance spectra are plotted in the Bode format in Fig 5.4. From the graphical perspective, the Bode plots obtained for the three different interfacial preconditioning methods correspond well to the typical Bode plot of a non-Faradaic, uncoated system expressed by ECM 1 shown in Fig 2.7. While all spectra collectively adopt a resistive impedance modulus $|Z|$ at the high frequency end, $|Z|$ adopts a capacitive behavior towards the lower frequency end with significant differences between the three preconditioning methods. For this reason, it is reasonable to assume the high frequency data to be dominated by the electrolyte resistance R_E and the lower frequency end by the interfacial impedance contribution CPE_{DL}. The greatest impact of interfacial impedance on the measured data is observed for the interdigitated structure equipped with the MHDA SAM whereas the interfacial impedance appears lowest when pretreated by the UV/ozone cleaning method. When excluding the lowest frequency decade, the data shown in Fig 5.4 can be adequately modelled with ECM 1. At frequencies between 10 and 100 Hz, interfacial impedance behavior inconsistent with a mere constant phase element becomes visible in the phase angle Φ plot which might potentially derive from a chemical interaction of the chloride anion and the gold surface [161].

The best-fit estimates for the individual circuit components of ECM 1 are listed in table 5.3. As the electrodes were tested against identical aqueous 0.5 mM KCl reference media, the circuit parameters representing the bulk impedance contribution R_E and C_{Geo} are in good agreement with only minor influence of the interfacial pretreatment method. It is important to note however, that the data does not allow for an optimal extraction of C_{Geo} considering that C_{Geo} exerts only marginal influence on the impedance response within the recorded frequency range. The slightly underestimated C_{Geo} for the MHDA SAM pretreated electrode chip might
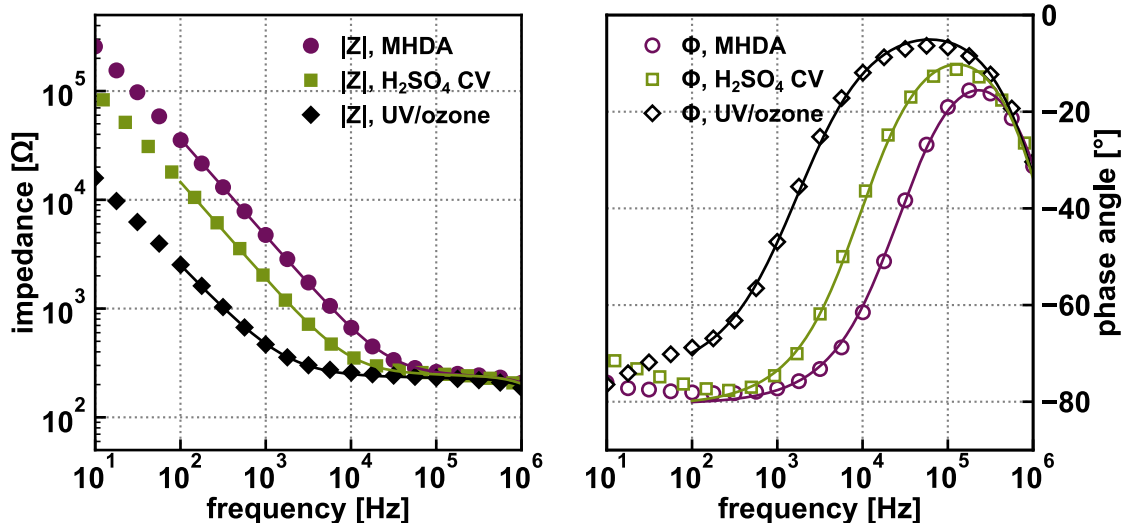
Figure 5.4. Bode plot representation of the impedance data sets for the experiments outlined in table 5.2. The data fit curve obtained with ECM 1 at frequencies larger than 100 Hz is plotted alongside the raw data for frequencies. The associated goodness of fit parameters χ^2 range below $6.5 \cdot 10^{-4}$.

Table 5.3. Numerical best-fit ECM 1 parameters obtained from the data fits. The derived parameters C_{DL} and $\bar{c}_{DL}$ are presented without uncertainty as they represent only rough estimates based on the Brug formula. Within the scope of this chapter, parasitic contributions to the measured impedance data are not specifically compensated for.

Interfacial Pretreatment	R_E [Ω]	C_{Geo} [pF]	Q_{DL} [nS·s$^{\alpha_{DL}}$]	α_{DL} [-]	C_{DL} [nF]	$\bar{c}_{DL}$ [µF/cm^2]
H$_2$SO$_4$ CV	244±3	430±20	210±10	0.90±0.01	66	2.5
UV/ozone	231±1	440±10	1920±80	0.83±0.00	430	16
MHDA SAM	242±2	370±10	87±2	0.89±0.00	24	0.90

stem from modelling difficulties due to significant interfacial contributions to the impedance data even at the high frequency end combined with a slight change in the effective relative permittivity due to the presence of the SAM molecules.

The constant phase exponent α_{DL} of solid/liquid interfaces is occasionally reported to range between 0.8 and 1.0 (e.g. [162]) which is also observed for the data discussed here. When applying R_E, Q_{DL} and α_{DL} to the Brug formula in equation 2.16 an equivalent value for the double layer capacitance C_{DL} can be approximated and is shown in table 5.3. As the C_{DL} parameter represents only an estimate of the inherently distributed interfacial impedance contributions, error propagation across the Brug formula is not meaningful and therefore omitted. Normalization of C_{DL} to ηA_{IDE} and accounting for the serial connection of the double layer capacitance at the oppositely charged electrode fingers provides access to the area normalized double layer capacitance $\bar{c}_{DL}$ which facilitates the interpretation. When taking a look at the cleaning methods investigated, $\bar{c}_{DL}$ of the UV/ozone treated electrode structure compares almost an order of magnitude larger than the corresponding value of the H$_2$SO$_4$ CV treated electrode. For a clean metal surface, $\bar{c}_{DL}$ is said to approximately range between 10 - 50 µF/cm^2

[20]. Dielectric contaminants present at the interface between metal and electrolyte reduce the measured $\bar{c}_{DL}$. For this reason, when evaluating the cleaning methods on the basis of $\bar{c}_{DL}$, the UV/ozone treatment appears to provide significantly improved metal surfaces cleanliness than the H_2SO_4 CV pretreatment strategy tested in this work.

In an extensive study conducted by Fischer et al. [163] several different gold cleaning methods were compared using Faradaic measurements as well as the elemental composition obtained by x-ray photoelectron spectroscopy as evaluation criteria. Similar to the observations discussed here, their electrochemical investigations did not find a significant surface cleaning effect obtained by H_2SO_4 CV [163]. On the other hand, the authors did not observe a reliable cleaning effect of the UV/ozone treatment for their experiments either, which Fischer et al. however attributed to a possible contamination of their photoreactor [163]. By contrast, the UV/ozone surface treatment in this work appeared to provide a reliable cleaning effect.

With regard to the impedance response of the IDE chip pretreated with the MHDA SAM, it is perfectly reasonable to approach impedance data analysis from the perspective of ECM 2. After all, the MHDA SAM effectively constitutes a dielectric thin film covering the electrode surface. When assuming the MHDA SAM impermeable to ionic migration and a full surface coverage, thus setting $R_C \to \infty$, and assigning CPE behavior to C_C, ECM 2 would provide an identical impedance data fit as ECM 1 in Fig 5.4. Following this line of thought, the C_{DL} parameter of the MHDA coated IDE experiment in table 5.3 could be interpreted as the coating capacitance C_C imparted by the MHDA SAM. Application of equation 4.3 would then lead to

$$\frac{d_{C,MHDA}}{\varepsilon_{r,C,MHDA}} \simeq 0.98nm. \tag{5.4}$$

With the help of an educated guess such as equating $\varepsilon_{r,C,MHDA}$ to the bulk relative permittivity of n-hexadecane amounting to $\varepsilon_r = 2.0$ [164], the MHDA thickness $d_{C,MHDA}$ can be approximated to roughly 2 nm which appears to be a reasonable estimate. It is important to note however that $d_{C,MHDA}$ is likely to be overestimated following this approach as the roughened edges of the electrode fingers visible in Fig 5.3 would cause the the effective interfacial surface area to increase beyond ηA_{IDE} which is not accounted for when applying C_{DL} from table 5.3 to equation 4.3. To avoid confusion of terminology in the subsequent chapters when working with the HKUST-1 thin films, the interfacial impedance contributions of an MHDA functionalized gold surface will be continued to be referred to as the double layer effect.

To finalize the assessment, the interfacial impedance contribution measured with the automated experimental system provides area normalized $\bar{c}_{DL}$ values consistent with conventional impedimetric setups. As the UV/ozone treatment appeared to provide adequately clean electrode surfaces at minimal work effort it was henceforth utilized as the preferred pretreatment method for every subsequent impedance measurement as well as SAM preparation.

5.3. Assessment of Bulk Contributions to the Impedance Response

The evaluation of bulk contributions to the impedance response obtained with interdigitated electrode played a central role in this work and was therefore addressed in detail. The results

and interpretation of the data sets discussed in this chapter have been published separately in [165].

Within the framework of equivalent circuit modelling, the bulk contribution to the impedance data imparted by the sample medium in between the electrode structure is conventionally regarded to be comprised of a parallel connection of geometric capacitance C_{Geo} and electrolyte resistance R_E [18]. Recent studies suggest that the inhomogeneous potential and current distributions developing in the sample volume stimulated by the IDE geometry, however, give rise to a considerable *geometry-induced frequency dispersion* affecting both R_E and C_{Geo} [166, 167, 168]. For this reason, it was investigated whether the conventional modelling of bulk impedance contributions with real and frequency invariant R_E and C_{Geo} circuit components was reasonably applicable to the data generated within the scope of this work. A second objective was to ascertain the possibility to obtain conclusive bulk information ($\kappa_M, \varepsilon_{r,M}$) of the sample fluid pumped through the flow cell equipped with either the 5- or 10 µm-IDE chip. For this purpose, the impedance measurement system was comprehensively tested against a total of nine well-defined, homogeneous sample media.

Table 5.4. Outline of the experimental impedance data discussed in chapter 5.3. The spectra are disclosed in chapter 3.3 of the supplementary research data.

no.	sample medium	frequency range	RMS voltage		ECM
			5 µm-IDE	10 µm-IDE	
1	nitrogen	100 kHz - 1 MHz	1500 mV	2800 mV	1, b)
2	1-butanol	100 kHz - 1 MHz	370 mV	810 mV	1, a)
3	ethanol	100 kHz - 1 MHz	290 mV	630 mV	1, a)
4	water	100 kHz - 1 MHz	79 mV	230 mV	1, a)
5	54 mol-% ethanol in water (mixture)	100 kHz - 1 MHz	205 mV	450 mV	1, a)
6	22 mol-% ethanol in water (mixture)	100 kHz - 1 MHz	135 mV	310 mV	1, a)
7	CRM $\kappa_M(25°C) = 1410$ µS/cm	5 kHz - 5 MHz	50 mV	70 mV	1
8	CRM $\kappa_M(25°C) = 25.0$ µS/cm	5 kHz - 5 MHz	90 mV	190 mV	1
9	saturated KCl solution (aqueous)	5 kHz - 5 MHz	20 mV	17 mV	1 c)

A detailed list outlining the sample media and measurement conditions is provided in table 5.4. To enhance confidence in the general validity of the data and evaluation procedure, the impedance spectra were recorded as triplicates confirming stationarity of the measurement carried out with both the 5 and 10 µm-IDE structures. Sample media 1-6 served as dielectric reference media (DRMs) whose temperature dependent permittivity values are available from the literature. Sample media 7 and 8 represented certified KCl in water solutions and were used as conductivity reference media (CRMs). The voltage amplitudes and designated frequency ranges were optimized to allow the current response to be recorded at an optimal signal-to-noise ratio within a single current measurement range of the potentiostat. The impedance response

ECM 1   ECM 1, a)   ECM 1, b)   ECM 1, c)
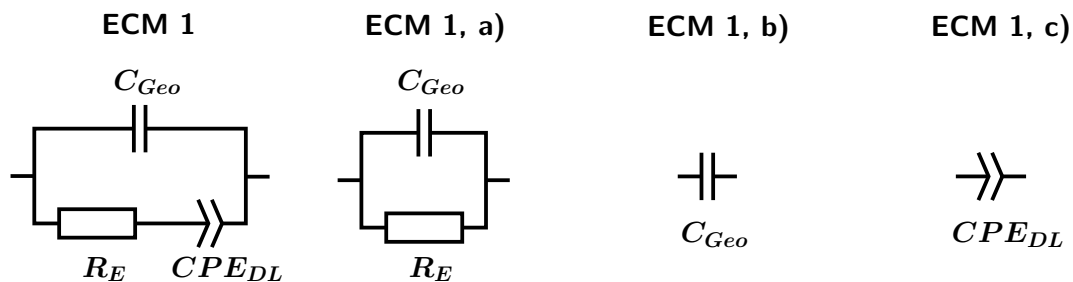
Figure 5.5. ECM 1 and practical simplifications thereof accounting for a) negligible interfacial contributions, b) negligible migration of charge carriers and c) negligible bulk contributions due to a large sample medium conductivity.

of the sample media Z_S was expected to comply with ECM 1 or even simplifications thereof which is indicated in the rightmost column of table 5.4 and in Fig 5.5.

Following an impedance data fit, the extracted R_E and C_{Geo} can be converted into the tangible sample medium properties *relative static permittivity* ε_r via equation 2.26 and *electrolytic conductivity* κ_M via equation 2.22. To assess whether the conventional theory of bulk impedance contribution may be reasonably applied to the data collected with this work's impedance measurement setup, the estimates for ε_r and κ_M are subsequently compared to reference values computed from literature data. The reference values were subject to an expanded uncertainty owing to i) the standard uncertainty stated in the literature source, ii) temperature uncertainty stated in the literature source and iii) temperature uncertainty of this measurement estimated at $\pm 0.5°\text{C}$. The computation of the reference values is comprehensively disclosed in the Appendix B

5.3.1. Pinpointing Cell Constant and Parasitic Contributions to the Impedance Response

Following the theoretical framework outlined in Fig 4.6 B), the parasitic contributions are distinguished between those imparted by the electrical integration of the IDE chip into the measurement system and the IDE chip itself. The parasitics of the electrical connection to the IDE chip stem from the potentiostat cell cable and connection module of the flow cell and can be assessed in a straightforward manner with the help of an *open* and *short* measurement. For this purpose, impedance data was taken using the assembled flow cell with (i) no IDE chip installed (*open*) and (ii) a copper platelet inserted into the designated IDE socket of the base module (*short*). The corresponding spectra are displayed in Fig 5.6.

With no conduction path between the potentiostat leads during the *open* measurement, the current signal is limited to the unintentional parasitic coupling between conductors in the measurement system. Accordingly, the impedance data shown in Fig 5.6 A) may be reasonably fit to the single stray capacitor $C_{P,1} = (1.0 \pm 0.0)$ pF. The *short* measurement on the other hand aims to quantify the current flow limitation through the cell cable and the flow cell connection module. A resistor in series with an inductor provides an adequate data fit to the impedance response of the *short* measurement shown in Fig 5.6 B) with $R_{P,1} = (0.1 \pm 0.0)$ Ω and $L_{P,1} = (80 \pm 0.0)$ nH.
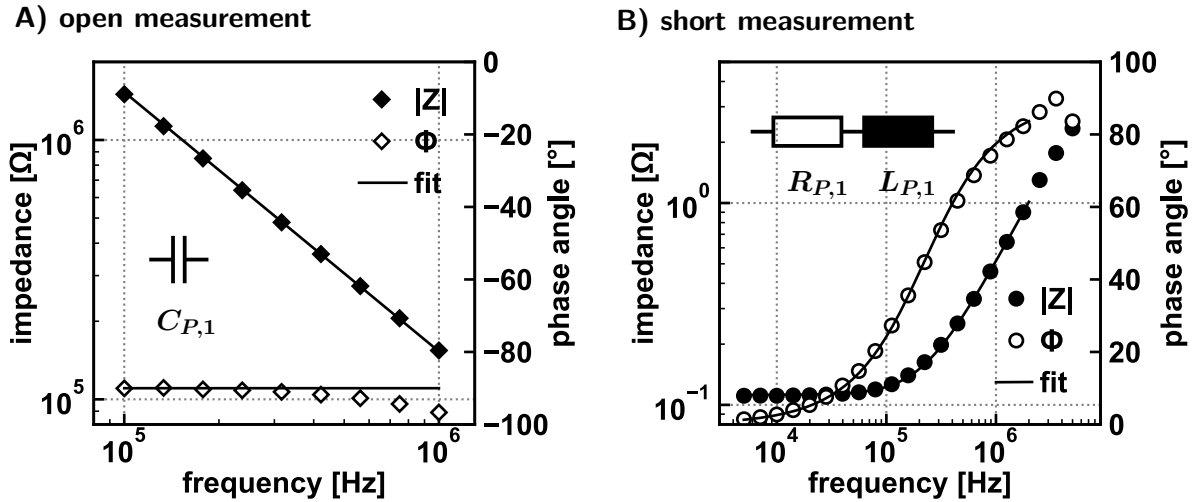
Figure 5.6. Impedance data collected using the measurement system A) without IDE chip and B) with the IDE chip replaced by a copper platelet. Numerical analysis of the impedance spectra suggest $C_{P,1} = (1.0\pm0.0)$ pF, $R_{P,1} = (0.1\pm0.0)$ Ω and $L_{P,1} = (80\pm0)$ nH. Minor inconsistencies are visible in the data such as phase angles below -90° in A) or above +90° in B) which may stem from the extreme measurement conditions at the high frequency end of the spectra.

In contrast to the determination of $R_{P,1}$, $L_{P,1}$ and $C_{P,1}$, a similarly straightforward open and short measurement to directly pinpoint the parasitic contributions of the IDE chips $R_{P,2}$, $L_{P,2}$ and $C_{P,2}$ did not appear feasible. With a separately measured conductivity of κ_M=330 mS/cm however, the impedance response of the saturated, aqueous KCl solution shown in Fig 5.7 A) appears to provide an adequate perspective on the parasitic contributions similar to a *short* measurement. Application of κ_M together with the theoretical cell constants $K_{Cell,theo}$ from table 5.1 to equation 2.22 would provide estimated electrolyte resistances of $R_E = 0.06$ Ω for the 5 µm and $R_E = 0.12$ Ω for the 10 µm-IDE geometry. The impedance data sets collected for the saturated KCl solution are shown in Fig 5.7 A) and exhibit resistive plateaus located nearly two orders of magnitude above the estimated R_E values which serves as a strong indication that ionic migration through the bulk of of the saturated KCl solution does not constitute the bottleneck of current flow through the impedance measurement system. Also, the phase angle rising above 0° at the high frequency end is a clear indication of inductive current flow limitation imparted by the parasitic L_P associated to the cabling. Accordingly, the impedance data recorded for the saturated KCl solution may be reasonably modelled with a serial connection of R_P, L_P and the interfacial contribution CPE_{DL} while neglecting the bulk R_E as well as C_{Geo} contribution.

The determination of the third parasitic circuit parameter C_P is intricate, as C_P acts directly in parallel to the geometric capacitance of the sample medium C_{Geo}. Therefore a single dielectric measurement with subsequent equivalent circuit fit can only ascertain the respective sum of C_P and C_{Geo}. When compensating the impedance data collected for the six DRMs by R_P and L_P, one arrives at the capacitance values plotted in Fig 5.7 B). In a previously published study on the impedance response of interdigitated structures [169], no substantial difference in C_P+C_{Geo} between a measurement recorded in nitrogen and water could be observed which was attributed

A)

B)
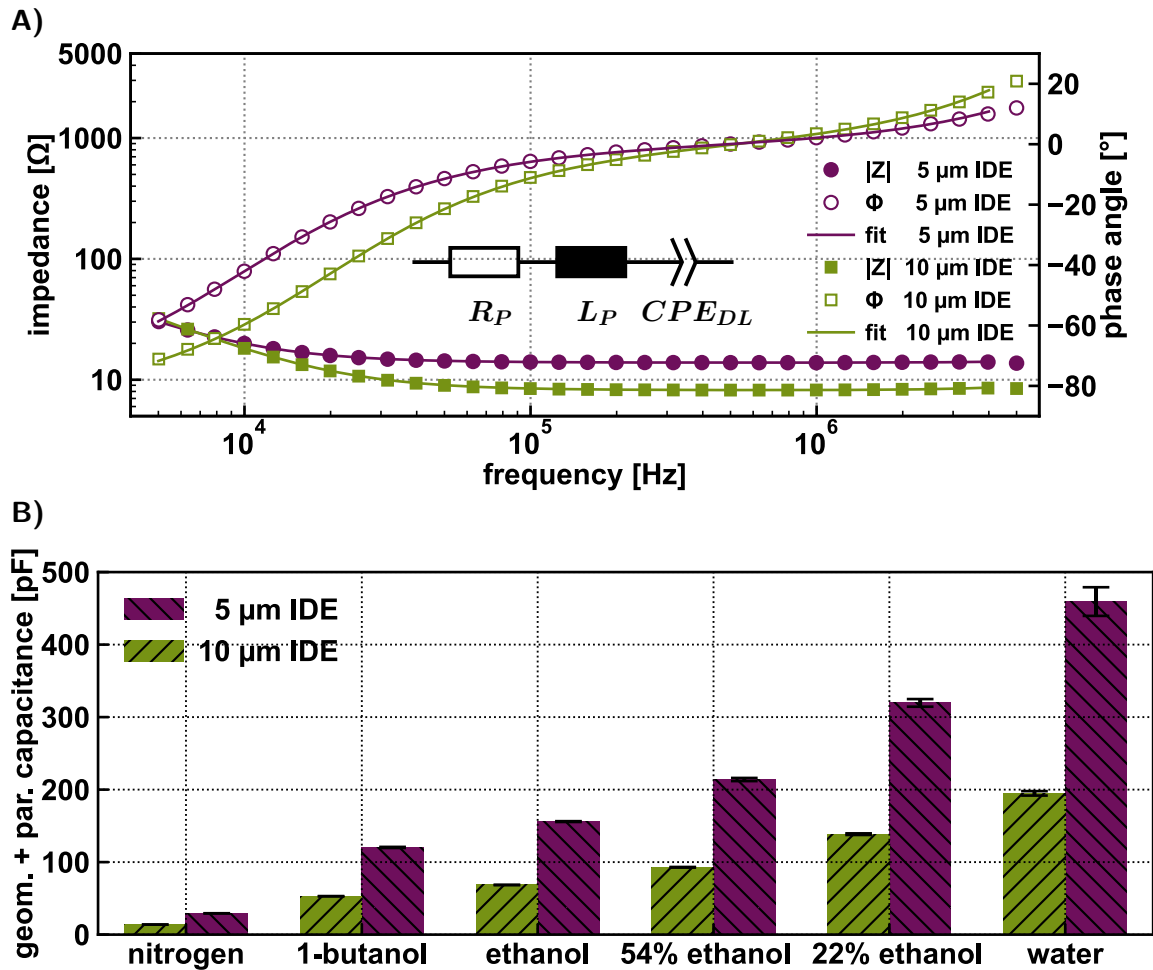
Figure 5.7. A) Bode representation of the impedance response recorded for the saturated KCl solution with both the 5 and 10 µm-IDE structure. An equivalent circuit model comprised of only R_P, L_P and CPE_{DL} provides an excellent representation of the measured spectra at $\chi^2 = 8 \cdot 10^{-6}$. The impedance data above 4 MHz appeared unstable and was not included in the data fit. B) Total capacitance (geometric + parasitic) extracted from the impedance response of the six dielectric reference media. A strong dependence of the total capacitance on the sample medium in contact with the interdigitated area as well as on the actual IDE structure is observed. It follows that the parasitic capacitance of this work's impedance measurement system has been adequately minimized to facilitate conclusive dielectric measurements of the sample media in contact with the interdigitated area.

to a disproportionately large C_P of the author's measurement system. The contrasting results shown in Fig 5.7 B) suggest C_P to be sufficiently minimized in this work's measurement system meaning the dielectric properties of the sample medium in contact with the interdigitated area have a significant influence on the measured, equivalent sum of $C_P + C_{Geo}$. To obtain an experimental estimate of K_{Cell} and C_P, the total capacitance values measured for nitrogen and ethanol may be chosen as calibration media and applied to equation 4.8 together with their estimated ε_r reference values computed from the literature data as outlined in chapter 4.2.4. K_{Cell} and the parasitic contributions reduced to those imparted by the IDE chip itself through application of equations 4.5- 4.7 are listed in table 5.5. Experimental values for K_{Cell} have been reported to be usually 10 - 20 % smaller than $K_{Cell,theo}$ computed with equation 2.32 [67] which is also observed in this study when comparing $K_{Cell,theo}$ in table 5.1 with K_{Cell} in

table 5.5 for both the 10 and 5 µm-geometries. While the data evaluation procedure provides identical estimates for $L_{P,2}$, the parasitic metal thin film resistance $R_{P,2}$ of the 5 µm-IDE is roughly 70 % larger than of its 10 µm counterpart. A plausible explanation could be a slight variability of the electrode film thickness during the production process of the IDE chips which would effectively influence the film resistance between the contact pad and the interdigitated area. However, considering the magnitude of mismatch of $R_{P,2}$ between the two electrode chips investigated, the bottleneck of electron conduction might potentially also be imparted along the electrode fingers themselves. In addition to $R_{P,2}$, a significant mismatch in $C_{P,2}$ is observed which, however, is consistent with the computed potential distribution of the IDE structure in Fig 2.12. An IDE chip's stray capacitance $C_{P,2}$ may be understood as an equivalent *geometric capacitance* corresponding to the actual electrode substrate located below the interdigitated area. To substantiate this claim, the final row of table 5.5 represents the application of $C_{P,2}$ and K_{Cell} to equation 2.26. This approach provides remarkably similar relative permittivity values for both the 5 and 10 µm-IDE which fall within the expected value range for glasses [53]. Accordingly, IDE structures may be used to analyze not only sample media placed onto the interdigitated area but also to analyze the substrate material onto which the interdigitated structure is deposited. With regard to table 5.5, the minor discrepancy between the relative permittivity of the electrode substrate computed with the 5 and 10-µm data may stem from neglecting the finite metal film thickness when applying K_{Cell} and $C_{P,2}$ to equation 2.26.

Table 5.5. Experimental cell constants and parasitic model parameters of the 5 and 10 µm-IDE chip.

parameter	unit	5 µm-IDE	10 µm-IDE
K_{Cell}	m^{-1}	1.68±0.01	3.89±0.02
$R_{P,2}$	Ω	13.7±0.1	8.0±0.1
$L_{P,2}$	nH	30±10	30±10
$C_{P,2}$	pF	23.1±0.1	10.6±0.1
$\frac{C_{P,2}K_{Cell}}{\varepsilon_0}$	–	4.4±0.0	4.7±0.0

5.3.2. Extraction of Relative Static Permittivity

The static relative permittivity values determined for the dielectric reference media after compensation of parasitic contributions are listed in table 5.6 alongside the computed reference value. The permittivity values for nitrogen and ethanol are italicized to highlight the appropriation of their impedance data for the estimation of K_{Cell} and C_P in the previous chapter.
There is a considerable overlap between the static permittivity values determined with the two IDE structures and the reference values stemming from dielectric measurements with conventional electrode geometries. A general tendency to overestimate the static permittivity values can however be observed in the data displayed in table 5.6. When analyzing the same sample medium, the 5 µm-IDE appears to provide slightly larger permittivity values than the 10 µm structure. Especially the data recorded for water appears significantly overestimated

Table 5.6. Relative permittivity values extracted from the impedance data recorded at $T = (21.0\pm0.5)$ °C when evaluating the full frequency range from 0.1 - 1 MHz. The nitrogen and ethanol data are italicized to highlight their appropriation to pinpoint K_{Cell} and C_P in the previous chapter. The computation of the reference values is discussed in the Appendix B

sample medium	relative static permittivity ε_r [-]		
	5 µm-IDE	10 µm-IDE	reference value
nitrogen	*1.0±0.0*	*1.0±0.0*	1.0±0.0
1-butanol	18.2±0.2	18.2±0.1	18.1±0.1
ethanol	*25.0±0.1*	*25.0±0.1*	25.0±0.1
water	82.6±3.8	80.5±1.4	79.9±0.3
54 mol-% ethanol in water (mixture)	36.0±0.4	35.7±0.2	36.3±0.7
22 mol-% ethanol in water (mixture)	56.1±1.0	55.8±0.5	55.0±1.1

with a disproportionate level of uncertainty.

The apparent bias affecting the relative permittivity extraction from the impedance data is likely caused by residual conductivities of the sample media giving rise to non-negligible interfacial contributions to the impedance response even at frequencies above 0.1 MHz. Owing to the complexity of interfacial contributions to the impedance response, active compensation thereof e.g. through addition of the CPE_{DL} circuit parameter to ECM 1 b) in Fig 5.5 does not provide reliable access to bulk permittivity values at satisfactory precision [44]. As an alternative, the evaluated frequency range may be truncated to the high frequency end to reduce the relative influence of interfacial contributions on the data.

When confining the static permittivity extraction to the frequency range 0.5 - 1 MHz, one arrives at the permittivity values provided in table 5.7. A comparison of the permittivity data between table 5.6 and 5.7 reveals that especially the high permittivity sample media appear to benefit from the change in evaluation procedure, whereas the frequency truncation has no effect on the data belonging to the low permittivity sample media. This observation is not surprising given that the relative permittivity of a solvent is a measure of the solvent molecule's capability to screen the electrostatic interaction of solvated ionic species [170]. The lower the relative permittivity of a solvent, the stronger solvated ionic species interact promoting the occurrence ion association [171]. Associated ions possess no net charge and therefore do not contribute to the electrolytic conductivity of a sample medium. For this reason, high permittivity dielectric reference media are more susceptible to residual conductivities imparted by fully solvated, ionic contaminants and, as a consequence, are more susceptible to undesired interfacial impedance contributions even at high frequencies in the upper kHz and MHz range.

The crucial question however is, how exactly the ionic contaminants enter the sample media under test. Interestingly, the measurements taken with the 5 µm-IDE appear to be more strongly affected by residual conductivities than the data collected with the 10 µm-IDE. Applying the electrolyte resistance parameter R_E to equation 2.22 provides an electrolytic conductivity of the deionized water used as sample medium 4 of (1.2±0.1) µS/cm with the 10 µm-IDE data and

Table 5.7. Relative permittivity values extracted from the impedance data when reducing the evaluated frequency bandwidth to 0.5 - 1 MHz.

sample medium	relative static permittivity ε_r		
	5 µm-IDE	10 µm-IDE	reference value
nitrogen	*1.0±0.0*	*1.0±0.0*	1.0±0.0
1-butanol	18.2±0.2	18.2±0.1	18.1±0.1
ethanol	*25.0±0.1*	*25.0±0.1*	25.0±0.1
water	80.8±0.8	79.9±0.4	79.9±0.3
54 mol-% ethanol in water (mixture)	35.9±0.4	35.7±0.1	36.3±0.7
22 mol-% ethanol in water (mixture)	55.6±0.3	55.6±0.2	55.0±1.1

(5.7±0.3) µS/cm with the 5 µm-IDE data. In contrast, a separate measurement of the water stock solution with a commercial conductivity probe suggested a conductivity value between 0.5 and 0.7 µS/cm. As the experiments were carried out in quick succession with an extensive rinsing step in between, a general ionic contamination of the measurement system is ruled out. A possible explanation for the apparent increase in conductivity might be leaching of ions from the glass substrate into the sample medium above. As a matter of fact, the slow but steady release of ions from a glass storage container has been identified as the major contributing factor reducing the long term stability of low conductivity CRMs [172]. If true, ion leaching from the electrode substrate would lead to the formation of an ionic concentration gradient perpendicular to the interdigitated area. As the effective sensing range of the 5 µm-IDE structure is half the size of its 10 µm variant, the 5 µm electrode would provide a closer picture of the diffusive boundary layer, i.e., detect a greater conductivity. Potentially, the UV/ozone cleaning step used for the electrode preparation could have a detrimental effect on the structural integrity of the glass substrate or impose significant surface acidity which would increase the apparent ionic concentration in close proximity to the interdigitated area.

5.3.3. Extraction of Electrolytic Conductivity

The impedance data recorded for the CRMs used as sample media 7 and 8 is displayed in Fig 5.8. From a purely mathematical perspective, despite the data being significantly influenced by parasitic contributions, ECM 1 alone would be able to provide a decent data fit to the impedance spectra displayed. The influence of parasitics on the impedance response is deceptive; R_P acts in series to R_E whereas C_P acts in parallel to C_{Geo}. In order to eliminate the bias at which R_E is estimated from the data, the parasitics need to be thoroughly compensated for, e.g., through expansion of ECM 1 with the parasitic circuit components as proposed in Fig 5.8 B). Application of the best-fit estimates of R_E together with the respective K_{Cell} data to equation 2.22 provides the conductivity values listed in table 5.8. The correlation between the computed reference values and the experimental estimates clearly indicate the possibility to characterize the conductive properties with IDE geometries. The irregular discrepancies of the conductivity values in table 5.8 however suggest the influence of several confounding effects compromising
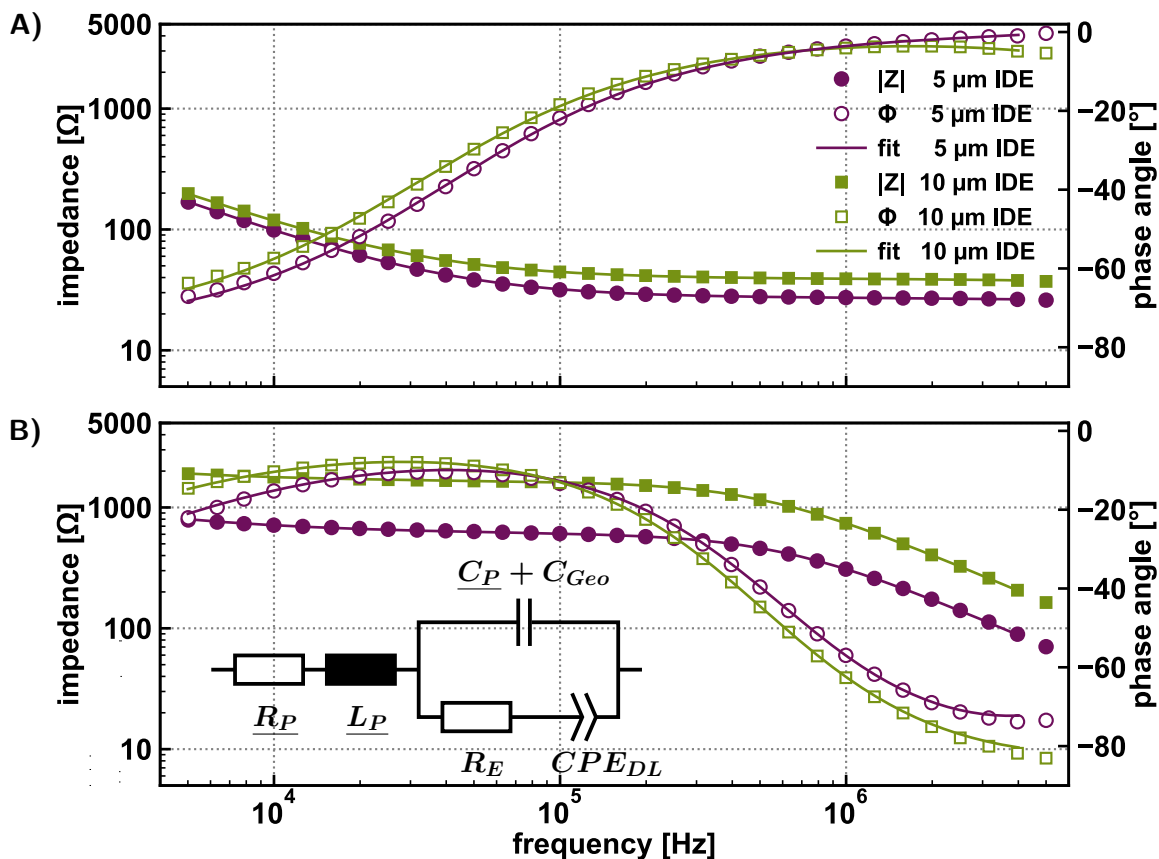
Figure 5.8. Bode representation of the impedance spectra of the conductivity reference media A) $\kappa_M(25°C)$=1410 µS/cm and B) $\kappa_M(25°C)$=25.0 µS/cm recorded with both the 5 and 10 µm-IDE geometry. The parasitic model parameters in the ECM inserted in B) were kept constant during data fit.

the accuracy of the measurement. For the high conductivity CRM, the 5 and 10 µm-IDE provide identical estimates slightly below the reference value yet still with overlapping error margins. By contrast, in case of the less conductive CRM, the evaluation of the impedance data collected with both IDE geometries significantly overestimates the sample medium conductivity. As was observed in the previous chapter, the same sample medium appears more conductive when analyzed with the 5 µm structure than with the 10 µm geometry. Again, the leaching of ions from the substrate underneath into the sample medium above the interdigitated area would appear as a plausible explanation potentially producing an offset of around 5 µS/cm for the 5 µm and 1 µS/cm for the 10 µm-IDE. Attributing the discrepancy of conductivity estimates for the low conductivity CRM to a constant offset rather than a relative bias is supported by the data collected for the high conductivity CRM for which the offset would have an insignificant effect on the measurement.

It is worth stressing that the values of K_{Cell} were computed on the basis of the dielectric measurements conducted with nitrogen and ethanol. Conventionally, K_{Cell} of a conductivity probe is obtained through calibration measurements conducted with CRMs. If the IDEs in this study had been calibrated accordingly, the corresponding K_{Cell} would have been considerably compromised by the apparent increase in the sample medium conductivity as shown for the

Table 5.8. Comparison of the electrolytic conductivity values extracted from the impedance data of the conductivity reference media recorded at $T = (21.0 \pm 0.5)$ ℃ with the expected values.

sample medium	electrolytic conductivity κ_M [μS/cm]		
	5 μm-IDE	10 μm-IDE	reference value
CRM $\kappa_M(25°) = 1410$ μS/cm	1270 ± 30	1270 ± 20	1300 ± 10
CRM $\kappa_M(25°) = 25.0$ μS/cm	28.6 ± 0.4	24.1 ± 0.3	22.9 ± 0.3

low conductivity CRM in table 5.8. Interestingly, a slight dependence of a conductivity probe's K_{Cell} on the actual conductivity level is consistently reported in the literature [38]. Likewise, the influence of geometry-induced frequency dispersion on R_E, which was reported for IDEs owing to the inhomogeneous potential and current distributions [166], may also be interpreted on the basis of a frequency dependence of K_{Cell}. Finite element simulations of the impedance response of a 5 μm-IDE structure suggest the effective K_{Cell} to increase by approximately 10 % when reducing the frequency from f_{CR} to the R_E/CPE_{DL} relaxation frequency [166].

5.3.4. Concluding Remarks

The data discussed in this chapter confirms the reasonable applicability of the conventional modelling approach of the bulk impedance contribution by a parallel connection of R_E and C_{Geo} for the IDE structures employed in this work. Similar to other impedance sample cell geometries, the contribution of both interfacial and parasitic effects to the measured impedance response need to be considered when trying to extract the bulk properties ε_r and κ_M. While accurate measurements of ε_r with this work's impedance measurement system appears feasible, the reliability of κ_M estimates is not guaranteed at low conductivity levels owing to the potential introduction of ionic contaminants into the system.

Throughout this work, a slight variability in K_{Cell} and the parasitic circuit components from chip to chip was observed which may possibly originate from tolerances of, e.g., the metal film thickness during manufacturing process. For this reason, K_{Cell} and C_P were determined for each electrode chip through dielectric measurements with nitrogen, ethanol and 1-butanol. In contrast, L_P and R_P were not determined separately as their influence on the subsequent impedimetric thin film characterization was considered negligible.

5.4. Assessment of High-Frequency Limitations of the Impedance Measurement Setup

Having access to impedance data recorded at frequencies well above f_{CR} is beneficial for the accurate measurement of ε_r of a sample medium to avoid overlap with sizable interfacial impedance contributions to the data. The potentiostat used for impedance measurement uptake in this work was limited to a maximum AC frequency of 5 MHz which is roughly equivalent to an f_{CR} value imparted by a moderately conductive aqueous reference medium of only 220 μS/cm

at 20 °C. For this reason, accurate determination of ε_r was only feasible for sample media with a sufficiently low conductivity which raises the question whether an upgrade of the impedance measurement system to higher frequencies could have improved the measurement capabilities of the impedance system in this work.

A practical upper limit for capacitance measurements represents the resonance frequency f_{Res} of the capacitance C in question and the self-inductance L of the system.

$$f_{Res} = \frac{1}{2\pi\sqrt{LC}} \tag{5.5}$$

At frequencies exceeding f_{Res}, current flow through the system under test is limited by inductive effects quickly preventing a conclusive measurement of C. With this in mind, the resonance frequency of L_P with C_{Geo} would put an upper frequency limit for the measurement of ε_r. Given that C_P acts in parallel to C_{Geo}, the respective f_{Res} would calculate as

$$f_{Res} = \frac{1}{2\pi\sqrt{L_P\left(C_P + C_{Geo}\right)}} = \frac{1}{2\pi\sqrt{L_P\left(C_P + \frac{\varepsilon_0\varepsilon_r}{K_{Cell}}\right)}}. \tag{5.6}$$

When assuming an aqueous sample medium, equation 5.6 would suggest a maximum measurement frequency of approximately 23 MHz for the 5 µm and 35 MHz for the 10 µm electrode geometry. For this reason, an upgrade of the impedance measurement hardware alone would not have significantly improved the measurement capabilities of the system. With regard to equation 5.6, f_{Res} could be increased to larger frequencies by, e.g., reducing L_P below the current value of (110 ± 10) nH which however would not be practical given that the connecting leads are already as short and direct as possible. An alternative approach would be to deposit the IDE structure on, e.g., polyethylene with $(\varepsilon_r = 2.0\ldots2.5$ [53]) rather than glass which would lead to a decrease in C_P and hence a slight increase in f_{Res}. A third and final option is increasing K_{Cell} of the IDE structure by, e.g., decreasing the amount of electrode fingers or increasing its spatial wavelength λ. Increasing K_{Cell} however is not without consequences as the desired parameter C_{Geo} will be lowered accordingly thereby decreasing the potential signal-to-noise ratio of the measurement. Provided that $C_{Geo} + C_P$ is reduced to the order of 10 pF and appropriate measurement hardware is available, accurate capacitance measurements have been suggested feasible up to $\sim$100 MHz [61]. Impedance measurements in the upper MHz range might however be further complicated by the skin or proximity effect leading to frequency dependent parasitics [173]. Also, the complex frequency dependence of ε_r is likely to become relevant as outlined in chapter 2.3.1.

In broadband dielectric spectroscopy (BDS), which is used to analyze the interaction of a sample medium with electromagnetic waves in the frequency range from 1 µHz to 1 THz, a variety of different sample cells are required to cover the entirety of 18 frequency decades [22]. From the perspective of BDS, IDEs would classify as low-frequency sample cells used for measurements of up to the low MHz range. By contrast, the MHz range itself is customarily covered with reflectometry sample cells [19].

6. Impedimetric Investigation of the HKUST-1 Thin Films Grown on the IDE structures

6.1. In situ Monitoring of the Coating Process

Owing to the novelty and conclusiveness of the impedance data evaluation procedure, this chapter has been published separately in [130]. The slight numerical discrepancies between this chapter and [130] derive from the absence of temperature uncertainty considerations in the evaluation procedure of [130].

Throughout the cycle-by-cycle coating process, impedance spectra were recorded during the final 30 - 35 seconds of metal and linker precursor solution exposure steps. Consequently, the native precursor solutions not only initiated and sustained the continuous thin film synthesis but also served as the actual reference media for the impedimetric analysis of the developing HKUST-1 coating. A total of 205 growth cycles were completed for the sample discussed in this chapter with the details of the recorded impedance raw data comprehensively outlined in table 6.1. Calibration measurements of the 5 µm-electrode chip to be coated suggested $K_{Cell} = (1.67 \pm 0.01)$ m^{-1} and $C_P = (24.1 \pm 0.3)$ pF.

Table 6.1. Outline of the experimental data discussed in chapter 6.1. The spectra were recorded with an MHDA functionalized 5 µm-IDE chip and are disclosed in chapter 4.1 of the supplementary research data.

sample medium	coating	frequency range	RMS voltage
1 mM CuAc in 100 mol-% ethanol (metal solution)	HKUST-1 SURMOF (cycle 1, 5, 10, 15,..., 205)	20 Hz - 2 MHz	10 mV
0.2 mM BTC in 75 mol-% ethanol (linker solution)	HKUST-1 SURMOF (cycle 1, 5, 10, 15,..., 205)	20 Hz - 2 MHz	10 mV
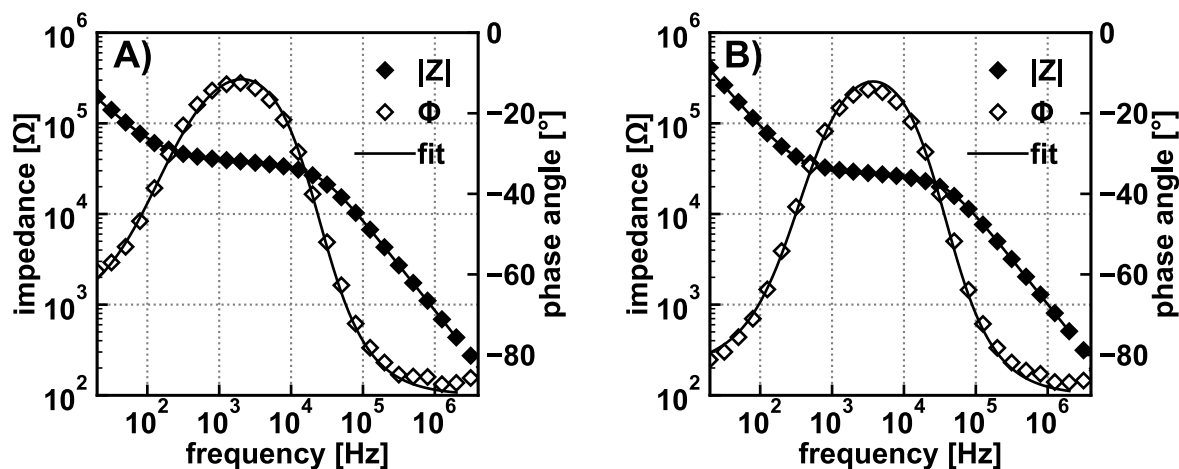
Figure 6.1. Bode representation of the impedance data collected during the first A) linker and B) metal exposure step. An ECM 1 fit to the data yields χ^2 in the order of 0.001.

6.1.1. Impedimetric Characterization of the Precursor Solutions

The impedance responses collected during first growth cycle are displayed in Fig 6.1 and provide useful reference data on the liquid precursor solutions. Both spectra are dominated by capacitive behavior at the high and low-frequency end separated by a narrow frequency range of primarily resistive behavior. While the formation of HKUST-1 islands sets in already during the initial growth cycles, the data may still be reasonably modelled with ECM 1 suggesting the amount as well as surface coverage of the HKUST-1 crystalline phase on the electrode surface to be small.

The ECM 1 best-fit estimates for the electrolyte resistance R_E and the geometric capacitance C_{Geo} compensated by the parasitic C_P are listed in table 6.2 together with the parameters derived thereof. The relative permittivity $\varepsilon_{r,M}$ of the metal precursor solution is equivalent to that of pure ethanol stated in table 5.6. Accordingly, the minor amount of copper (II) acetate present in the metal solution does not appear to significantly alter the bulk dielectric properties of the ethanolic sample medium. The 20 % increase in $\varepsilon_{r,M}$ when comparing linker to metal precursor solution stems from the presence of 25 mol-% water in the linker solution. The electrolytic conductivity κ_M of the metal solution on the other hand exceeds the κ_M value of the linker solution by roughly 30 %. Still, both precursor solutions feature remarkably low conductivity values given the absolute solute concentration; an observation which will be substantiated in chapter 6.2 when taking a look at ethanolic solutions of potassium chloride. The relatively low conductivity values of the precursor solution in table 6.2 indicate a low degree of complete ionic dissociation of the respective precursor species. The linker precursor *benzene-1,3,5-tricarboxylic acid* is a weak tribasic acid which will only partially deprotonate when dissolved. Likewise the conductivity data indicates that only a minor portion of the metal precursor *copper (II) acetate* (CuAc) dissociates into copper cations and acetate anions. Similar observations have been reported elsewhere suggesting that CuAc is able to retain its dimeric paddlewheel form in solution [174]. More detailed studies might be necessary to characterize the exact chemical state of the precursor species in the respective solutions such as degree of

deprotonation/dissociation.

Owing to their low ionic conductivity values, both precursor solutions coincidentally represent particularly useful reference media for the unhindered determination of the effective bulk permittivity $\varepsilon_{r,eff}$ throughout the thin film synthesis. With the characteristic relaxation frequencies f_{CR} ranging in the tens of kHz, $\varepsilon_{r,eff}$ can be safely obtained at the high frequency end of the recorded spectrum which is unencumbered by interfacial effects. However, as a current measurement range change introduced minor artifacts into the data recorded between 0.5 - 1 MHz, $\varepsilon_{r,eff}$ was alternatively determined based on impedance values collected at six frequencies in the 1 - 2 MHz range.

Table 6.2. Characterization results of the bulk properties of both precursor solutions. The characteristic relaxation frequencies f_{CR} of the precursor solutions are well within the recordable frequency range of the experimental setup which allows the reliable tracking of the bulk dielectric properties during the thin film synthesis.

parameter	unit	metal solution	linker solution
C_{Geo}	pF	132.8±0.5	159.5±0.5
R_E	kΩ	27.4±0.3	35.9±0.4
$\varepsilon_{r,M}$	–	25.0±0.1	30.1±0.1
κ_M	nS/cm	609±6	465±6
f_{CR}	kHz	43.7±0.5	27.7±0.3

6.1.2. Qualitative Description of the Impedance Data Collected during the Coating Process

The data shown in Fig 6.1 provides a useful point of reference representing the impedance response of the uncoated IDE structure. Any deviation from this reference state may therefore be unequivocally attributed to the influence of the developing HKUST-1 thin film. With this in mind, the impedance response recorded during the growth cycles 1, 40, 100 and 200 are plotted in Fig 6.2. For both the data collected with the linker and metal precursor solution, the continuation of the growth process brings about a gradual change in the impedance response. On a fundamental level, the formation of the coating decreases the current flow through the IDE structure i.e., increases the impedance modulus across the entire frequency spectrum. However, the changes to the impedance response are much more pronounced at the frequency range below f_{CR} than above. Additionally, a substantial difference on how the impedance spectra of the linker and metal solution develop can be observed as more and more growth cycles are being completed.

In case of the linker data shown in Fig 6.2 A), the initial phase angle peak appears to gradually split into two. A more pronounced peak moving towards the low frequency end of the spectrum and a less pronounced peak at roughly 8 kHz which shrinks in size as more cycles are being completed. Similar to the linker data, the metal data in Fig 6.2 B) features a shrinking phase angle peak located between 10 and 20 kHz, however, is devoid of the more pronounced
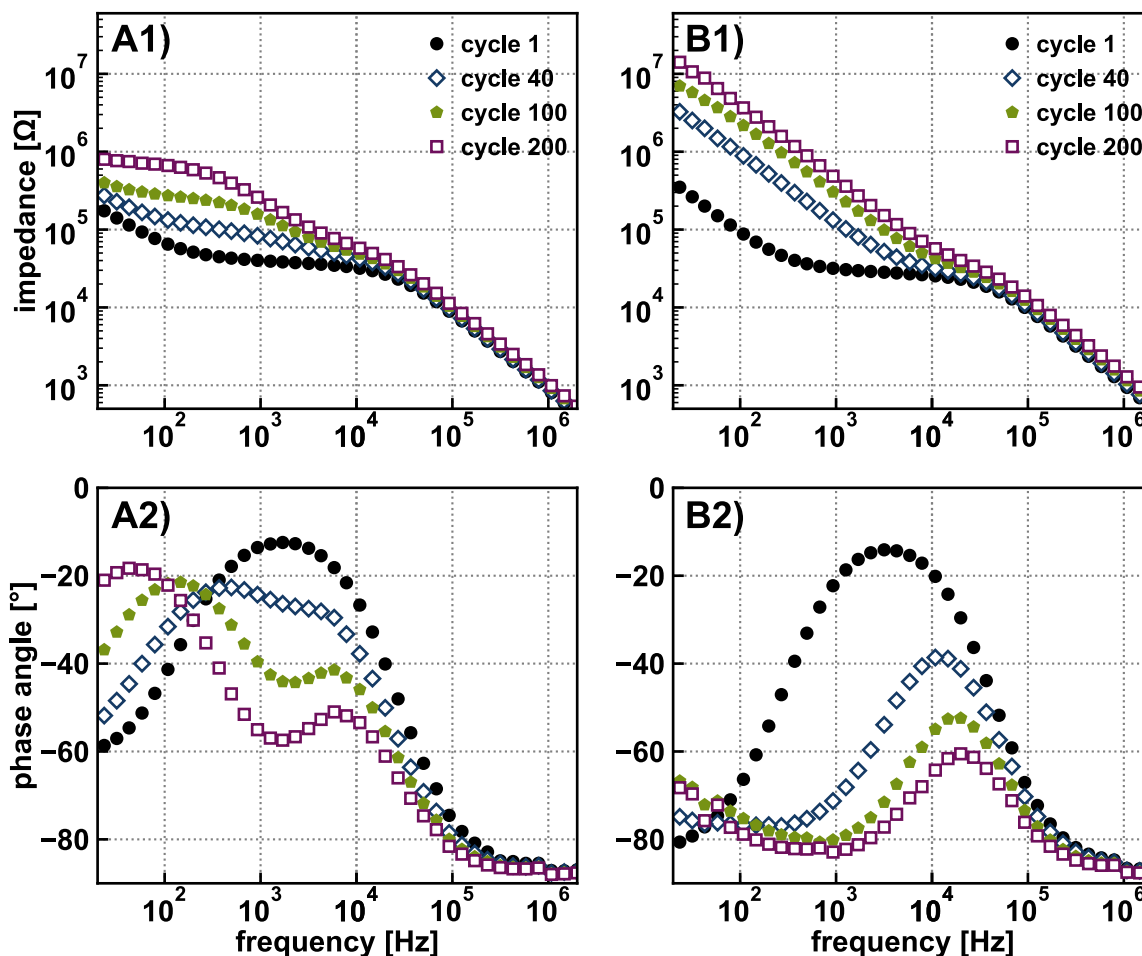
Figure 6.2. Impedance spectra recorded throughout the HKUST-1 coating process during the exposure step with A) the linker and B) the metal precursor solution at different growth cycles.

peak at the low frequency end of the spectrum. Also, the low frequency impedance modulus recorded during the metal step increases much more significantly than during the linker step.

6.1.3. Equivalent Circuit Modelling and Interpretation

When trying to interpret the impedance data plotted in Fig 6.2 in accordance to the theoretical framework established by ECM 2, it is reasonable to assign the phase angle peak which gradually decreases in size to the charging of the coating capacitance C_C via the R_E branch. Provided the coating thickness increases continuously during each growth cycle, equation 3.1 would propose a gradual decline in C_C which would likewise prompt a decrease in the associated phase angle peak dominance. If accurate, it would follow that the more pronounced low frequency phase angle peak is related to the charging of the double layer capacitance at the electrode surface via the coating resistance R_C branch. The gradual movement towards smaller frequencies as observed for the linker data could be explained by an increase in R_C owing to a continuous film growth in accordance to equation 3.3. The absence of the low frequency phase angle peak in the metal data might indicate an inhibition of ionic migration through the coating; the potential origin of which will be addressed in detail in the following chapter. The apparent increase in the

phase angle at the low frequency end observable in the metal data recorded during cycle 100 and 200 but not during cycle 40 is unlikely to be related to any physicochemical effect accounted for in ECM 2. For this reason as well as to avoid having to treat C_C as a constant phase element which would complicate further analysis, the metal data was truncated to the frequency range 2 kHz - 2 MHz for ECM 2 data fit while setting R_C to infinity. In contrast, as the impedance response recorded during the linker steps appeared to be appropriately represented by ECM 2, the linker data was not truncated for the purpose of data fitting.

The best-fit estimates for C_C are plotted in Fig 6.3 A) as a function of the growth cycles starting from the 40$^{\text{th}}$ exposure step. The determination of C_C from the linker data prior to cycle 40 is problematic as the influence of C_C and the double layer effect CPE_{DL} cannot be unambiguously separated from one another. A potential reason might be a spatial inhomogeneity stemming from an incomplete surface coverage of the individual HKUST-1 islands developing on the electrode surface owing to the underlying Volmer-Weber growth mechanism [85]. Starting from cycle 40 however, C_C may be accurately identified from the linker data data. In Fig 6.3 A), both the coating capacitance during the linker step $C_{C,LS}$ and during the metal step $C_{C,MS}$ decrease hyperbolically as a function of the growth cycles completed. Particularly revealing is that during the same cycle, $C_{C,LS}$ is consistently 2.0 - 2.4 times larger than $C_{C,MS}$. During the final 100 growth cycles, the ratio $C_{C,LS}/C_{C,MS}$ seems to have converged to a constant value of 2.3±0.1. When taking a look at the underlying equation 3.1 for C_C, a reversible change in the dielectric properties of the HKUST-1 coating i.e., the coating's relative permittivity $\varepsilon_{r,C}$ depending on the solvent environment would serve as a plausible explanation. Also, a potential reversible change in the coating thickness d_C might play a role as a result of a breathing effect observed for some MOF types [175].

A significant change in d_C depending on the solvent environment may however be safely ruled out when taking a look at how the electrolyte resistance R_E, shown in Fig 6.3 B), develops during the coating process. According to the ECM 2 fit, both the electrolyte resistance during the linker step $R_{E,LS}$ and metal step $R_{E,MS}$ increase as a function of the growth cycles. Fundamentally, R_E accounts for the ionic migration in the liquid reference medium within the portion of the IDE's sensing range not yet occupied by the dielectric coating. For this reason, the decrease in ionic migration i.e., increase in R_E in Fig 6.3 B) is consistent with the notion of a growing amount of HKUST-1 phase present in the active sensing range of the IDE as more and more growth cycles are being completed. Even more revealing however is the ratio $R_{E,LS}/R_{E,MS}$ which appears to remain fairly constant over the course of the coating process. Accordingly, it is reasonable to assume the volume occupied by the HKUST-1 during the same growth cycle not to change significantly depending on the different solvent environments of the linker and metal precursor solutions.

For this reason, it follows that the converged coating capacitance ratio observed in Fig 6.3 A) during the final 100 growth cycles may be equated with

$$\frac{C_{C,LS}}{C_{C,MS}} = 2.3 \pm 0.1 = \frac{\varepsilon_{r,C,LS}}{\varepsilon_{r,C,MS}}. \tag{6.1}$$
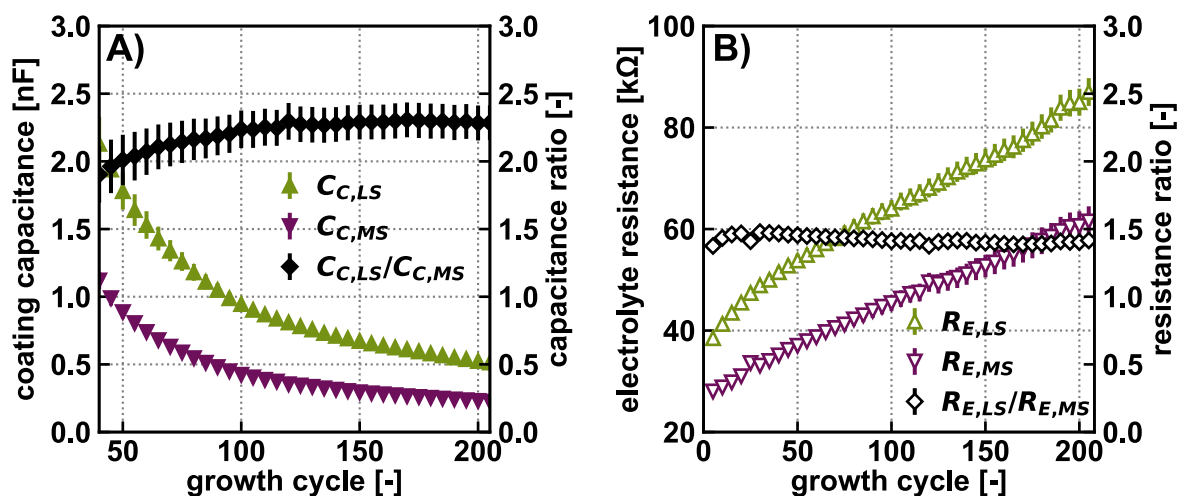
Figure 6.3. A) Coating capacitance C_C and B) electrolyte resistance R_E as a function of the growth cycles completed recorded during both the metal and linker precursor solution exposure step.

The reversible change in the relative permittivity of the coating $\varepsilon_{r,C}$ depending on the solvent environment is likely to derive from the intrusion of solvent molecules into the internal HKUST-1 pore structure thereby significantly affecting its dielectric properties. While the metal solution is purely ethanolic, the linker solution contains 25 mol-% water which might be responsible for the permittivity ratio expressed in equation 6.1. The initial increase in $C_{C,LS}/C_{C,MS}$ in Fig 6.3 A) is likely caused by the incremental increase in coating thickness d_C between metal and linker step during the same cycle which however becomes negligible in relative terms once d_C grows large. A similar, yet less pronounced, behavior can also be observed in the ratio $R_{E,LS}/R_{E,MS}$ during the initial growth cycles shown in Fig 6.3 B).

Both the C_C data plotted in Fig 6.3 A) and the deduction of equation 6.1 provide crucial information on the thin film growth. Yet, in order to gain access to the coating thickness d_C, additional information is required to pinpoint the respective coating permittivity values $\varepsilon_{r,C,LS}$ and $\varepsilon_{r,C,MS}$. While many studies resort to an educated guess to estimate $\varepsilon_{r,C}$ at this stage of the data evaluation process, see for instance [119] or [5], the impedance spectra recorded during the HKUST-1 growth holds distinctive information on $\varepsilon_{r,C}$ separate from C_C. As the thin film is likely to occupy a sizeable fraction of the total sample volume within the IDE's sensing range, $\varepsilon_{r,C}$ enters not just C_C but also bulk geometric capacitance C_{Geo} of the entire IDE sensor. Particularly beneficial in this regard are the f_{CR} values of the precursor solutions facilitating the accurate determination of C_{Geo} from the impedance data. When corrected by the cell constant K_{Cell} and ε_0 via equation 3.6, C_{Geo} may be readily converted into the effective bulk permittivity $\varepsilon_{r,eff}$ displayed as a function of the growth cycles in Fig 6.4 A). During the first cycle, $\varepsilon_{r,eff}$ is equivalent to the respective reference medium permittivities $\varepsilon_{r,M}$ values disclosed in table 6.2. Both the effective relative permittivity recorded during the linker step $\varepsilon_{r,eff,LS}$ and metal step $\varepsilon_{r,eff,MS}$ continuously decrease as more and more growth cycles are being completed. Over the course of 205 growth cycles, $\varepsilon_{r,eff,LS}$ drops by 22.5 % whereas $\varepsilon_{r,eff,MS}$ decreases 32.5 %. Consequently, both coating permittivities $\varepsilon_{r,C,LS}$ and $\varepsilon_{r,C,MS}$ can be deduced to be smaller than their respective reference medium permittivities $\varepsilon_{r,M,LS}$ and

$\varepsilon_{r,M,MS}$. To quantify $\varepsilon_{r,C,MS}$ and $\varepsilon_{r,C,LS}$, the attempt could be made to model the $\varepsilon_{r,eff}$ in Fig 6.4 A) with the help of the theoretical framework laid out by equations 3.12-3.14 which would also provide estimate for the coating thickness d_C as a function of the growth cycles. However, considering the non-ideality of the IDE geometry exemplified by e.g. the electron micrographs shown in Fig 5.3, a modelling approach of such complexity would not be justified. A more generalized modelling approach may be realized using the interpolation equation 3.15 which relies on the arbitrary interpolation parameter ζ. For every growth cycle and precursor solution exposure step, a relationship between $\varepsilon_{r,eff}$, $\varepsilon_{r,M}$ and the desired $\varepsilon_{r,C}$ may be established via

$$\varepsilon_{r,eff,LS}(cycle) = \varepsilon_{r,C,LS} \cdot \zeta_{LS}(cycle) + \varepsilon_{r,M,LS} \cdot (1 - \zeta_{LS}(cycle)) \tag{6.2}$$

and

$$\varepsilon_{r,eff,MS}(cycle) = \varepsilon_{r,C,MS} \cdot \zeta_{MS}(cycle) + \varepsilon_{r,M,MS} \cdot (1 - \zeta_{MS}(cycle)). \tag{6.3}$$

To match the number of unknown variables $\varepsilon_{r,C,LS}$, $\varepsilon_{r,C,MS}$, $\zeta_{LS}(cycle)$ and $\zeta_{MS}(cycle)$ to the amount of modelling equations 6.1 - 6.3, one additional relationship must be established. To keep the modelling simple, equating $\zeta_{LS}(cycle)$ and $\zeta_{MS}(cycle)$ appears as a practical solution in this regard, such as

$$\zeta_{MS}(cycle) \approx \zeta_{LS}(cycle) = \zeta(cycle). \tag{6.4}$$

Solving the system of equations 6.1 - 6.4 for the final 100 growth cycles provides an averaged $\varepsilon_{r,C,MS} = 6.7\pm0.5$ and $\varepsilon_{r,C,LS} = 15.2\pm0.4$. A recently published study specifies the relative permittivity of an HKUST-1 single crystal devoid of any guest molecules as 2.8±0.3 [176]. When saturated with ethanol from the gas phase, the relative permittivity of the HKUST-1 single crystal was reported at 7.5 during the first and 7.4 during the second inclusion cycle [176]. Accordingly, the value of $\varepsilon_{r,C,MS}$ may very well be attributed to the presence of ethanol molecules in the coating's internal pore structure. The slightly decreased value of $\varepsilon_{r,C,MS}$ at 6.7±0.5 in comparison to the relative permittivity of a single HKUST-1 crystal may potentially derive from an increased defect density of the polycrystalline SURMOF thin film in comparison to a single crystal. By contrast, an HKUST-1 single crystal saturated with water instead of ethanol may exhibit a relative permittivity of up to 64 [176]. Accordingly, the coating permittivity of the HKUST-1 thin film when exposed to the linker precursor solution $\varepsilon_{r,C,LS}$ of 15.2±0.4 indicates the uptake of both ethanol and water molecules from the reference solution into the pore structure of the coating. The well reproducible adaptation of $\varepsilon_{r,C}$, depending on the reference medium the coating is exposed to, strongly suggests the unhindered access of solvent molecules to the internal pore structure of the HKUST-1 thin film.

With $\varepsilon_{r,C}$ determined, conversion of the coating capacitance C_C into the coating thickness d_C becomes feasible. Application of $\varepsilon_{r,C,LS}$ and $C_{C,LS}$ to equation 4.3 provides an estimate of d_C as a function of the completed growth cycles as plotted in Fig 6.4 B). From cycle 105 onwards, the data suggests a near constant growth rate of (1.5±0.3) nm per cycle. In fact, the material addition to the growing HKUST-1 crystallographic framework during a single growth step ranges below the characteristic HKUST-1 cubic lattice constant a of 2.63 nm [90]
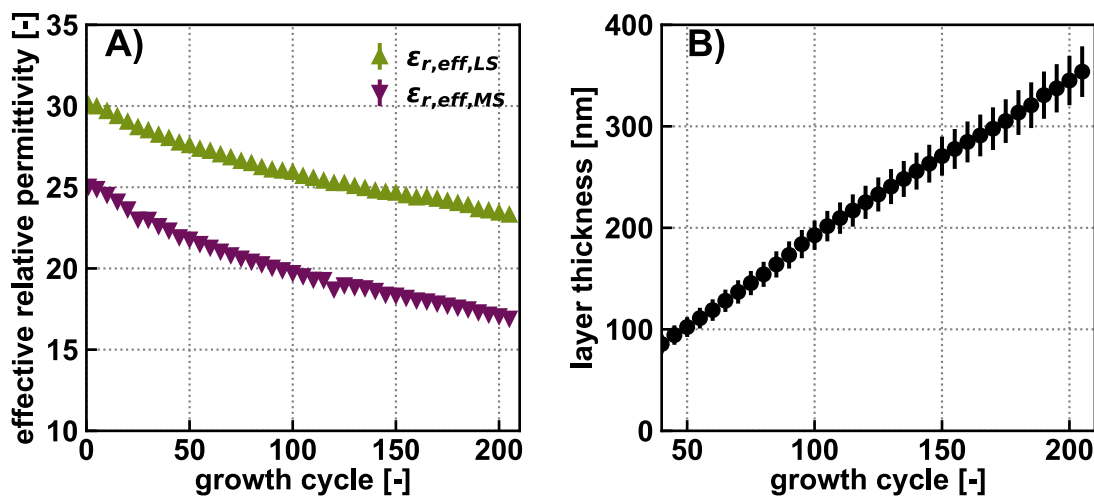
Figure 6.4. A) Effective relative permittivity $\varepsilon_{r,eff}$ within the IDE sensing range during both the linker and metal step as a function of growth cycles. The joint mathematical processing of the data shown in A) with the help of equation 6.1 allows the estimation of the coating thickness plotted in B). During the final 100 growth cycles, the data suggests a linear increase in coating thickness at a rate of (1.5 ± 0.3) nm per growth cycle.

signifying the strongly self-limiting nature of the cycle-by-cycle coating process.

6.1.4. Validation of Impedance Data Evaluation Procedure

To verify the impedimetric characterization methodology, the coated electrode structure was visualized by scanning electron microscopy after the completion of the 205 growth cycles. The micrograph displayed in Fig 6.5 A) was obtained from the backscattered electron (BSE) signal and shows the tilted cross section of the coated IDE chip. With heavier elements producing a greater amount of backscattered electrons, the BSE contrast mode allows for a qualitative discrimination of different sample regions based on their atomic composition. As both the electrode substrate (glass) and the dielectric coating (HKUST-1) are composed of light-weight elements, the golden electrode fingers produce the greatest BSE contrast and thus can easily be identified in Fig 6.5 A). The sections of strongest brightness in the micrograph shown in Fig 6.5 A) are located directly at the cross sectional area at which the IDE chip was cleaved in two during the sample preparation step. This observation suggests direct exposure of the golden electrode finger to the primary electron beam to occur only at the cross section. Judging from the absence of bright spots or cracks along the coated electrode fingers, the HKUST-1 thin film appears to completely cover the golden electrode surface. The complete surface coverage together with the absence of excessive surface roughness may explain the conclusiveness at which the coating capacitance C_C can be extracted from the impedance data.

The closeup of the cross section is shown in Fig 6.5 B) which was obtained from the secondary electron signal. For comparative reasons, the final coating thickness value d_C, as obtained from the evaluation process of the impedance data collected during the growth process, has been added to the micrograph which corresponds well to the coating thickness observed under the microscope. The agreement between the impedimetric estimate of d_C with the microscopic
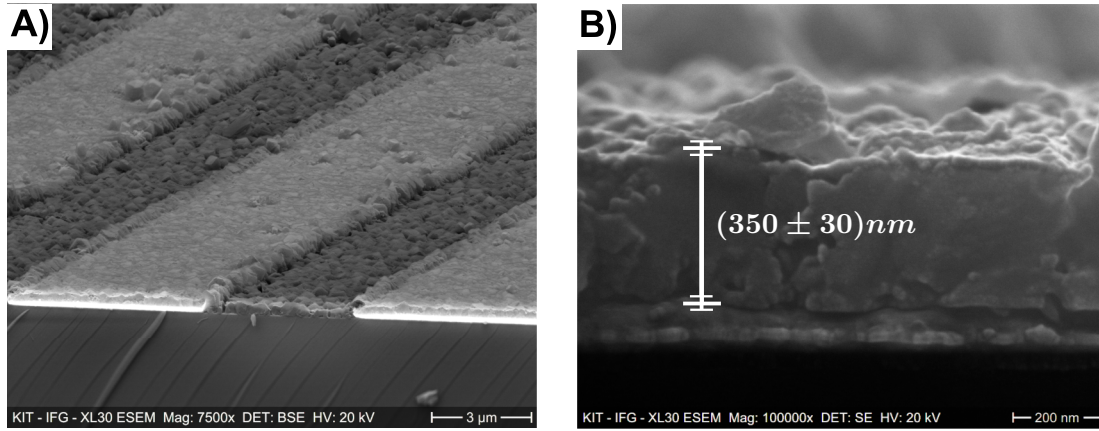
Figure 6.5. Scanning electron micrographs of the coated IDE structures following 205 growth cycles. The tilted cross section visualized by the backscattered electron contrast mode in A) indicates complete surface coverage of the electrode fingers. A closeup of the coating cross section is shown in B). For comparative purpose, the impedimetric thickness estimate following 205 growth cycles is overlaid onto the micrograph which corresponds well to the actual coating thickness.

cross section also strengthens the validity of the $\varepsilon_{r,C}$ values derived earlier during the evaluation process.

6.1.5. Comparison with Alternative in situ Monitoring Techniques of the Coating Process

With the impedance spectra collected during the coating process extensively evaluated, it is worthwhile to put the information gained by the impedimetric characterization procedure into perspective. There are a variety of in situ thin film analysis strategies which provide comparable information on a nano-coating process and could be reasonably considered complementary to the impedimetric approach discussed in this work. To simplify notation, the characterization method described in this chapter will be referred to as *interdigitated-impedance spectroscopy* (ID-IS).

Shekhah et al., for instance, employed time-resolved surface plasmon resonance (SPR) to track the cycle-by-cycle HKUST-1 growth on an MHDA functionalized gold surface. The changes to the SPR signal as a function of time provided clear evidence of the self-terminated growth pattern [96]. Up to now however, an in-depth SPR analysis of the HKUST-1 coating process appears to be missing. When modelled in detail, SPR spectra may be used to compute tangible physical properties of a thin film covering the SPR sensor [177]. Similar to ID-IS demonstrated above, SPR data is sensitive to both changes to the coating and the respective reference medium the coating is exposed to. While changes to the geometric capacitance C_{Geo} of the IDE sensor derive from the static permittivity mismatch between coating $\varepsilon_{r,C}$ and reference medium $\varepsilon_{r,M}$ coupled to an effective coating thickness d_C, signal changes to an SPR sensor on the other hand derive from a refractive index mismatch between coating and reference medium coupled to an effective coating thickness [177].

Another method which has been extensively used to analyze the HKUST-1 growth mechanism

involves the time-resolved quartz crystal microbalance (QCM) technique [178]. In comparison to SPR and ID-IS, modelling of QCM data recorded during a coating process may become remarkably straightforward. Provided the coating is stiff as well as homogeneously distributed across the sensor surface, changes to the QCM signal are customarily interpreted on the basis of the Sauerbrey equation [179] to obtain the time-resolved amount of sample mass deposited on the sensor surface area. Similar to SPR and ID-IS, an effective coating thickness may be deduced from QCM data by using an educated guess concerning the volumetric mass density of the coating material.

In stark contrast to the in-situ SPR [96] and QCM [178] studies on the HKUST-1 growth mechanism published earlier, the ID-IS method demonstrated in this chapter does not provide time resolved data on the coating process. The reason is that owing to modelling difficulties, the system investigated by ID-IS must not change within the timeframe the spectrum is recorded (roughly 30 s in this study). Therefore, the impedance spectra were recorded during the final rather than initial seconds of the precursor solution exposure steps due to the saturation of mass uptake within a few minutes following initial exposure as suggested by QCM data [178]. Accordingly, the QCM and SPR data may be used to deduce kinetic time constant of the actual coating process. Similar opportunities for the deduction of time constant could also be pursued by impedimetric techniques, e.g. when tracking the time-resolved changes to the impedance response at a predefined, constant AC frequency rather than to rely on an extensive frequency spectrum. Practical insights on the potential of single-frequency impedance analysis is provided in the appendix E. Irrespective of the absence of transient effects, the ID-IS characterization method described in this chapter provides a variety of distinguishing information on the native HKUST-1 SURMOF formation process not yet covered by complementary methods of analysis. Particularly noteworthy in this regard are the coating thickness d_C and steady growth rate of the model thin film in Fig 6.4 B) which could be conclusively validated using scanning electron microscopy in Fig 6.5. Also, ID-IS clearly substantiates the accessibility of the coating's internal pore structure to the solvent molecules of the reference medium as evidenced by the reproducible shift in coating permittivity in equation 6.1. Additionally, the impedance raw data visualized in Fig 6.2 indicates a significant change of the ionic transport properties of the coating when exposed to the metal and linker precursor solution. The peculiar behavior of the coating resistance in the impedimetric growth data has motivated a separate, more detailed study investigating the impedance response of the HKUST-1 SURMOF coated electrode structure to a well-defined ionic reference system which will be addressed in the following chapter.

6.2. Phenomenological Assessment of the Ionic Migration through the HKUST-1 Thin Film

The impedance spectra in Fig 6.2 indicate an unexpected yet significant variability of the ionic migration through the HKUST-1 coating depending on the reference medium applied. In order to gain a better understanding on pivotal parameters influencing the ionic transport properties of the HKUST-1 SURMOF, the coating experiment discussed in the previous chapter was repeated in a slightly modified fashion. In addition to the metal, linker and rinse solutions, a variety of testing solutions were prepared and connected to the flow distributor valve. A complete list detailing the precursor and testing solutions is provided in the leftmost column of table 6.3. The testing solutions were prepared from potassium chloride (KCl) dissolved in ethanolic solutions of varying water content. Solvated KCl is a frequently encountered benchmark electrolyte and as such was chosen as ionic reference system to test the transport properties of the coating.

Table 6.3. Outline of the experimental details discussed in chapter 6.2. The impedance spectra were recorded with an MHDA covered 10 µm-IDE chip and are disclosed in chapter 4.2 of the supplementary research data.

sample medium	coating	frequency range	RMS voltage
1 mM CuAc in 100 mol-% ethanol	HKUST-1 cycle 1, 5, 10, 15, 20, 25,..., 200	2 Hz - 3 MHz	25 mV
0.2 mM BTC in 75 mol-% ethanol	HKUST-1 cycle 1, 5, 10, 15, 20, 25..., 200	2 Hz - 3 MHz	25 mV
0.05 mM KCl in 100 mol-% ethanol	HKUST-1 cycle 0, 50, 100, 150, 200	2 Hz - 3 MHz	25 mV
0.05 mM KCl in 90 mol-% ethanol	HKUST-1 cycle 0, 50, 100, 150, 200	2 Hz - 3 MHz	25 mV
0.05 mM KCl in 80 mol-% ethanol	HKUST-1 cycle 0, 50, 100, 150, 200	2 Hz - 3 MHz	25 mV
0.05 mM KCl in 70 mol-% ethanol	HKUST-1 cycle 0, 50, 100, 150, 200	2 Hz - 3 MHz	25 mV
0.05 mM KCl in 60 mol-% ethanol	HKUST-1 cycle 0, 50, 100, 150, 200	2 Hz - 3 MHz	25 mV
0.1 mM KCl in 90 mol-% ethanol	HKUST-1 cycle 0, 50, 100, 150, 200	2 Hz - 3 MHz	25 mV
0.2 mM KCl in 90 mol-% ethanol	HKUST-1 cycle 0, 50, 100, 150, 200	2 Hz - 3 MHz	25 mV
0.1 mM KCl in 70 mol-% ethanol	HKUST-1 cycle 0, 50, 100, 150, 200	2 Hz - 3 MHz	25 mV
0.2 mM KCl in 70 mol-% ethanol	HKUST-1 cycle 0, 50, 100, 150, 200	2 Hz - 3 MHz	25 mV

The testing solutions were prepared from gravimetric mixtures of ethanolic and aqueous stock solutions at the designated volumetric KCl concentration. The influence of the excess volume of ethanol/water mixtures on the ionic concentration was neglected.

The HKUST-1 thin film itself was grown for a total of 200 growth cycles and impedance spectra were collected during the metal and linker steps as in the previous experiment. However, following the completion of growth cycles 50, 100, 150 and 200, the coating process was interrupted and the HKUST-1 coating sequentially exposed to the designated testing solutions. The impedance responses of the coated electrode structure to the testing solutions was recorded during the final seconds of the individual 300 s exposure steps. After all testing solutions were consecutively supplied to the coated electrode structure, the growth process was resumed. The experiment which will be addressed in this chapter was conducted about one year after the initial growth experiment discussed in the previous chapter. The HKUST-1 coating process was performed at largely identical conditions. The flow selection valve was replaced from the initial QMIX Valve to the MUX Distributor. Also, the rinse step was streamlined from initially 10 s at elevated flow rate to 90 s at the identical flow rate as the linker and metal precursor solution. Lastly, the preconditioning step for the MHDA functionalization of the electrode structures was changed from cyclic voltammetry in sulfuric acid to UV/ozone dry-etching. Due to a reduced relative influence of the roughened edges which deviate from the ideal IDE structure, a 10 µm-IDE chip was used for the experiment. A photograph of the experimental setup which was taken during measurement of the data discussed in this chapter is shown in Fig 4.2.

Excerpts of the growth data of the HKUST-1 coating are provided in Fig 6.6. The hyperbolic decrease of the coating capacitances $C_{C,MS}$ and $C_{C,LS}$ as a function of the growth cycles in Fig 6.6 A) agrees well with the previous data in Fig 6.3. Again, the coating capacitance ratio $C_{C,LS}/C_{C,MS}$ converges to a near constant value of 2.3±0.1 during the latter half of the coating process. Conversion of $C_{C,LS}$ into the coating thickness d_C using the previously determined $\varepsilon_{r,C,LS} = 15.2\pm0.4$ suggests a linear relationship between d_C and amount of growth cycles as shown in Fig 6.6 B). The slightly elevated growth rate of (2.4±0.3) nm per cycle may potentially derive from a reduced efficiency of the rinse step. Judging from the artifacts from the data in Fig 6.6, the interruption and subsequent resumption of the coating process after cycle 50, 100, 150 and 200 as well as the exposure to the testing solution did not appear to adversely affect the structural integrity of the coating.

6.2.1. Preliminary Considerations on the Ionic Migration

The physical model conceptualized in ECM 2 accounts for two separate impedimetric contributions of ionic migration. Ionic migration through the reference medium is accounted for with the electrolyte resistance R_E while the ionic migration through the coating is modelled separately with the coating resistance R_C following the buildup of the coating capacitance C_C. The rate of ionic migration depends on, among other, the surrounding matrix the ion is migrating through. In liquid media for instance, a direct relationship between the liquid bulk viscosity and the ionic drift velocity may be established via equation 2.19. When addressing ionic migration through solid media such as a thin film covering an electrode surface, it is reasonable to consider how
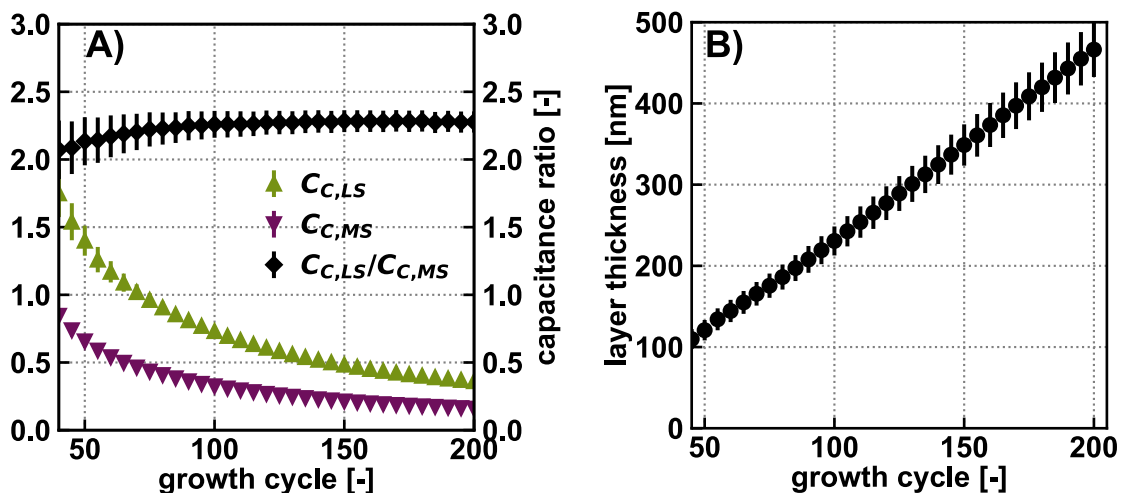
Figure 6.6. Summary of the growth data of the HKUST-1 coating exposed to the KCl testing solutions discussed in chapter 6.2. The hyperbolic decrease of the coating capacitances in A) as well as their ratio converging to 2.3±0.1 is well reproducible. The coating thickness in B) reveals a slightly increased growth rate of (2.4±0.3) nm per cycle which may stem from a reduced efficiency of the rinse step in comparison to the sample discussed in the previous chapter.

the solid medium may potentially sustain ionic pathways. Occasionally, it is assumed that the dielectric coating itself is impermeable to ionic migration. Thus, R_C is interpreted to arise from the degradation of a formerly intact coating through the formation of cracks, delaminated areas or water pockets thereby exposing the bare electrode surface to the reference medium [112]. To sort out potential ambiguities concerning the interpretation of R_C in the data, the coated IDE chips were visualized by scanning electron microscopy following the completion of the impedance data uptake.

At first sight, the topview micrograph in Fig 6.7 A) reveals an inhomogeneous coating covering the interdigitated area. Especially the coating covering the glass substrate between the electrode fingers appears roughened with portions of the HKUST-1 material delaminated. By contrast, the structural integrity of the coating covering the electrode fingers does not appear to be compromised. The closeup of the coated electrode finger in Fig 6.7 B) indicates a homogeneous thin film of reduced grain size and devoid of structural artifacts covering the electrode surface. The morphological differences of the HKUST-1 material which has formed on the glass and MHDA-functionalized gold surface puts the spotlight on the influence of surface chemistry on the coating process. The substrate was most likely still under the influence of the UV/ozone pretreatment step which is known to introduce hydroxyl terminal groups to glass surfaces [180]. On the other hand, the MHDA functionalization of gold surfaces introduces carboxyl terminal groups covering the electrode fingers. Previous studies have shown that an HKUST-1 SURMOF adopts a preferential [111] orientation at hydroxyl-terminated surfaces and, conversely, a preferential [100] growth direction on carboxyl-terminated surfaces [96]. Given the truncated octahedral shape of the HKUST-1 grain displayed in Fig 2.16 A), a quadratic facet develops perpendicular to the [100] crystallographic direction whereas a truncated triangular facet is indicative to the [111] direction. In fact, the closeup of the coated finger in Fig 6.7
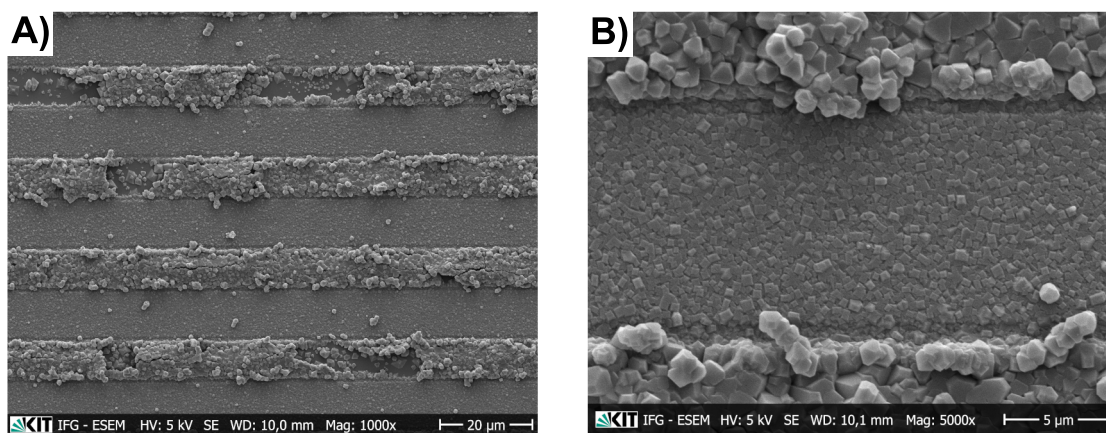
Figure 6.7. Topview electron micrographs of the coated electrode structure following 200 growth cycles as well as exposure to the testing solutions. The HKUST-1 coating covering the glass substrate appears cracked and partially delaminated whereas the HKUST-1 SURMOF grown on the MHDA-functionalized gold fingers seems intact. With regard to the morphology of HKUST-1 nuclei illustrated in Fig 2.16, the relative abundance of rectangular facets of the coating on the electrode finger shown in B) is a strong indication towards preferential [100] orientation of the HKUST-1 SURMOF. Given the HKUST-1 crystalline structure displayed in Fig 2.15, it is reasonable to assume a significant availability of the square shaped 0.9 x 0.9 nm pores penetrating the coating in orthogonal direction i.e., in parallel to the electric potential gradient.

B) clearly shows the coating to be canopied by square-shaped facets which conforms well with the reported [100] crystallographic orientation on MHDA-terminated surfaces [96]. While individual triangular facets can be identified from the HKUST-1 material deposited on the glass surface, a qualitative evaluation of the preferential growth orientation of the coating based on morphological aspects does not appear reasonable given the structural inhomogeneity of the thin film. The partial delamination of the HKUST-1 material from the glass substrate may indicate a reduced adhesive contact to the host surface or an increased buildup of internal stress in comparison to the HKUST-1 SURMOF developing on the MHDA-terminated gold surface during the coating process.

Judging from the micrographs in Fig 6.7, the impedance data obtained during the experiment were collected with an intact HKUST-1 coating covering the electrode surface with no apparent irregularities visible even on the microscopic level. Consequently, it is safe to attribute the R_C values in this chapter to an ionic migration process through the actual coating material i.e., the HKUST-1 SURMOF.

The reversible change in coating permittivity expressed in equation 6.1 clearly indicates the presence of an internal pore structure and its accessibility to the solvent molecules water and ethanol. Accordingly, one may assume the very same porous structure to be accessible to ionic migration as well. In particular, the 3D-pore framework comprised of regular square shaped channels of 0.9 x 0.9 nm in size penetrating the HKUST-1 material appears as a plausible ionic pathway. On a fundamental level however, mass transport of guest molecules through metal-organic framework materials such as HKUST-1 may occur both along the crystalline voids of the lattice (intracrystalline) and along potential gaps at the grain boundaries (intercrystalline) [181]. While it cannot be excluded whether relevant intercrystalline pathways penetrating the

coating may exist, judging from the micrographs in Fig 6.7, if present such gaps would be unlikely to be more than a few nm in size.

In general, the electrolytic conductivity of the coating κ_C is assumed to range below the electrolytic conductivity of the liquid reference medium κ_M. The mismatch between κ_C and κ_M leads to the accumulation of ionic species at the interface between reference medium and, as such, gives rise to the coating capacitance C_C. When considering the modelling of κ_M in equation 2.21 and κ_C in accordance to equation 3.4, two principal phenomena can be identified which are likely to reduce the rate of ionic migration in the coating in comparison to the liquid phase above. First, it is plausible to assume the ionic diffusion coefficient of the ionic species inside the coating $\delta_{i,C}$ to be smaller than the ionic diffusion coefficient of the liquid medium $\delta_{i,M}$ owing to detrimental host-guest interactions which may slow down the overall migration process in the coating material. Another factor worth considering is ionic partitioning at the interface between the coating and liquid reference medium which is modelled with the partitioning coefficient $P_{MC,i}$. As a consequence, the molar concentration of ionic species, i.e., amount of charge carriers in the nanoporous coating is likely to differ significantly from the ionic concentration in the liquid reference medium.

In order to gain a better understanding, what factors may contribute to a potential ionic partitioning between the HKUST-1 coating and the ethanolic KCl reference systems, one may take a look at how the effect of ionic partitioning is treated in other applications involving mass transfer in nanoporous materials. In the field of nanofiltration for instance, the ionic rejection at polymeric membranes featuring pore sizes of 2 nm and below [182] is in general assumed to arise from an interplay of at least three different exclusion mechanisms [123, 124].

Firstly, if the size of a solute species approaches or exceeds the actual pore size of the nanoporous material, a steric partitioning of the respective species at the liquid/membrane interface is assumed. The ionic radii of potassium cations and chloride anions which are used as reference ionic species in this chapter are on the order of 0.3 nm in aqueous solutions [183]. While comparable data for ethanolic solutions are unavailable, the ionic radius may be inferred not to undergo drastic changes from one solvent to another. Therefore, in comparison to the intracrystalline pore diagonal of the HKUST-1 lattice estimated at 1.3 nm [90], steric exclusion of potassium cations and chloride anions from the HKUST-1 coating is unlikely to play a dominant role on the rate of ionic migration.

A second ionic partitioning effect, referred to as Donnan exclusion, becomes relevant for nanoporous materials carrying net electric charges. Since the defect-free HKUST-1 framework is electrically neutral [90], interference of the Donnan exclusion effect on the ionic migration penetrating the HKUST-1 coating will be considered negligible as well in this chapter.

Lastly, a third exclusion mechanism related to the change in solvation energy $\Delta W_{S,i}$ experienced by an ionic species i moving across the liquid/membrane interface is often inferred. As the solvation energy is tied to the relative permittivity of the surrounding matrix, the associated partitioning effect is referred to as dielectric exclusion. For energetic reasons, charged ionic species prefer solvation in high permittivity media. Accordingly, the transfer of an ionic species

from a high permittivity liquid medium into a nanoporous material of lower permittivity requires the overcoming of a "work of charge" $\Delta W_{S,i}$ [123]. While the details of the dielectric exclusion phenomenon are intricate to model [184], $\Delta W_{S,i}$ is often approximated with the Born model [185], which within the scope of this chapter may be formulated as

$$\Delta W_{S,B,i} = \frac{N_A z_i^2 e^2}{8\pi\varepsilon_0 r_i}\left(\frac{1}{\varepsilon_{r,C}} - \frac{1}{\varepsilon_{r,M}}\right) \tag{6.5}$$

It is important to stress that the primary advantage of formulating $\Delta W_{S,i}$ in accordance to equation 6.5 is found in its simplicity [124]. The underlying assumptions of the Born equation are difficult to justify in a nanoporous environment [124]. Given the disparity of $\varepsilon_{r,C}$ and $\varepsilon_{r,M}$ observed in chapter 6.1, a significant influence of the dielectric exclusion effect on the migration of potassium cations and chloride anions through the HKUST-1 coating can be assumed. To facilitate the assessment of the dielectric exclusion phenomenon, it is reasonable to formulate a Born ratio γ_{Born} with the help of a reference state in the form of

$$\gamma_{Born} = \frac{\Delta W_{S,B,i}}{\Delta W_{S,B,i,0}} = \frac{\frac{1}{\varepsilon_{r,C}} - \frac{1}{\varepsilon_{r,M}}}{\frac{1}{\varepsilon_{r,C,0}} - \frac{1}{\varepsilon_{r,M,0}}}. \tag{6.6}$$

Interestingly, while $\varepsilon_{r,C}$ is in fact unknown in most attempts to model a nanofiltration process and therefore used as a regression parameter [124], interdigitated impedance spectroscopy (ID-IS) provides explicit access to both $\varepsilon_{r,M}$ and $\varepsilon_{r,C}$ in addition to κ_M related to the ionic flux penetrating the nanoporous coating. Accordingly, ID-IS may prove to be an unprecedented opportunity for the characterization of the dielectric exclusion phenomenon for nanoporous materials in general.

6.2.2. Influence of the Water Content in the Reference Medium

Judging from the data sets collected during the coating process, the solvent composition of the reference medium appears to exert a profound influence on the bulk dielectric properties of the HKUST-1 SURMOF. With regard to the dielectric exclusion mechanism, variations in the dielectric properties are likely to coincide with variations to the ionic transport properties of a nanoporous coating. To investigate the relationship between dielectric and conductive properties of the HKUST-1 thin film, ethanolic testing solutions of varying water content were used in the experiment. Given the incompatibility of HKUST-1 with ethanolic media of elevated water content [152], the molar fraction of water was capped at 40 mol-%. To focus exclusively on the influence of the solvent composition, only the testing solutions at a constant ionic concentration of 0.05 mM will be addressed in this chapter.

Prior to the coating process, the MHDA-functionalized electrode to be coated was used to record impedance spectra of all testing solutions. The impedance response collected with the uncoated electrode structure for the ethanolic 0.05 mM KCl testing solutions at a water content of 0, 10, 20 and 40 mol-% are plotted in Fig 6.8 A). With a capacitive behavior at the high- and low-frequency end of the spectrum separated by a short interval of resistive current domination, the data corresponds well to the theoretical framework of ECM 1. Despite
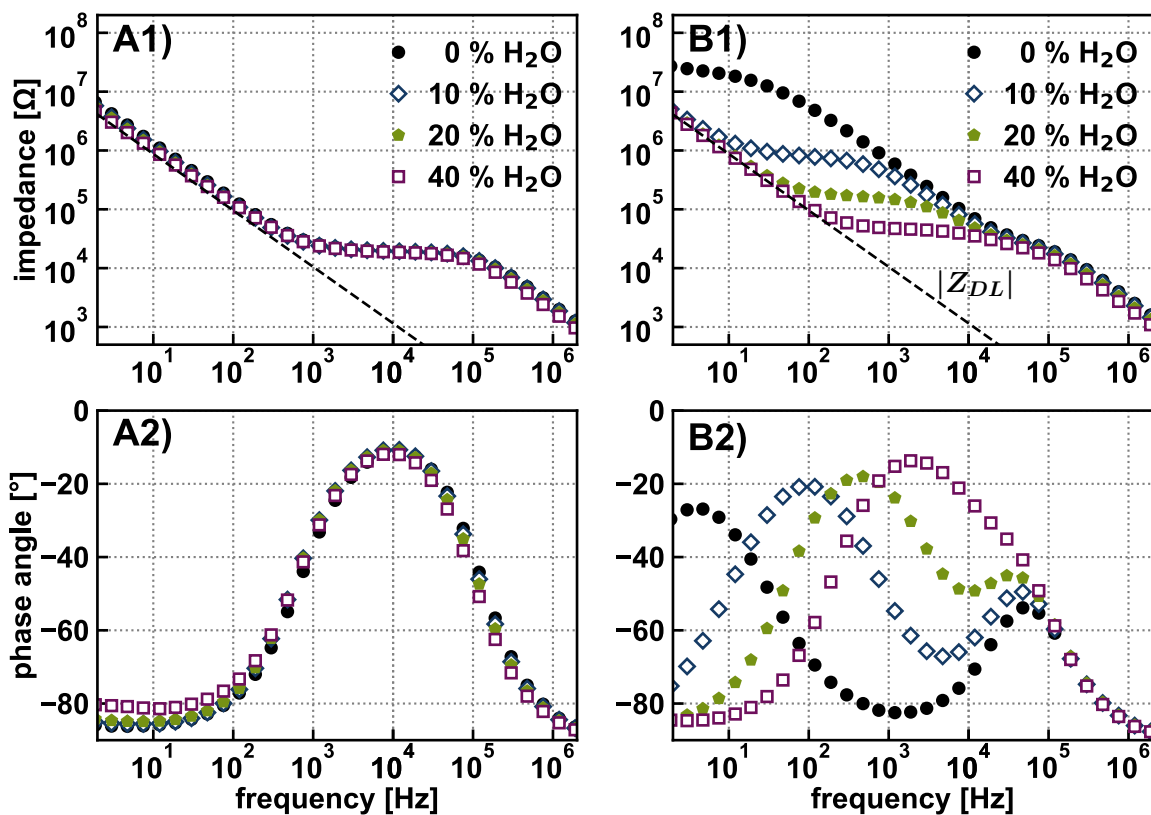
Figure 6.8. Impedance spectra of the ethanolic testing solutions at 0, 10, 20, 40 mol-% water content and an ionic concentration of 0.05 mM KCl when recorded with the A) uncoated electrode structure and B) electrode fingers covered by a 200 cycles HKUST-1 SURMOF estimated at (470$\pm$30) nm in thickness. Irrespective of the coating, the spectra appear to approach a largely identical capacitive behavior at the low frequency end of the spectra which is interpreted to derive from the double layer effect at the electrode surface. Accordingly, the differences in the impedance data sets shown in B) may be largely attributed to variations of the ionic transport properties of the HKUST-1 SURMOF.

the variation in water content, the testing solutions provide remarkably similar impedance responses when stimulated by the uncoated electrode structure. Minor differences are visible in the capacitive behavior located at the high-frequency end of the data stemming from a change in the bulk relative permittivity $\varepsilon_{r,M}$ upon variation of the solvent composition. Likewise, the changing solvent composition seems to have a minor effect on the non-ideal double layer effect at the low frequency end of the spectrum as well. By contrast, the resistive section of the impedance spectra roughly ranging from 1 - 100 kHz appears to remain largely unaffected from the variation of the solvent composition. In accordance to the electrolyte resistance R_M model parameter of ECM 1, it is safe to conclude that the testing solutions in question support an essentially identical magnitude of ionic migration in the liquid-phase.

In comparison to the spectra collected with the uncoated electrode structure shown in Fig 6.8 A), the data in B) which were recorded following the completion of the HKUST-1 coating process show a significant variability of the impedance response depending on the water content of the testing solutions. As with the linker growth data in Fig 6.2 A), the spectra in Fig 6.8 B) feature two separate phase angle peaks. The first, less pronounced peak is located between 10 and 100 kHz for all testing solutions. The second peak by contrast shifts towards smaller

frequencies as the water content decreases. At the highest water content of 40 mol-%, the first and second phase angle peak appear to be largely overlaid. When comparing the absolute impedance for the uncoated and coated case in Fig 6.8, the distinct influence of the coating on the impedance data can be identified. The smaller the water content of the testing solution the greater the discrepancy between the impedance data collected with the coated and uncoated electrode. Most notably however, despite the variations of the impedance data in Fig 6.8 B), all spectra in A) and B) seem to approach a largely identical low-frequency double layer capacitance. To substantiate this observation, the absolute impedance contribution of the suggested double layer effect $|Z_{DL}|$ modelled by a constant phase element using $Q_{DL} = 21.5$ nS$\cdot s^{\alpha_{DL}}$ and $\alpha_{DL} = 0.96$ was added to the experimental data in A1) and B1). Surprisingly the presence of the coating does not appear to interfere with the magnitude of electric double capacitance at the electrode surface. Owing to the remarkable consistency of the interfacial double layer effect irrespective of the presence of the HKUST-1 thin film, the significant differences in the impedance data in Fig 6.8 A) and B) can be concluded to derive primarily from variations in the ionic transport properties of the coating material.

To quantify the variability of characteristic properties of the HKUST-1 SURMOF depending on the reference medium composition, the impedance spectra in Fig 6.8 can be reasonably modelled with ECM 2. With the coating thickness d_C available from the data collected during the coating process, the coating capacitance values C_C can be directly converted into the relative permittivity of the coating $\varepsilon_{r,C}$ via equation 4.3. Likewise, the direct conversion of the coating resistance R_C into an effective electrolytic conductivity of the coating κ_C via equation 4.4 is possible. To allow for a direct comparison of coating and testing solution properties, $\varepsilon_{r,M}$ and $\varepsilon_{r,C}$ are jointly plotted in Fig 6.9 A) whereas κ_M and κ_C are provided in B). The $\varepsilon_{r,C}$ and κ_C values for the 0 and 10-mol% testing solutions were obtained from two separate data fits as the non-ideal behavior of the coating capacitance deserved special attention. For this reason, the data fit was limited to the frequency range above 50 kHz while treating the coating capacitance as an ideal capacitor to pinpoint $\varepsilon_{r,C}$. κ_M on the other hand was obtained with a data fit to the complete spectrum while treating the coating capacitance as a constant phase element.

When adjusting the water content from initially 0 to 40 mol-%, $\varepsilon_{r,M}$ is observed to increase from 24.6±0.1 to 33.6±0.1 whereas $\varepsilon_{r,C}$ increases at a more rapid pace from initially 6.5±0.9 to 26.7±3.1. Owing to the overlap of coating capacitance C_C contribution and double layer effect in the impedance raw data collected with the 40 mol-% testing solution, C_C and accordingly $\varepsilon_{r,C}$ are subject to relatively large uncertainty. The steady increase in $\varepsilon_{r,M}$ as a function of the water content is in line with previously published data on the dielectric properties of ethanol-water mixtures [58]. The simultaneous rise in $\varepsilon_{r,C}$ indicates that the solvent composition of the reference medium also affects the guest molecule composition within the porous structure of the HKUST-1 material. The permittivity data plotted in Fig 6.9 A) clearly shows that relative mismatch between $\varepsilon_{r,C}$ and $\varepsilon_{r,M}$ continuously decreases as more and more water is added to the ethanolic testing solutions. To quantify the potential consequences on the dielectric exclusion
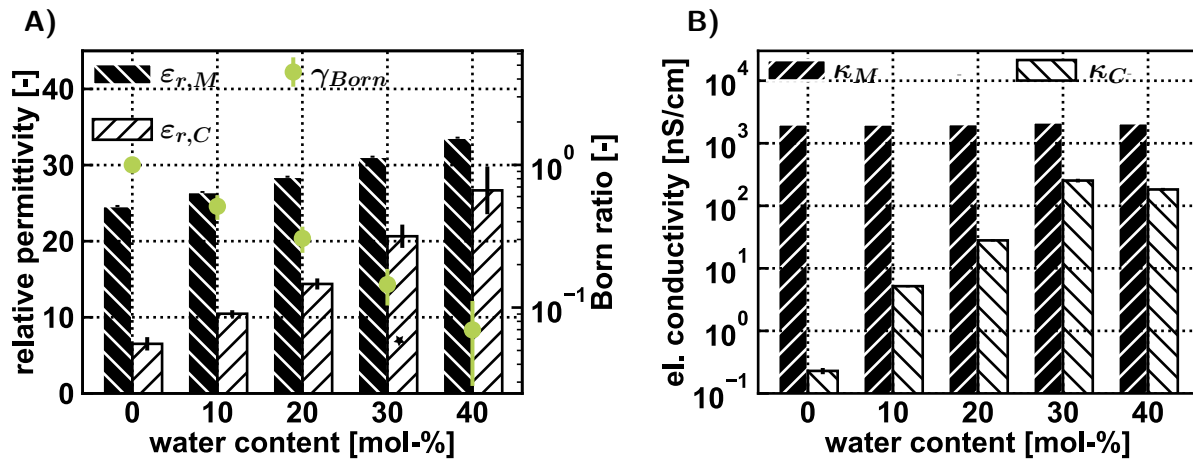
Figure 6.9. Comparison of the A) dielectric and B) conductive properties of the ethanolic testings solutions containing 0.05 mM KCl and the HKUST-1 coating as a function of the water content. The data marked with the asterisk corresponds to a testing solutions of 0.1 mM KCl concentration which was added due to modelling difficulties of the 0.05 mM data.

effect, the Born ratio γ_{Born} calculated in accordance to equation 6.6 has been added to Fig 6.9 A). For this purpose, the permittivity mismatch of the purely ethanolic testing solution was used as the reference state. On the logarithmic scale, a near linear relationship between γ_{Born} and the water content of the testing solutions can be observed. γ_{Born} drops from 1.0 at 0 mol-% water (the reference state) to 0.07±0.04 at 40 mol-% water content.

Assuming the dielectric exclusion phenomenon represents the primary bottleneck curtailing ionic migration through the HKUST-1 thin film, the drop in γ_{Born} might explain the significant increase in κ_C in Fig 6.9 B) as more and more water is added to the testing solutions. Starting from 0 mol-% to 30 mol% water, each time the water content is raised by 10 mol-%, κ_C steps up by almost an order of magnitude whereas the κ_C values extracted for the 30 and 40 mol% testing solutions are largely identical. However, even the largest κ_C value in Fig 6.9 B) still remains below the corresponding κ_M value by roughly one order of magnitude.

In contrast to $\varepsilon_{r,M}$, κ_M remains essentially unaffected by the increase in water content from 0 to 40 mol-%. Given the comparably small κ_M of (2100±100) nS/cm and the known issues of κ_M determination with IDE structures demonstrated in chapter 5.3, the question should be addressed whether KCl is in fact the primary ionic species imparting electrolytic conductivity to the testing media. Hawes and Kay have published an extensive study conducted at 25 ℃ detailing the electrolytic conductivity of ethanol/water mixtures containing KCl as sample electrolyte [58]. They specify the molar conductance of KCl in pure ethanol at infinite dilution $\Lambda_{M,KCl,0}$ at 45.4 $\frac{Scm^2}{mol}$ with $\Lambda_{M,KCl,0}$ remaining largely unchanged at low water content. Accordingly, for an ethanol-water mixture at 79.29 weight-% ethanol (equivalent to 36.68 mol-% water content), $\Lambda_{M,KCl,0}$ is reported at 44.1 $\frac{Scm^2}{mol}$. For comparison, $\Lambda_{M,KCl,0}$ increases to 149.9 $\frac{Scm^2}{mol}$ in purely aqueous solutions [58]. Normalization of the κ_M values in Fig 6.9 A) to the KCl concentration provides an estimated molar conductivity of $\Lambda_{M,KCl} = (41\pm2)\ \frac{Scm^2}{mol}$ which corresponds sufficiently well to the data published by Hawes and Kay [58]. $\Lambda_{M,KCl}$ is reasonable to range below $\Lambda_{M,KCl,0}$ due to e.g. ionic association. Importantly, $\Lambda_{M,KCl}$ does not exceed

$\Lambda_{M,KCl,0}$ which would contradict the common theory of electrolytic conductivity and indicate significant ionic contamination. While the native conductivity of ethanol-water mixtures devoid of KCl was not explicitly determined within the scope of the experiment, the 25 mol-% rinse solutions used during the coating process was prepared from the identical source of ethanol and water as the testing solutions. Supplementary impedance data recorded for the rinse solution is provided in the Appendix E which suggests a native conductivity ranging between 30 and 35 nS/cm. Hawes and Kay specified the native conductivity of their ethanol-water mixtures at a comparable water content as 20 nS/cm [58]. Accordingly, one may assume ionic migration of solvated KCl species to contribute between 98 - 99 % to the measured $\kappa_M = (2100\pm100)$ nS/cm of the testing solutions. The remaining 1 - 2 % are likely to originate from autoprotonation reactions of the solvent molecules and the presence of trace amounts of unidentified ionic contaminants.

6.2.3. Influence of the Ion Content in the Reference Medium

The magnitude of the ionic migration current is related to the amount of charge carriers available. The purpose of this chapter is to investigate how κ_C changes when the HKUST-1 coating is offered an increased amount of ionic species dissolved in the testing solutions. The ionic concentration was varied from initially 0.05 to 0.1 and 0.2 while maintaining a constant water content of 10 or 30 mol-% respectively.

The impedance spectra of the testing solutions at 10 mol-% water content collected prior to the coating process are plotted in Fig 6.10 A). The variation of the ionic concentration leads to profound changes to the resistively dominated section of the impedance response. By contrast, the capacitive behavior at the high- and low-frequency end of the spectra remain unaffected. As with the testing solution data discussed in the previous chapter, the impedance spectra in Fig 6.10 A) comply well with the theoretical framework of ECM 1.

Following the 200 cycle HKUST-1 coating process, exposure of the electrode structure to the testing solutions provide the impedance responses plotted in Fig 6.10 B). The impedance spectra collected with the coated electrode structure contain two separate phase angle peaks which is consistent with the previously discussed observations. Upon increase in KCl concentration, the less pronounced phase angle peak appears to shift towards higher frequencies whereas the second phase angle peak remain in position at roughly 100 Hz. While the movement of the phase angle peak at the high-frequency end of the spectrum indicates an increased rate of charging of the coating capacitance, the simultaneous stationarity of the second phase angle peak suggests no significant change to the charging current supplying the double layer at the interface between coating and electrode surface.

Modelling of the impedance spectra with ECM 1 in the uncoated and with ECM 2 in the coated case provides access to the dielectric and conductive properties of both the testing media and the HKUST-1 coating which are plotted in Fig 6.11. The permittivity data in A) indicate no significant changes to $\varepsilon_{r,M}$ upon variation of the KCl concentration. While the solvation of ionic species may in fact alter the bulk dielectric properties of an electrolyte solution, this phenomenon appears to become relevant only at elevated ionic concentrations of 100 mM
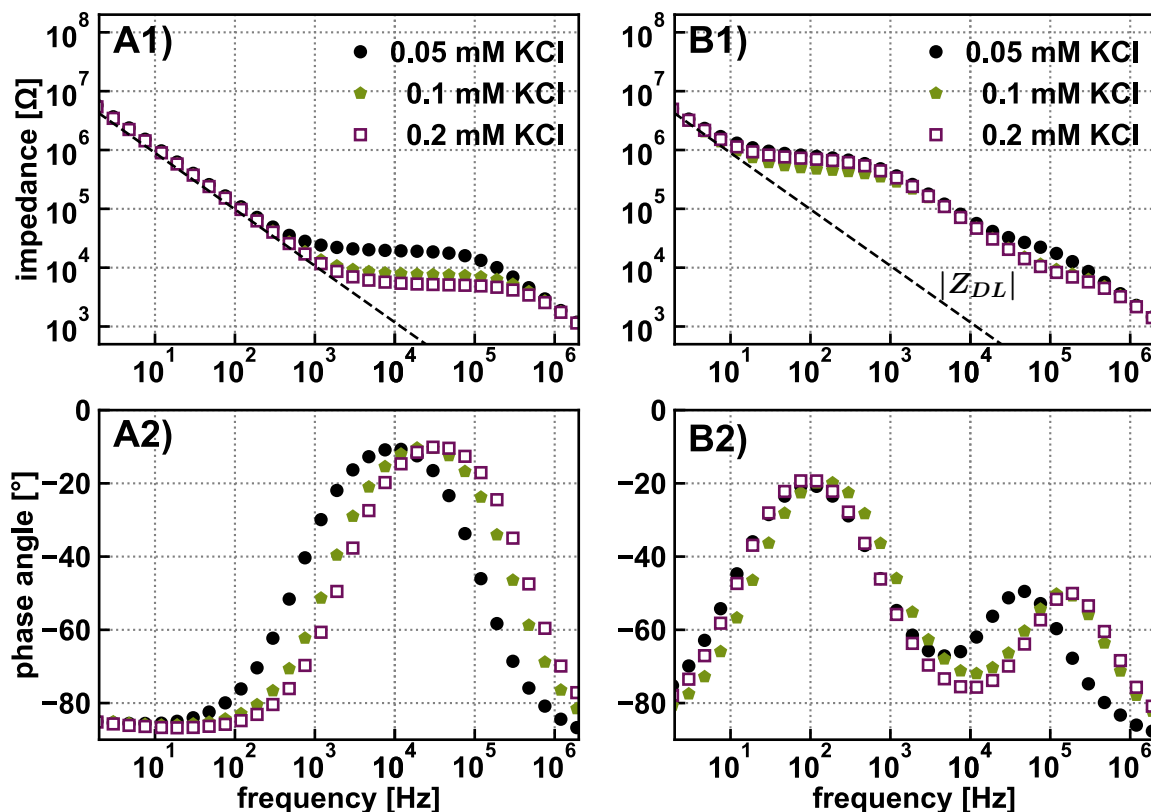
Figure 6.10. Impedance spectra recorded with the ethanolic testing solutions at 10 mol-% water content and varying ionic concentration using the A) uncoated, B) HKUST-1 coated electrode structure following 200 growth cycles.

and above (e.g. [186]). Similar to $\varepsilon_{r,M}$, $\varepsilon_{r,C}$ appears not to be influenced by the increased amount of ionic species in the reference medium as observed during the exposure to the testing solution containing 10 mol-% water. Contrary to this observation, $\varepsilon_{r,C}$ obtained at the solvent composition of 30 mol-% water varies significantly when changing the electrolyte concentration from initially 0.05 mM to 0.1 and 0.2 mM. Interestingly however, $\varepsilon_{r,C}$ observed with the 0.1 and 0.2 mM testing solutions are identical which puts the spotlight on the validity of the $\varepsilon_{r,C}$ obtained with the 0.05 mM testing solution. The problem may arise due to modelling difficulties of the impedance raw data resulting into unreasonable best-fit estimates for C_C. As observed in Fig 6.8 B), the two phase angle peaks related to the charging of the coating and double layer capacitance tend to overlap at elevated water concentrations which complicates the extraction of C_C. By shifting the less pronounced phase angle peak related to the charging of the coating capacitance to higher frequencies (see Fig 6.10 B)), the individual influence of coating and double layer capacitance become more easily separable which facilitates the modelling of the impedance data. Accordingly, the best-fit estimates of $\varepsilon_{r,C}$ obtained with the more conductive testing media appear more reliable than the $\varepsilon_{r,C}$ estimate stemming from the 0.05 mM KCl data. In contrast to $\varepsilon_{r,M}$ in Fig 6.11 A), κ_M is strongly dependent on the amount of solvated ionic species which is also supported by the best fit estimates shown in B). At the concentration levels investigated, a near linear relationship between the ionic concentration of KCl and κ_M is found i.e., a doubling of the ionic concentration coincides with a doubling of κ_M. Remarkably
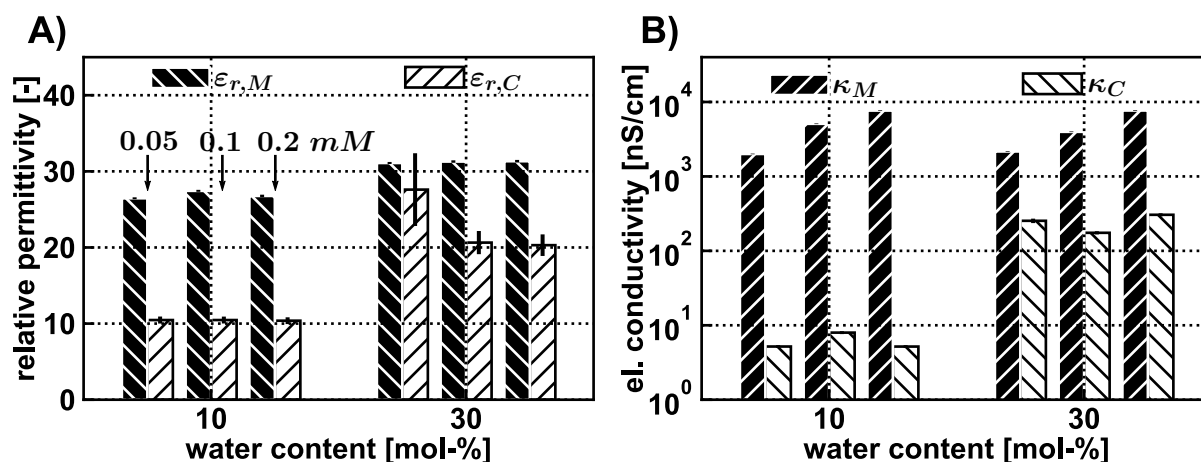
Figure 6.11. Comparison of the A) dielectric and B) conductive properties of the ethanolic testings solutions containing 0.05, 0.1 and 0.2 mM KCl and the HKUST-1 coating as a function of the water content in the testing solutions.

however, no comparable unambiguous relationship between ionic concentration in the testing solution and κ_C can be identified in the data. The primary factor affecting κ_C appears to be the water content of the testing solutions. Based on Fig 6.11 B), one might cautiously surmise κ_C to remain largely unaffected by the increased amount of potassium and chloride ions offered in the reference medium. If true, the question concerning the physical origin of κ_C might need to be reconsidered which will be addressed in section 6.2.5

6.2.4. Influence of the Coating Thickness

The coating thickness d_C is the final factor of influence on κ_C which will be discussed in this chapter. The testing solutions were supplied to the coated structure following the completion of growth cycle 50, 100, 150 and 200. Accordingly, impedance data of the testing solutions in contact to the HKUST-1 SURMOF at an estimated d_C of (120±10), (230±30), (350±30), (470±30) nm are available. Given the vast amount of data, the focus is laid on the data collected with two representative testing solutions at a KCl concentration of 0.05 mM.

To visualize the effect of d_C on the impedance raw data, the spectra collected with the testing solutions containing 0 mol-% and 20 mol-% water are shown in Fig 6.12. On a qualitative level, the testing solution data in Fig 6.12 compares reasonable well to the growth data in Fig 6.2. The initial phase angle peak obtained with the uncoated electrode structure splits into two separate peaks once the electrode surface is covered with the HKUST-1 material. In the case of the ethanolic testing solution with 0 mol-% water content, the two phase angle peaks appear already well separated after only 50 completed growth cycles. On the other hand, the two phase angle peaks observed with the testing solution at 20 mol-% water content increasingly separate from one another as the coating thickness increases yet remain significantly overlapped even after 200 growth cycles. When modelled appropriately, the impedance spectra displayed in Fig 6.12 reveal quantitative information on the dielectric and conductive properties of both the coating and testing solution which is plotted in Fig 6.13. At 0 mol-% water content,
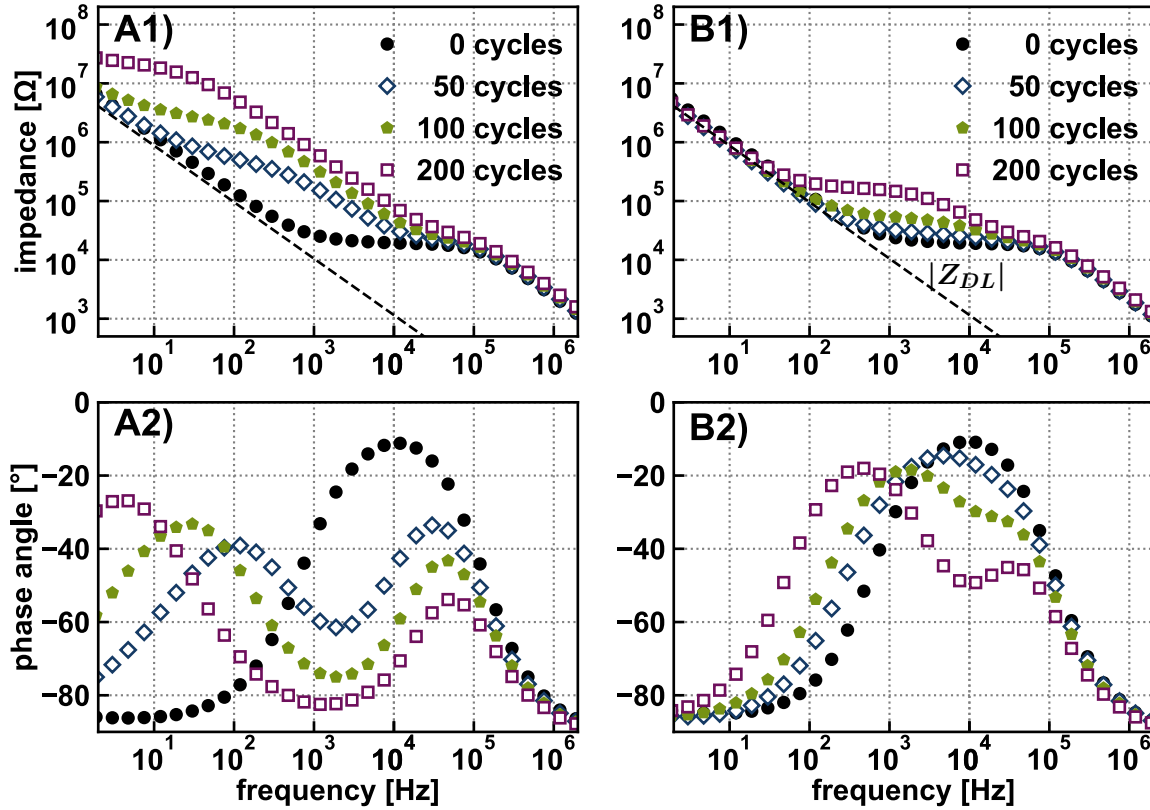
Figure 6.12. Development of the impedance response collected with the 0.05 mM KCl testing solutions containing A) 0 and B) 20 mol-% water as an increasing amount of HKUST-1 growth cycles are being completed.

the data in A) clearly indicates $\varepsilon_{r,C}$ to be invariant to the HKUST-1 coating thickness. The apparent decrease in $\varepsilon_{r,C}$ observed for 20 mol-% testing solution as more growth cycles are being completed is again likely to originate from modelling difficulties given the overlap of C_C and the double layer contribution in the raw data. For this reason, it cannot be ruled out that the $\varepsilon_{r,C}$ observed for 20 mol-% testing solution may in truth remain just as invariant to d_C as $\varepsilon_{r,C}$ observed with the 0 mol-% testing solution. As the dielectric properties of the HKUST-1 thin film are strongly influenced by the guest (solvent) molecules occupying the internal porous network, a constant $\varepsilon_{r,C}$ in Fig 6.13 A) indicates that the specific internal pore volume as well as the accessibility thereof do not change during the coating process.

The conductivity data in Fig 6.13 B) shows a clear trend towards decreasing κ_C values as d_C increases. In comparison to the initial testing procedure of the HKUST-1 coating conducted after the completion of 50 growth cycles, κ_C is observed to drop by 87 % for the 0 mol-% and by 69 % for the 20 mol-% testing solution following the completion of 200 growth cycles. With regard to equation 3.4, the reduction in κ_C could be explained by both decrease in the ionic partitioning factor $P_{MC,i}$ or the ionic diffusion coefficient in the coating $\delta_{i,C}$. On a fundamental level, both the ionic partitioning into the coating on the basis of the steric, Donnan and dielectric exclusion mechanism as well as $\delta_{i,C}$ should remain invariant to the spatial extension of a homogeneous coating. For this reason, the decrease in κ_C may indicate minor changes to the coating microstructure during the growth process such as the potential closing
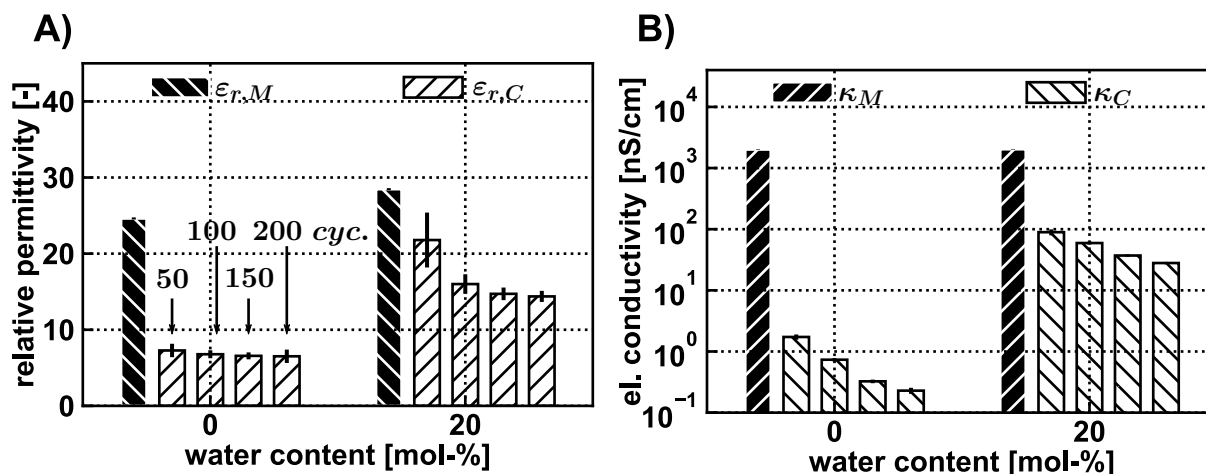
Figure 6.13. A) Dielectric and B) conductive properties of the HKUST-1 coating as a function of the growth cycles completed when exposed to 0.05 mM KCl testing solutions at 0 and 20 mol-% water content. The growth data in Fig 6.6 B) suggests a coating thickness of (120 ± 10), (230 ± 30), (350 ± 30), (470 ± 30) nm after 50, 100, 150 and 200 growth cycles, respectively. The properties of the testing solutions have been added for comparative purposes.

of intracrystalline ionic pathways.

6.2.5. Discussion

The experimental results presented thus far demonstrate the complexity of the ionic transport process through the HKUST-1 thin film and its dependence to the reference medium the coating material is exposed to. Within the individual parameters and value ranges investigated, the water content of the ethanolic testing solutions revealed itself to be the single most significant factor of influence with the potential to increase κ_C by at least three orders of magnitude. On the one hand, the increase in water content was shown to likely coincide with a decrease in the ionic partitioning between coating and reference medium which would result into an increase in the effective charge-carrier concentration in the HKUST-1 coating in the form of potassium cations and chloride anions from the liquid reference medium. However, the hypothesis that the solvent composition of the reference medium influences κ_C primarily on the basis of the dielectric partitioning phenomenon of charge carriers between reference medium and the coating's internal pore network is challenged by the data presented in Fig 6.11 B). κ_C appears to remain largely invariant to a variable amount of potassium cations and chloride anions offered from the reference medium as potential charge carriers for the ionic migration through the HKUST-1 material. Accordingly, a more intricate relationship between κ_C and the solvent composition of the reference medium which goes beyond the aforementioned dielectric partitioning effect may need to be taken into consideration.

As a matter of fact, several studies on the conductive properties of HKUST-1 are available in the literature which may facilitate the understanding of the data presented herein. While the HKUST-1 material in this work was prepared as a thin film of intergrown nuclei, related impedimetric research on HKUST-1 customarily relies on pelletized powder samples [187, 188] or large single crystals [176]. Also, guest molecules are primarily supplied from the gas phase

rather than from the liquid phase.

The open metal sites (OMS) of the crystalline framework were suggested to have a distinct influence on the bulk ionic conductivity of HKUST-1 when impregnated with guest molecules. In particular, the OMS allow for a strong interaction of the framework with polar protic solvent molecules such as water, methanol or ethanol via coordinative bond formation [189]. Given the Lewis acidity of the binding site, proton donation of coordinated molecules to other hydroxylic guest molecules is facilitated [187] thereby amplifying the charge carrier concentration available for ionic migration. As a result of the charge transport mechanism, HKUST-1 has been mentioned in the context of solid-state proton conductors [189].

Jeong et al. studied pelletized HKUST-1 samples when exposed to methanolic vapor [187]. They reported proton conductivities of 430 nS/cm under these conditions which could be increased to 15 000 nS/cm upon saturation of the OMS with water molecules prior to the measurement [187]. In contrast, the coordination of ethanol molecules to the OMS prior to the measurement reduced the conductivity to 200 nS/cm which lead the authors to conclude the influence of ethanol on the proton conduction effect to be negligible [187].

Owing to evident differences in terms of experimental procedure, the κ_C values of the HKUST-1 thin film discussed in this chapter cannot be directly compared to the data published by Jeong et al. For the HKUST-1 thin film studied in this work a peak conductivity of $\kappa_C = 300$ nS/cm was obtained when exposed to the 0.2 mM KCl ethanolic test solution at 30 mol-% water content.

As a consequence of the suspected chemical interaction of the HKUST-1 framework with the solvent molecules providing an additional source of ionic species (protons) to serve as an explanation for the relationship between κ_C and the solvent composition, it is reasonable to question whether ionic species present in the reference medium exert any significant influence on κ_C. In a broader sense, the question challenges the idea of ionic guest species such as potassium cations and chloride anions being able to migrate through the nanoporous HKUST-1 coating. To address the question in a systematic way, the impedance responses of the HKUST-1 coated electrode system exposed to a variety of well-defined yet diverse set of ionic reference systems at an identical solvent composition would be required. Any variation in κ_C which could be correlated to the size, charge number or ionic concentration of the respective ionic species would provide evidence to the idea of guest ion migration through the HKUST-1 material. By contrast, the absence of any variation of κ_C under these conditions would indicate the relationship between κ_C and the solvent composition to be exclusively based on the supposed proton conduction mechanism.

As the testing solutions investigated during the experiment were exclusively based on KCl, an unequivocal answer to the question above cannot be provided based on the evidence currently available. Still, it is possible to compare the testing solution data with the impedance spectra collected during the exposure to the respective precursor solutions. In Fig 6.14 A), the final impedance spectra of the coated electrode system when exposed to the metal precursor and the purely ethanolic testing solution are contrasted. While the solvent composition is
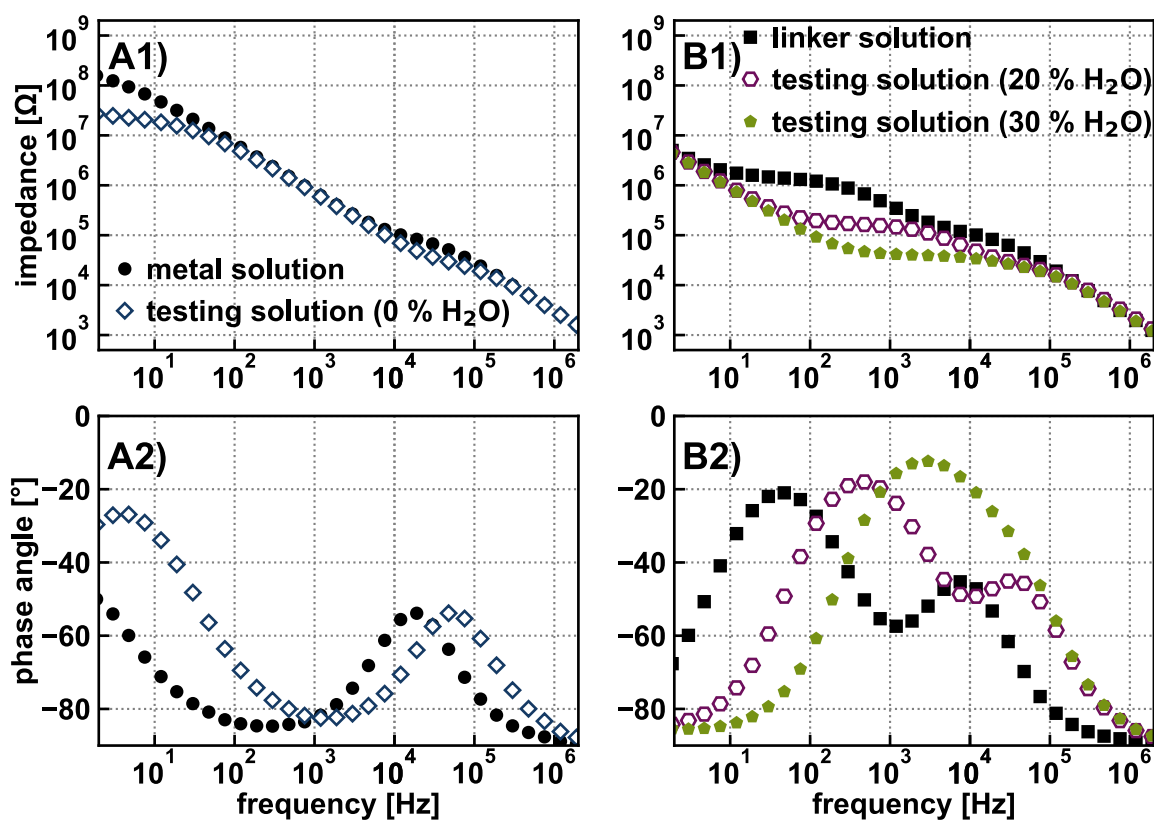
Figure 6.14. Comparison of the impedance data collected during the exposure of the HKUST-1 coating to the precursor and selected testing solutions following 200 growth cycles. From a generalized perspective, the impedance spectra in A) were recorded with two reference media of identical solvent composition. The two reference media differ however in terms of solute species with the metal solution containing 1 mM CuAc and the testing solution 0.05 mM KCl. The impedance data in B) were collected with ethanolic reference media at 20, 25 and 30 mol-% water content. Again, the testing solutions contained 0.05 mM KCl whereas the linker solution contained 0.2 mM BTC as potential ionic species. The impedance data in A) and B) oppose the idea that the migration current through the HKUST-1 film can be exclusively attributed to the proton conduction phenomenon.

identical in both cases, the testing solution contains 0.05 mM KCl whereas the metal solution contains 1 mM CuAc as solute species. The portions of the two impedance spectra in A1) dominated by the capacitive effects of C_{Geo} and C_C are identical meaning exposure to the two reference media leads to equal dielectric properties of the HKUST-1 coating. The variations in impedance modulus $|Z|$ between 10 and 100 kHz derive from a slight mismatch in the migration current in the liquid reference media which is plausible as κ_M of the testing solution amounts to (2010 ± 10) nS/cm in comparison to (640 ± 10) nS/cm of the metal solution. The more important variation however is found at the low frequency end of the spectrum in Fig 6.14 A) given that $|Z|$ in the testing solution data levels off between 20 and 40 MΩ whereas exposure to the metal precursor solution leads $|Z|$ to increase beyond the 100 MΩ threshold. An ECM 2 data modelling of the testing solution impedance spectrum leads to an estimated κ_C value of (0.23 ± 0.03) nS/cm. Provided ECM 2 is applicable to the entire impedance spectrum collected during the metal exposure step, a data fit would predict a maximum κ_C value of 0.03 nS/cm. Accordingly, κ_C is shown to vary by at least one order of magnitude despite equal solvent composition.

A similar observation can be made when taking a look at the spectra shown in Fig 6.14 B) effectively comparing the impedance response of the coated electrode system to ethanolic reference media at 20, 25 and 30 mol-% water content. Importantly however, the linker solution at 25 mol-% water content contains 0.2 mM BTC whereas the two testing solutions at 20 and 30 mol-% contain 0.05 mM KCl as solute species. Following the general trend that a rise in water content coincides with a significant increase in κ_C as observed in chapter 6.2.2, one would expect κ_C of the linker solution to range in between the κ_C values of the 20 and 30 mol-% testing solutions. Contrary to this assumption however, an ECM 2 data fit to the testing solutions provides κ_C values of (28 ± 1) and (250 ± 20) nS/cm for the testing solutions at 20 and 30 mol-%, respectively, whereas modelling of the linker data provides a κ_C of only (3.7 ± 0.3) nS/cm.

The comparison of the precursor and testing solution data therefore evidently contradicts the idea that κ_C derives solely from the interplay between solvent composition and proton conduction phenomenon. With regard to the interpretation of the impedance spectra contrasted in Fig 6.14, caution should be warranted. Based on the κ_M values of the precursor solutions, it is safe to conclude that only a minor fraction of the dissolved precursor species undergo solvation into ionic species. Accordingly, non-specific adsorption of uncharged species such as the CuAc paddlewheel or the undissociated BTC molecule to the coating surface or the internal pore structure of HKUST-1 could potentially affect the ionic transport properties of the coating as well. For this reason, further experiments will be required to gain a better understanding of the complex ionic transport properties of the HKUST-1 thin film.

7. ZIF-8 Model Thin Film

7.1. XRD and SEM Characterization of the Thin Films
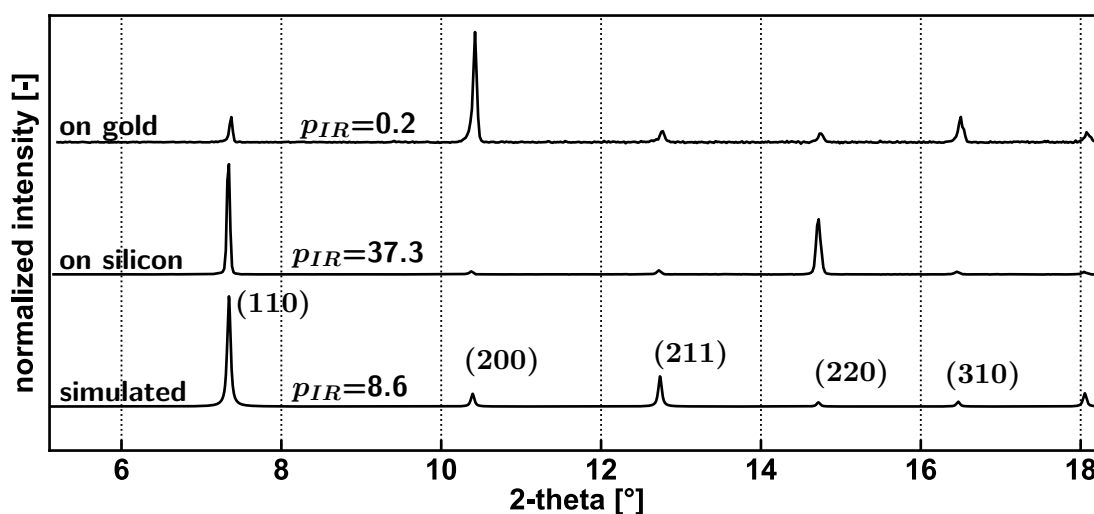
Figure 7.1. X-ray diffractograms of the ZIF-8 thin film prepared on a silicon and gold surface together with the simulated powder pattern. The powder pattern was modelled using the CIF deposited by the authors of [100]. The reproducibility of the individual peak positions provides clear evidence of the ZIF-8 crystalline phase for all sample surfaces coated. When choosing the peak intensity ratio p_{IR} of the (110) to the (200) reflex as evaluation criterion, the UV/ozone cleaned silicon surface appears to impart a preferential [110] growth direction on the nucleated ZIF-8 crystallites. In contrast, a UV/ozone cleaned gold surface appears to favor the ZIF-8 thin film formation along the [100] direction.

In contrast to the HKUST-1 SURMOF coating process which has already been extensively studied and accordingly is relatively well-understood, the ZIF-8 coatings obtained under aqueous synthesis conditions deserved initial investigation by both SEM and XRD prior to the actual impedimetric characterization. For this purpose, UV/ozone cleaned silicon and gold surfaces were chosen as model substrates to be tested.

The successful synthesis of the ZIF-8 crystalline phase on both model surfaces following a two cycle coating process is validated by the the x-ray diffractograms shown in Fig 7.1. The peak

positions correspond well to the simulated powder pattern which was modelled on the basis of the crystallographic data published by [100]. Reflexes associated to crystalline phases other than ZIF-8 are absent within the recorded 2-θ range. In addition, the XRD data reveals a preferential crystallographic orientation into the [110] direction for the ZIF-8 crystalline phase deposited on the silicon surface and into the [200] direction on the gold surface. The occurence of a preferential crystallographic orientation is a clear indication that the ZIF-8 material deposited on the sample surfaces originated from a heterogeneous nucleation process rather than a random attachment of individual ZIF-8 crystals from the mother solution.
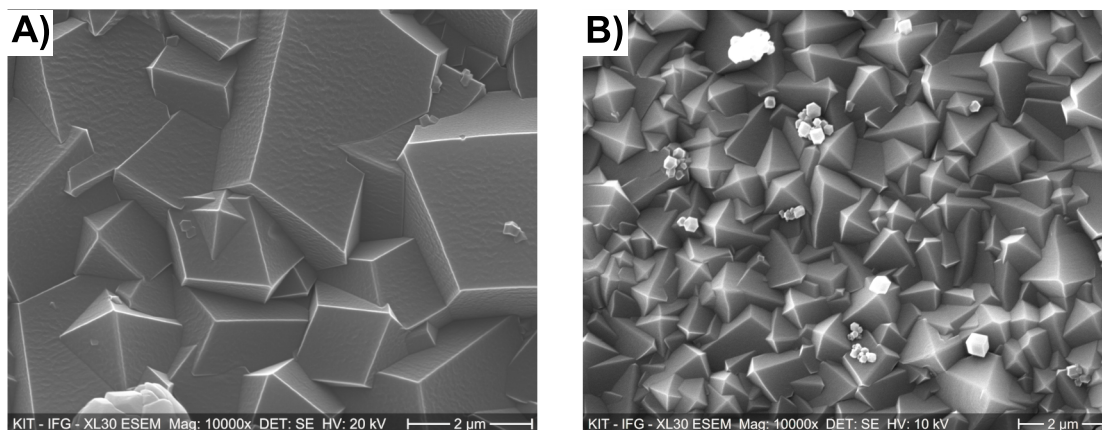
Figure 7.2. Topview scanning electron micrographs of the ZIF-8 coating prepared on a UV/ozone pretreated A) silicon and B) gold surface. In both cases the thin film is comprised of individual, intergrown crystallites. The thin film morphology differs greatly depending on the surface it is formed. In A), primary feature of the thin film are the planar rhombic facets exposed in parallel to the coated silicon surface. In contrast, the micrograph shown in B) is dominated by individual vertices incident to a total of four edges protruding from the coating. With regard to the ZIF-8 crystallite morphology shown in Fig 2.16, a rhombic facet is indicative to the [110] whereas a vertex incident to four edges develops in the [100] growth direction. The two micrographs were recorded at varying image resolution settings resulting in the slight variation of the scale bar length despite the apparent identical magnification factor.

Representative electron micrographs of the ZIF-8 coated silicon and gold surfaces provided in Fig 7.3 indicate a complete surface coverage. The coating appears to be composed of individual crystallites intergrown into a compact, pinhole-free thin film. Given that the micrographs in A) and B) both depict a ZIF-8 thin film, the different appearance of the coating between the gold and silicon sample is in fact particularly striking. The topview appearance of the thin film does however add up to the XRD data in Fig 7.2 when recalling the rhombic dodecahedral morphology of ZIF-8 crystallites shown in Fig 2.16. The rhombic facets visible in A) correspond well to the preferential crystallographic [110] orientation. Likewise, the vertices protruding from the thin film in B) which are incident to four individual edges usually develop along the main crystallographic axis. Owing to the conclusive results collected for both the ZIF-8 coated gold and silicon model surfaces, the synthesis strategy was subsequently tested on IDE chips. To gain a better understanding on the influence of the completed growth cycles on the resulting film thickness and morphology, the coated IDE structures were extensively imaged through scanning electron microscopy as displayed in Fig 7.3.
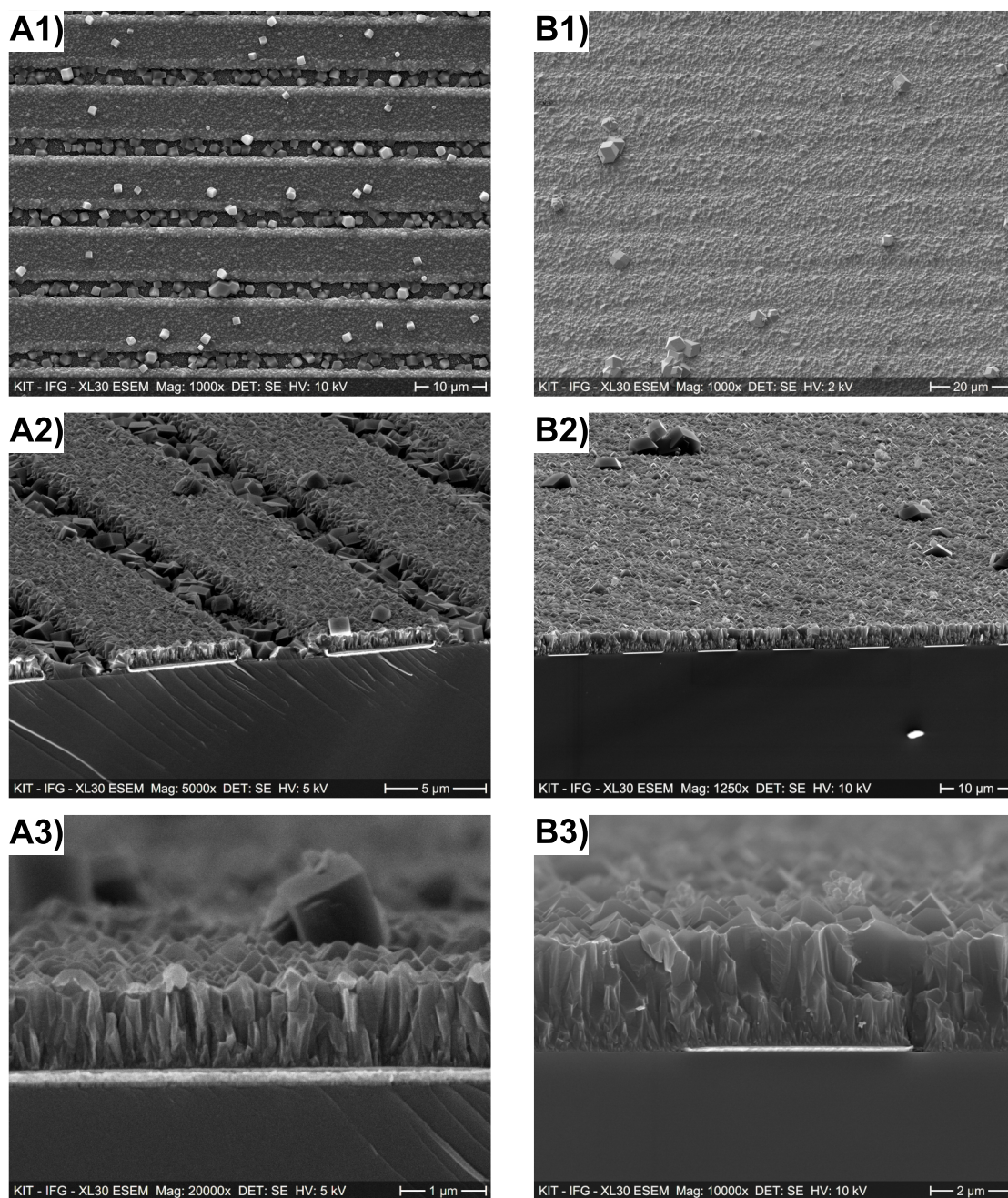
Figure 7.3. Scanning electron micrographs of the ZIF-8 coating prepared on IDE chips after A) one and B) two growth cycles depicted from the 1) topview, 2) tilted cross sectional and 3) cross sectional perspective. After a single growth cycle, the gold electrode fingers appear to be fully covered by the ZIF-8 thin film whereas surface coverage on the glass surface in between the fingers is incomplete. By contrast, two growth cycles provide a homogeneous coating covering the complete interdigitated area. Judging from the cross sectional micrographs in 3), a film thickness of $\sim$900 nm is received after one and $\sim$2800 nm after two growth cycles.

Interestingly, a single coating cycle provides completely covered electrode fingers whereas the surface coverage of the spacing in between the fingers appears incomplete. Thus, the ZIF-8 crystalline phase appears to preferentially nucleate and grow on gold rather than on glass surfaces. A homogeneously covered interdigitated area is only obtained after two growth cycles as seen in Fig 7.3 B). From a morphological perspective, the coating appears again to be primarily dominated by individual vertices protruding from the thin film incident to four edges

indicating preferential [100] orientation. The cross sectional micrographs suggest a coating thickness of 900 nm after a single and about 2800 nm after two immersion steps. Thus, in comparison to the HKUST-1 SURMOF growth discussed in the previous chapter, the aqueous ZIF-8 coating process provides a significantly increased film thickness.

7.2. Impedimetric Characterization

Table 7.1. Outline of the experimental data discussed in chapter 7. The impedance spectra were recorded with a 10 µm-IDE chip and are disclosed in chapter 5 of the supplementary research data.

sample medium	coating	frequency range	RMS voltage
air	—	10 kHz - 1 MHz	2800 mV
100 mol-% ethanol	—	10 kHz - 5 MHz	630 mV
air	ZIF-8, 1 cycle	2 Hz - 5 MHz	25 mV
100 mol-% ethanol	ZIF-8, 1 cycle	2 Hz - 5 MHz	25 mV
1 mM KCl in 100 mol-% ethanol	ZIF-8, 1 cycle	2 Hz - 5 MHz	25 mV

With the successful synthesis of homogeneous ZIF-8 coating confirmed by XRD and SEM, the impedance response of a coated IDE chip was subsequently tested using air, ethanol and 1 mM KCl dissolved in ethanol as reference media. A 10 µm-IDE chip coated by a single growth cycle was chosen for the first trial to guarantee the coating thickness d_C remains about an order of magnitude smaller than the IDE sensing range d_S. Accordingly, the evaluation of the coating capacitance C_C in accordance to equation 4.3 was assumed adequately justified. The experimental details of the data sets discussed in this chapter are listed in table 7.1.

The impedance response taken with the dielectric sample media air and ethanol provided conclusive information about the effective relative permittivity $\varepsilon_{r,eff}$ which is plotted in Fig 7.4 A). In the case of air, an $\varepsilon_{r,eff}$ value of 1.0±0.0 with the uncoated and 2.7±0.1 with the coated electrode structure is obtained. As d_C is significantly smaller than d_S, it is safe to assume that the relative permittivity $\varepsilon_{r,C}$ of the ZIF-8 coating is in fact larger than 2.7. Given that ZIF-8 is frequently cited as a promising candidate for to be used for low ε_r-dielectrics in microelectronic applications [190] this result is particularly surprising. The data published by Eslava et al. [107] for instance suggest $\varepsilon_{r,C} = 2.23\pm0.05$ for a ZIF-8 coating prepared with methanolic precursor solutions. Potentially, the larger $\varepsilon_{r,C}$ of the ZIF-8 coating studied in this work may stem from polar guest molecules trapped inside the porous framework. Removal of residual guest molecules might require an improved activation process [191].

When exposed to the ethanolic sample media, an $\varepsilon_{r,eff}$ value of 25.0±0.1 for the uncoated and 15.6±0.2 for the coated electrode structure can be extracted from the impedance data. As was observed with the HKUST-1 SURMOF in chapter 6, the permeation of the ZIF-8 thin film by the solvent molecules of the sample medium it is exposed to may be assumed thereby altering its dielectric properties. However, with regard to the ZIF-8 aperture size of
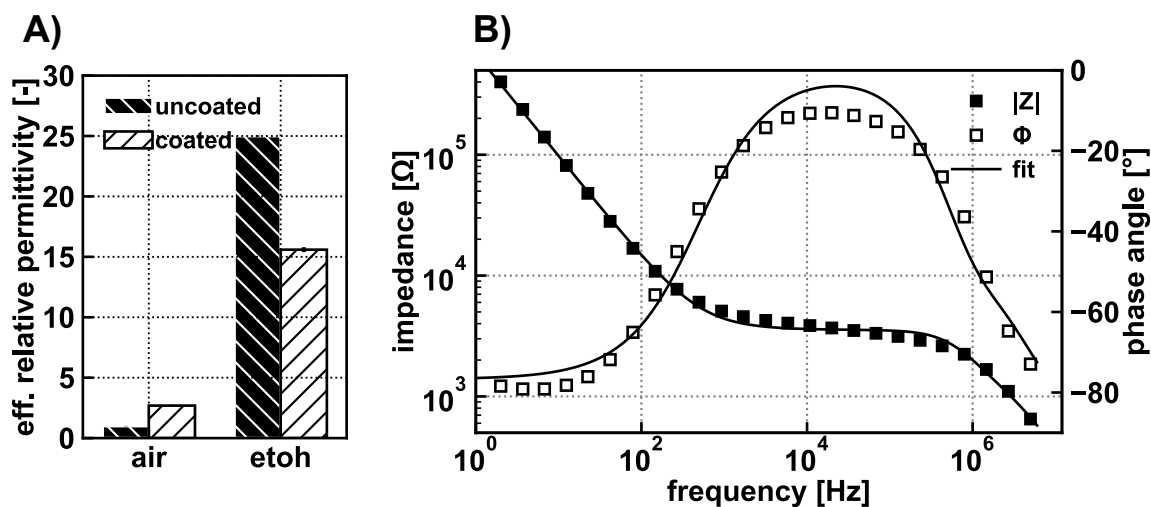
Figure 7.4. A) Influence of the ZIF-8 coating on the measured effective relative permittivity $\varepsilon_{r,eff}$ using air and ethanol as reference media within the frequency interval 0.5-1.0 MHz. B) Bode representation of the impedance response collected for the ZIF-8 coated electrode structure exposed to the 1 mM KCl ethanolic solution. As indicated by the best-fit curve, the data cannot be reasonably modelled by ECM 2 yielding an unconvincing $\xi^2 > 0.01$. All impedance data recorded at (21.0 ± 0.5) ℃.

only 0.34 nm, the mobility of ethanol molecules inside the intracrystalline ZIF-8 pore network is likely to be impaired by considerable steric effects. Still, in contrast to rigid molecular sieves of comparable aperture size, intrusion of guest molecules into the internal porous network is thought to be the facilitated by the inherent structural flexibility of ZIF-8 [175].

In order to gain access to the coating's $\varepsilon_{r,C}$ as well as to characterize its ionic permeability, impedance data was collected using an electrolyte solution of 1 mM KCl in ethanol as reference medium. The bode representation thereof is shown in Fig 7.4. Interestingly, the impedance response is marked by only a single phase angle peak and the data can be broadly divided capacitively dominated at the high and low frequency end as well as primarily resistive behavior from approximately 1 kHz to 100 kHz. The capacitive response at the high frequency end is equivalent to the impedance data collected with the ethanolic sample medium devoid of ionic species and can therefore be easily identified as the contribution stemming from C_{Geo}. The capacitive behavior at the low frequency end of the spectrum on the other hand may potentially be assigned to either a non-ideal coating C_C or double layer capacitance C_{DL}. An approximation of the low frequency impedance data from 2 - 10 Hz with a single capacitor suggests $C = (180\pm20)$ nF. To safely allocate the estimated C to either C_C or C_{DL} it is worth considering physically meaningful value ranges. For instance, with regard to the decline in $\varepsilon_{r,eff}$ in Fig 7.4 A) detected for the ethanolic sample media upon coating with ZIF-8, it is reasonable to project $\varepsilon_{r,C}$ of the ZIF-8 coating in contact with the ethanolic sample medium to range between 5 - 10. Accordingly, when applying $\varepsilon_{r,C}$ as well as $d_C \approx 900$ nm to equation 4.3 one would expect C_C to range between 60 and 120 pF, rather than nF. Therefore, judging from the order of magnitude of C, the low frequency impedance data is likely to originate from the double layer effect.

Modelling of the impedance spectrum shown in Fig 7.4 B) with ECM 2 does not yield satisfactory data fits. While high and low frequency end of the impedance data may be reasonably

assigned to C_{Geo} and CPE_{DL} the physical processes giving rise to the depicted impedance response as a whole is not adequately accounted for by ECM 2. Accordingly, no quantitative assessment of the coating in terms of C_C and R_C can be made. The primary issue appears to be the ionic migration towards the electrode surface which appears more complex than modelled with R_E, R_C and C_C in ECM 2. What stands out is however that the ZIF-8 coating, in stark contrast to the HKUST-1 SURMOF discussed in chapter 6.2, does not impart a sizeable mass transport limitation on ionic species migrating towards the electrode surface. Furthermore, the area normalized double layer capacitance $\overline{c}_{DL}$ can be estimated at 12 - 14 µF/cm² which is comparable to the $\overline{c}_{DL}$ value of an uncoated electrode surface. Accordingly, ionic species appear to have largely unobstructed access to the entire electrode surface despite the supposed presence of the ZIF-8 coating.

As the pore size of HKUST-1 is roughly 2.5 times larger than the intracrystalline aperture of the ZIF-8 structure, a ZIF-8 coating should, in theory, be characterized by a reduced ionic permeability than the HKUST-1 SURMOF. Additionally, ionic migration would have to proceed along the crystallographic [100] direction owing to the preferential orientation of the ZIF-8 crystallites on the electrode fingers which has been reported unfavorable in comparison to mass transport along the [110] and [111] directions [192]. The opposing observations indicate that the ionic species are offered an alternative pathway towards the electrode surface and thus are not forced to penetrate the intracrystalline pores of the ZIF-8 structure.

To elucidate the unexpected impedance response, the coated IDE chip was imaged by scanning electron microscopy following the impedimetric characterization. As evidenced in Fig 7.5 A), the tested coating did not fully cover the entire electrode area. The uncoated portion of the interdigitated area coincided with the surface area exposed to the greatest liquid shear load within the polymeric flow cell. Accordingly, a local delamination of the brittle ZIF-8 coating due to fragmentation with subsequent flake-off appears plausible. The heterogeneous surface coverage is a likely explanation to the peculiar impedance behavior displayed in Fig 7.4 B). Even more revealing, however, is the closeup of the intergrown ZIF-8 crystallites. While the structural appearance of the coating in Fig 7.5 B) is undoubtedly reminiscent of a pristine ZIF-8 thin film prepared on gold displayed in Fig 7.2 B), the coating tested in the impedance measurement system appears to have developed a pronounced mesoporosity. The formation of an additional pore structure penetrating the ZIF-8 coating is likely to facilitate ionic migration from the reference medium towards the actual electrode surface.

The delamination of the coating from the electrode surface in Fig 7.5 A) stemming from insufficient adhesion could potentially be addressed with an adequate chemical surface functionalization. However, the morphological degradation of the coating as observed in Fig 7.5 B) is more challenging to resolve. A possible factor compromising the structural integrity might be the deformation of ZIF-8 under the influence of an electric field. At field strengths exceeding several 10^5 V/m, the ZIF-8 lattice was reported to undergo structural transformation from the cubic space group $I\overline{4}3m$ into polymorphs belonging to the trigonal $R3m$ and monoclinic Cm space groups [102]. While a minor structural deformation of ZIF-8 coating might have occurred
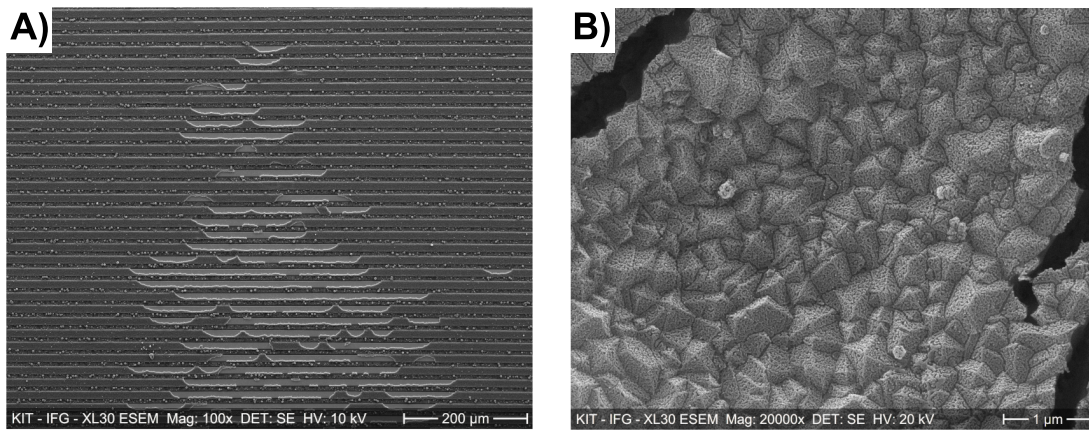
Figure 7.5. Scanning electron micrographs of the ZIF-8 coating taken after exposure to ethanolic sample media. The brittle coating seems to flake off when subject to liquid shear in the experimental setup as can be seen in A). In addition, when observed at higher magnification in B), the coating appears to have developed an extensive mesoporosity indicating a partial structural collapse of the metal-organic framework.

as a result of the AC voltage perturbation, the RMS voltage of 25 mV induces a nominal field strength $E_0 = 2.5 \cdot 10^3$ V/m which with regard to the IDE potential distribution in Fig 2.12 is unlikely to trigger widespread polymorphic transformation of the coating material during the measurement. An alternative explanation could therefore be a chemical incompatibility of ZIF-8 with the ethanolic sample media. While the water stability of ZIF-8 has been studied in great detail [108, 109], comparable research on the compatibility with ethanol appears to be absent. However the fact that ZIF-8 is most commonly synthesized in methanol rather than ethanol may hint towards undesirable chemical interactions.

As was stressed in chapter 3, the impedance response of a dielectric thin film is strongly influenced by both the coating morphology and its material properties. Scanning electron microscopy proved vital to interpret the impedance response in Fig 7.4 on the basis of incomplete surface coverage and structural degradation rather than unexpected (di-)electric properties exerted by the ZIF-8 material itself. In fact, the morphological inhomogeneity of the coating during the testing prevented a conclusive impedimetric characterization of the coating material in this chapter.

8. Conclusion and Outlook

Impedance spectroscopy provides a variety of unique opportunities for the analysis of thin film coatings in contact with fluidic reference media. Purposeful application of the measurement technique however requires a conceptual awareness of the underlying charge transport processes as well as a careful experimental design. Having access to impedance data of both the uncoated and coated system is particularly beneficial to isolate the distinct influence of the coating and, accordingly, alleviate potential ambiguities during data interpretation.

In this work, a comprehensive collection of impedimetric thin film analysis strategies has been presented and compiled together into one, consistent theoretical framework. While the collection is far from exhaustive and limited to the influence of a single homogeneous coating, the associated equivalent circuit model contains a total of five different circuit parameters in the non-Faradaic case which increases to seven in the Faradaic case. Isolated evaluation of the individual circuit components will provide only limited information on the coating and may necessitate costly assumptions during data analysis. Given that the informative value of the individual circuit components is mutually interconnected by, e.g., the coating thickness, a system of equation should be established to substantiate the data interpretation approach.

As a mean to demonstrate the practical application of the collected characterization strategies, a unique experimental setup was designed within the scope of this work. The setup allowed a sequential supply of up to twelve different fluidic reference media to an interdigitated electrode chip which was housed in a custom-built, polymeric flow cell and electrically connected to a potentiostat with frequency response analyzer. The experimental system could be operated in a fully automated way and generate impedance data at selected time intervals by making use of the programming interface of the pneumatic pump system, flow selection valve and potentiostat.

Measurement of the interfacial impedance contributions collected under non-Faradaic conditions revealed that the UV-ozone surface treatment was superior to the cyclovoltammetric treatment with diluted sulfuric acid to provide a clean gold surface. To validate the functionality of the experimental setup as well as to verify the possibility to obtain tangible material properties

using interdigitated microchip sensors, the impedance measurement system was tested against a variety of dielectric and conductive reference media. The extraction of reliable electrolytic conductivity and relative static permittivity values with interdigitated structures required careful treatment and compensation of unavoidable parasitic contributions to the impedance response. Still, reliable conductivity values appeared to be more challenging to reproduce than the relative permittivity values. A plausible explanation could be an increased leaching of ionic species from the glass substrate into the reference medium following the initial UV-ozone dry etching step. With regard to the HKUST-1 model thin film, the native cycle-by-cycle coating process could be successfully implemented into impedance measurement setup. The data collected during the thin film growth process correlate well with the equivalent circuit model for a coated electrode system. A combined evaluation approach of the geometric and coating capacitance values collected during both the linker and metal precursor solution exposure step provided access to the respective coating permittivity values. Given the difference in solvent composition of the two precursor solutions, the variability of the coating permittivity from 6.7±0.5 during the metal to 15.2±0.4 during the linker exposure step clearly indicate reversible access of solvent molecules to the internal pore structure of HKUST-1. Furthermore, the impedance data indicated a linear growth rate of (1.5±0.3) nm/cycle as well as an estimated final layer thickness of (350±30) nm which compared well to the layer thickness observed with the scanning electron microscope.

A slight alteration of the coating process to include a variety of different testing solutions provided an additional opportunity to assess the ionic transport properties of the growing HKUST-1 coating. The solvent composition of the reference electrolyte was shown to be single most dominant factor influencing the migration current penetrating the coating. A 40 mol-% increase in water content of the ethanolic reference media coincided with a rise in the electrolytic conductivity of the coating across three orders of magnitude. Based on the chemical properties of the HKUST-1 material, the relationship between solvent composition and electrolytic conductivity of the coating is most likely to primarily derive from a strong interaction of the water molecule with the open metal sites of the crystalline framework imparting a considerable proton conductivity. Still, guest-ion migration through the coating material could still be of relevance.

Finally, interdigitated electrode structures were coated with a high-quality ZIF-8 thin film using a refined aqueous synthesis procedure. ZIF-8 was shown to preferably nucleate in the [100] direction which was confirmed by both x-ray diffraction and from morphological aspects using scanning electron microscopy. Due to an unanticipated chemical incompatibility of the coating material with the ethanolic reference media, the impedimetric characterization method however did not provide conclusive information on the conductive or dielectric properties of the ZIF-8 material.

Owing to the historic development of impedimetric thin film research, the modelling approach compiled and demonstrated within the scope of this work relied exclusively on the equivalent circuit representation of the coated electrode system in contact with a fluidic reference medium. As is schematically outlined in Fig 4.5, the equivalent circuit modelling of a coated

interdigitated electrode structure requires a few intricate assumptions which, depending on the individual system under investigation, may not always be reasonably justified. To transcend the general limitations of equivalent circuit modelling, a direct physical modelling approach of the frequency dependent current-voltage relationship of a coated interdigitated structure starting from a Poisson-Nernst-Planck system of equation could be developed in the future.

With regard to the impedimetric analysis of nanoporous coatings, the experimental data discussed in this work presents a variety of potential opportunities for future research. While the accessibility of solvent molecules to the nanoporous structure of the HKUST-1 framework is clearly confirmed by the changes in the relative static permittivity, at the current state of knowledge it is not possible to reliably estimate the molar solvent composition inside the pore structure. Owing to steric and chemical interaction between the nanoporous material and the solvent molecules, a partitioning of the solvent composition at the interface between reference medium and nanoporous coating is highly likely. To resolve this issue, a dielectric mixture model would need to be devised taking into account the nanoporous material and the individual solvent molecules.

Likewise, the complex ionic transport properties of the nanoporous HKUST-1 material provide ample opportunities for future research. The variation of the solvent composition or the ionic species in general might prove useful to establish a more generalized picture of the migration process. Also, by changing the orientation of the HKUST-1 thin film from [111] to [100], e.g., through functionalization of the electrode surface with hydroxylic rather than carboxylic terminal groups, a potential anisotropy of the ionic transport properties could be investigated.

Bibliography

[1] Eite Tiesinga, Peter J. Mohr, David B. Newell, and Barry N. Taylor. CODATA Recommended Values of the Fundamental Physical Constants: 2018. *Journal of Physical and Chemical Reference Data*, 50(3):033105, 2021.

[2] Lawrence Young. Anodic oxide films. part 4.—the interpretation of impedance measurements on oxide coated electrodes on niobium. *Transactions of the Faraday Society*, 51:1250–1260, 1955.

[3] J. W. Diggle, Thomas C. Downie, and C. W. Goulding. Anodic oxide films on aluminum. *Chemical Reviews*, 69(3):365–405, 1969.

[4] Digby D. Macdonald. The point defect model for the passive state. *Journal of the Electrochemical Society*, 139(12):3434, 1992.

[5] Julio J. Suay, Enrique Giménez, T Rodrıguez, K Habbib, and Juan J. Saura. Characterization of anodized and sealed aluminium by EIS. *Corrosion Science*, 45(3):611–624, 2003.

[6] A. Amirudin and D. Thieny. Application of electrochemical impedance spectroscopy to study the degradation of polymer-coated metals. *Progress in Organic Coatings*, 26(1):1–28, 1995.

[7] Florian Mansfeld and Martin Kendig. Electrochemical impedance spectroscopy of protective coatings. *Materials and Corrosion*, 36(11):473–483, 1985.

[8] Chun Ho, Ian D. Raistrick, and Richard A. Huggins. Application of A-C Techniques to the Study of Lithium Diffusion in Tungsten Trioxide Thin Films. *Journal of The Electrochemical Society*, 127(2):343–350, 1980.

[9] Pier Paolo Prosini, Marida Lisi, Daniela Zane, and Mauro Pasquali. Determination of the chemical diffusion coefficient of lithium in $LiFePO_4$. *Solid State Ionics*, 148(1):45–51, 2002.

[10] Alberto Perrotta, Santiago J. García, and Mariadriana Creatore. Ellipsometric Porosimetry and Electrochemical Impedance Spectroscopy Characterization for Moisture Permeation Barrier Layers. *Plasma Processes and Polymers*, 12(9):968–979, 2015.

[11] Alberto Perrotta, Santiago J. García, Jasper J. Michels, Anne-Marije Andringa, and Mariadriana Creatore. Analysis of Nanoporosity in Moisture Permeation Barrier Layers by Electrochemical Impedance Spectroscopy. *ACS Applied Materials & Interfaces*, 7(29):15968–15977, 2015.

[12] Jamila Boudaden, Armin Klumpp, Hanns-Erik Endres, and Ignaz Eisele. Capacitive CO_2 Sensor. *Proceedings*, 1(4), 2017.

[13] Maria Kitsara, Dimitrios Goustouridis, Stavros Chatzandroulis, Margarita Chatzichristidi, Ioannis Raptis, Theodore Ganetsos, Rui Igreja, and Carlos J. Dias. Single chip interdigitated electrode capacitive chemical sensor arrays. *Sensors and Actuators B: Chemical*, 127(1):186–192, 2007. Special Issue: Eurosensors XX The 20th European Conference on Solid-State Transducers.

[14] Il-Doo Kim, Avner Rothschild, Byong Hong Lee, Dong Young Kim, Seong Mu Jo, and Harry L. Tuller. Ultrasensitive Chemiresistors Based on Electrospun TiO_2 Nanofibers. *Nano Letters*, 6(9):2009–2013, 2006.

[15] Forest I. Bohrer, Corneliu N. Colesniuc, Jeongwon Park, Manuel E. Ruidiaz, Ivan K. Schuller, Andrew C. Kummel, and William C. Trogler. Comparative Gas Sensing in Cobalt, Nickel, Copper, Zinc, and Metal-Free Phthalocyanine Chemiresistors. *Journal of the American Chemical Society*, 131(2):478–485, 2009.

[16] Núria Blanco-Cabra, Maria José López-Martínez, Betsy Verónica Arévalo-Jaimes, María Teresa Martin-Gómez, Josep Samitier, and Eduard Torrents. A new biofilmchip device for testing biofilm formation and antibiotic susceptibility. *npj Biofilms and Microbiomes*, 7(1):1–9, 2021.

[17] Cheng-Hsin Chuang and Muhammad Shaikh. *Point-of-Care Diagnostics - New Progresses and Perspectives*, chapter Label-free impedance biosensors for Point-of-Care diagnostics, pages 171–201. 2017. ISBN 978-953-56942-4-3.

[18] Vadim F Lvovich. *Impedance spectroscopy: applications to electrochemical and dielectric phenomena*. John Wiley & Sons, 2012. ISBN 978-0-470-62778-5.

[19] William Henry Hunter Woodward. *Broadband Dielectric Spectroscopy: A Modern Analytical Technique*. American Chemical Society, 2021. ISBN 9780841298484.

[20] Mark E. Orazem and Bernard Tribollet. Electrochemical impedance spectroscopy, John Wiley & Sons, 2nd edition, 2017. ISBN 9781119341222.

[21] J Ross Macdonald and Evgenij Barsoukov. *Impedance spectroscopy: theory, experiment, and applications*. John Wiley & Sons, 3rd edition, 2018. ISBN 9781119381860.

[22] Friedrich Kremer and Andreas Schönhals. *Broadband dielectric spectroscopy*. Springer Science & Business Media, 2002. ISBN 978-3-642-62809-2.

[23] Andrzej Lasia. Electrochemical Impedance Spectroscopy and its Applications, Springer Science & Business Media, 2014. ISBN 978-1-4614-8932-0.

[24] Morris Slurzburg and William Osterheld. *Essentials of Electricity for Radio and Television*. McGraw-Hill Book Company, 2nd edition, 1950.

[25] José M. Pingarrón, Ján Labuda, Jiří Barek, Christopher M. A. Brett, Maria Filomena Camões, Miroslav Fojta, and D. Brynn Hibbert. Terminology of electrochemical methods of analysis (IUPAC Recommendations 2019). *Pure and Applied Chemistry*, 92(4):641–694, 2020.

[26] David J. Griffiths. *Introduction to electrodynamics*. Pearson, 4th edition, 2013. ISBN 978-0-321-85656-2.

[27] James D. Patterson and Bernard C. Bailey. *Solid-State Physics : Introduction to the Theory*. Springer International Publishing AG, 3rd edition, 2018. ISBN 978-3-319-75322-5.

[28] Bob Eisenberg, Xavier Oriols, and David Ferry. Dynamics of Current, Charge and Mass. *Computational and Mathematical Biophysics*, 5(1):78–115, 2017.

[29] Paul Ben Ishai, Mark S Talary, Andreas Caduff, Evgeniya Levy, and Yuri Feldman. Electrode polarization in dielectric measurements: a review. *Measurement science and technology*, 24(10):102001, 2013.

[30] Francesco Ciucci. Modeling electrochemical impedance spectroscopy. *Current Opinion in Electrochemistry*, 13:132–139, 2019.

[31] Wolfgang G. Bessler. A new computational approach for SOFC impedance from detailed electrochemical reaction–diffusion models. *Solid State Ionics*, 176(11):997–1011, 2005.

[32] Andrzej Lasia. The Origin of the Constant Phase Element. *The Journal of Physical Chemistry Letters*, 13(2):580–589, 2022.

[33] Gertjan Brug, A.L.G. van den Eeden, Margaretha Sluyters-Rehbach, and Jan H. Sluyters. The analysis of electrode impedances complicated by the presence of a constant phase element. *Journal of Electroanalytical Chemistry and Interfacial Electrochemistry*, 176(1):275–295, 1984.

[34] Florian Mansfeld. Technical Note: Concerning the Display of Impedance Data. *Corrosion*, 44(8):558–559, 08 1988.

[35] Christopher M.A. Brett and Ana M.O. Brett. *Electrochemistry — Principles, methods and applications*. Oxford University Press Inc., 1993. ISBN 0-19-855388-9.

[36] Yizhak Marcus and Glenn Hefter. Ion Pairing. *Chemical Reviews*, 106(11):4585–4621, 2006.

[37] Freek Brinkmann, Niels Ebbe Dam, Eva Deák, Francesca Durbiano, Enzo Ferrara, Judit Fűkő, Hans D Jensen, Michal Máriássy, Rubina H Shreiner, Petra Spitzer, et al. Primary methods for the measurement of electrolytic conductivity. *Accreditation and quality assurance*, 8(7):346–353, 2003.

[38] Carsten Thirstrup and Lisa Deleebeeck. Review on Electrolytic Conductivity Sensors. *IEEE Transactions on Instrumentation and Measurement*, 70:1–22, 2021.

[39] ISO 7888:1985, *Water quality; Determination of electrical conductivity*.

[40] ASTM D5391 - 14, *Standard Test Method for Electrical Conductivity and Resistivity of a Flowing High Purity Water Sample*.

[41] ASTM D1125 - 14, *Standard Test Methods for Electrical Conductivity and Resistivity of Water*.

[42] Dongming He, Mark A. Shannon, and Norman R. Miller. Micromachined Silicon Electrolytic Conductivity Probes With Integrated Temperature Sensor. *IEEE Sensors Journal*, 5(6):1185–1196, 2005.

[43] Hartley C Eckstrom and Christoph Schmelzer. The Wien Effect: Deviations of Electrolytic Solutions from Ohm's Law under High Field Strengths. *Chemical Reviews*, 24(3):367–414, 1939.

[44] Andrew P. Gregory and Robert N. Clarke. Tables of the Complex Permittivity of Dielectric Reference Liquids at Frequencies up to 5 GHz. *NPL Report MAT 23*, 2012.

[45] James E. Anderson. The Debye-Falkenhagen effect: experimental fact or friction? *Journal of Non-Crystalline Solids*, 172:1190–1194, 1994.

[46] IEEE Standard Definitions of Terms for Radio Wave Propagation. *IEEE Std 211-1997*, pages 1–44, 1997.

[47] Silvia E Braslavsky. Glossary of terms used in photochemistry, (IUPAC Recommendations 2006). *Pure and Applied Chemistry*, 79(3):293–465, 2007.

[48] Dinesh Kumar, Nazir Ahmad, Vipin Kumar, Vikash Kumar Jha, Shobha Kulshrestha, Richa Saini, and Manoj S. Shekhawat. Various polarization mechanisms involved in ionic crystals. *AIP Conference Proceedings*, 2220(1):040036, 2020.

[49] Udo Kaatze. Techniques for measuring the microwave dielectric properties of materials. *Metrologia*, 47(2):S91–S113, 2010.

[50] P. Petong, Reinhard Pottel, and Udo Kaatze. Water-Ethanol Mixtures at Different Compositions and Temperatures. A Dieletric Relaxation Study. *The Journal of Physical Chemistry A*, 104(32):7420–7428, 2000.

[51] Udo Kaatze. Complex permittivity of water as a function of frequency and temperature. *Journal of Chemical and Engineering Data*, 34(4):371–374, 1989.

[52] Andrew P. Gregory and Robert N. Clarke. Traceable measurements of the static permittivity of dielectric reference liquids over the temperature range 5–50 °C. *Measurement Science and Technology*, 16(7):1506–1516, 2005.

[53] Günter Lüttgens, Sylvia Lüttgens, and Wolfgang Schubert. *Static Electricity: Understanding, Controlling, Applying*. John Wiley & Sons, 1st edition, 2017. ISBN 978-3-527-80332-3.

[54] Ari Sihvola. Mixing Rules with Complex Dielectric Coefficients. *Subsurface sensing technologies and applications*, 1(4):393–415, 2000.

[55] Enis Tuncer, Yuriy V. Serdyuk, and Stanislaw M. Gubanski. Dielectric Mixtures: Electrical Properties and Modeling. *IEEE Transactions on Dielectrics and Electrical Insulation*, 9(5):809–828, 2002.

[56] Alessandro D'Aprano, Dorina I Donato, and Eugenio Caponetti. The Static Dielectric Constant of Solutions of Water in n-Alcohols at 15, 25, 35, and 45°C. *Journal of Solution Chemistry*, 8(2):135–146, 1979.

[57] Penrose S. Albright and Louis J. Gosting. Dielectric Constants of the Methanol-Water System from 5 to 55°. *Journal of the American Chemical Society*, 68(6):1061–1063, 1946.

[58] James L. Hawes and Robert L. Kay. Ionic Association of Potassium and Cesium Chlorides in Ethanol-Water Mixtures from Conductance Measurements at 25°. *The Journal of Physical Chemistry*, 69(7):2420–2431, 1965.

[59] Rocío Ponce Ortiz, Antonio Facchetti, and Tobin J. Marks. High-k Organic, Inorganic, and Hybrid Dielectrics for Low-Voltage Organic Field-Effect Transistors. *Chemical Reviews*, 110(1):205–239, 2010.

[60] Willi Volksen, Robert D. Miller, and Geraud Dubois. Low Dielectric Constant Materials. *Chemical Reviews*, 110(1):56–110, 2010.

[61] ASTM D150 - 18, *Standard Test Methods for AC Loss Characteristics and Permittivity (Dielectric Constant) of Solid Electrical Insulation*.

[62] Kyung Geun Bang, Jae Wook Kwon, Jae Won Lee, et al. Measurement of the degree of cure of glass fiber–epoxy composites using dielectrometry. *Journal of Materials Processing Technology*, 113(1-3):209–214, 2001.

[63] Magdalena Tarnacka, Olga Madejczyk, Mateusz Dulski, M. Wikarek, Sebastian Pawlus, Karolina Adrjanowicz, Kamil Kaminski, and Marian Paluch. Kinetics and Dynamics of the Curing System. High Pressure Studies. *Macromolecules*, 47(13):4288–4297, 2014.

[64] K. Nörtemann, Jannicke Hilland, and U. Kaatze. Dielectric Properties of Aqueous NaCl Solutions at Microwave Frequencies. *The Journal of Physical Chemistry A*, 101(37):6864–6869, 1997.

[65] Alexander V. Mamishev, Kishore Sundara-Rajan, Fumin Yang, Yanqing Du, and Markus Zahn. Interdigital Sensors and Transducers. *Proceedings of the IEEE*, 92(5):808–845, 2004.

[66] Chon-ung Kim, Guofeng Li, Jie Li, Hakchol Jong, Cholwu Ro, Yunho Song, Gilhung Pak, and Songil Im. Numerical analysis on effective electric field penetration depth for interdigital impedance sensor. *Journal of Physics: Conference Series*, 418(1):012020, 2013.

[67] Wouter Olthuis, Wim Streekstra, and Piet Bergveld. Theoretical and experimental determination of cell constants of planar-interdigitated electrolyte conductivity sensors. *Sensors and Actuators B: Chemical*, 24(1-3):252–256, 1995.

[68] Louis Royer. Recherches expérimentales sur l'épitaxie ou orientation mutuelle de cristaux d'espèces différentes. *Bulletin de Minéralogie*, 51(1):7–159, 1928.

[69] Harald Brune. *Surface and Interface Science*, chapter Epitaxial Growth of Thin Films, pages 421–492. John Wiley & Sons, Ltd, 2013. ISBN 978-3-527-68056-6.

[70] Ivan V Markov. *Crystal Growth for Beginners*. World Scientific Publishing Co. Pte. Ltd., 3rd edition, 2017. ISBN 9789813143425.

[71] Phuong Pham, Pratibha Goel, Samir Kumar, and Kavita Yadav. 21st *Century Surface Science*. IntechOpen, 2020. ISBN 978-1-78985-200-4.

[72] Justinas Palisaitis and Remigijus Vasiliauskas. Epitaxial growth of thin films. Physics of Advanced Materials Winter School, 2008.

[73] Frederick Charles Frank and Johannes Hendrik Van der Merwe. One-dimensional dislocations. II. Misfitting monolayers and oriented overgrowth. *Proceedings of the Royal Society of London. Series A. Mathematical and Physical Sciences*, 198(1053):216–225, 1949.

[74] Stuart R Batten, Neil R Champness, Xiao-Ming Chen, Javier Garcia-Martinez, Susumu Kitagawa, Lars Öhrström, Michael O'Keeffe, Myunghyun Paik Suh, and Jan Reedijk. Terminology of metal–organic frameworks and coordination polymers (IUPAC Recommendations 2013). *Pure and Applied Chemistry*, 85(8):1715–1724, 2013.

[75] Chiara Crivello, Semih Sevim, Octavio Graniel, Carlos Franco, Salvador Pané, Josep Puigmartí-Luis, and David Muñoz-Rojas. Advanced technologies for the fabrication of MOF thin films. *Mater. Horiz.*, 8:168–178, 2021.

[76] Jinxuan Liu and Christof Wöll. Surface-supported metal–organic framework thin films: fabrication methods, applications, and challenges. *Chem. Soc. Rev.*, 46:5730–5770, 2017.

[77] Alessandro Micero, Tawheed Hashem, Hartmut Gliemann, and Aline Léon. Hydrogen Separation Performance of UiO-66-NH2 Membranes Grown via Liquid-Phase Epitaxy Layer-by-Layer Deposition and One-Pot Synthesis. *Membranes*, 11(10), 2021.

[78] Roland A. Fischer and Christof Wöll. Layer-by-Layer Liquid-Phase Epitaxy of Crystalline Coordination Polymers at Surfaces. *Angewandte Chemie International Edition*, 48(34):6205–6208, 2009.

[79] Nour Nijem, Katrin Fürsich, Stephen T. Kelly, Caleb Swain, Stephen R. Leone, and Mary K. Gilles. HKUST-1 Thin Film Layer-by-Layer Liquid Phase Epitaxial Growth: Film Properties and Stability Dependence on Layer Number. *Crystal Growth & Design*, 15(6):2948–2957, 2015.

[80] Ritesh Haldar and Christof Wöll. Hierarchical assemblies of molecular frameworks—MOF-on-MOF epitaxial heterostructures. *Nano Research*, 14(2):355–368, 2021.

[81] A. Lisa Semrau and Roland A. Fischer. High-quality thin films of uio-66-nh2 by coordination modulated layer-by-layer liquid phase epitaxy. *Chemistry – A European Journal*, 27(33):8509–8516, 2021.

[82] Ritesh Haldar, Mariana Kozlowska, Michael Ganschow, Samrat Ghosh, Marius Jakoby, Hongye Chen, Farhad Ghalami, Weiwei Xie, Shahriar Heidrich, Yusuke Tsutsui, et al. Interplay of structural dynamics and electronic effects in an engineered assembly of pentacene in a metal–organic framework. *Chemical science*, 12(12):4477–4483, 2021.

[83] Gero Decher. Fuzzy nanoassemblies: toward layered polymeric multicomposites. *science*, 277(5330):1232–1237, 1997.

[84] Joseph J. Richardson, Jiwei Cui, Mattias Bjornmalm, Julia A. Braunger, Hirotaka Ejima, and Frank Caruso. Innovation in Layer-by-Layer Assembly. *Chemical reviews*, 116(23):14828–14867, 2016.

[85] Monica L. Ohnsorg, Christopher K. Beaudoin, and Mary E. Anderson. Fundamentals of MOF Thin Film Growth via Liquid-Phase Epitaxy: Investigating the Initiation of Deposition and the Influence of Temperature. *Langmuir*, 31(22):6114–6121, 2015.

[86] Qiang Li, Joshua Gies, Xiu-Jun Yu, Yu Gu, Andreas Terfort, and Martin Kind. Concentration-Dependent Seeding as a Strategy for Fabrication of Densely Packed Surface-Mounted Metal–Organic Frameworks (SURMOF) Layers. *Chemistry – A European Journal*, 26(23):5185–5189, 2020.

[87] Xiu-Jun Yu, Jin-Liang Zhuang, Julian Scherr, Tarek Abu-Husein, and Andreas Terfort. Minimization of Surface Energies and Ripening Outcompete Template Effects in the Surface Growth of Metal–Organic Frameworks. *Angewandte Chemie International Edition*, 55(29):8348–8352, 2016.

[88] Guusje Delen, Zoran Ristanović, Laurens D. B. Mandemaker, and Bert M. Weckhuysen. Mechanistic Insights into Growth of Surface-Mounted Metal-Organic Framework Films Resolved by Infrared (Nano-) Spectroscopy. *Chemistry – A European Journal*, 24(1):187–195, 2018.

[89] Luiz G. S. Albano, Tatiana P. Vello, Davi H. S. de Camargo, Ricardo M. L. da Silva, Antonio C. M. Padilha, Adalberto Fazzio, and Carlos C. B. Bufon. Ambipolar Resistive Switching in an Ultrathin Surface-Supported Metal–Organic Framework Vertical Heterojunction. *Nano Letters*, 20(2):1080–1088, 2020.

[90] Stephen S.-Y. Chui, Samuel M.-F. Lo, Jonathan P.H. Charmant, A. Guy Orpen, and Ian D. Williams. A chemically functionalizable nanoporous material $[Cu_3(TMA)_2(H_2O)_3]_n$. *Science*, 283(5405):1148–1150, 1999.

[91] Hong Ki Kim, Won Seok Yun, Min-Bum Kim, Jeung Yoon Kim, Youn-Sang Bae, JaeDong Lee, and Nak Cheon Jeong. A Chemical Route to Activation of Open Metal Sites in the Copper-Based Metal–Organic Framework Materials HKUST-1 and Cu-MOF-2. *Journal of the American Chemical Society*, 137(31):10009–10015, 2015.

[92] Kuen-Song Lin, Abhijit Krishna Adhikari, Chi-Nan Ku, Chao-Lung Chiang, and Hua Kuo. Synthesis and characterization of porous HKUST-1 metal organic frameworks for hydrogen storage. *International journal of hydrogen energy*, 37(18):13865–13871, 2012.

[93] Christopher H Hendon and Aron Walsh. Chemical principles underpinning the performance of the metal–organic framework HKUST-1. *Chemical Science*, 6(7):3674–3683, 2015.

[94] J. Raziel Álvarez, Elí Sánchez-González, Eric Pérez, Emilia Schneider-Revueltas, Ana Martínez, Adriana Tejeda-Cruz, Alejandro Islas-Jácome, Eduardo González-Zamora, and Ilich A. Ibarra. Structure stability of HKUST-1 towards water and ethanol and their effect on its CO_2 capture properties. *Dalton Trans.*, 46:9192–9200, 2017.

[95] Osama Shekhah, Hui Wang, Stefan Kowarik, Frank Schreiber, Michael Paulus, Metin Tolan, Christian Sternemann, Florian Evers, Denise Zacher, Roland A Fischer, et al. Step-by-step route for the synthesis of metal-organic frameworks. *Journal of the American Chemical Society*, 129(49):15118–15119, 2007.

[96] Osama Shekhah, Hui Wang, Denise Zacher, Roland A. Fischer, and Christof Wöll. Growth Mechanism of Metal–Organic Frameworks: Insights into the Nucleation by Employing a Step-by-Step Route. *Angewandte Chemie International Edition*, 48(27):5038–5041, 2009.

[97] Maryiam Shöâeè, Jonathan R. Agger, Michael W. Anderson, and Martin P. Attfield. Crystal form, defects and growth of the metal organic framework HKUST-1 revealed by atomic force microscopy. *CrystEngComm*, 10:646–648, 2008.

[98] Aleksandra Schejn, Lavinia Balan, Véronique Falk, Lionel Aranda, Ghouti Medjahdi, and Raphaël Schneider. Controlling ZIF-8 nano-and microcrystal formation and reactivity through zinc salt variations. *CrystEngComm*, 16(21):4493–4500, 2014.

[99] Xiao-Chun Huang, Yan-Yong Lin, Jie-Peng Zhang, and Xiao-Ming Chen. Ligand-Directed Strategy for Zeolite-Type Metal–Organic Frameworks: Zinc(II) Imidazolates with Unusual Zeolitic Topologies. *Angewandte Chemie International Edition*, 45(10):1557–1559, 2006.

[100] William Morris, Caitlin J. Stevens, R.E. Taylor, C. Dybowski, Omar M. Yaghi, and Miguel A. Garcia-Garibay. NMR and X-ray study revealing the rigidity of zeolitic imidazolate frameworks. *The Journal of Physical Chemistry C*, 116(24):13307–13312, 2012.

[101] Neel Rangnekar, Nitish Mittal, Bahman Elyassi, Jürgen Caro, and Michael Tsapatsis. Zeolite membranes–a review and comparison with MOFs. *Chemical Society Reviews*, 44(20):7128–7154, 2015.

[102] Alexander Knebel, Benjamin Geppert, Kai Volgmann, Daniil I. Kolokolov, Alexander G. Stepanov, Jens Twiefel, Paul Heitjans, Dirk Volkmer, and Jürgen Caro. Defibrillation of soft porous metal-organic frameworks with electric fields. *Science*, 358(6361):347–351, 2017.

[103] Helge Bux, Fangyi Liang, Yanshuo Li, Janosch Cravillon, Michael Wiebcke, and Jürgen Caro. Zeolitic Imidazolate Framework Membrane with Molecular Sieving Properties by Microwave-Assisted Solvothermal Synthesis. *Journal of the American Chemical Society*, 131(44):16000–16001, 2009.

[104] David Fairen-Jimenez, Stephen A. Moggach, Michael T. Wharmby, P. A. Wright, Simon Parsons, and Tina Düren. Opening the Gate: Framework Flexibility in ZIF-8 Explored by Experiments and Simulations. *Journal of the American Chemical Society*, 133(23):8900–8902, 2011.

[105] Yu-Ri Lee, Min-Seok Jang, Hye-Young Cho, Hee-Jin Kwon, Sangho Kim, and Wha-Seung Ahn. ZIF-8: A comparison of synthesis methods. *Chemical Engineering Journal*, 271:276–280, 2015.

[106] Chih-Wei Tsai and Ernie H.G. Langner. The effect of synthesis temperature on the particle size of nano-ZIF-8. *Microporous and Mesoporous Materials*, 221:8–13, 2016.

[107] Salvador Eslava, Liping Zhang, Santiago Esconjauregui, Junwei Yang, Kris Vanstreels, Mikhail R. Baklanov, and Eduardo Saiz. Metal-Organic Framework ZIF-8 Films As Low-κ Dielectrics in Microelectronics. *Chemistry of Materials*, 25(1):27–33, 2013.

[108] Huifeng Zhang, Man Zhao, and Y.S. Lin. Stability of zif-8 in water under ambient conditions. *Microporous and Mesoporous Materials*, 279:201–210, 2019.

[109] Huifeng Zhang, Defei Liu, Ying Yao, Baoquan Zhang, and Y.S. Lin. Stability of ZIF-8 membranes and crystalline powders in water at room temperature. *Journal of Membrane Science*, 485:103–111, 2015.

[110] Helge Bux, Christian Chmelik, Rajamani Krishna, and Jürgen Caro. Ethene/ethane separation by the MOF membrane ZIF-8: Molecular correlation of permeation, adsorption, diffusion. *Journal of Membrane Science*, 369(1):284–289, 2011.

[111] Isabel Cristina Pereira Margarit-Mattos. EIS and organic coatings performance: Revisiting some key points. *Electrochimica Acta*, 354:136725, 2020.

[112] Florian Mansfeld. Use of electrochemical impedance spectroscopy for the study of corrosion protection by polymer coatings. *Journal of applied electrochemistry*, 25(3):187–202, 1995.

[113] L Beaunier, I Epelboin, JC Lestrade, and Hisasi Takenouti. Etude electrochimique, et par microscopie electronique a balayage, du fer recouvert de peinture. *Surface Technology*, 4(3):237–254, 1976.

[114] Dora M. Brasher and A. H. Kingsbury. Electrical measurements in the study of immersed paint coatings on metal. I. Comparison between capacitance and gravimetric methods of estimating water-uptake. *Journal of Applied Chemistry*, 4(2):62–72, 1954.

[115] Carmen Pérez, A. Collazo, M. Izquierdo, Pedro Merino, and X. Ramon Nóvoa. Characterisation of the barrier properties of different paint systems: Part i. experimental set-up and ideal fickian diffusion. *Progress in Organic Coatings*, 36(1):102–108, 1999.

[116] Carmen Pérez, A. Collazo, M. Izquierdo, Pedro Merino, and X. Ramon Nóvoa. Characterisation of the barrier properties of different paint systems: Part II. Non-ideal diffusion and water uptake kinetics. *Progress in Organic Coatings*, 37(3):169–177, 1999.

[117] Sylvain Amand, Marco Musiani, Mark E. Orazem, Nadine Pébère, Bernard Tribollet, and Vincent Vivier. Constant-phase-element behavior caused by inhomogeneous water uptake in anti-corrosion coatings. *Electrochimica Acta*, 87:693–700, 2013.

[118] Bryan Hirschorn, Mark E. Orazem, Bernard Tribollet, Vincent Vivier, Isabelle Frateur, and Marco Musiani. Determination of effective capacitance and film thickness from constant-phase-element parameters. *Electrochimica acta*, 55(21):6218–6227, 2010.

[119] Mark E. Orazem, Isabelle Frateur, Bernard Tribollet, Vincent Vivier, Sabrina Marcelin, Nadine Pébère, Annette L Bunge, Erick A. White, Douglas P Riemer, and Marco Musiani. Dielectric properties of materials showing constant-phase-element (CPE) impedance response. *Journal of The Electrochemical Society*, 160(6):C215, 2013.

[120] Changqing Liu, Q. Bi, Adrian Leyland, and Allan Matthews. An electrochemical impedance spectroscopy study of the corrosion behaviour of PVD coated steels in 0.5 N NaCl aqueous solution: Part II.: EIS interpretation of corrosion behaviour. *Corrosion Science*, 45(6):1257–1273, 2003.

[121] John M. McIntyre and Ha Q. Pham. Electrochemical impedance spectroscopy; a tool for organic coatings optimizations. *Progress in Organic coatings*, 27(1-4):201–207, 1996.

[122] Viatcheslav Freger and Sarit Bason. Characterization of ion transport in thin films using electrochemical impedance spectroscopy: I. Principles and theory. *Journal of Membrane Science*, 302(1-2):1–9, 2007.

[123] Anthony Szymczyk and Patrick Fievet. Investigating transport properties of nanofiltration membranes by means of a steric, electric and dielectric exclusion model. *Journal of Membrane Science*, 252(1):77–88, 2005.

[124] Andriy Yaroshchuk, Merlin L. Bruening, and Emiliy Zholkovskiy. Modelling nanofiltration of electrolyte solutions. *Advances in Colloid and Interface Science*, 268:39–63, 2019.

[125] Jörg Titz, G. H. Wagner, H. Spähn, M. Ebert, Klaus Jüttner, and Wolfgang J. Lorenz. Characterization of Organic Coatings on Metal Substrates by Electrochemical Impedance Spectroscopy. *Corrosion*, 46(3):221–229, 03 1990.

[126] Mark C. Zaretsky, Patrick Li, and James R. Melcher. Estimation of thickness, complex bulk permittivity and surface conductivity using interdigital dielectrometry. *IEEE Transactions on Electrical Insulation*, 24(6):1159–1166, 1989.

[127] Mark C. Zaretsky, Lama Mouayad, and James R. Melcher. Continuum properties from interdigital electrode dielectrometry. *IEEE Transactions on Electrical Insulation*, 23(6):897–917, 1988.

[128] Markus Zahn and Shi-Woo Rhee. Electric field effects on the equilibrium and small signal stabilization of electrofluidized beds. *IEEE Transactions on Industry Applications*, (1):137–147, 1984.

[129] Rui Igreja and Carlos J. Dias. Analytical evaluation of the interdigital electrodes capacitance for a multi-layered structure. *Sensors and Actuators A: Physical*, 112(2):291–301, 2004.

[130] Benedikt Sapotta, Matthias Schwotzer, Christof Wöll, and Matthias Franzreb. On the Integration of Dielectrometry into Electrochemical Impedance Spectroscopy to Obtain Characteristic Properties of a Dielectric Thin Film. *Electroanalysis*, 34(3):512–522, 2022.

[131] Rui Igreja and Carlos J. Dias. Extension to the analytical model of the interdigital electrodes capacitance for a multi-layered structure. *Sensors and Actuators A: Physical*, 172(2):392–399, 2011.

[132] Wilson Tato and Dieter Landolt. Electrochemical determination of the porosity of single and duplex PVD coatings of titanium and titanium nitride on brass. *Journal of the Electrochemical Society*, 145(12):4173, 1998.

[133] Eugenii Katz, Lital Alfonta, and Itamar Willner. Chronopotentiometry and Faradaic impedance spectroscopy as methods for signal transduction in immunosensors. *Sensors and Actuators B: Chemical*, 76(1):134–141, 2001.

[134] Rashida Akter, Bongjin Jeong, Yong-Mi Lee, Jong-Soon Choi, and Md. Aminur Rahman. Femtomolar detection of cardiac troponin I using a novel label-free and reagent-free dendrimer enhanced impedimetric immunosensor. *Biosensors and Bioelectronics*, 91:637–643, 2017.

[135] Ronghui Wang, Yun Wang, Kentu Lassiter, Yanbin Li, Billy Hargis, Steve Tung, Luc Berghman, and Walter Bottje. Interdigitated array microelectrode based impedance immunosensor for detection of avian influenza virus H5N1. *Talanta*, 79(2):159–164, 2009.

[136] Liju Yang, Yanbin Li, and Gisela F. Erf. Interdigitated Array Microelectrode-Based Electrochemical Impedance Immunosensor for Detection of Escherichia coli O157:H7. *Analytical Chemistry*, 76(4):1107–1113, 2004.

[137] Jun Huang. Diffusion impedance of electroactive materials, electrolytic solutions and porous electrodes: Warburg impedance and beyond. *Electrochimica Acta*, 281:170–188, 2018.

[138] Emil Warburg. Ueber die Polarisationscapacität des Platins. *Annalen der Physik*, 311(9):125–135, 1901.

[139] Juan Bisquert, Germà Garcia-Belmonte, Paulo Bueno, Elson Longo, and Louis O.S. Bulhões. Impedance of constant phase element (CPE)-blocked diffusion in film electrodes. *Journal of Electroanalytical Chemistry*, 452(2):229–234, 1998.

[140] Donald R. Franceschetti, J. Ross Macdonald, and Richard P. Buck. Interpretation of Finite-Length-Warburg-Type Impedances in Supported and Unsupported Electrochemical Cells with Kinetically Reversible Electrodes. *Journal of the Electrochemical Society*, 138(5):1368, 1991.

[141] Giovanni Barbero. Theoretical interpretation of Warburg's impedance in unsupported electrolytic cells. *Physical Chemistry Chemical Physics*, 19(48):32575–32579, 2017.

[142] Viatcheslav Freger. Diffusion impedance and equivalent circuit of a multilayer film. *Electrochemistry communications*, 7(9):957–961, 2005.

[143] Juan Bisquert and Albert Compte. Theory of the electrochemical impedance of anomalous diffusion. *Journal of Electroanalytical Chemistry*, 499(1):112–120, 2001.

[144] https://github.com/spyder ide/spyder/graphs/contributors.

[145] Frederik Kotz, Patrick Risch, Dorothea Helmer, and Bastian E. Rapp. Highly Fluorinated Methacrylates for Optical 3D Printing of Microfluidic Devices. *Micromachines*, 9(3), 2018.

[146] Peter Van Gerwen, Wim Laureyn, Wim Laureys, Guido Huyberechts, Maaike Op De Beeck, Kris Baert, Jan Suls, Willy Sansen, P. Jacobs, Lou Hermans, and Robert Mertens. Nanoscaled interdigitated electrode arrays for biochemical sensors. *Sensors and Actuators B: Chemical*, 49(1):73–80, 1998.

[147] Stefan Partel, Stephan Kasemann, Volha Matylitskaya, Christine Thanner, Can Dincer, and Gerald Urban. A simple fabrication process for disposable interdigitated electrode arrays with nanogaps for lab-on-a-chip applications. *Microelectronic Engineering*, 173:27–32, 2017.

[148] Ortwin Göttmann, Udo Kaatze, and P Petong. Coaxial to circular waveguide transition as high-precision easy-to-handle measuring cell for the broad band dielectric spectrometry of liquids. *Measurement Science and Technology*, 7(4):525, 1996.

[149] L. Grant Hector and Donald L. Woernley. The Dielectric Constants of Eight Gases. *Phys. Rev.*, 69:101–105, Feb 1946.

[150] Maurice Cox, Peter Harris, and Bernd R.-L. Siebert. Evaluation of measurement uncertainty based on the propagation of distributions using Monte Carlo simulation. *Measurement Techniques*, 46(9):824–833, 2003.

[151] Zheng Wang, Katia Rodewald, Raghavender Medishetty, Bernhard Rieger, and Roland A. Fischer. Control of Water Content for Enhancing the Quality of Copper Paddle-Wheel-Based Metal–Organic Framework Thin Films Grown by Layer-by-Layer Liquid-Phase Epitaxy. *Crystal Growth & Design*, 18(12):7451–7459, 2018.

[152] Kai Müller, Jasleen Singh Malhi, Jonas Wohlgemuth, Roland A Fischer, Christof Wöll, Hartmut Gliemann, and Lars Heinke. Water as a modulator in the synthesis of surface-mounted metal–organic framework films of type HKUST-1. *Dalton Transactions*, 47(46):16474–16479, 2018.

[153] Carmen Munuera, Osama Shekhah, Hui Wang, Christof Wöll, and Carmen Ocal. The controlled growth of oriented metal–organic frameworks on functionalized surfaces as followed by scanning force microscopy. *Phys. Chem. Chem. Phys.*, 10:7257–7261, 2008.

[154] Osama Shekhah, Raja Swaidan, Youssef Belmabkhout, Marike Du Plessis, Tia Jacobs, Leonard J. Barbour, Ingo Pinnau, and Mohamed Eddaoudi. The liquid phase epitaxy approach for the successful construction of ultra-thin and defect-free ZIF-8 membranes: pure and mixed gas transport study. *Chemical Communications*, 50(17):2089–2092, 2014.

[155] Elvia P. Valadez Sánchez, Hartmut Gliemann, Katja Haas-Santo, Christof Wöll, and Roland Dittmeyer. ZIF-8 SURMOF Membranes Synthesized by Au-Assisted Liquid Phase Epitaxy for Application in Gas Separation. *Chemie Ingenieur Technik*, 88(11):1798–1805, 2016.

[156] Hyuk Taek Kwon and Hae-Kwon Jeong. In Situ Synthesis of Thin Zeolitic–Imidazolate Framework ZIF-8 Membranes Exhibiting Exceptionally High Propylene/Propane Separation. *Journal of the American Chemical Society*, 135(29):10763–10768, 2013.

[157] Guang Lu, Omar K Farha, Weina Zhang, Fengwei Huo, and Joseph T Hupp. Engineering ZIF-8 Thin Films for Hybrid MOF-Based Devices. *Advanced Materials*, 24(29):3970–3974, 2012.

[158] Shunsuke Tanaka, Tomoko Shimada, Kosuke Fujita, Yoshikazu Miyake, Koji Kida, Katsunori Yogo, Joeri F.M. Denayer, Miki Sugita, and Takahiko Takewaki. Seeding-free aqueous synthesis of zeolitic imidazolate framework-8 membranes: How to trigger preferential heterogeneous nucleation and membrane growth in aqueous rapid reaction solution. *Journal of Membrane Science*, 472:29–38, 2014.

[159] Koji Kida, Kosuke Fujita, Tomoko Shimada, Shunsuke Tanaka, and Yoshikazu Miyake. Layer-by-layer aqueous rapid synthesis of ZIF-8 films on a reactive surface. *Dalton Transactions*, 42(31):11128–11135, 2013.

[160] Lothar Spieß. Moderne Röntgenbeugung : Röntgendiffraktometrie für Materialwissenschaftler, Physiker und Chemiker, Springer Spektrum, 3rd edition, 2019. ISBN 978-3-8348-8232-5.

[161] R. P. Frankenthal and D. J. Siconolfi. The Anodic Corrosion of Gold in Concentrated Chloride Solutions. *Journal of The Electrochemical Society*, 129(6):1192–1196, 1982.

[162] Piotr Zoltowski. On the electrical capacitance of interfaces exhibiting constant phase element behaviour. *Journal of Electroanalytical Chemistry*, 443(1):149–154, 1998.

[163] Lee M. Fischer, Maria Tenje, Arto R. Heiskanen, Noriyuki Masuda, Jaime Castillo, Anders Bentien, Jenny Émneus, Mogens H. Jakobsen, and Anja Boisen. Gold cleaning methods for electrochemical detection applications. *Microelectronic Engineering*, 86(4):1282–1285, 2009. MNE '08.

[164] TM Aminabhavi, SK Raikar, MI Aralaguppi, RS Khinnavar, SS Joshi, and RH Balundgi. Dielectric studies of liquids and liquid mixtures. *Indian journal of technology*, 31:739–739, 1993.

[165] Benedikt Sapotta, Matthias Schwotzer, and Matthias Franzreb. Practical insights into the impedance response of interdigitated electrodes: Extraction of relative static permittivity and electrolytic conductivity. *Electroanalysis, accepted*.

[166] Arthur Dizon and Mark E. Orazem. On the impedance response of interdigitated electrodes. *Electrochimica Acta*, 327:135000, 2019.

[167] Arthur Dizon and Mark E. Orazem. On experimental determination of cell constants for interdigitated electrodes. *Electrochimica Acta*, 337:135732, 2020.

[168] Arthur Dizon, Chen You, and Mark E. Orazem. The influence of current and potential distribution on the measurement of dielectric permittivity. *Electrochimica Acta*, 391:138957, 2021.

[169] Sunil Rana, Robin H. Page, and Calum J McNeil. Impedance spectra analysis to characterize interdigitated electrodes as electrochemical sensors. *Electrochimica Acta*, 56(24):8559–8563, 2011.

[170] Geoffrey M. Geise, Donald R. Paul, and Benny D. Freeman. Fundamental water and salt transport properties of polymeric materials. *Progress in Polymer Science*, 39(1):1–42, 2014.

[171] Yizhak Marcus and Glenn Hefter. Ion pairing. *Chemical Reviews*, 106(11):4585–4621, 2006.

[172] Rubina H. Shreiner. Stability of standard electrolytic conductivity solutions in glass containers. *Journal of research of the National Institute of Standards and Technology*, 107(5):393, 2002.

[173] Herbert Bristol Dwight. Skin Effect and Proximity Effect in Tubular Conductors. *Transactions of the American Institute of Electrical Engineers*, XLI:189–198, 1922.

[174] Ryutaro Tsuchida, Shoichiro Yamada, and Hiroji Nakamura. Structure of Cupric Salts of Mono-carboxylic Fatty Acids. *Nature*, 178(4543):1192–1193, 1956.

[175] Jürgen Caro. Are MOF membranes better in gas separation than those made of zeolites? *Current Opinion in Chemical Engineering*, 1(1):77–83, 2011. Open issue 1/1.

[176] Arun S. Babal, Abhijeet K. Chaudhari, Hamish H.-M. Yeung, and Jin-Chong Tan. Guest-Tunable Dielectric Sensing Using a Single Crystal of HKUST-1. *Advanced Materials Interfaces*, 7(14):2000408, 2020.

[177] Richard B. M. Schasfoort. *Handbook of Surface Plasmon Resonance*. The Royal Society of Chemistry, 2nd edition, 2017. ISBN 978-1-78262-730-2.

[178] Vitalie Stavila, Joanne Volponi, Aaron M. Katzenmeyer, Matthew C. Dixon, and Mark D. Allendorf. Kinetics and mechanism of metal–organic framework thin film growth: systematic investigation of HKUST-1 deposition on QCM electrodes. *Chem. Sci.*, 3:1531–1540, 2012.

[179] Günter Sauerbrey. Verwendung von Schwingquarzen zur Wägung dünner Schichten und zur Mikrowägung. *Zeitschrift für physik*, 155(2):206–222, 1959.

[180] Shin-ichi Amma, Seong H. Kim, and Carlo G. Pantano. Analysis of Water and Hydroxyl Species in Soda Lime Glass Surfaces Using Attenuated Total Reflection (ATR)-IR Spectroscopy. *Journal of the American Ceramic Society*, 99(1):128–134, 2016.

[181] Conor H. Sharp, Brandon C. Bukowski, Hongyu Li, Eric M. Johnson, Stefan Ilic, Amanda J. Morris, Dilip Gersappe, Randall Q. Snurr, and John R. Morris. Nanoconfinement and mass transport in metal–organic frameworks. *Chem. Soc. Rev.*, 50:11530–11558, 2021.

[182] William J. Koros, Yi H. Ma, and Takeo Shimidzu. Terminology for membranes and membrane processes (IUPAC Recommendations 1996). *Pure and Applied Chemistry*, 68(7):1479–1489, 1996.

[183] Yizhak Marcus. Ionic Radii in Aqueous Solutions. *Chemical Reviews*, 88(8):1475–1498, 1988.

[184] Andrij E. Yaroshchuk. Dielectric exclusion of ions from membranes. *Advances in Colloid and Interface Science*, 85(2):193–230, 2000.

[185] Max Born. Volumen und hydratationswärme der ionen. *Zeitschrift für Physik*, 1(1):45–48, 1920.

[186] Yizhak Marcus. Evaluation of the Static Permittivity of Aqueous Electrolytes. *Journal of Solution Chemistry*, 42(12):2354–2363, 2013.

[187] Nak Cheon Jeong, Bappaditya Samanta, Chang Yeon Lee, Omar K. Farha, and Joseph T. Hupp. Coordination-Chemistry Control of Proton Conductivity in the Iconic Metal–Organic Framework Material HKUST-1. *Journal of the American Chemical Society*, 134(1):51–54, 2012.

[188] Simona Sorbara, Nicola Casati, Valentina Colombo, Filippo Bossola, and Piero Macchi. The Dielectric Behavior of Protected HKUST-1. *Chemistry*, 4(2):576–591, 2022.

[189] Dae-Woon Lim and Hiroshi Kitagawa. Proton Transport in Metal–Organic Frameworks. *Chemical Reviews*, 120(16):8416–8467, 2020.

[190] Mikhail Krishtab, Ivo Stassen, Timothée Stassin, Alexander John Cruz, Oguzhan Orkut Okudur, Silvia Armini, Chris Wilson, Stefan De Gendt, and Rob Ameloot. Vapor-deposited zeolitic imidazolate frameworks as gap-filling ultra-low-k dielectrics. *Nature communications*, 10(1):1–9, 2019.

[191] Yichang Pan, Wei Liu, Yingjie Zhao, Chongqing Wang, and Zhiping Lai. Improved ZIF-8 membrane: Effect of activation procedure and determination of diffusivities of light hydrocarbons. *Journal of Membrane Science*, 493:88–96, 2015.

[192] Osama Shekhah and Mohamed Eddaoudi. The liquid phase epitaxy method for the construction of oriented ZIF-8 thin films with controlled growth on functionalized surfaces. *Chemical Communications*, 49(86):10079–10081, 2013.

[193] Rubina H. Shreiner and Kenneth W. Pratt. Standard reference materials: primary standards and standard reference materials for electrolytic conductivity. *NIST special publication*, 260:142, 2004.

A. Research Data

The research data supporting this thesis has been disclosed in the online repository *KITOpen-Data* and is accessible via

https://doi.org/10.5445/IR/1000150710

B. Computation of Reference Values for the Static Relative Permittivity and Electrolytic Conductivity at the Measurement Temperature

The Monte Carlo method was used to compute reference values for the relative static permittivity ε_r and electrolytic conductivity κ_M together with the associated uncertainty (coverage factor = 2) at the measurement temperature $\mathsf{T} = (21.0 \pm 0.5)$ °C $= (\mathsf{T}_\mu \pm \gamma_{T2})$. Let Γ denote either ε_r or κ_M. With $\Gamma(25°C)$ and $\Gamma(20°C)$ reported in literature sources, $\Gamma(T)$ could be obtained through linear interpolation by computing the temperature slope t_S via

$$t_S = \frac{\Gamma(25°C) - \Gamma(20°C)}{25°C - 20°C}. \tag{8.1}$$

To obtain an expanded uncertainty of $\Gamma(T)$, the standard uncertainty γ_S in the literature source, the temperature uncertainty γ_{T1} in the literature source as well as the temperature uncertainty γ_{T2} of this measurement was accounted for. The values and reference sources used for $\Gamma(25°C)$ and $\Gamma(20°C)$ are provided in table B.1, the values and reference sources for γ_S, γ_{T1} and γ_{T2} are comprehensively listed in table B.2. Let $rnd(\mu, \sigma)$ denote the random sampling from a normal distribution with the expectation μ and the standard deviation σ. The randomly sampled temperature T_{rnd} can be calculated as

$$T_{rnd} = rnd(T_\mu, \gamma_{T2}/2) + rnd(0, \gamma_{T1}/2). \tag{8.2}$$

Subsequently, a randomly sampled reference value Γ_{rnd} at T_{rnd} can be calculated by making use of t_S

$$\Gamma_{rnd} = \Gamma(20°C) + t_S \cdot (T_{rnd} - 20°C) + rnd(0, \gamma_S/2) \tag{8.3}$$

The number of Monte Carlo trials was set to 1 000 000. An estimate for $\Gamma(T)$ was obtained via averaging of the randomly generated Γ_{rnd} data set. Likewise, the expanded uncertainty associated with $\Gamma(T)$ was estimated from the square root of the variance of the Γ_{rnd} dataset.

Table B.1. Input parameters used to compute the reference values for both CRMs and DRMs at the measurement temperature.

no.	sample medium	Γ	$\Gamma(20°C)$	$\Gamma(25°C)$
1	nitrogen	ε_r [-]	1.00	1.00
2	1-butanol	ε_r [-]	17.53 [44]	18.19 [44]
3	ethanol	ε_r [-]	24.43 [44]	25.16 [44]
4	water	ε_r [-]	78.55 [44]	80.29 [44]
5	54 mol-% ethanol in water (mixture)	ε_r [-]	35.4 [50]	36.5 [50]
6	22 mol-% ethanol in water (mixture)	ε_r [-]	55.2 [50]	54.4 [50]
7	CRM $\kappa_M(25°) = 1410$ µS/cm	κ_M [µS/cm]	1410 [39]	1270 [193]
8	CRM $\kappa_M(25°) = 25.0$ µS/cm	κ_M [µS/cm]	25.00 [a]	22.38 [a]

[a] certificate of analysis, disclosed in research data

Table B.2. Input uncertainties (stated at a coverage factor $k=2$) used to compute the reference values for both CRMs and DRMs at the measurement temperature.

no.	sample medium	γ_S	γ_{T1}	γ_{T2}
1	nitrogen	-	-	-
2	1-butanol	0.04 [44]	0.05 °C [44]	0.50 °C
3	ethanol	0.04 [44]	0.05 °C [44]	0.50 °C
4	water	0.20 [44]	0.05 °C [44]	0.50 °C
5	54 mol-% ethanol in water (mixture)	0.70 [50]	0.05 °C [50]	0.50 °C
6	22 mol-% ethanol in water (mixture)	1.1 [50]	0.05 °C [50]	0.50 °C
7	CRM $\kappa_M(25°) = 1410$ µS/cm	5 µS/cm [a]	0.05 °C [a]	0.50 °C
8	CRM $\kappa_M(25°) = 25.0$ µS/cm	0.17 µS/cm [b]	0.05 °C [b]	0.50 °C

[a] conservative estimate, [b] certificate of analysis, disclosed in research data

C. X-ray Diffractogram of HKUST-1 SURMOF coatings

The X-ray diffractograms of two HKUST-1 SURMOF samples prepared within the scope of this work together with the simulated powder pattern are shown in Fig C.1. The powder pattern was generated using the CIF deposited by the authors of [90]. The peak positions of the HKUST-1 SURMOF samples corresponds well with the simulated pattern which validates the presence of the HKUST-1 crystalline phase. The HKUST-1 SURMOF on the IDE structure covered an area of only roughly 12.5 mm^2 which is why the diffraction pattern could only be recorded at an unfavorable signal-to-noise ratio with the measurement hardware available. Importantly, the diffraction data of the HKUST-1 SURMOF on the IDE structure derives from both the HKUST-1 phase which developed on the MHDA-functionalized gold surface as well as on the glass substrate in between the electrode fingers which are likely to impart two different preferential crystallographic orientations. On the whole, the diffraction data collected with the
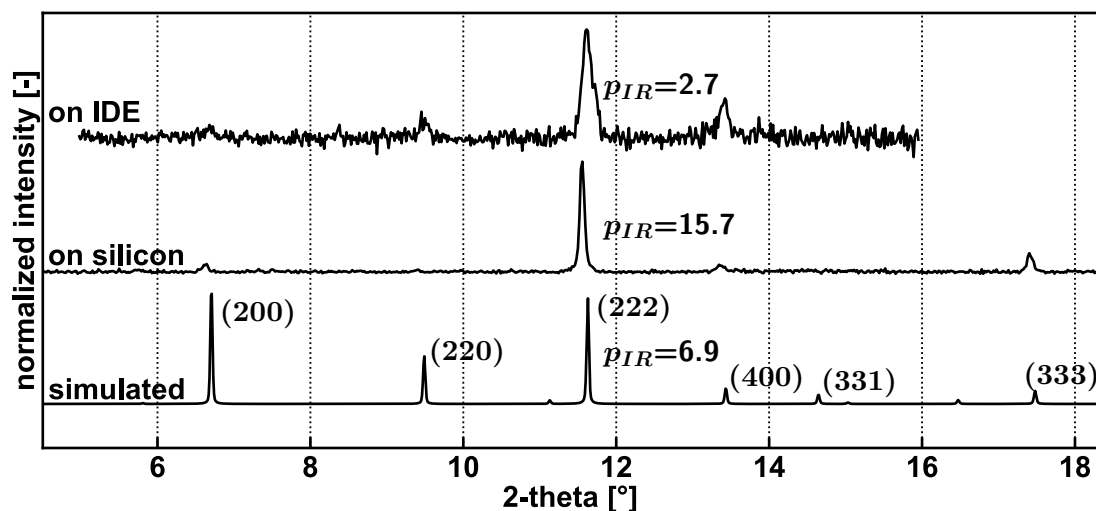
Figure C.1. X-ray diffraction pattern of a 205 cycle HKUST-1 SURMOF grown on an MHDA functionalized interdigitated electrode structure and a 40 cycle HKUST-1 SURMOF grown on a UV-ozone activated silicon surface as well as the simulated powder pattern. The reproducibility of the individual peak positions clearly indicate the presence of the HKUST-1 crystalline phase at the sample surfaces. When choosing the peak intensity ratio p_{IR} of the (222) to (400) reflex as evaluation criterion, the data would suggest a preferential [111] orientation of the HKUST-1 SURMOF covering the silicon surface and a preferential [100] orientation of the HKUST-1 SURMOF covering the interdigitated area.

coated IDE sample however indicate a minor preference in the (100) when using the peak intensity ratio of the (222) and (400) reflexes as evaluation criterion.

For comparative reasons, the X-ray diffraction data of a separate HKUST-1 SURMOF sample synthesized for a total of 40 growth cycles on a silicon surface has been added to Fig C.1. Owing to a coated surface area of a little more than 100 mm^2 the diffraction pattern could be recorded at a more favorable signal-to-noise ratio than for the HKUST-1 coating on the IDE chip. The peak intensity ratio of the (222) and (400) reflexes would indicate a general tendency towards preferential crystallographic orientation into the [111] direction. The corresponding topview electron micrographs of the sample are provided in Fig C.2. Even after the completion of 40 growth cycles, the HKUST-1 SURMOF did not reach full coverage of the host silicon surface. The sample is rather comprised of well distinguishable individual HKUST-1 nuclei of roughly equal size which have not yet intergrown into a single, compact layer (Volmer-Weber growth model).

D. Coating Resistance and Conductivity of the HKUST-1 SURMOF during the Linker Solution Exposure Step

In contrast to the impedance data recorded during the exposure step with the metal precursor solution, the linker data permitted a reliable quantification of the coating resistance $R_{C,LS}$. The best-fit estimates of $R_{C,LS}$ for both HKUST-1 SURMOF samples discussed in this work are plotted in Fig D.3 as a function of the completed growth cycles. As the coating thickness d_C is available from the combined evaluation of the coating and geometric capacitance, $R_{C,LS}$ may
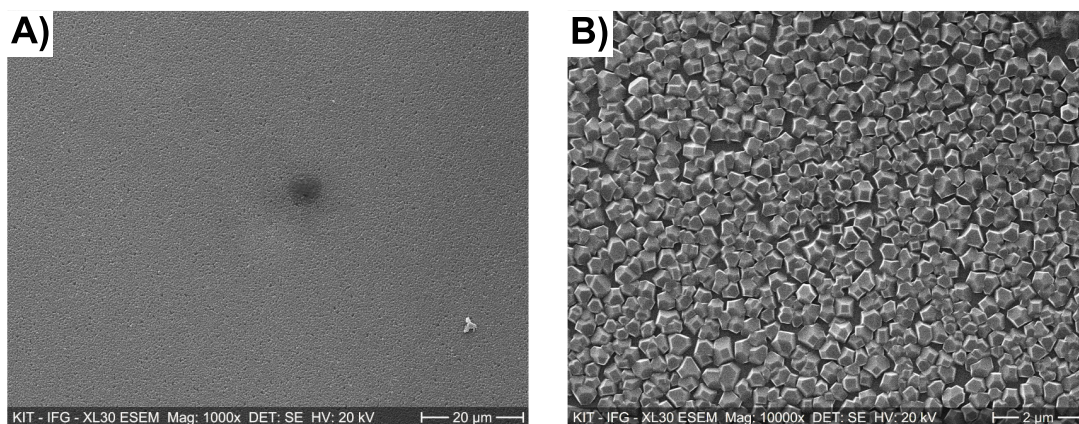
Figure C.2. Scanning electron micrographs of an HKUST-1 SURMOF sample after the completion of 40 growth cycles on a UV-ozone activated silicon surface at A) 1000- and B) 10000-fold magnification. The sample was slightly damaged during the focussing process of the electron beam resulting into the dark spot in A). The sample has not yet reached full surface coverage. The individual HKUST-1 nuclei with their square-shaped and truncated triangular facets can be easily identified which compare well to the usual HKUST-1 morphology shown in Fig 2.16.

be converted into an electrolytic conductivity of the coating during the linker step $\kappa_{C,LS}$ via equation 4.4. A steady decrease in $\kappa_{C,LS}$ can be observed as the HKUST-1 coating thickness increases which is consistent with the data discussed in chapter 6.2.4. Accordingly, the slight mismatch between $\kappa_{C,LS}$ in Fig D.3 A) and B) during the same growth cycle is likely to originate from the slightly increased film thickness and growth rate of the HKUST-1 sample in B).
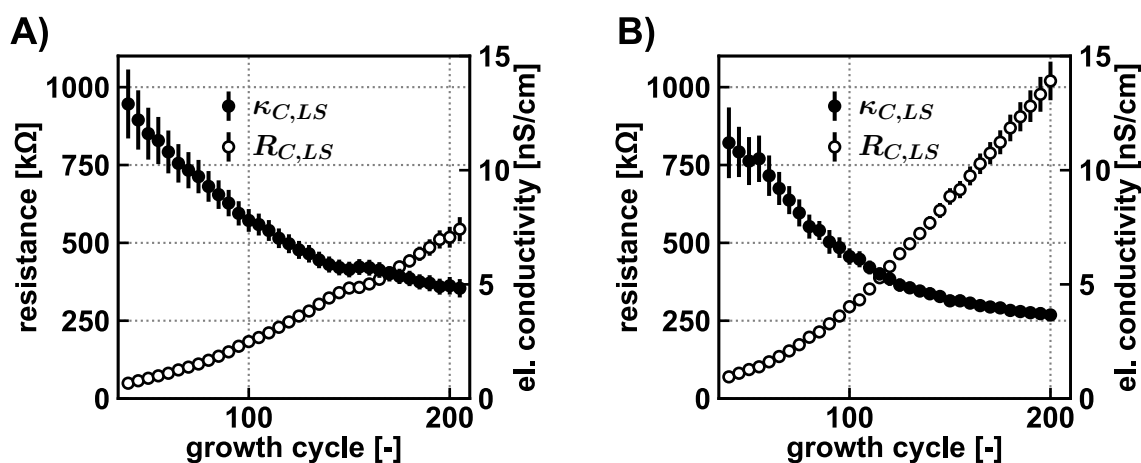

Figure D.3. Best-fit estimates of the coating resistance during the linker step $R_{C,LS}$ as a function of the growth cycle for A) the HKUST-1 SURMOF sample discussed in chapter 6.1 and B) the HKUST-1 SURMOF sample discussed in chapter 6.2. The electrolytic coating conductivity during the exposure step to the linker precursor solution $\kappa_{C,LS}$ computed via equation 4.4 is shown as well.

E. Single Frequency Impedance Analysis of first HKUST-1 Growth Cycle

Reliable evaluation of an impedance spectrum requires the system under investigation to remain quasi-stable and not to change significantly during the time-frame the spectrum is recorded. Consequently, impedance spectroscopy as a measurement technique is incapable of providing tangible information on transient processes taking place on a timescale of a few minutes and below. Still, it is possible to keep track of transient processes by impedimetric techniques when recording the AC current response at a constant frequency rather than to rely on a spectrum of frequencies. Single frequency data can however only be reasonably modelled in case the system under investigation is already well understood. For mathematical reasons, the impedance data should be collected at a frequency which is only influenced by a maximum of two variable charge transport processes (see chapter 2.1 for more information).

During the experiment discussed in chapter 6.2, a variety of single frequency data was collected which is made available in the research data for further evaluation by interested readers. The flow rate of the precursor and testing solutions ranged between 1 and 2 µL/s with the swept volume between the flow selection valve and the sensing chamber guiding the flow across the interdigitated area at about 40 µL.

To provide initial insights into the data, the single frequency data of the first HKUST-1 growth cycle recorded at 100 kHz is displayed in Fig E.4 A). To facilitate the understanding, the individual time intervals are highlighted during which the respective rinse, metal and linker solution was supplied to the flow cell. The uptake of the single frequency data was interrupted during metal and linker solution exposure to record the complete impedance spectra. The influence of interfacial contributions to the impedance response in A) can be assumed negligible given the f_{CR} values of the precursor solutions disclosed in table 6.2 range below the single frequency of 100 kHz. When compensating the parasitic influence of R_P, L_P and C_P, the impedance data can be modelled as a parallel connection of R_E and C_{Geo} providing access to $\varepsilon_{r,M}$ and κ_M shown in Fig E.4 B) through conversion with K_{Cell}. The transient data clearly indicate a rapid exchange of the liquid medium in the sensing chamber upon movement of the flow selection valve. As discussed in the main text, $\varepsilon_{r,M}$ is related to the solvent composition and converges to 24.9 for the purely ethanolic metal solution and to 30.3 for the ethanolic rinse and linker solutions at 25 mol-% water content. On the other hand, κ_M is related to the presence of ionic species which is why a significantly larger κ_M is detected for the precursor solutions than for the rinse solution. Judging from the κ_M data during the initial 180 seconds of the experiment, the rinse solution appears to feature a native conductivity of roughly 30 - 35 nS/cm.

Particularly surprising are the detected conductivity peaks of up to 2000 nS/cm when exchanging the metal precursor with the rinse solution or vice versa. A plausible explanation could be that the sudden rise in $\varepsilon_{r,M}$ might entail an increased amount of dissociated copper and acetate ions from the metal solution. Additionally, in comparison to the final rinse step following the exposure to the linker solution, the removal rate of the ionic species from the sensing chamber as

indicated by κ_M appears to be significantly retarded during the rinsing step following the metal exposure. With regard to the current knowledge on the growth mechanism of the HKUST-1 SURMOF [88], this observation might stem from the delayed removal of loosely physisorbed CuAc species adsorbed to the fluidic walls of the setup as well as the interdigitated area of the sensor chip. Another interesting feature of the rinse step following metal exposure is the apparent increase of $\varepsilon_{r,M}$ up to 30.4 thereby slightly exceeding the actual $\varepsilon_{r,M}$ of the rinse solution by 0.1. Accordingly, the single frequency analysis of the coating process provides unique opportunities to establish further insights into the coating process which have yet to be realized.
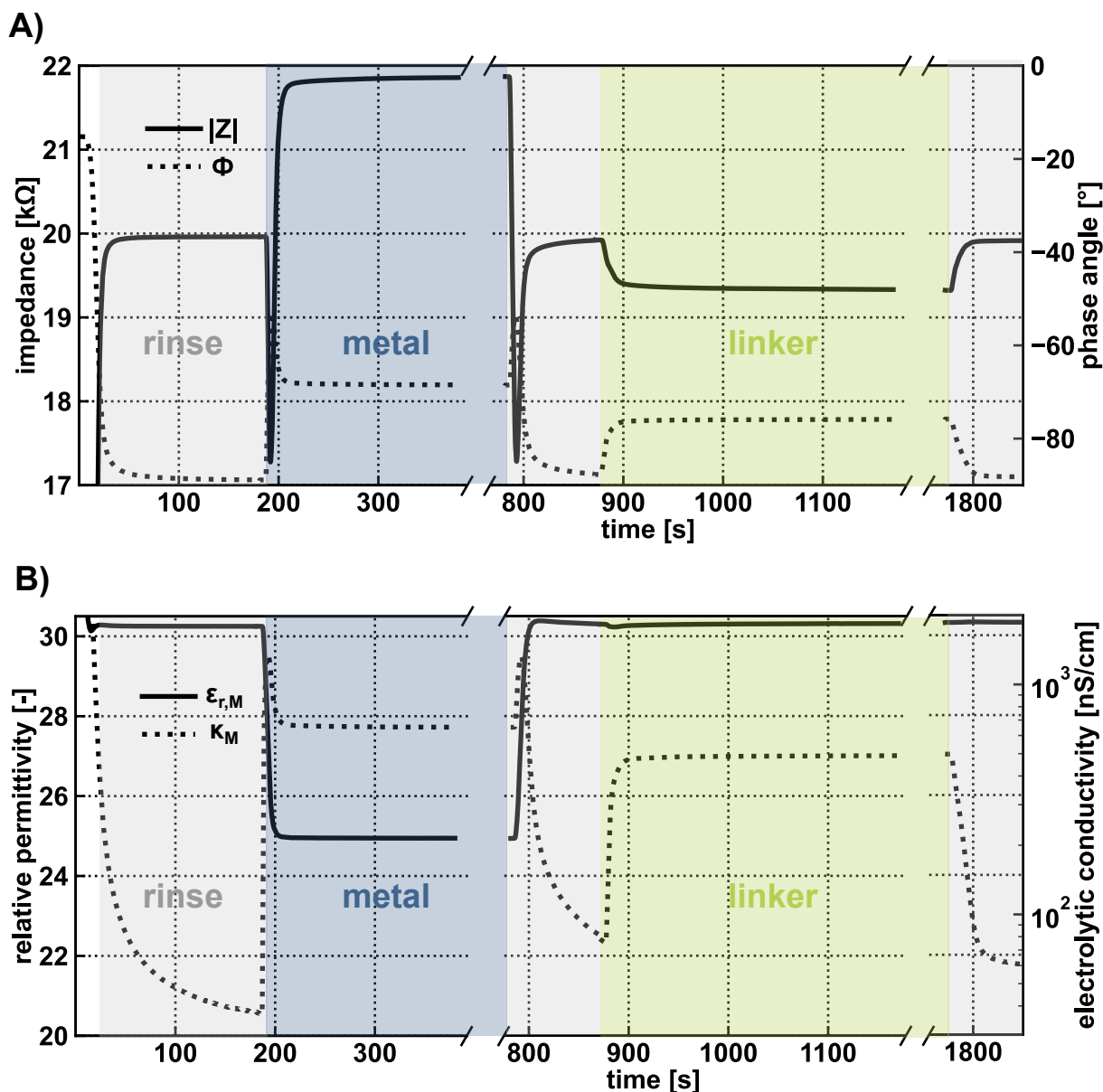

Figure E.4. Single frequency data at 100 kHz collected during the first growth cycle of the HKUST-1 sample discussed in chapter 6.2. The raw data is provided in A) which can be converted into the relative permittivity $\varepsilon_{r,M}$ and electrolytic conductivity κ_M of the liquid medium in contact with the interdigitated structure shown in B) following compensation of parasitic effects and assuming negligible interfacial impedance contributions. To facilitate the understanding, the individual time intervals are highlighted during which the respective rinse, metal and linker solution were supplied to the flow cell housing the interdigitated electrode chip.

Publications

Peer Reviewed Papers

Benedikt Sapotta, Jongmin Q. Kim, Norbert Willenbacher and Siyoung Q. Choi. Deformation of soft particles with controlled elasticity by liquid–liquid interfacial tension. *Soft Matter*, 15(23):4609-4613, 2019.

Shin Young Kim, **Benedikt Sapotta**, Gilsoo Jang, Yong-Heack Kang and Hyun-Goo Kim. Prefeasibility Study of Photovoltaic Power Potential Based on a Skew-Normal Distribution. *Energies*, 13(3):676, 2020.

Alexei Nefedov, Ritesh Haldar, Zhiyun Xu, Hannes Kühner, Dennis Hofmann, David Goll, **Benedikt Sapotta**, Stefan Hecht, Marjan Krstić, Carsten Rockstuhl, Wolfgang Wenzel, Stefan Bräse, Petra Tegeder, Egbert Zojer and Christof Wöll. Avoiding the Center-Symmetry Trap: Programmed Assembly of Dipolar Precursors into Porous, Crystalline Molecular Thin Films. *Advanced Materials*, 33(35):2103287, 2021.

Benedikt Sapotta, Matthias Schwotzer, Christof Wöll and Matthias Franzreb. On the Integration of Dielectrometry into Electrochemical Impedance Spectroscopy to obtain Characteristic Properties of a Dielectric Thin Film. *Electroanalysis*, 34(3):512–522, 2022.

Bahram Hosseini Monjezi, **Benedikt Sapotta**, Sarah Moulai, Jinju Zhang, Robert Oestreich, Bradley P. Ladewig, Klaus Müller-Buschbaum, Christoph Janiak, Tawheed Hashem, and Alexander Knebel. Metal-Organic Framework MIL-68(In)-NH2 on the Membrane Test Bench for Dye Removal and Carbon Capture. *Chemie Ingenieur Technik*, 94(1-2):135–144, 2022.

Benedikt Sapotta, Matthias Schwotzer and Matthias Franzreb. Practical Insights into the Impedance Response of Interdigitated Electrodes: Extraction of Relative Static Permittivity and Electrolytic Conductivity. *Electroanalysis*, *accepted*

Conference Contributions

Benedikt Sapotta, Haneol Kim, Hyun-Goo Kim, Yong-Heack Kang. Study on the Heat Flux Uniformity and Spillage Characteristics of a Rotating Flat Receiver for a Solar Furnace. *2018 KSES Spring Annual Conference*, Daegu. **Oral Presentation**

Benedikt Sapotta, Matthias Schwotzer, Christof Wöll, Matthias Franzreb. In Situ Monitoring of HKUST-1 Thin Film Growth by Impedance Spectroscopy. *14th International Workshop on Impedance Spectroscopy 2021*, Online. **Oral Presentation**

Benedikt Sapotta, Matthias Schwotzer, Christof Wöll, Matthias Franzreb. Impedimetric Analysis of Liquid Phase Partitioning into the nanoporous Copper Benzene-1,3,5-Tricarboxylate Metal-Organic Framework. *5th International Conference on Applied Surface Science 2022*, Palma. **Poster**